Fracture toughness and fracture energy of inorganic and non-metallic glass

Theany To

UNIVERSITE MATIERE BRETAGNE MOLECULES LOIRE ET MATERIAUX

UNIVERSITÉ DE RENNES 1

THESE DE DOCTORAT DE

L'UNIVERSITE DE RENNES 1
COMUE UNIVERSITE BRETAGNE LOIRE

ECOLE DOCTORALE N° 596
Matière Molécules et Matériaux
Spécialité : Mécanique des Solides, des Matériaux, des Structures et des Surfaces

Par

Theany TO

Fracture toughness and fracture energy of inorganic and non-metallic glass

Thèse présentée et soutenue à « Rennes», le « 27/02/19 »
Unité de recherche : Département Mécanique et Verres, Institut de Physique de Rennes, UMR 6251

Rapporteurs avant soutenance :

Veronique LAZARUS	Professeur	ENSTA
Cindy L. ROUNTREE	Resp. Projet	CEA

Composition du Jury :

Morten Mattrup SMEDSKJÆR	Professeur	AAU
Veronique LAZARUS	Professeur	ENSTA
Cindy L. ROUNTREE	Resp. Projet	CEA
Directeur de thèse		
Tanguy ROUXEL	Professeur	IPR

Invité(s)

Stephanie DESCHANEL	Maître de conférences	INSA-Lyon
Fabrice CELARIE	Maître de conférences	IPR
Clément ROUX-LANGLOIS	Dr., Prof. Lycée	PTSI

ពេលយើងមានអារម្មណ៍លំបាក យើងកំពុងរៀនអ្វីមួយ !

When we feel difficult, we learn!

Quand on se sent difficile, on apprend!

Acknowledgement

This work was supported by the European Research Council through the Advanced Grant 320506 (DAMREG) of the 7th framework program “Ideas”.

I would like to take this occasion to express my deep sense of gratitude to Prof. Tanguy Rouxel for being my supervisor during this three-year journey called PhD. Thanks for his encouragement, suggestions, lessons and friendship. I would also like to thank Drs. Fabrice Célarié and Clément Roux-Langlois for their help and advice. I am also thankful to Drs. Yann Gueguen and Patrick Houizot for providing help and idea from time to time.

I am sincerely thankful to Prof. Jean-Christophe Sangleboeuf, Dr. Jean-Pierre Guin and IPR staffs for their warm welcome during my stay in Department of Mechanics and Glasses, IPR.

It is my pleasure to work with Leonardo Sant’Ana Gallo, Zhao Yue Yao, Pièrre Mexeix, Garth Scannell, Kacper Januchta, Julien Moriceau, Christina Stabler and Tanguy Lacondemine. I would like to thank them for allowing me to break their beautiful glasses (under the name of cooperation). I do not forget Rodrigo, Corentin, Benjamin, Marion I, Marion II, Mariette, Eric, Didier, Raveth, Gildas, Mohamed, Taoufik, Guillaume, Gwénolé, Misaki as well as other PhD students for spending their time with me in the laboratory.

Also, special thanks to Rithymarady, N’Goan and Abdesamad for working with me during their internship for master degree. I want to thank also Mikael Le Fur, Vincent Burgand, Hervé Orain and Julien Chollet for their help in sample preparation and machine set-up.

My deepest appreciation goes to SBC association for providing me an accommodation during these years. I would particularly like to thank to Sambath, Sophy, Piseth, Pisey, Lyheng, Khundadino, Mongkul, Mme OU, Sounean, Yeakleang, Visal, Try and others who shared the accommodation and experiences with me during my PhD.

Last but not least, I would like to express my gratitude to my parents, brother and sister and friends for always encouraging, supporting and caring for all time.

Rennes,

January, 2019 Theany TO

Table of contents

I. General introduction

Glass is a fascinating material because of a unique combination of properties, such as the ability to be shaped at relatively low temperature (~$1.1T_g$) by viscoplastic forming, transparency, hardness, stiffness, and durability. Over the years, glass has been widely used in many applications as a structural material in the automotive sector, or in building industry, and as a material for nuclear waste confinement, optics, telecommunication, medicine and arts.

With this large demand, glass scientists have been looking for stronger and tougher glasses to improve the life duration of glass parts and to reduce the consumption of starting materials [1]. In order to meet these objectives, several techniques were developed. Thermal or chemical tempering induces compressive stresses at the surfaces of glass. By means of second phase particles or fibers (composite route) or in-situ precipitation of a crystallized phase (glass-ceramic route), it was attempted to improve the mechanical performance (hardness, toughness, strength) with some remarkable success [2–6].

Still, the intrinsic strength (that is the optimum strength reached in the absence of any extrinsic flaws) of glass, as measured for instance on pristine fibers, is much larger than the one used by glass engineers, and the one resulting from fracture experiments conducted on relatively large samples [7–13]. The theoretically calculated strength of window glass is about 35000 MPa [14] while the experimental tensile strength of a window float glass is about 125 MPa [9]. Flaws on glass surface (caused during manufacturing or transportation) prevent the glass from reaching its intrinsic strength. The tensile strength of a silica glass fiber, with a pristine surface, was measured in vacuum at 77 K and found of about 14000 MPa [15] while the one of a normal polished silica glass plate is about 100 MPa [10].

As for any brittle material, the strength of glass depends much on the flaw population characteristics (distribution, size, etc.). Besides, cracks are usually very sharp (even considered as atomically sharp) and fracture occurs with the typical features associated with brittleness (low fracture surface energy and toughness). Therefore, it is of paramount importance to estimate the intrinsic fracture toughness of glass, and to further examine what can be done by playing on the composition and on the microstructure.

I.1. Fracture mechanics of brittle materials

I.1.a. Fundamentals of fracture mechanics

A classical paper by Griffith in 1921 [16] explained the role of flaws in the fracture of brittle materials. A precursor to the this was the stress analysis by Inglis in 1913 [17]. Inglis analyzed a

plate containing an elliptical flaw with a length 2*c* (along the Y-axis) and a width 2*b* (along the X-axis) under a uniform applied tensile stress σ (**Fig. I-1**). The minimum radius of curvature (ρ) is at the vertex of the major-axis of the elliptical flaw and is expressed as $\rho = b^2/c$. The stress at the corner of the flaw (σ_c) is expressed as:

$$\sigma_c = \sigma\left(1+2\frac{c}{b}\right) = \sigma\left(1+2\sqrt{\frac{c}{\rho}}\right) \qquad \text{(I.1)}$$

Interestingly, in case $b << c$ (for a narrow flaw), $2\sqrt{(c/\rho)} >> 1$ and Eq. I.1 can be reduced to $\sigma_c/\sigma = \sim 2c/b = 2\sqrt{(c/\rho)}$. This ratio is the stress concentration factor at the border of the elliptical hole (long axis end).

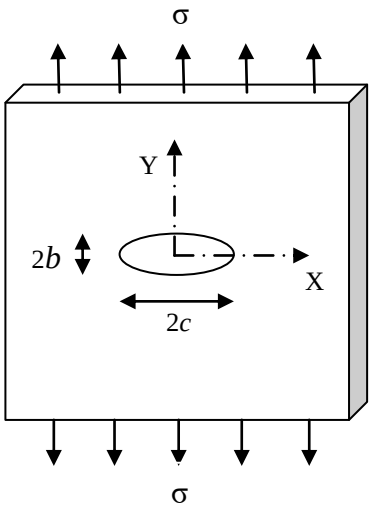

Fig. I-1: Plate containing elliptical flaw under uniform tensile stress

Starting from Inglis analysis, Griffith considered the case of an "infinitely" narrow elliptical flaw of length 2*c*, by supposing $b \rightarrow 0$ in **Fig. I-1**, subjected to a constant tensile stress. Griffith chose glass as a model material in his study as it is supposed that glass behaves in a linear elastic manner, and that the crack tip in glass is atomically sharp [18,19]. A relationship between the fracture strength and the fracture surface energy was formulated from the laws of energy conservation. The critical stress at which failure occurs (σ_f) is expressed as:

$$\sigma_f = \sqrt{\frac{2E'\gamma}{\pi c}}, \qquad \text{(I.2)}$$

where *E'* is Young's modulus *E* in plane stress, and $E/(1+v^2)$ in plane strain, where *v* is Poisson's ratio, γ is the fracture surface energy and *c* is the critical crack length. Eq. I.2 provides the dependence of the strength on the crack size, whereas *E'* and γ are dependent on the glass compositions. "*c*" in Eq. I.2 is usually much larger than the interatomic spacing, so that the strength is much smaller than the ideal intrinsic strength.

I.1.b. Ultimate strength of glass

For years, glass makers and glass researchers have tried to measure and predict the ultimate (or intrinsic) strength of glasses. Most models predict the intrinsic strength from the intrinsic strain of glasses. Gupta and Kurkjian [20] formed an expression to calculate the intrinsic failure stresses from high intrinsic failure strain of a glass by taking into account the fact that the elastic behavior can no longer be considered linear in regard of the high level of stress (> 10 GPa). They proposed the following expressions for the non-linear elastic behavior (σ: stress; ε: strain):

$$\sigma = Y_0.\varepsilon + \frac{Y_1}{2}\varepsilon^2 + \frac{Y_2}{6}\varepsilon^3, \tag{I.3}$$

$$Y(\varepsilon) = Y_0 + \frac{Y_1}{2}\varepsilon + \frac{Y_2}{6}\varepsilon^2, \tag{I.4}$$

where Y_0, Y_1 and Y_2 are second-, third-, and fourth-order modulus, respectively. The intrinsic failure strain (ε_f) is obtained when $Y(\varepsilon_f)=0$. Although they showed that the fourth-order modulus was necessary and enough to obtain a promising intrinsic strain and stress results, it is still questionable whether higher order modulus should be included in the expressions. Kurkjian *et al*. [7] predicted the intrinsic failure strain from the energy landscape-based model. As a glass forms from liquid during cooling at a fictive temperature (T_f), the glass transition barrier in the potential energy landscape-based model is then proportional to T_f. Considering the correlation between intrinsic failure and glass transition barrier, the intrinsic failure can be expressed as:

$$\varepsilon_f = \frac{\theta}{1 + \frac{Y_1}{3Y_0}\theta^{1/2} + \frac{Y_2}{12Y_0}\theta}, \tag{I.5}$$

where $\theta = (2\lambda RT_f/VY_0)^{1/2}$, λ is a dimensionless constant, R is the gas constant, and V is the molar volume of the glass. The high values of θ correspond to high values of failure strain. They concluded that the parameter (T_f/VY_0) is also a measure of the intrinsic strain to failure and may be useful to study the composition dependence. However, there were no experimental investigations to support this approach. Other modeling routes include microscopic molecular dynamics (MD) simulations to predict the intrinsic failure stress. Molecular dynamics simulation is a numerical tool based on classical dynamics and used to study interaction between atoms and molecules. Interatomic potential and initial atomic configuration are the main parameters. Soules and Busby [21] used repulsive and columbic attractive terms in the Born-Mayer-Huggin (BMH) form in their MD study of silica glass strength. They found failure strain of 23% and failure strength of 24 GPa. Using the same potential, Simmons [22] found a failure strain of 20% and failure strength of 30 GPa in his study of silica glass in uniaxial tension. Using Beest-Kramer-Santen (BKS) potential, Liao [23] found failure strain of 22% and failure strength of 13 GPa. These three simulators concluded that the fracture process involved the nucleation, growth, and coalescence of cavities.

Most experimental investigations assessed the intrinsic strength of glasses in uniaxial tension or two-point bending on glass fibers supposed to have a pristine surface [15,24–27].

I.1.c. Crack tip and glass fracture

How sharp the crack tip of glass is and how glass fractures, are still matters of controversy. Irwin-Orowan [28] proposed a small-scale zone for non-linear element, which eliminates the crack-tip singularity as shown in **Fig. I-2**. In this situation, the applied stress is transmitted to the crack-tip process zone by the linear elastic region. Two hypotheses can be considered. In the first one, the fracture occurs in a brittle manner, i.e. $G_c \approx 2\gamma$, where G_c is the critical crack extension force and γ is the surface energy, and the crack tip is atomically sharp. In the second one, fracture occurs in a ductile plastic manner, i.e $G_c >> 2\gamma$, and the crack tip is blunted.

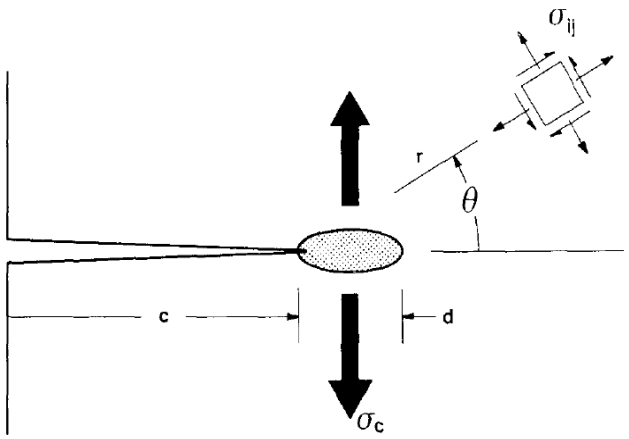

Fig. I-2: Parameters of crack-tip zone model [18].

In the case of metallic and polymeric materials, G_c is several orders of magnitude greater than 2γ as fracture occurs according to plastic crack-tip separation process [18]. This means that most of the energy spread in the fracture process is not used to create the new surface but instead is dissipated in the irreversible deformation of the surrounding region. In the case of brittle materials, measured G_c is mostly found to be 2 or 3 times larger than the predicted 2γ value, and the measurements (as well as the predictions) are usually not very accurate. In a classical study of glass fracture, Marsh [29] suggested that fracture of glass was ductile plastic and the crack tip was blunted. On the contrary, Hillig [30] concluded to a sharp crack tip. Lawn et al. [18] observed the crack tip process zone in four different ceramics by means of transmission electronic microscopy (TEM) and concluded that the crack tip is atomically sharp for ideally brittle solids.

I.1.d. Slow crack growth

When a glass sample is fractured at relatively low velocity (typically $\leq \sim 10^{-4}$ m·s^{-1}) in a humid environment, a slow crack growth is mostly observed, at $K_I << K_{Ic}$, which is explained by water molecules reacting with glass at the crack tip, according to a stress-corrosion chemical process.

Wiederhorn [31] used double cantilever beam (DCB) method to study this "fatigue" like behavior. He found that the stress intensity factor, K_I, increases with increasing crack velocity until some thresholds are reached, where the crack is too fast for water molecules to meet its front (**Fig. I-3**). Moreover, in order to reach the thresholds, one needs to produce a greater crack velocity at large humidity content; for instance, in order to reach the threshold a crack velocity of ~$2 \cdot 10^{-7}$ m·s^{-1} is required at a relative humidity of 0.017 % while ~$2 \cdot 10^{-4}$ m·s^{-1} is required at a relative humidity of 100 %. Later on, Michalske and Freiman [32] created a successful model (**Fig. I-4**) to study the effect of humidity. This effect was studied more recently by means of atomic force microscopy (AFM). Using AFM, Célarié *et al.* [33] concluded that the fracture process in a window glass involves the nucleation, growth, and coalescence of cavities, consistently with works by Soules and Busby [21], Simmons [22] and Liao [23] on the intrinsic strength of glass by means of MD simulation. Notwithstanding, Guin and Wiederhorn [34], also used AFM to study the profile of two opposite fracture surfaces (**Fig. I-5**) obtained for K_I near the fatigue threshold, and found that there has not been any evidence of cavitation.

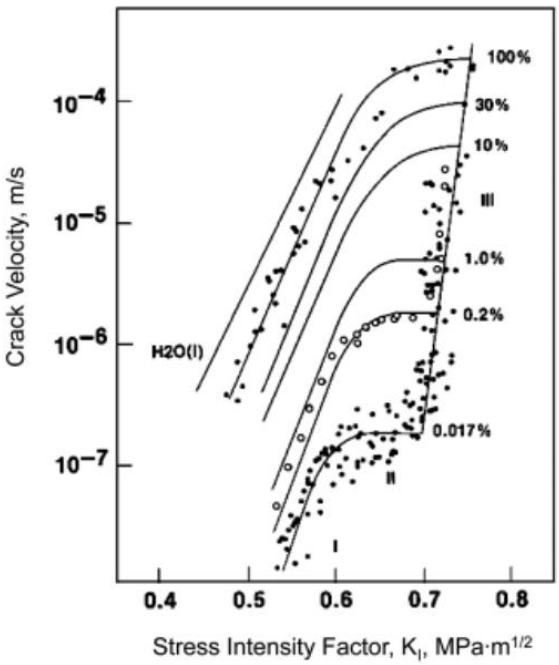

Fig. I-3: Crack growth data in soda-lime-silica glass. After Wiederhorn [31]. [109]

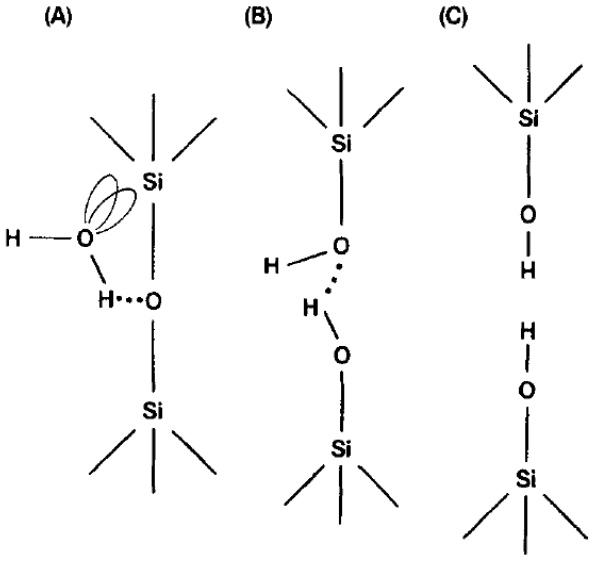

Fig. I-4: Representation of the proposed reaction between water and a strain Si-O-Si bond at the crack tip. Reaction step involve; (a) adsorption of water to Si-O bond, (b) concerted reaction involving simultaneous proton and electron transfer and (c) formulation of surface hydroxyls [32].

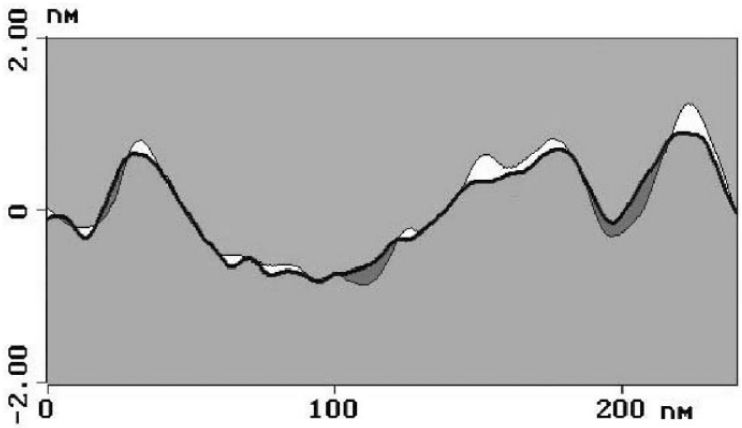

Fig. I-5: Parameters of crack-tip zone model [18].

I.2. Fracture toughness of brittle materials

In the 1950s, Irwin and Orowan [35–37] extended the concept of Griffith and popularized the concepts of 'stress intensity factor' and 'critical stress intensity factor'. The critical stress intensity factor in the crack opening mode (or fracture toughness, K_{Ic}) is mostly determined by means of the expression below:

$$K_{Ic} \propto \sigma\sqrt{c} \ (\propto : \text{proportional}), \tag{I.6}$$

where σ is the actual fracture stress of a sample with a pre-existing flaw of length c (critical crack size). The proportionality constant in Eq. I.6 (typically ~1-2) depends on the loading characteristics, and on the specimen and crack geometries.

In spite of the paramount importance of K_{Ic} for brittle materials, the determination of the intrinsic characteristic is still challenging. There is no standard method in the case of glass yet, but for ceramics. Many methods were developed and applied on measuring the K_{Ic} of glasses. In the 1970s – 1980s, many researchers used flat slab methods, such as Double Cantilever Beam (DCB) or Double Torsion (DT) [38–40]. Just a bit later in the middle 1970s, another method namely – Indentation Fracture (IF), mostly Vickers (Vickers Indentation Fracture, VIF), was proposed and calibrated using previous methods. VIF became rapidly popular because of its ease, simplicity, and little time and cost consuming [41–45]. Later on (mostly after 1980) the beam methods such as Single-Edge Notched Beam (SENB), Single-Edge Precracked Beam (SEPB), Chevron-Notched Beam (CNB), Surface-Crack in Flexure (SCF), etc. were introduced and applied on glass [38,39,46–57]. Common fracture toughness test configurations and advantages and drawbacks of these methods are reported in [54] and [49]. Three methods, cracks (artificial flaws) were introduced by means of the different methods, namely i) Vickers Indentation Fracture (VIF), ii)

Chevron Notched Beam (CNB), iii) Single edge precrack through a beam using a bridge-flexure anvil (SEPB), are presented below.

I.2.a. VIF

VIF is based on the measurement of the indentation corner cracks and relies on idealized crack pattern under the indent. VIF is then applicable to small specimens and suitable to study surface damage and the onset of crack initiation. However, there are some concerns while applying this method to determine the fracture toughness of glasses. The first concern is the determination of the crack pattern under the indent. The crack pattern was, mostly, divided into radial-median (also called half-penny) and Palmqvist (surface-radial) as shown in **Fig. I-6** and an exhaustive review can be found in [44,45]. Niihara *et al.* [58] reported the two different patterns by showing the excellent linearity when they plotted a dimensionless fracture toughness parameter versus crack length/indentation length ratio l/a and c/a, where c is the corner crack length and $l = c - a$. Following the proposition of [58], Rizkalla *et al.* found that most glasses in their study were of the Palmqvist type rather than radial-median. However, for soda-lime-silicate glass, they argued that the crack pattern remained questionable with the proposition of Niihara *et al.* [58]. Ray and Dutta [59] reported the same problem while using VIF method to determine the fracture toughness of soda-lime-silicate glass from fourteen different formulae. They also reported that the crack pattern in soda-lime-silicate glass could be either Palmqvist or radial-median type depending on the applieded load. Despite those careful observations and the numerous studies on various glasses, the crack patterns under the indents remain debatable. Niihara *et al.* [58] and Lankford [60] suggested that when the c/a ratio is lower than 2.5 the surface cracks extending from the indentation corners remain near the surface and form the so-called Palmqvist pattern, as opposed to the radial-median pattern. In VIF method, fracture toughness was mostly calculated using Eq. I.7 for radial-median crack pattern [61] and Eq. I.8 for Palmqvist crack pattern [58].

$$K_C = (0.016 \pm 0.004)(E/H)^{1/2}.P/c^{3/2} \quad \text{(I.7)}$$

$$K_C = 0.018\, E^{2/5}H^{3/5}a.l^{-0.5} \quad \text{(I.8)}$$

where E is Young's modulus, H is Meyer's hardness ($H = P/(2a^2)$), where P is the indentation load, a is the half indentation diagonal length, c is the half crack length, and l is equal to $c - a$ as shown in **Fig. I-6**. It is noteworthy that the prefactor in the right-hand side of Eqs (I.7) and (I.8) were calibrated using chiefly ceramic materials and including a soda-lime-silica glass. Unlike most polycrystalline ceramics, glasses are known to allow for a significant densification upon indentation loading, because of i) pressure in the GPa range beneath the indenter and of ii) a relatively large amount of free volume [62]. The physics behind these equations (isochoric plasticity) is thus put

into question in the case of glasses, and K_{Ic} values obtained by means of self-consistent techniques on various glasses might hardly compare with VIF ones, with perhaps the exception of soda-lime-silica glass.

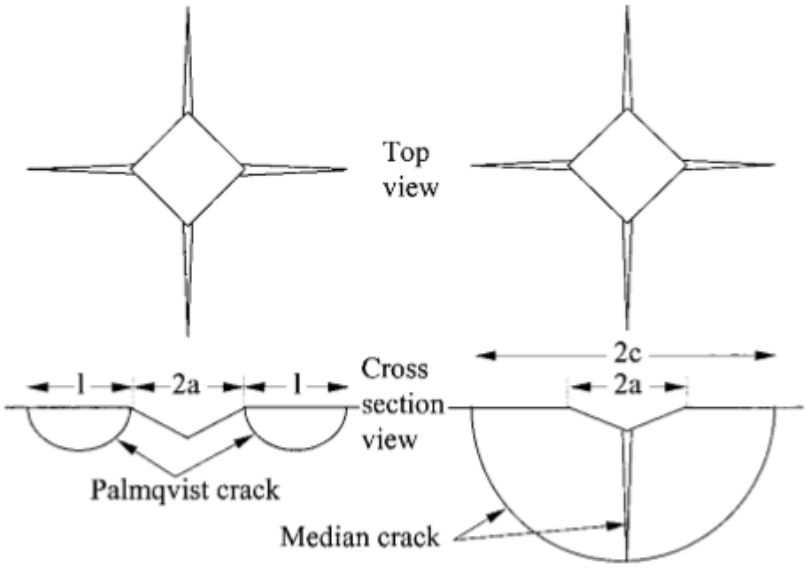

Fig. I-6: Geometry of Palmqvist (left) and radial-median (right) cracks around Vickers indentation [59].

I.2.b. CNB

CNB method is known as a self-consistent standard method [63]. The method requires the machining of a V-shape notch (so-called chevron) in the middle of a beam. This shape is achieved by means of a two-step cutting procedure, involving two straight through cuts. The chevron-notched beam is then loaded in bending mode (the tip of the remaining V-shape ligament being in the tensile side). Under the assumption that a planar crack with a straight front is propagating, the value of the maximal load (which corresponds to a critical crack extension) was tabulated as a function of K_{Ic} and the specimen geometry [64]. There are two stages in the performance of CNB technique (the note machining and the final bending fracture) [63–65]. The difficulty in CNB method is to properly cut the chevron-notch. In the final fracture, three- or four-point bending can be used according to the length of the specimen. An advantage of CNB test is the

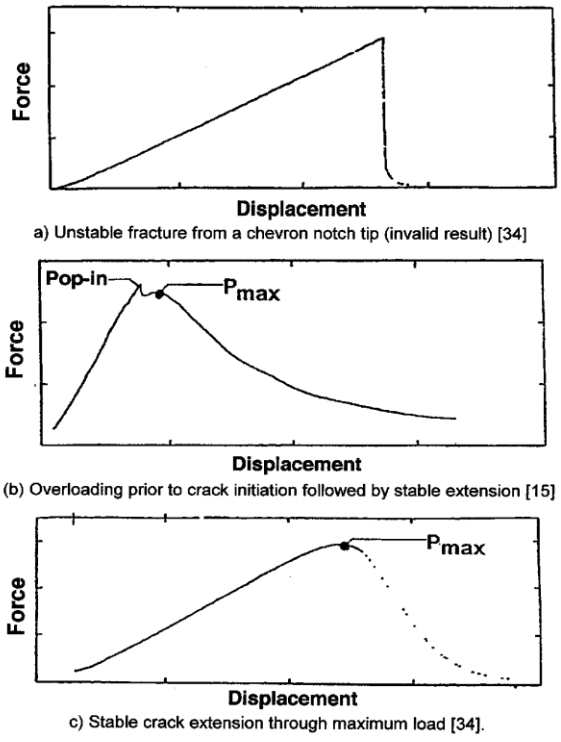

Fig. I-7: Illustrative Applied Force-Displacement Curve: (a) Unstable fracture from Chevron Tip (Invalid), (b) Overloading Prior to Crack initiation Followed by Stable Extension and Stable Crack Extension Through Maximum Force [61].

increase of specimen compliance as the crack front propagates from the chevron notch tip to bigger and bigger chevron notch section, which results in, mostly, stable test as shown in **Fig. I.7-c**. After measuring the geometry in-situ, K_{Ic} can be calculated either using the maximum load (P_{max}) or from the work of fracture (*wof*),

$$wof = \int_0^{u_f} P \mathrm{d}u \,, \tag{I.9}$$

where P is the load (Z-axis) and u is the displacement (Z-axis), u_f is the final deflection corresponding to complete fracture, and *wof* is related to the fracture surface energy by, $wof = 2\gamma A$, where γ is the fracture surface energy, and A is an in-plane fracture surface (geometrical area). K_{Ic} can then be calculated from the equation proposed by Irwin-Griffith similarity principle [35]:

$$K_{Ic} = \sqrt{2\gamma E'}, \tag{I.10}$$

where E' is taken equal to E in the case of plane stress and to $E/(1-\nu^2)$ in case of plane strain. According to the specimen geometry, K_{Ic} can be calculated from the formula developed by Munz *et al.* [66]:

$$K_{Ic} = \frac{P_{max}}{B\sqrt{W}} Y^*_C \,, \tag{I.11}$$

where B and W are the specimen broadness and height respectively, and Y^*_C is the critical dimensionless geometric coefficient calculated from both Slice and STCA (Straight Through Crack Assumption) approximation [64,67–69], and associated with the maximum load (P_{max}). In the Slice model, the fracture chevron section is divided into many narrow slices and each slice is taken as a straight-through cracked section. In the STCA model, the fracture chevron section is taken as a straight-through cracked section with the same crack length and thickness as the chevron crack front (b in **Fig. I-8**). Comparing with numerical simulation, Y^*_C for chevron-notch shape with $a_1/W \geq 1$ is applicable for STCA approximation and vice versa. Recently, ASTM-C1421 set chevron-notch test specimens into four specific geometries corresponding to four specific formulae of Y^*_C.

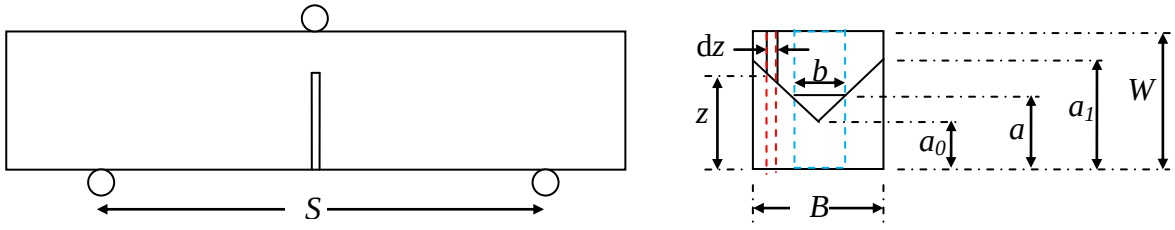

Fig. I-8: Three-point bending with chevron notch geometry. The red-dash box shows the slice model geometry and blue-dash box shows the STCA model geometry.

I.2.c. SEPB

SEPB is a self-consistent method that was originally developed for structural ceramics, and where an "ideal" crack (atomically sharp) is introduced [63,70]. This method involves two steps: precracking stage, and final fracture stage. In the precracking stage, indentation (normally Vickers or Knoop indentation) or straight notch was performed on parallelepiped specimens. The indented specimen was then placed into a bridge-indentation flexure (**Fig. I-9**) by positioning the indented or notched surface on the groove of the anvil. During compression, the lower part of the specimen is loaded in tension while the upper is submitted to a compressive stress. When the load is sufficient, the pop-in precrack is induced, which extends until the crack front reaches the side in compression. Similar to the CNB, the precrack specimen is fractured in three- or four-point bending.

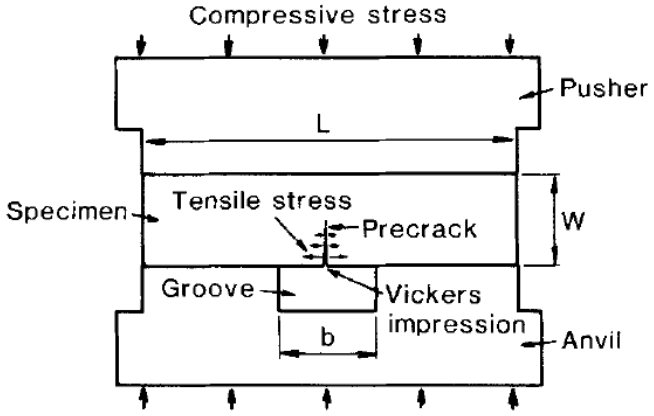

Fig. I-9: Schematic of bridge-indentation method. Specimen is sandwiched by a flat pusher and an anvil having a central groove [70].

I.3. Composition dependence of K_{Ic} of glass

I.3.a. Previous experiments

Influence of compositions

Shinkai *et al.* [71] studied E and K_{Ic} of ternary PbO-ZnO-B_2O_3 glasses with B_2O_3 of 30 to 70 mol% and PbO/ZnO of 1:0, 3:1, 1:1, 1:3 and 0:1. E and K_{Ic} were measured by resonance frequency and surface crack in flexure (SCF) methods, respectively. In SCF technique, Vicker indentation of a load of 5 N was indented in the tensile surface of the tested specimens, and later, in order to remove the residual stress, the indented specimens were annealed five minutes. They found that both E and K_{Ic} were increased with increasing of B_2O_3 content for all PbO/ZnO ratios, and were decreased with increasing of PbO/ZnO ratio for all B_2O_3 level (**Fig. I-10**). They also concluded that viscous flow at the crack tip in their studied glasses is very limited.

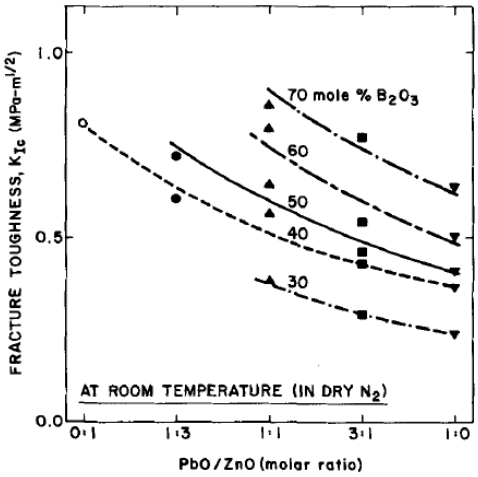

Fig. I-10: Effects of PbO/ZnO ratio and B2O3 content on KIc for the PbO-ZnO-B2O3 glasses [71].

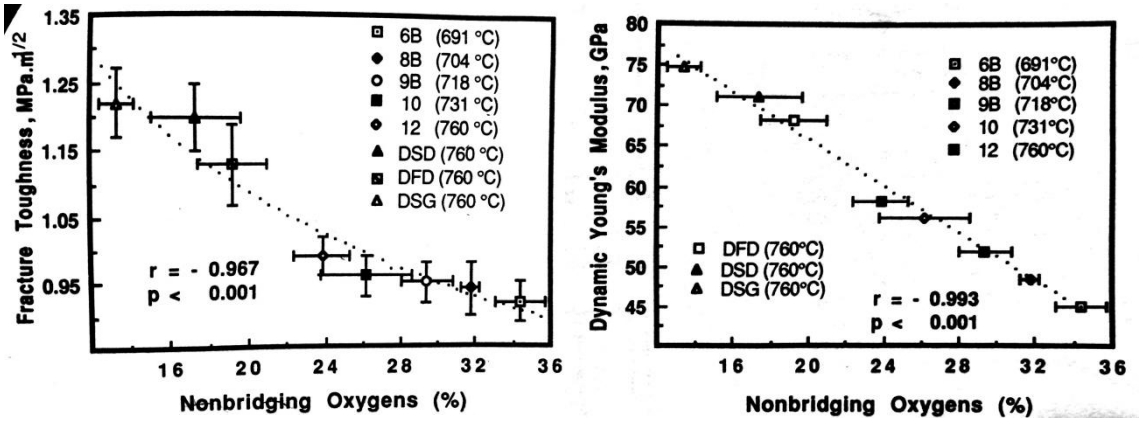

Fig. I-11: Effect of nonbridging oxygens on the fracture toughness (left) and dynamic Young's modulus (right) of eight glass formulation synthesized by wet-chemical methods [72].

Rizkalla *et al.* [72] studied the effect of nonbridging oxygen on the fracture toughness of five compositions of SiO_2-Na_2O-K_2O systems (noted as 6B, 8B, 9B, 10 and 12 in **Fig. I-11**) and three compositions of SiO_2-Al_2O_3-K_2O-Na_2O-CaO-MgO-Li_2O-TiO_2 systems (noted as DSD, DFD and DSG in **Fig. I-11**). They used ultrasonic method to determine Young's modulus *E* and VIF method by means of Blendell's equation [73] to calculate K_{Ic} of these eight glass compositions. They found that both *E* and K_{Ic} decreased while the nonbridging oxygen increased (**Fig. I-11**). By increasing the nonbridging oxygen from ~13 % to ~34 %, *E* decreases from ~75 GPa to ~45 GPa and K_{Ic} decreases from 1.22 to 0.92 MPa.√m. This trend is associated with the relative packing density, the weakening of the Si-O network and the higher concentration of ionic bonds in the network.

Miyata and Jinno [74], on the study of K_{Ic} and γ of PbO-B_2O_3 glasses by means of VIF method using Lawn and Fuller's equation [75], showed that the increasing of PbO from 20.3 to 60 mole% lead to the decreasing of γ from 4 to 2.24 $J \cdot m^{-2}$ (in **Fig. I-12** with k = 0.7) that is according to the decreasing of K_{Ic} from 0.83 to 0.5 MPa.√m.

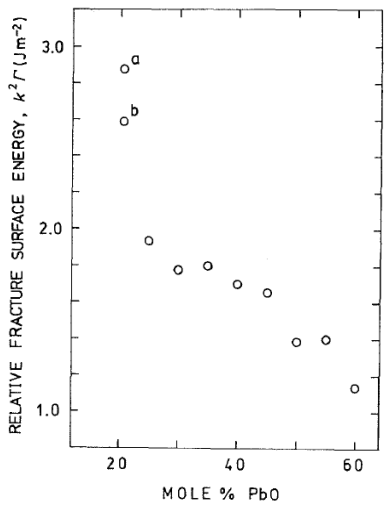

Fig. I-12: Variation of relative fracture surface energy of PbO-B_2O_3 glasses with mole% [74].

Miura *et al.* [76] studied the unusual elastic and mechanical behaviors of copper phosphate ($yCuO_x$-$(100 - y)P_2O_5$ with y = 45, 50, 55) glasses with difference copper valence states ($R(Cu^+) = Cu^+/(Cu^+ + Cu^{2+})$) at room temperature and relative humidity of 64 %. They found that to increase the fracture toughness K_{Ic} as well as ν and γ_f, they needed to increase $R(Cu^+)$. On the other hand, the increasing of this copper valence states lead to the decreasing of T_g, H_v, *E*, θ_D.

Influence of a phase-separation and glass structure

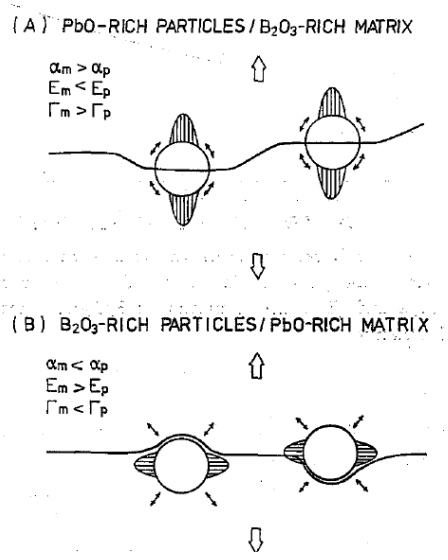

Fig. I-13: schematic of fracture paths expected for $PbO\text{-}B_2O_3$ immiscible glasses. Arrows around each particle represent residual thermal stresses in the matrix. Shaded areas represent stress-concentrated regions in the matrix produced by elastic mismatch. The subscripts *m* and *p* refer to the matrix and particle, respectively [77].

Miyata and Jinno [77] studied mechanical properties of $PbO\text{-}B_2O_3$ phase-separated glasses: B_2O_3-rich particles/PbO-rich matrix and PbO -rich particles/B_2O_3-rich matrix. The effect of amount of each phase and microstructure on the properties was proved. Normally, the second phase dispersion in glass leads to the increase of fracture surface energy as well as fracture toughness. This is because the second phase takes a role as obstacle for the crack growth extension. On the other hand, second phase dispersion might have micro structure crack which lead to lower fracture surface energy and toughness. For glass composite with B_2O_3-rich matrix, the fracture part is expected to go through the particle (**Fig. I-13A**). However, during seeking the easy-breaking part in the material, the crack suffers local deviation from its previous part plane. Fracture surface energy and toughness were found to be dependent of volume fraction of dispersion. In case of composite with PbO-rich matrix, the theory of Lange-Evans [78,79] can explain the increase in γ with increasing dispersion (**Fig. I-13B**).

Seal *et al.* [80] studied on the effect of separated phases on K_{Ic} of ternary $SiO_2\text{-}B_2O_3\text{-}Na_2O$ glasses by means of VIF method using Lawn and Fuller's equation [75]. In this ternary system, they fixed the Na_2O composition to equal to 10 wt% and varied the other two compositions by increasing SiO_2 from 20 to 60 wt%. They found that K_{Ic} increases from 0.98 to 1.54 MPa·√m (for 20 to 60 wt% of SiO_2), and concluded that phase separation have improved the fracture toughness of the glass studied.

When some crystals or some nano-structure show up in the glass matrix, the fracture toughness is mostly changed. Schultz *et al.* [81] studied on the single crystal cleavage of brittle materials. They showed that K_{Ic} of brittle polycrystalline aggregate is greater than that of single crystal cleavage

because the polycrystalline aggregate lacks the continuity of cleavage crack. Nishiyama *et al.* [82] studied on synthesis of nanocrystalline bulk SiO_2 stishovite with very high toughness. K_{Ic} of nanocrystalline bulk SiO_2 is eight times greater than that of stishovite single crystal. On the study of electrically conductive grapene nanoplatelet/boron carbide (GNP/B_4C) composites with high hardness and toughness, Tan *et al.* [83] indicated that only with 4 vol% of GNPs, K_{Ic} increases from 2.32 to 5.26 MPa·√m.

I.3.b. Modelling approaches

Different approaches were developed worldwide to predict or to calculate fracture toughness in order to understand the composition dependence. Some are using simple pictures of the solid or of the atomic organization while others are using modern numerical tools such as density functional theory (DFT), ab-initio molecular dynamic (MD) simulation and topological constraint approaches (TC) [1,84–93].

TC is a theory in which a mechanical truss replaces and simplifies the complex atomic structure. In this theory, atoms are connected to each other by the chemical interactions constraining the bond lengths and angles, and the connection can be presented in three states: flexible, isostatic and rigid [94–96]. In flexible connection (the number of degree of freedom per atom $n_c = 3$), degrees of freedom allow for local deformation; in isostatic connection ($n_c < 3$), the system is rigid but free of eigen-stress; and in rigid ($n_c > 3$), the connection is blocked and the eigen-stress is present. Bauchy *et al.* [97] used the TC approach in combination with MD to study the fracture toughness of densified sodium silicate glasses (NS) and calcium-silicate-hydrates (CSH). They found that the resistances to fracture for both glasses and their fracture toughness behaviors are the most optimal in isostatic system. They concluded that this theory is promising for composition design of tougher materials.

For the simple approach using the atomic organization of glass, the theoretical value for toughness ($K_{Ic}^{the.}$) was calculated by means of expression Eq. I.10 using experimental values for the elastic moduli and an estimation of the theoretical fracture surface energy ($\gamma_{the.}$) based on the interatomic bond energy and the bond concentration along a fracture surface, assuming the easiest path for the crack [86]. King and Antonelli [90] use this approach by converting the fracture energy of crystalline material to that of amorphous material by the ratio of the density of the amorphous material versus the density of the single crystalline material.

Rouxel [86] has predicted the fracture surface energy of a variety of glasses ranging from amorphous silica to metallic glasses and demonstrated a good agreement between the SEPB experiment and the modelling when the diatomic energy (fission enthalpy) is considered. On the other hand, when using the compound dissociation enthalpy, he found that the theoretical toughness is somewhat smaller than the one of the experiment ($K_{Ic,theo} \approx 0.7 K_{Ic,exp}$). He has predicted the crack path in the glass matrix and drawn the relation between the fracture toughness and the glass compositions. He has also collected data of fracture toughness of glasses from chalcogenide group to metallic group and has simply summarized them in a graphic (**Fig. I-14**).

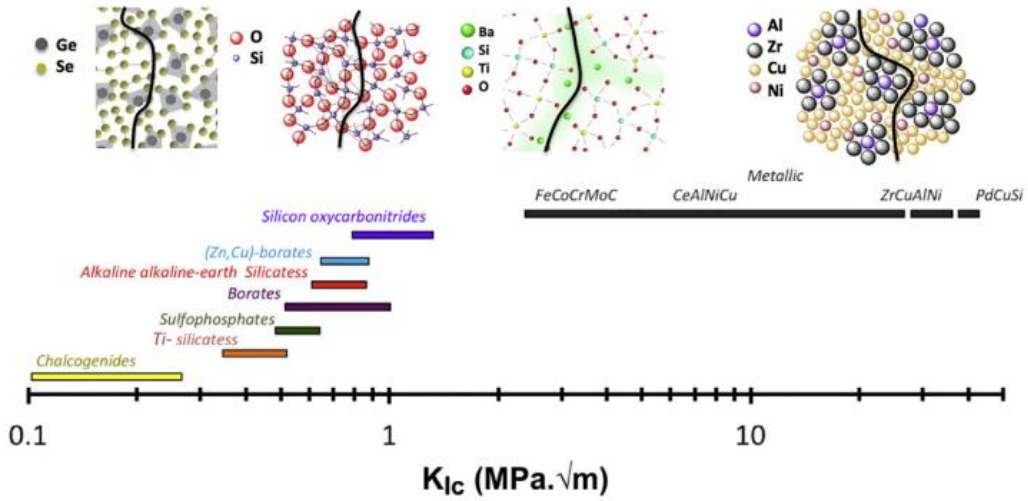

Fig. I-14: The apparent fracture toughness of glasses, as obtained by means of various experimental methods. The schematic drawings depict the expected crack path, tending to follow the weakest links of the atomic network (for example the Ba-O bonds in the BaO(30)-TiO2(30)-SiO2(40) glass) [86].

Table 1. 1: Glass compositions investigated in this research work.

Glass	**Compositions (mol%)**	K_{Ic}	**Ref.**
Silica	SiO_2(100)	0.69	Corning
Planilux	SiO_2(72)Na_2O(13.4)CaO(9.6)MgO(4)Al_2O_3(0.6)	0.70	Saint Gobain
Optiwhite	SiO_2(72.7)Na_2O(13)CaO(8.8)MgO(4.3)Al_2O_3(1)	0.67	Pilkington
Borofloat33	SiO_2(81)Na_2O(4)B_2O_3(13)Al_2O_3(2)	0.65	Schott
BK7	SiO_2(70)Na_2O(9.5)B_2O_3(11.5)K_2O(7.5)BaO(1.5)	0.82	
Series1		2.02	Ivoclar Vivadent AG R&D
Series2		3.06	
Series3		4.46	

	$SiO_2(25)Na_2O(25)B_2O_3(50)$	0.66	Kacper JANUCHTA, AAU (Denmark)
	$SiO_2(50)Na_2O(25)B_2O_3(12.5)Al_2O_3(12.5)$	0.79	
	$Na_2O(25)B_2O_3(62.5)Al_2O_3(12.5)$	0.67	
	$SiO_2(37.5)Na_2O(25)B_2O_3(12.5)Al_2O_3(25)$	0.58	
	$SiO2(25)Na_2O(25)B_2O_3(25)Al_2O_3(25)$	0.58	
	$Na_2O(25)B_2O_3(45)Al_2O_3(30)$	0.67	
C1-SiOC	$SiO_2(70.2)SiC(29.3)C_{free}(0.5)$	0.73	Christina STABLER, TUD (Germany)
C12-SiOC	$SiO_2(54.8)SiC(14.1)C_{free}(31.1)$	0.99	
SiHfOC	$SiO_2(63.2)SiC(13.4)C_{free}(18.7)HfO_2(4.6)$	0.99	
SiZrOC	$SiO_2(60.8)SiC(14.5)C_{free}(16.9)ZrO_2(7.8)$	0.91	
x00	$SiO_2(70)BaO(30)$	0.61	Pièrre MEXEIX, UR1 (France)
x01	$SiO_2(60)TiO_2(10)BaO(30)$	0.55	
x02	$SiO_2(50)TiO_2(20)BaO(30)$	0.51	
x03	$SiO_2(40)TiO_2(30)BaO(30)$	0.42	
PCB_0	$PbO(50)B_2O_3(50)$	0.28	Zhao yue YAO, UR1 (France)
PCB_1	$PbO(49)CuO(1)B_2O_3(50)$	0.39	
PCB_10	$PbO(40)CuO(10)B_2O_3(50)$	0.42	
PCB_20	$PbO(30)CuO(20)B_2O_3(50)$	0.50	
PCB_30	$PbO(20)CuO(30)B_2O_3(50)$	0.53	
ZCB_0	$ZnO(50)B_2O_3(50)$	0.40	
ZCB_1	$ZnO(49)CuO(1)B_2O_3(50)$	0.56	
ZCB_10	$ZnO(40)CuO(10)B_2O_3(50)$	0.71	
	$SiO_2(86)Na_2O(10)TiO_2(4)$	0.68	Garth SCANNELL, RPI (USA)
	$SiO_2(81)Na_2O(15)TiO_2(4)$	0.61	
	$SiO_2(76)Na_2O(20)TiO_2(4)$	0.61	
	$SiO_2(71)Na_2O(25)TiO_2(4)$	0.60	

I.4. Temperature dependence of properties of glass

For an homogenous material adapting an elastic behavior, the Irwin-Griffith similarity principle give: $K_{Ic} = \sqrt{(E\gamma/(1-\nu^2))}$. At the atomic scale, Young's modulus (E) can be related to the force required to change the interatomic spacing [98]. For a given atomic displacement from equilibrium, the force is usually smaller as the temperature goes up. This results in a decrease of the elastic moduli as the temperature is increased. Such a trend was observed on a window glass [47,99], with a slow decrease of E from RT to T_g, and a rapid drop beyond T_g. However, Shinkai's [47] and

Spinner's [100] experiments on fused silica glass from room temperature to about T_g showed the opposite trend i.e. E of fused silica glass slightly increased. Poisson's ratio ν at elevated temperature from room temperature to about T_g was shown to slightly increase in both float and silica glasses [47]. High temperature measurement of the fracture toughness are scarcely reported, and most of them are on ceramics and glass ceramics [101–108] and only a few studies on glasses [39,47,99].

I.5. Objectives and outline

In order to assess the problem of surface flaws and to evaluate the strength of glass parts with controlled surface flaws, the first part of the present work is focused on bi-axial flexure experiments. The ring-on-ring configuration was chosen in the experiment, and a-SiO_2 and a window float glass with different surface conditions were studied. The aim of this experiment is to determine the critical surface flaw size of the 6 µm diamond paste polish and sand blasting treated a-SiO_2 glass as well as its strength and reliability and compare those parameters to the as-processed float glass. The work is presented in chapter 2 (paper I).

The second objective of this work is to identify a suitable experimental method to measure the fracture toughness of glass and to optimize the experimental protocol to reach reliable data with a minimum amount of trials. SEPB, CNB and VIF methods were applied to four oxide glasses with Young's moduli ranging from 64 GPa to 82 GPa. A home-made uniaxial mechanical machine was designed and equipped with ceramic set-up and camera, in order to get stable fracture tests, so that K_{Ic} can be estimated either from the critical load for crack extension or from the overall energy spent to create the fracture surface. Since the experiment is performed in room environment, the possibility for stress-corrosion was also considered. These researches are presented in chapter 3 (paper II).

The third objective of the present work is to study the composition dependence of fracture toughness. The SEPB method (paper II) was applied to commercial glasses and to laboratory glasses as well. Glass ceramics and ceramics were also studied. The Na_2O-Al_2O_3-B_2O_3-SiO_2 glass system with fixed soda content is studied in chapter 3 (paper III). Then four dense SiOC glass ceramics were investigated. Two glass ceramics with two different amounts of segregated carbon were synthesized and then toughness was investigated to highlight the impact of the segregated carbon. The other two glass ceramics consist of 5 vol. % of zirconium or hafnium and the impact of these two additives was also investigated and presented in chapter 4 (paper IV). The last part is focused on laboratory glasses, glass ceramics and ceramics, and reported as complements in chapter 4.

The fourth objective of the research work is to study the temperature and environment dependences of fracture toughness. The SEPB method (paper II) was applied to three grades of glass with different transition temperatures, T_g, at elevated temperatures. Each grade was tested at different temperatures: from room temperature to $1.11T_g$. Another SEPB experiment was introduced in an inert atmosphere (in a close box filled with argon gas) at ambient temperature to assess the influence of stress-corrosion. This is the first time that both precrack and bending steps in the SEPB method are performed in inert atmosphere (paper V).

I.6. References

[1] L. Wondraczek, J.C. Mauro, J. Eckert, U. Kühn, J. Horbach, J. Deubener, T. Rouxel, Towards ultrastrong glasses, Adv. Mater. 23 (2011) 4578–4586.

[2] R.D. Rawlings, Bioactive glasses and glass-ceramics, Clin. Mater. 14 (1993) 155–179.

[3] V.M. Sglavo, D.J. Green, Flaw-insensitive ion-exchanged glass: II, production and mechanical performance, J. Am. Ceram. Soc. 84 (2001) 1832–1838.

[4] M. Bornapour, M. Celikin, M. Cerruti, M. Pekguleryuz, Magnesium implant alloy with low levels of strontium and calcium: The third element effect and phase selection improve bio-corrosion resistance and mechanical performance, Mater. Sci. Eng. C. 35 (2014) 267–282.

[5] I.W. Donald, Methods for improving the mechanical properties of oxide glasses, J. Mater. Sci. 24 (1989) 4177–4208.

[6] B.M. Novak, Hybrid nanocomposite materials-between inorganic glasses and organic polymers, Adv. Mater. 5 (1993) 422–433.

[7] C.R. Kurkjian, P.K. Gupta, R.K. Brow, The strength of silicate glasses: what do we know, what do we need to know?, Int. J. Appl. Glas. Sci. 1 (2010) 27–37.

[8] I. Naray-Szabo, J. Ladik, Strength of silica glass, Nature. 188 (1960) 226–227.

[9] M.H. Krohn, J.R. Hellmann, D.L. Shelleman, C.G. Pantano, G.E. Sakoske, Biaxial flexure strength and dynamic fatigue of soda--lime--silica float glass, J. Am. Ceram. Soc. 85 (2002) 1777–1782.

[10] C.A. Klein, Characteristic strength, Weibull modulus, and failure probability of fused silica glass, Opt. Eng. 48 (2009) 113401-1–10.

[11] T.C. Baker, F.W. Preston, The effect of water on the strength of glass, J. Appl. Phys. 17 (1946) 179–188.

[12] F.O. Anderegg, Strength of Glass Fires, Ind. Eng. Chem. 31 (1939) 290–298.

[13] W.C. Levengood, Effect of origin flaw characteristics on glass strength, J. Appl. Phys. 29 (1958) 820–826.

[14] R. Horm, Résistance de verre de silice pour application aérospatiale par la méthode de la flextion be-axiale, anneau-sur-anneau, Master 2 Report, Univ. Rennes 1. (2018).

[15] B.A. Proctor, I. Whitney, J.W. Johnson, The strength of fused silica, Proc. R. Soc. Lond. A. 297 (1967) 534–557.

[16] A.A. Griffith, M. Eng, VI. The phenomena of rupture and flow in solids, Phil. Trans. R. Soc. Lond. A. 221 (1921) 163–198.

[17] C.E. Inglis, Stresses in a plate due to the presence of cracks and sharp corners, Trans Inst Nav. Arch. 55 (1913) 219–241.

[18] B.R. Lawn, B.J. Hockey, S.M. Wiederhorn, Atomically sharp cracks in brittle solids: an electron microscopy study, J. Mater. Sci. 15 (1980) 1207–1223.

[19] H. Tanaka, Y. Bando, Y. Inomata, M. Mitomo, Atomically Sharp Crack in 15R Sialon, J. Am. Ceram. Soc. 71 (1988) C32–C33.

[20] P.K. Gupta, C.R. Kurkjian, Intrinsic failure and non-linear elastic behavior of glasses, J. Non. Cryst. Solids. 351 (2005) 2324–2328.

[21] T.F. Soules, R.F. Busbey, The rheological properties and fracture of a molecular dynamic simulation of sodium silicate glass, J. Chem. Phys. 78 (1983) 6307–6316.

[22] J.H. Simmons, What is so exciting about non-linear viscous flow in glass, molecular dynamics simulations of brittle fracture and semiconductor--glass quantum composites, J. Non. Cryst. Solids. 239 (1998) 1–15.

[23] D. Liao, Atomistic simulation of strength and deformation of ceramic materials, PhD thesis, Massachusetts Institute of Technology, 2001.

[24] C.R. Kurkjian, P.K. Gupta, R.K. Brow, N. Lower, The intrinsic strength and fatigue of oxide glasses, J. Non. Cryst. Solids. 316 (2003) 114–124.

[25] N.P. Lower, R.K. Brow, C.R. Kurkjian, Inert failure strains of sodium aluminosilicate glass fibers, J. Non. Cryst. Solids. 344 (2004) 17–21.

[26] N.P. Lower, R.K. Brow, C.R. Kurkjian, Inert failure strain studies of sodium silicate glass fibers, J. Non. Cryst. Solids. 349 (2004) 168–172.

[27] R.K. Brow, N.P. Lower, C.R. Kurkjian, TPB test provides new insight to fiber strength, quality, (2005).

[28] G.R. Irwin, Handbook of physics, in: Vol. 6, Springer, Berlin, 1958: pp. 551–590.

[29] Dm. Marsh, Plastic flow in glass, Proc. R. Soc. Lond. A. 279 (1964) 420–435.

[30] W.B. Hillig, Plastic Behavior and Fracture in Glass, Microplasticity, Eds., CJ McMahon. Interscience, New York. (1968) 383.

[31] S.M. Wiederhorn, Influence of Water Vapor on Crack Propagation in Soda Lime Glass, J. Am. Ceram. Soc. 50 (1967) 407–414.

[32] T.A. Michalske, S.W. Freiman, A molecular interpretation of stress corrosion in silica, Nature. 295 (1982) 511–512.

[33] F. Célarié, S. Prades, D. Bonamy, L. Ferrero, E. Bouchaud, C. Guillot, C. Marlière, Glass Breaks like Metal, but at the Nanometer Scale, Phys. Rev. Lett. 90 (2003) 075504-1–4.

[34] J.-P. Guin, S.M. Wiederhorn, Fracture of silicate glasses: ductile or brittle?, Phys. Rev. Lett. 92 (2004) 215502-1–4.

[35] G.R. Irwin, Analysis of stresses and strains near the end of a crack traversing a plate, J. Appl. Mech. 24 (1957) 361–364.

[36] G.R. Irwin, Fracture, in: S. Flügge (Ed.), Elast. Plast. / Elastizität Und Plast., Springer Berlin Heidelberg, Berlin, Heidelberg, 1958: pp. 551–590.

[37] E. Orowan, Fracture and strength of solids, Reports Prog. Phys. 12 (1949) 185–232.

[38] S.M. Wiederhorn, A.G. Evans, D.E. Roberts, A fracture mechanics study of the Skylab windows, in: Fract. Mech. Ceram., Springer, 1974: pp. 829–841.

[39] S.M. Wiederhorn, H. Johnson, A.M. Diness, A.H. Heuer, Fracture of Glass in Vacuum, J. Am. Ceram. Soc. 57 (1974) 336–341.

[40] S.W. Freiman, T.L. Baker, J.B. Wachtman Jr, A computerized fracture mechanics data base for oxide glasses, Am. Ceram. Soc. Bull. 64 (1985) 1452–1455.

[41] A.G. Evans, E.A. Charles, Fracture toughness determinations by indentation, J. Am. Ceram. Soc. 59 (1976) 371–372.

[42] B. Lawn, R. Wilshaw, Indentation fracture: principles and applications, J. Mater. Sci. 10 (1975) 1049–1081.

[43] M.T. Laugier, Toughness determination of some ceramic tool materials using the method of Hertzian indentation fracture, J. Mater. Sci. Lett. 4 (1985) 1542–1544.

[44] C.B. Ponton, R.D. Rawlings, Vickers indentation fracture toughness test Part 1 Review of literature and formulation of standardised indentation toughness equations, Mater. Sci. Technol. 5 (1989) 865–872.

[45] C.B. Ponton, R.D. Rawlings, Vickers indentation fracture toughness test Part 2 Application and critical evaluation of standardised indentation toughness equations, Mater. Sci. Technol. 5 (1989) 961–976.

[46] J.A. Salem, L.J. Ghosn, Back Face Strain for Monitoring Stable Crack Extension in Precracked Flexure Specimens, J. Am. Ceram. Soc. 93 (2010) 2804–2813.

[47] N. Shinkai, R.C. Bradt, G.E. Rindone, Fracture toughness of fused SiO2 and float glass at elevated temperatures, J. Am. Ceram. Soc. 64 (1981) 426–430.

[48] A.A. Wereszczak, C.E. Anderson, Borofloat and Starphire float glasses: a comparison, Int. J. Appl. Glas. Sci. 5 (2014) 334–344.

[49] T. Rouxel, S. Yoshida, The fracture toughness of inorganic glasses, J. Am. Ceram. Soc. 100 (2017) 4374–4396.

[50] S. Dériano, A. Jarry, T. Rouxel, J.-C. Sangleboeuf, S. Hampshire, The indentation fracture toughness (K C) and its parameters: the case of silica-rich glasses, J. Non. Cryst. Solids. 344 (2004) 44–50.

[51] T. Fett, K. Germerdonk, A. Grossmuller, K. Keller, D. Munz, Subcritical crack growth and threshold in borosilicate glass, J. Mater. Sci. 26 (1991) 253–257.

[52] M. Inagaki, K. Urashima, S. Toyomasu, Y. Goto, M. Sakai, Work of fracture and crack healing in glass, J. Am. Ceram. Soc. 68 (1985) 704–706.

[53] J.-K. Park, K. Yasuda, Y. Matsuo, Effect of crosshead speed on the fracture toughness of Soda-lime glass, Al2O3 and Si3N4 ceramics determined by the surface crack in flexure (SCF) method, J. Mater. Sci. 36 (2001) 2335–2342.

[54] G.D. Quinn, J.J. Swab, Adventures and Misadventures in Applying ASTM Standard Test Method C 1421 to Measurements of the Fracture Toughness, KIC, of Glasses, Mech. Prop. Perform. Eng. Ceram. Compos. XI. 606 (2017) 29–44.

[55] G.D. Quinn, J.J. Swab, Fracture toughness of glasses as measured by the SCF and SEPB methods, J. Eur. Ceram. Soc. 37 (2017) 4243–4257.

[56] K. Reddy, E.H. Fontana, J.D. Helfinstine, Fracture Toughness Measurement of Glass and Ceramic Materials Using Chevron Notched Specimens, J. Am. Ceram. Soc. 71 (1988) C-310-C-313.

[57] J. Salem, R. Tandon, Test method variability in slow crack growth properties of sealing glasses, Int. J. Fatigue. 32 (2010) 557–564.

[58] K. Niihara, R. Morena, D.P.H. Hasselman, Evaluation ofK Ic of brittle solids by the indentation method with low crack-to-indent ratios, J. Mater. Sci. Lett. 1 (1982) 13–16.

[59] K.K. Ray, A.K. Dutta, Comparative study on indentation fracture toughness evaluations of soda--lime--silica glass, Br. Ceram. Trans. 98 (1999) 165–171.

[60] J. Lankford, Indentation microfracture in the Palmqvist crack regime: implications for fracture toughness evaluation by the indentation method, J. Mater. Sci. Lett. 1 (1982) 493–495.

[61] G.R. Anstis, P. Chantikul, B.R. Lawn, D.B. Marshall, A critical evaluation of indentation techniques for measuring fracture toughness: I, direct crack measurements, J. Am. Ceram. Soc. 64 (1981) 533–538.

[62] S. Yoshida, J.-C. Sangleboeuf, T. Rouxel, Quantitative evaluation of indentation-induced densification in glass, J. Mater. Res. 20 (2005) 3404–3412.

[63] ASTM C1421-10, Standard Test Methods for Determination of Fracture Toughness of Advanced Ceramics at Ambient Temperature, ASTM International, West Conshohocken, PA, 2010.

[64] D. Munz, R.T. Bubsey, J.E. Srawley, Compliance and stress intensity coefficients for short bar specimens with chevron notches, Int. J. Fract. 16 (1980) 359–374.

[65] D. Munz, R.T. Bubsey, J.L. Shannon Jr, Fracture toughness determination of Al2O3 using four-point-bend specimens with straight-through and chevron notches, J. Am. Soc. Ceram. 63 (1980) 300–305.

[66] D. Munz, R.T. Bubsey, J.L. Shannon, Performance of chevron-notch short bar specimen in determining the fracture toughness of silicon nitride and aluminum oxide, J. Test. Eval. 8 (1980) 103–107.

[67] J.I. Bluhm, Slice synthesis of a three dimensional “work of fracture” specimen, Eng. Fract.

Mech. 7 (1975) 593–604.

[68] S.-X. Wu, Fracture toughness determination of bearing steel using chevron-notch three point bend specimen, Eng. Fract. Mech. 19 (1984) 221–232.

[69] T. Rouxel, Y. Laurent, Fracture characteristics of SiC particle reinforced oxynitride glass using chevron-notch three-point bend specimens, Int. J. Fract. 91 (1998) 83–101.

[70] T. Nose, T. Fujii, Evaluation of Fracture Toughness for Ceramic Materials by a Single-Edge-Precracked-Beam Method, J. Am. Ceram. Soc. 71 (1988) 328–333.

[71] N. Shinkai, R.C. Bradt, G.E. Rindone, Elastic Modulus and Fracture Toughness of Ternary PbO-ZnO-B2O3 Glasses, J. Am. Ceram. Soc. 65 (1982) 123–126.

[72] A.S. Rizkalla, D.W. Jones, E.J. Sutow, Effect of nonbridging oxygens on the fracture toughness of synthesized glasses, Br. Ceram. Trans. J. 91 (1992) 12–15.

[73] J.E. Blendell, The origins of internal stresses in polycrystalline AL2O3 and their effects on mechanical properties, PhD thesis, Massachusetts Institute of Technology, 1979.

[74] N. Miyata, H. Jinno, Fracture toughness and fracture surface energy of lead borate glasses, J. Mater. Sci. Lett. 1 (1982) 156–158.

[75] B.R. Lawn, E.R. Fuller, Equilibrium penny-like cracks in indentation fracture, J. Mater. Sci. 10 (1975) 2016–2024.

[76] T. Miura, T. Watanabe, Y. Benino, T. Komatsu, R. Sato, Unusual elastic and mechanical behaviors of copper phosphate glasses with different copper valence states, J. Am. Ceram. Soc. 84 (2001) 2401–2408.

[77] N. Miyata, H. Jinno, Mechanical Properties of PbO-B_2 0_3 Immiscible Glasses, Bull. Inst. Chem. Res. Kyoto Univ. 59 (1981) 196–206.

[78] A.G. Evans, A method for evaluating the time-dependent failure characteristics of brittle materials-and its application to polycrystalline alumina, J. Mater. Sci. 7 (1972) 1137–1146.

[79] F.F. Lange, The interaction of a crack front with a second-phase dispersion, Philos. Mag. 22 (1970) 983–992.

[80] A.K. Seal, P. Chakraborti, N.R. Roy, S. Mukherjee, M.K. Mitra, G.C. Das, Effect of phase separation on the fracture toughness of SiO 2-B 2 O 3-Na 2 O glass, Bull. Mater. Sci. 28 (2005) 457–460.

[81] R.A. Schultz, M.C. Jensen, R.C. Bradt, Single crystal cleavage of brittle materials, Int. J. Fract. 65 (1994) 291–312.

[82] N. Nishiyama, S. Seike, T. Hamaguchi, T. Irifune, M. Matsushita, M. Takahashi, H. Ohfuji, Y. Kono, Synthesis of nanocrystalline bulk SiO2 stishovite with very high toughness, Scr. Mater. 67 (2012) 955–958.

[83] Y. Tan, H. Zhang, S. Peng, Electrically conductive graphene nanoplatelet/boron carbide composites with high hardness and toughness, Scr. Mater. 114 (2016) 98–102.

[84] A.A. El-Moneim, Quantitative analysis of elastic moduli and structure of B2O3--SiO2 and Na2O--B2O3--SiO2 glasses, Phys. B Condens. Matter. 325 (2003) 319–332.

[85] A. Bhatnagar, M.J. Hoffman, R.H. Dauskardt, Fracture and Subcritical Crack-Growth Behavior of Y-Si-Al-O-N Glasses and Si3N4 Ceramics, J. Am. Ceram. Soc. 83 (2000) 585–596.

[86] T. Rouxel, Fracture surface energy and toughness of inorganic glasses, Scr. Mater. 137 (2017) 109–113.

[87] S. Chakravarty, D.G. Georgiev, P. Boolchand, M. Micoulaut, Ageing, fragility and the reversibility window in bulk alloy glasses, J. Phys. Condens. Matter. 17 (2004) L1–L7.

[88] H. Zeng, Q. Jiang, Z. Liu, X. Li, J. Ren, G. Chen, F. Liu, S. Peng, Unique sodium phosphosilicate glasses designed through extended topological constraint theory, J. Phys. Chem. B. 118 (2014) 5177–5183.

[89] R.K. Kalia, A. Nakano, P. Vashishta, C.L. Rountree, L. Van Brutzel, S. Ogata, Multiresolution atomistic simulations of dynamic fracture in nanostructured ceramics and glasses, Int. J. Fract. 121 (2003) 71–79.

[90] S.W. King, G.A. Antonelli, Simple bond energy approach for non-destructive measurements of the fracture toughness of brittle materials, Thin Solid Films. 515 (2007) 7232–7241.

[91] J.J. Mecholsky Jr, Estimating theoretical strength of brittle materials using fractal geometry, Mater. Lett. 60 (2006) 2485–2488.

[92] R. Miller, E.B. Tadmor, R. Phillips, M. Ortiz, Quasicontinuum simulation of fracture at the atomic scale, Model. Simul. Mater. Sci. Eng. 6 (1998) 607–638.

[93] A. Tilocca, Structural models of bioactive glasses from molecular dynamics simulations, Proc. R. Soc. A Math. Phys. Eng. Sci. 465 (2009) 1003–1027.

[94] G.G. Naumis, Energy landscape and rigidity, Phys. Rev. E. 71 (2005) 26114-1–7.

[95] F. Wang, S. Mamedov, P. Boolchand, B. Goodman, M. Chandrasekhar, Pressure Raman effects and internal stress in network glasses, Phys. Rev. B. 71 (2005) 174201-1–8.

[96] M. V Chubynsky, M.-A. Briere, N. Mousseau, Self-organization with equilibration: A model for the intermediate phase in rigidity percolation, Phys. Rev. E. 74 (2006) 16116-1–9.

[97] M. Bauchy, B. Wang, M. Wang, Y. Yu, M.J.A. Qomi, M.M. Smedskjaer, C. Bichara, F.-J. Ulm, R. Pellenq, Fracture toughness anomalies: Viewpoint of topological constraint theory, Acta Mater. 121 (2016) 234–239.

[98] J.E. Shelby, Introduction to glass science and technology, Royal Society of Chemistry, 2007.

[99] T. Rouxel, J.-C. Sangleboeuf, The brittle to ductile transition in a soda-lime-silica glass, J. Non. Cryst. Solids. 271 (2000) 224–235.

[100] S.A.M. Spinner, Elastic moduli of glasses at elevated temperatures by a dynamic method, J. Am. Ceram. Soc. 39 (1956) 113–118.

[101] J.B. Quinn, I.K. Lloyd, Comparison of Methods to Determine the Fracture Toughness of Three Glass-Ceramics at Elevated Temperatures, J. Am. Ceram. Soc. 83 (2000) 3070–3076.

[102] A. Ghosh, M.G. Jenkins, K.W. White, A.S. Kobayashi, R.C. Brad, Elevated-temperature fracture resistance of a sintered α-silicon carbide, J. Am. Ceram. Soc. 72 (1989) 242–247.

[103] M. Mizuno, H. Okuda, VAMAS round robin on fracture toughness of silicon nitride, J. Am. Ceram. Soc. 78 (1995) 1793–1801.

[104] T. Fett, D. Munz, Determination of fracture toughness at high temperatures after subcritical crack extension, J. Am. Ceram. Soc. 75 (1992) 3133–3136.

[105] K.D. McHenry, R.E. Tressler, Fracture Toughness and High-Temperature Slow Crack Growth inSiC, J. Am. Ceram. Soc. 63 (1980) 152–156.

[106] A. Micski, B. Bergman, High temperature strength of silicon nitride HIP-ed with low amounts of yttria or yttria/alumina, J. Eur. Ceram. Soc. 6 (1990) 291–301.

[107] J.J. Brennan, K.M. Prewo, Silicon carbide fibre reinforced glass-ceramic matrix composites exhibiting high strength and toughness, J. Mater. Sci. 17 (1982) 2371–2383.

[108] J.L. Henshall, D.J. Rowcliffe, J.W. Edington, Fracture Toughness of Single-Crystal Silicon Carbide, J. Am. Ceram. Soc. 60 (1977) 373–375.

[109] S.W. Freiman, S.M. Wiederhorn, J.J. Mecholsky, Environmentally enhanced fracture of glass: A historical perspective, J. Am. Ceram. Soc. 92 (2009) 1371–1382.

II. The strength of glass as measured by bi-axial flexure on amorphous silica and window glass with different surface conditions

II.1. Abstract

The strength of fused silica glass was investigated by means of the biaxial flexure test, with the ring-on-ring configuration. An amorphous silica rod was cut into forty disk shape specimens, 35 mm in diameter, which were polished down to 6 µm diamond paste on both sides. Half of the specimens were then submitted to a surface treatment by means of sand blasting leading to a loss of the transparency (specimens become translucent). The treated specimens were tested by setting the treated surface face down on the tensile side. A statistical analysis of fracture, using either a two-parameter maximum likelihood method or a linear regression method using $P_i = (i - 0.5)/N$, shows that the untreated specimens (mean strength = 143 MPa) are stronger than the treated specimens (mean strength = 108 MPa) and as strong as a standard soda-lime-silica float glass (mean strength = 146 MPa; tin side on the tensile side). It is noteworthy that when Vickers indentations are performed on the tin surface of the float glass (tensile side), the strength of the specimen indented with a 0.2 N load is the same as the one of the product glass. This suggests that the critical surface flaw on the tin side of the float glass is about 10 µm. A clear correlation was found between the number of fragments after fracture and the elastic energy stored in the disks prior to fracture.

*Keywords***:** Glass strength, Sand blasting, Bi-axial flexure test, Ring-on-Ring

II.2. Introduction

Fused silica glass finds numerous applications as lenses, mirror substrates, UV and IR transmitting optics, metrology components and windows. It is thus essential to have a reliable strength value for the glass as prepared for a given application. Strength from 50 to 180 MPa is reported in the literature, depending on surface finish conditions [1–4]. Not-fine and fine polished a-SiO_2 specimens with different disk diameters from 25.4 to 228.6 mm were investigated in [2] (Neither diamond paste size nor roughness of the disk surfaces were mentioned in [2]). For the 25.4 mm specimen, mean strengths of 109 and 172 MPa were found in case of not-fine and fine surface finished specimens, respectively. In this study, the surface of a-SiO_2 disk shape specimen was polished down to a 6 µm diamond paste. The strength and Weibull's modulus were determined and the incidence of the surface preparation was investigated.

This chapter has been submitted as: R. Horm, T.To, F. Célarié, M. Le Fur, J. Chollet, H. Orain, T. Rouxel, The strength of glass as measured by bi-axial flexure on amorphous silica and window glass with different surface conditions, Exp. Mech., (2019).

The properties of the surface treated samples were compared to those of the as-polished ones. The properties of the a-SiO_2 samples were further compared with the ones of soda-lime-silica (SLS) glass (series 3 with as-processed "float" surface finish). For SLS glass, the tensile strength of the tin side was reported to be weaker than that of the air side [5–7]. In this study, we put the tin side of the 35 mm diameter disk specimen in tension during the experiment.

II.3. Materials and experimental techniques

II.3.a. Ring on Ring (RoR) configuration

Ring-on-Ring (RoR) biaxial flexure test was used to investigate the strength of the studied glasses in the ambient environment (temperature of 23 ºC and humidity of 60 %). A relatively high crosshead speed, of 2.8 mm·min^{-1} (= stress rate of 35 MPa·s^{-1}), was selected in order to eliminate the effect of humidity [8]. A SHIMADZU-AGS-X testing machine was used to apply the load (**Fig. II.1)**. The loading set-up consists of a 2 kN load cell (with the accuracy of ± 2 N), a stainless steel piston (load rod) and a silicon carbide ball (SiC, Mersen Boostec, FR) to transfer the load to the RoR device, a stainless steel holder to join the piston and the ball to the RoR device, 11 and 26 mm stainless steel load (inner and upper) and support (outer and bottom) rings. The ring thickness is of 4 mm. Between each ring and the specimen, there is a compliant layer used to assure the stability of the load from the rings to the specimen.

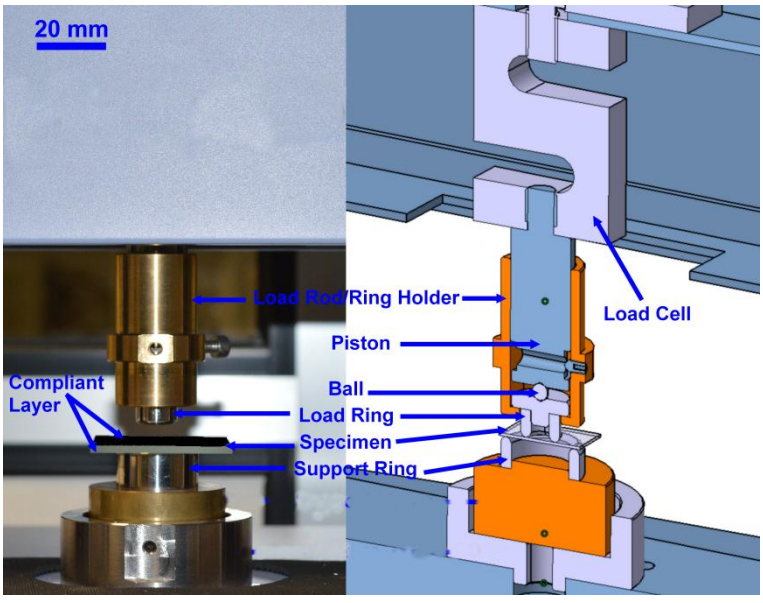

Fig. II.1 : Bi-axial testing set-up (photo on the left hand side and drawing on the right hand side).

II.3.b. Specimen and experiment

Two series of fused silica and one series of soda-lime-silica glass, each of them consisting of 20 specimens, were investigated. Series 1 consists of disks with both surfaces polished down to 6 µm

diamond paste (roughness average R_a ~ 0.001 µm), whereas series 2 consists of disks with one surface polished down to 6 µm diamond paste and the other surface treated by sand blasting to get a R_a of about 0.2 µm. Series 3 consists of disks with as-processed (float) surface finish (R_a ~ 0.002 µm). In all cases, disks are of 35 ± 0.1 mm in diameter and 2.1 ± 0.1 mm in thickness. Specimens were carefully checked by means of an optical microscope (Keyence MVH5000, Japan) both prior and after testing. A fractographic analysis was then conducted on the broken specimens using the fragments that were systematically collected.

Before the biaxial experiment, the load ring was aligned with the support ring using hollow cylinder called "aligner", and the specimen was numbered on the compressive surface (the upper surface in **Fig. II.1**) in order to facilitate the reconstruction of the disk shape after fracture using the numerous fragments. The glass surface which are set in tension (the lower surface in **Fig. II.1**) are the 6 µm polished, treated and tin side ones for series 1, 2 and 3, respectively. For series 3, five specimens were tested with as-processed float surfaces, five other specimens tested with a 10 N indent in the middle of the surfaces, five other specimens tested with a 5 N indent in the middle of the surfaces, and each one of the other five specimens tested with an indent load (in the middle of the surfaces) varying from 1 N to 0.05 N.

The specimens were then manipulated with gloves to avoid additional alteration of the surface by handling, and centered on the support ring with the accuracy within 2 % of the support ring diameter. A compliant layer was positioned between the support ring and the specimen and another layer between the specimen and the load ring (**Fig. II.1**) in order to minimize the friction and to help distributing the load equally on the contact surface. The cross-head was automatically stopped once the glass was broken. The broken pieces of glass were collected and used to reconstruct the disks to perform some fractographic analysis. The strength of specimen was calculated by means of Refs. [9–12] accounting for the actual position of the crack origin. If the crack origin is inside load ring, the radial (σ_r) and hoop (σ_θ) stress are the same and expressed by:

$$\sigma_r = \sigma_\theta = \frac{3F}{2\pi h^2}\left((1-\nu)\frac{D_s{}^2 - D_L{}^2}{2D^2} + (1+\nu)\ln\frac{D_s}{D_L}\right) \tag{II.1}$$

If not,

$$\sigma_r = \frac{3F}{2\pi h^2}\left((1-\nu)\frac{D_s{}^2 - D_L{}^2}{2D^2} - (1-\nu)\frac{d^2 - D_L^2}{2d^2} + (1+\nu)\ln\frac{D_s}{d}\right) \tag{II.2}$$

$$\sigma_\theta = \frac{3F}{2\pi h^2}\left((1-\nu)\frac{D_s^{\,2}-D_L^{\,2}}{2D^2}+(1-\nu)\frac{d^2-D_L^2}{2d^2}+(1+\nu)\ln\frac{D_s}{d}\right) \quad \text{(II.3)}$$

where F is the load (N) at fracture, D_S and D_L are the diameters of the support and load rings (mm) respectively, D is the test specimen diameter (mm), d is the diameter of the circle on which the crack origin is located, to the center of specimen (mm), h is the test specimen thickness (mm) and v is Poisson's ratio. Whenever the crack origin is in between the load ring and the support ring, the hoop stress was used to estimate the strength since the crack initiated tangentially, (see **Fig. II.2)**.

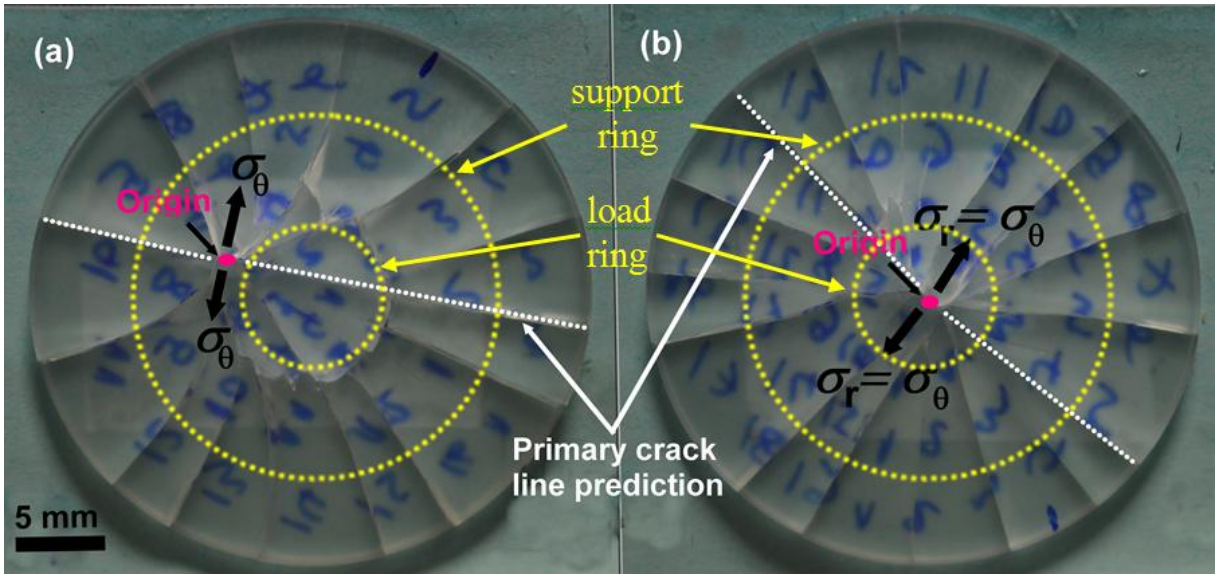

Fig. II.2 : Example of broken specimen (series 1), where the origin is outside the load ring for the left image and inside the load ring for the right one.

Density (ρ) was determined by means of Archimedes' principle of buoyancy in distilled water. The density was averaged from four measurements on the same piece of glass. The elastic moduli were determined by means of ultrasonic echography. Longitudinal (V_L) and transversal (V_T) wave velocities were calculated from the sample thickness and travel time, using 10 MHz transducer. Young's modulus (E) shear modulus (G), Poisson's ratio (v) and Bulk modulus (K) are expressed as:

$$E = \rho\frac{3V_L^2-4V_T^2}{\left(V_L/V_T\right)^2-1} \quad \text{(II.4)}$$

$$G = \rho V_T^2 \quad \text{(II.5)}$$

$$\nu = \frac{E}{2G}-1 \quad \text{(II.6)}$$

$$K = \frac{E}{3(1-2\nu)} \tag{II.7}$$

II.4. Data analysis and Weibull modulus

Table II.1 : Physical/Mechanical properties of fused silica glass (a-SiO_2); average ± standard deviation

Series	ρ (g/cm^3)	E (GPa)	G (GPa)	ν	K (GPa)
1 and 2	2.196 ± 0.004	69.7 ± 0.3	29.8 ± 0.2	0.17 ± 0.01	35.2 ± 0.5
3	2.474 ± 0.025	73.2 ± 1.1	29.7 ± 0.5	0.23 ± 0.02	46.0 ± 3.6

Mechanical properties such as density, Young's modulus, Poisson's ratio, shear modulus, and Bulk's modulus are given in **Table II.1**. Weibull approach [2,13–17] was used to analyze the strength data. The statistical distribution of the probability of fracture is written,

$$P_f = 1 - e^{-\left(\frac{\sigma_i}{\sigma_0}\right)^m}, \tag{II.8}$$

where m is the so-called Weibull modulus, σ_i is the experimented strength from each specimen and σ_0 is a normalization parameter. In this study, two methods (linear regression and maximum likelihood) were used to estimate Weibull's modulus (m). Linear regression method (LRL) generally provides the slope (m) and intercept (enable to calculate σ_θ) from the experimental fracture stress values and from probability expression:

$$m = \frac{\partial\left(\ln\left(\ln\frac{1}{1-P_i}\right)\right)}{\partial\ln(\sigma_i)}, \tag{II.9}$$

where an expression for P_i was introduced as,

$$P_i = \frac{i-0.5}{n} \quad , \tag{II.10}$$

where i is the rank of the specimen, by order of increasing strength, ranging from 1 to n.

The maximum likelihood method (MLE) is more reliable for determining the value of *m* from a set of fracture strengths, without any predetermined probability expression. Unlike linear regression, the MLE offers a unique solution for two-parameter Weibull distribution. As the sample size is increased, this estimator asymptotically converges to the true distribution parameters and the confidence interval narrows as well relative to the linear regression estimator. The equation corresponding to the maximum likelihood criterion is expressed as:

$$\sum_{i=1}^{n}\ln\left(\sigma_i\right)-n\frac{\sum_{i=1}^{n}\sigma_i^{\,m}\ln\left(\sigma_i\right)}{\sum_{i=1}^{n}\sigma_i^{\,m}}+\frac{n}{m}=0\,, \tag{II.11}$$

and the normalization stress is given by:

$$\sigma_0=\left[\frac{1}{n}\sum_{i=1}^{n}\sigma_i^{\,m}\right]^{\frac{1}{m}} \tag{II.12}$$

Table II.2: Summary results of strength of all series comparing to those from literatures. The average strengths were obtained from 20 specimens for series 1 and 2, and from 5 specimens for series 3.

Series	σ_{min} (MPa)	σ_{max} (MPa)	$\sigma_{50\%}$ (MPa)	$\sigma_m \pm$ std (MPa)	$\sigma_{c(lit.)} \pm$ std (MPa)
1	98	184	143	143 ± 25	172 ± 20 [2]
2	56	134	110	108 ± 19	109 ± 14 [2]
3	119	170	145	146 ± 19	125 [5]

Figure II.3 shows the Weibull moduli (m) and normalization stress (σ_0) of the three series by both maximum likelihood and the linear regression (using $P_i = (i-0.5)/m$) methods. Except for series 2, m calculated from MLE is greater than the one of LRL. *m* varies from 6.5 to 9. σ_c of series 1 (silica) and series 3 (soda-lime-silica) are equal to each other. In addition, the theoretical strength of both glasses, calculated based on atomic organization, is identical (about 34 GPa) and the fracture toughness of both glasses is also nearly identical (about 0.7 $MPa{\cdot}m^{0.5}$). Series 2 has the lowest strength. Compare to series 1, series 2 is also a silica glass but its tensile surface was treated, inducing the presence of larger surface flaws, and thus smaller strength values. The treatment is found to weaken the glass by about 30 %. **Table II.2** shows the maximum strength (σ_{max}), the minimum strength (σ_{min}), the strength at 50 % probability ($\sigma_{50\%}$), the mean strength (σ_m) with standard deviation and the strength from different literature sources ($\sigma_{c(lit.)}$). Series 1 and 2 are noted

as super polished and standard polished specimens, respectively. σ_c and $\sigma_{c(lit.)}$ of series 1 and 2 are in very good agreement. These good agreement indicates that super polished surface in the literature has the same condition of 6 µm diamond paste polished surface in this study; the standard polished surface in the literature has the same condition of the treated surface in this study. A slight lower strength for soda-lime-silica glass in the literature may be explained by different surface conditions as well.

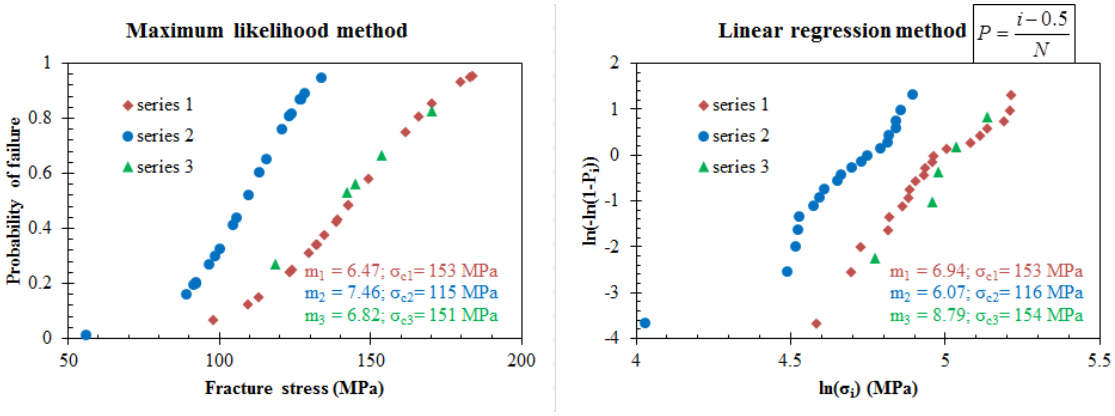

Fig. II.3: Weibull moduli (m) and normalization strength (σ_0) of series 1 (20 specimens), series 2 (20 specimens) and series 3 (5 specimens) by means of maximum likelihood method (on left hand side) and linear regression method (on right hand side).

II.5. Result and discussion

The surfaces condition of series 1 and series 2 were examined topographically by means of optical microscopy and AFM and are shown in **Fig. II.4**. For both series, scatters of flaws were identified at a magnification of ×5000. Remarkably, the flaws were clearly seen by AFM. Thus, the size of the critical surface flaws (c) for series 1 and series 2 were estimated at around 2 µm and 8 µm respectively.

To compare with the flaw size found by AFM, Griffith's theory in brittle fracture mechanics was applied to find the flaw depth at the onset of the fracture process. The critical surface flaw size (c) was calculated using the following equation:

$$c = \left(\frac{K_{Ic}}{\sigma_f Y}\right)^2 , \qquad \text{(II.13)}$$

where K_{Ic} is the fracture toughness (typically about 0.73 and 0.70 MPa·m$^{0.5}$ for fused silica and soda-lime-silica, respectively), Y is a geometric parameter (1.29 for a semi-elliptic surface crack and the rim crack size c/a = 1.4 [18]) and σ_f is the stress at failure.

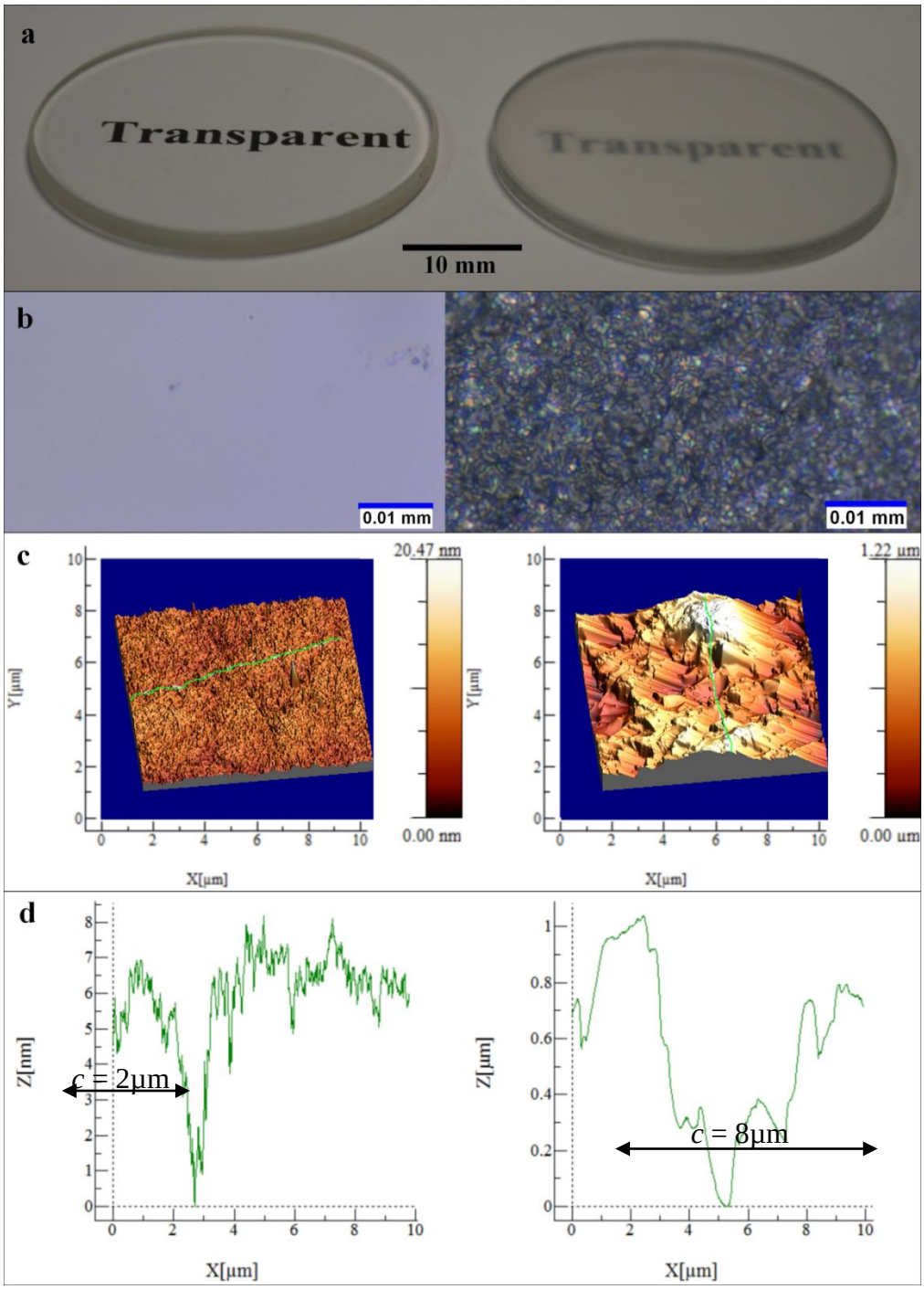

Fig. II.4: Surface condition investigation before experimentation (left: series 1 and right: series 2). a-surfaces investigated by a camera, b-2D surfaces investigated by a microscope, c-3D surfaces investigated by AFM and d-profile of image c.

Table II.3 shows the summary of flaw sizes on the tested specimen surface. The flaw sizes calculated using the $\sigma_{50\%}$ and σ_m have a good agreement from one to another, and in all series 1 and 2, the calculated flaw sizes range between 4 and 43 µm and are greater than the ones measured by means of AFM. This disagreement suggests the presence of relatively large flaw that are not visible

at the investigated surface neither by optical microscopes, nor by AFM. However, the calculated flaw size of series 1 is equal to the size of the finished mirror polish paste (6 µm) and the one of series 2 (treated surface) is double the size polishing paste. To verify the surface flaw size, the other fifteen specimens of series 3 were indented inner the support ring surface before the biaxial testing as presented in **Section 2** (**Fig. II.5**).

Table II.3: Summary results of flaw size corresponding to the strength and comparing to the one measured from AFM. NA: not available.

Series	$c(\sigma_{min})$ (µm)	$c(\sigma_{max})$ (µm)	$c(\sigma_{50\%})$ (µm)	$c(\sigma_m)$ (µm)	c(AFM) (µm)
1	14.15	4.02	6.65	6.66	2
2	43.35	7.57	11.24	11.65	8
3	8.83	4.33	5.95	5.86	NA

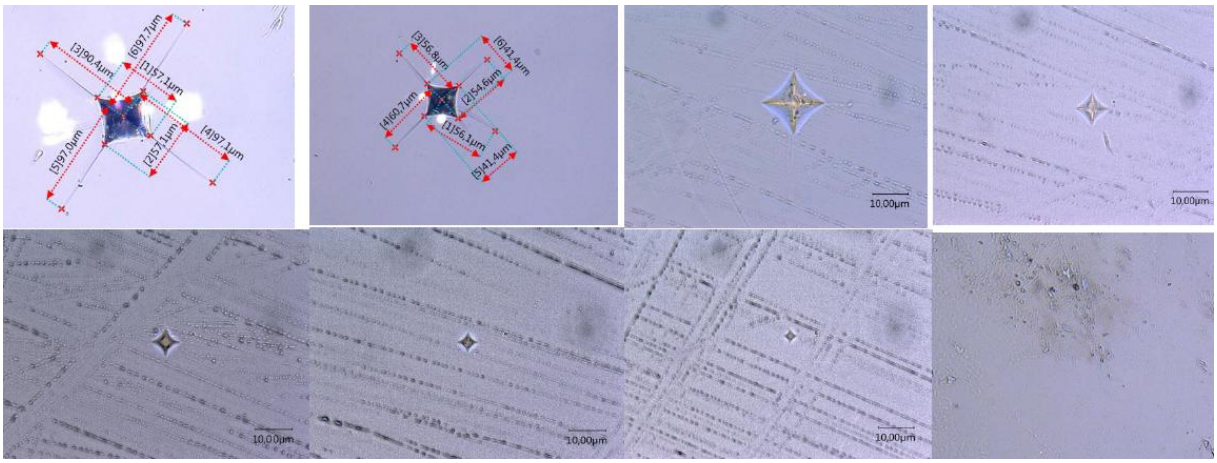

Fig. II.5: From left to right and top to down: 10 N, 5 N, 1 N, 0.3 N, 0.2 N, 0.1 N, 0.05 N indented and original (0 N) surface of series 3.

After biaxial test, the disks were reconstructed using the fragments. **Figure II.6** shows reconstructed specimens, which were indented with loads ranging from 0.05 to 10 N before flexure experimentation. The last four images in **Fig. II.6** (0, 0.05, 0.1 and 0.2 N) are very similar from one to another, likely because the flaw sizes (**Table II.4**), associated with the indentation cracking pattern at 0.05, 0.1 and 0.2 N, are smaller than or equal to the critical surface flaws. It can further be concluded that the flaw size at the surface of the float glass is between 8 to 12 µm. In contrast, the first four images, corresponding to the larger indentation loads, exhibit different fracture pattern with different numbers of fragments, always smaller than at lower load. The larger the indented load is, and the smaller the number of fragments becomes. This trend is correlated to the energy

stored in the testing specimen before fracture (**Fig. II.5, II.6**). $c_{calculated}$ and $c_{measured}$ are in very good agreement for the specimens with pre-indentation at a load larger than 1 N. This agreement may be explained by the half-penny cracking pattern of the indent when the indented load is high enough. The comparison between the measured surface flaws and the measured strengths is shown in **Fig. II.7**. When the indentation flaw size is greater than the critical surface flaw size (left hand side of the red dash line), the strengths are dependent on the indentation flaw side; however, when the indentation flaw size is smaller than the critical surface flaw size (right hand side of the red dash line), the strengths are not anymore dependent on the indentation flaw side. The black slop line is the fitted line with a slope of 0.55, which is corresponding to Y ~ 1.8. Using Y of 1.8 and σ_f of 34 GPa (theoretical strength of the SLS float glass) to apply in **Eq. II.13**, we obtain a surface flaw size (c) of about 0.13 nm which is the distance between two atoms in glass (the distance between Si and O is about 0.15 nm). This good agreement suggests that the slope of 0.55 is correct.

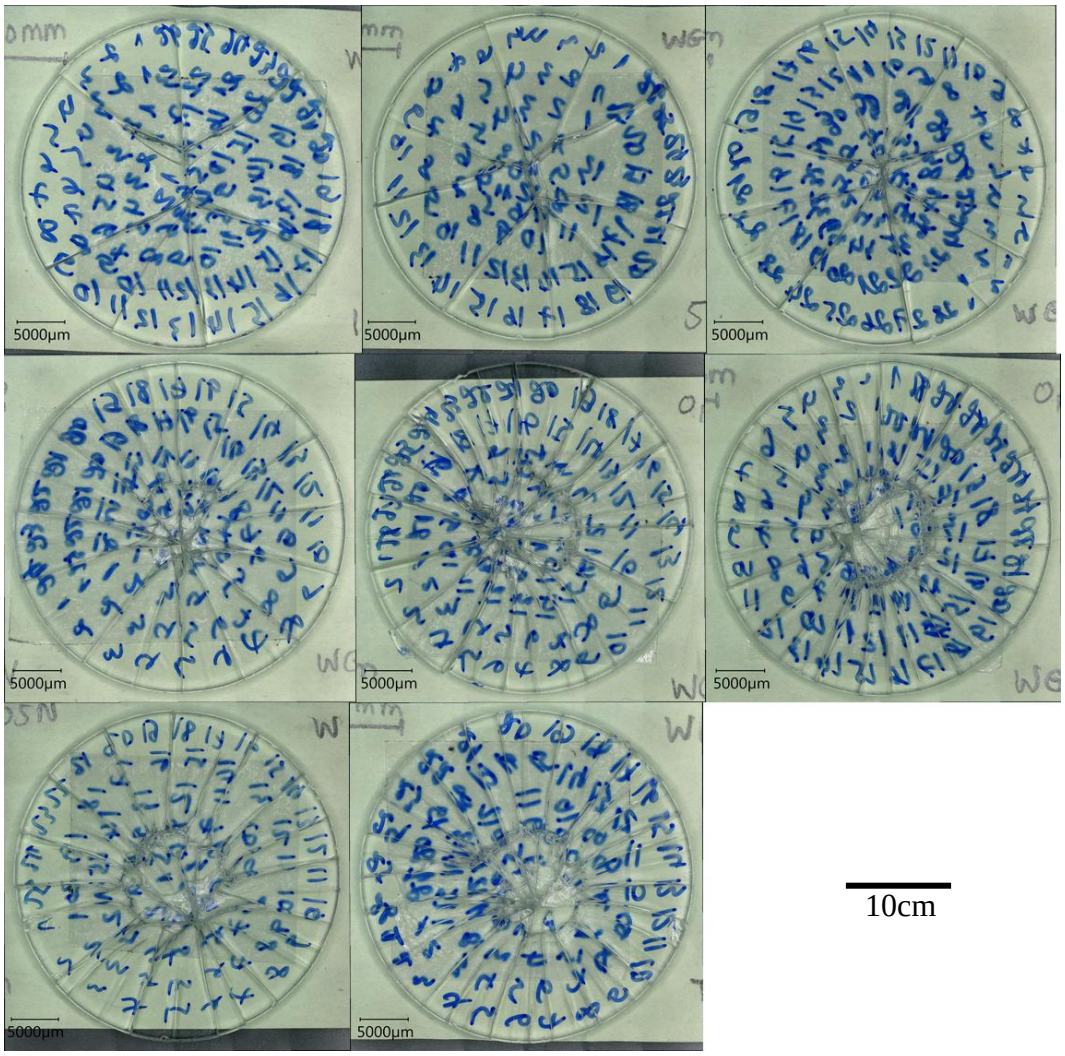

Fig. II.6: From left to right and top to down: fracture specimens of series 3 with 10 N, 5 N, 1 N, 0.3 N, 0.2 N, 0.1 N, 0.05 N and 0 N post-indented surfaces (**Fig. II.5**).

Table II.4: Average strength (σ_m) ± standard deviation or error, calculated flaw size ($c_{calulated}$) and optically measured flaw size ($c_{measured}$) of indent according to the indented load; NA: not available.

Indented load	σ (MPa)	$c_{calulated}$(µm)	$c_{measured}$ (µm)
10 N	58 ± 2 (std)	87.53	95.55
5 N	69 ± 3 (std)	61.85	60.18
1 N	103 ± 1 (error)	27.76	19.52
0.3 N	131 ± 1 (error)	17.16	10.32
0.2 N	154 ± 1 (error)	12.42	7.96
0.1 N	157 ± 1 (error)	11.95	5.70
0.05 N	149 ± 1 (error)	13.26	4.41
0 N	146 ± 19 (std)	13.81	NA

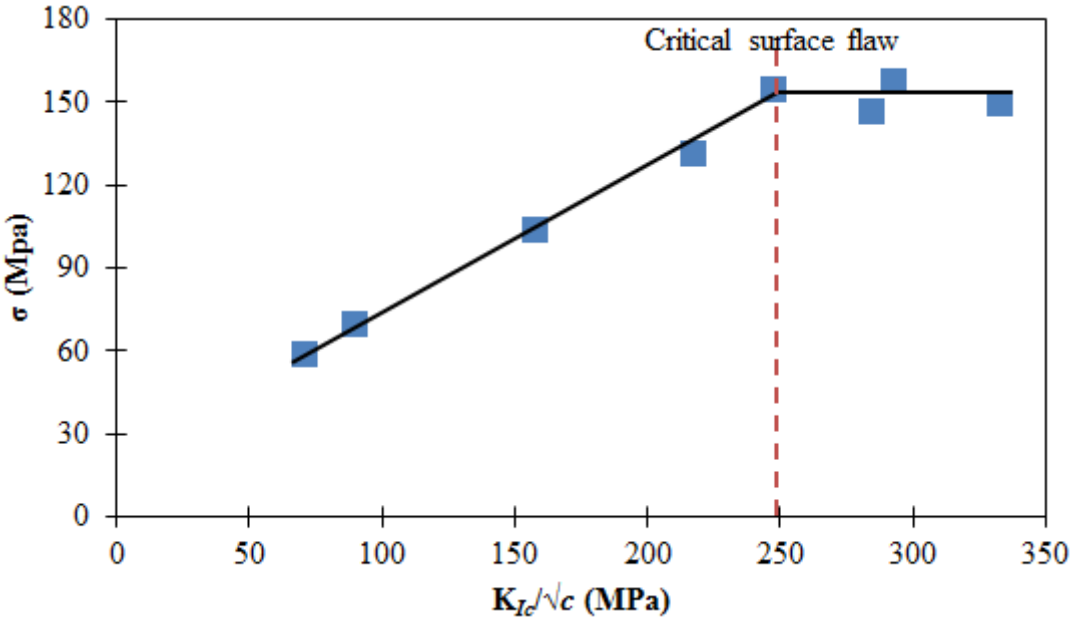

Fig. II.7: Measured strengths and flaws. The slope black like is fitted with the slope of 0.55. The red dash line shows the critical surface flaw.

The stored energy was calculated from the load-deflection curve, and the number of fragments was counted considering the large fragments located on the side, i.e. including the small ones in the middle (**Fig. II.8)**. The stored energy as a function of the number of fragments is illustrated in **Fig. II.9** for series 1 and 2. A linear correlation is discovered, with the same slope as of 0.0025. This suggests that the number of fragments does not depending on the surface condition, but the stored energy prior to fracture. Moreover, the fracture surface energy, calculated by accounting the stored energy divided by the fracture surface (= number of fracture line times radius of the specimen and times the thickness of the specimen), is equal to 68 J/m² for both series and is not dependent on the number of fragments (**Fig. II.9-bottom**). This fracture surface energy value is about 20 times larger than the one in the literature (~ 3.55 J/m²) [19]. This great difference suggests that the fracture surfaces may actually 20 times greater than the assuming surfaces because the angular fracture surfaces, second line fracture surfaces and the surfaces of the totally broken pieces were not counted in the assuming fracture surfaces.

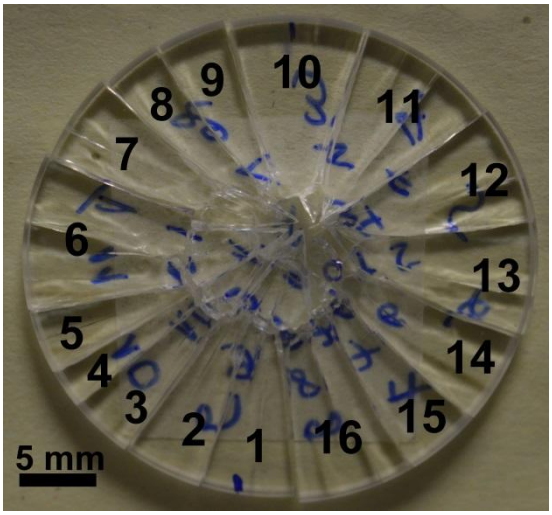

Fig. II.8 : Fragment number

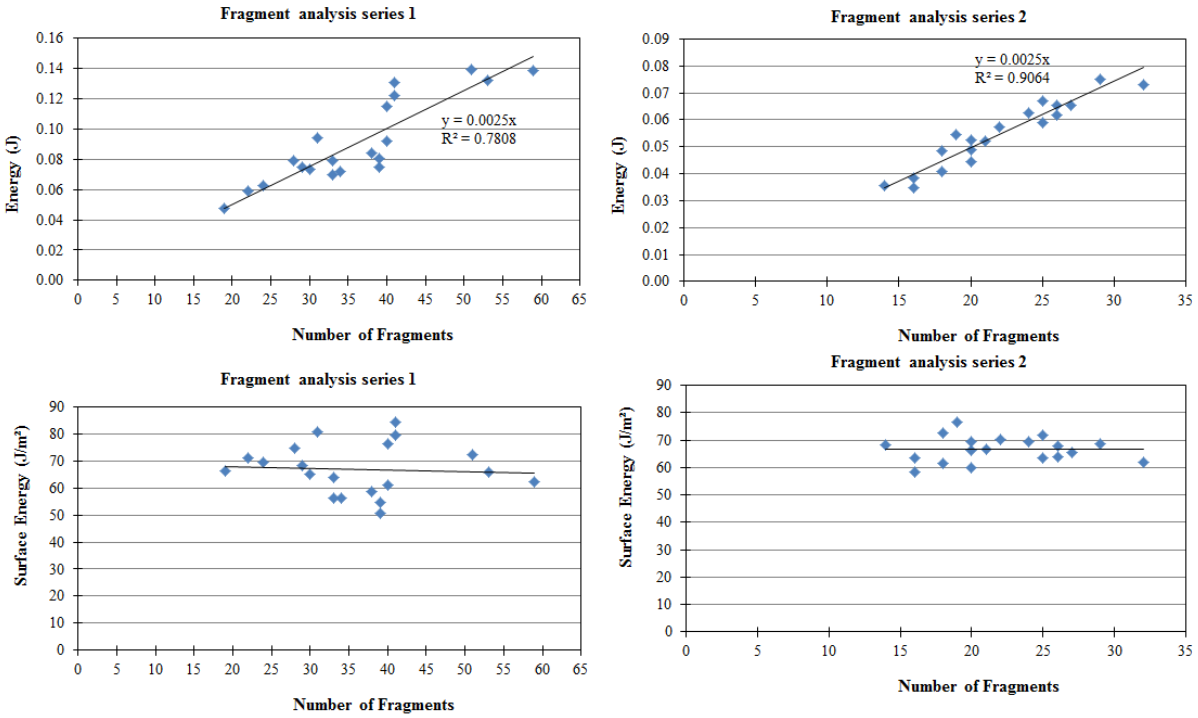

Fig. II.9: Top: Energy as the function of fragment number for series 1 (left) and series 2 (right); bottom: Surface energy as a function of fragment number for series 1 (left) and series 2 (right).

II.6. Conclusion

- The size of the critical surface flaws on the tin side of a soda-lime-silica float glass is about 8 to 12 µm as estimated by biaxial flexure test on 35 mm diameter disks.
- Fused silica glass, with a surface polished down to 6 µm, has the same strength (~ 150 MPa) as that of the soda-lime-silica float glass, and the surface-treated fused silica glass has lower strength (~ 110 MPa) than that of untreated fused silica glass.
- The Weibull modulus cannot be said to be dependent on the surface flaw.
- K_{Ic} can be predicted from the biaxial experiment once the crack pattern is known (in case of soda-lime-silica glass).
- The number of broken pieces of post-specimen is dependent on the stored energy in the specimen before fracture.
- The flaw size as small as the distance between two atoms (~ 130 pm) is obtained when taking the theoretical strength of 35 GPa.

II.7. Remarks

The strength of glass is considerably dependent on the flaw in glass. This suggests that glass engineers and scientists need to know another important property called the fracture toughness

(K_{Ic}). K_{Ic} is the resistance to the crack propagation and units in MPa·√m. Determining K_{Ic} is still challenging. Several methods have been developed to determine K_{Ic} of brittle materials and some methods (e.g. SEPB, CNB and SCF) have been standardized to determine K_{Ic} of ceramic. However, there has not been any standard method available in the case of glass yet. In the next chapter, three experimental methods have been performed, modified and discussed to trigger at least one consistent method in order to determine the K_{Ic} of glass.

II.8. References

[1] D.C. Harris, Materials for infrared windows and domes: properties and performance, SPIE press, 1999.

[2] C.A. Klein, Characteristic strength, Weibull modulus, and failure probability of fused silica glass, Opt. Eng. 48 (2009) 113401-1–10.

[3] M. Zaccaria, M. Overend, Validation of a simple relationship between the fracture pattern and the fracture stress of glass, in: Eng. Transparency. Int. Conf. Glas. Düsseldorf, Ger., 2012.

[4] P. Klocek, Handbook of infrared optical materials, CRC Press, 2017.

[5] M.H. Krohn, J.R. Hellmann, D.L. Shelleman, C.G. Pantano, G.E. Sakoske, Biaxial flexure strength and dynamic fatigue of soda--lime--silica float glass, J. Am. Ceram. Soc. 85 (2002) 1777–1782.

[6] M.H. Krohn, J.R. Hellmann, D.L. Shelleman, C.G. Pantano, G.E. Sakoske, Effect of enameling on the strength and dynamic fatigue of soda--lime--silica float glass, J. Am. Ceram. Soc. 85 (2002) 2507–2514.

[7] A.A. Wereszczak, T.P. Kirkland, M.E. Ragan, K.T. Strong Jr, H.-T. Lin, P. Patel, Size Scaling of Tensile Failure Stress in a Float Soda--Lime--Silicate Glass, Int. J. Appl. Glas. Sci. 1 (2010) 143–150.

[8] ASTM C1499-15, Standard Test Method for Monotonic Equibiaxial Flexural Strength of Advanced Ceramics at Ambient Temperature, (2015).

[9] S.P. Timoshenko, S. Woinowsky-Krieger, Theory of plate and shells, McGraw-Hill, New-York, 1959.

[10] F.F. Vitman, V.P. Pukh, A method for determining the strength of sheet glass, Ind. Lab. 29 (1963) 925–930.

[11] R.J. ROARK, W.C. YOUNG, Formulas for stress and strain, (1975) 624 p. : ill. ; 24 cm.

[12] H. Fessler, D.C. Fricker, A Theoretical Analysis of the Ring-On-Ring Loading Disk Test, J. Am. Ceram. Soc. 67 (1984) 582–588.

[13] S. et al. Ban, Effect of loading conditions on bi-axial flexure strength of dental cements, Dent. Mater. 8 (1992) 100–104.

[14] W. Weibull, A statistical distribution function of wide applicability, J. Appl. Mech. 18 (1951) 293–297.

[15] T. Rouxel, Mechanical Properties of Ceramics, in: P. Boch, J.-C. Niepce (Eds.), Ceram. Mater., John Wiley & Sons, 2000: pp. 263–324.

[16] J.W. Pepi, Strength Properties of Glass and Ceramics, Spie Press, 2014.

[17] D.C. Harris, Weibull Analysis and Area Scaling for Infrared Window Materials (U), Naval Air Warfare Center Weapons Division China Lake United States, Naval Air Warfare Center Weapons Division China Lake United States, 2016.

[18] Newman et al., An empirical stress-intensity factor equation for the surface crack, Eng. Fract. Mech. 15 (1981) 185–192.

[19] T. Rouxel, Fracture surface energy and toughness of inorganic glasses, Script. Mater. 137 (2017) 109–113.

III. Fracture toughness, fracture energy and slow crack growth of glass as investigated by the Single-Edge Precracked Beam (SEPB) and Chevron-Notched Beam (CNB) methods

III.1 Abstract

We show that the Single-Edge Precracked Beam (SEPB) test is not only suitable to the determination of the fracture toughness (K_{Ic}) of glass, but also offers a unique opportunity to assess the slow crack growth behavior in a single experiment lasting for few minutes. Besides, we found that it is possible to get either a stable or an unstable final fracture regime (pre-cracked specimen) depending on the testing parameters, and that the unstable case is preferable for the estimation of K_{Ic}. The "pop-in" precrack was found mostly to close completely once the load was suppressed on the bridge-flexure device. This led to a reopening event on the loading curves. It is noteworthy that all these original observations were made possible thanks to the design of a very stiff testing apparatus (6.7 $MN \cdot m^{-1}$) allowing for a cross-head speed as small as 0.01 $mm \cdot s^{-1}$. Results obtained on four grades of commercially available glasses are compared to those stemming from Vickers indentation cracking and chevron notched experiments.

Keywords: Fracture toughness, Vickers Indentation Fracture (VIF), Chevron-Notched Beam (CNB), Single-Edge Precracked Beam (SEPB), Stress-corrosion

III.2 Introduction

There is no standard method for the measurement of the fracture toughness (K_{Ic}) of glass. The difficulties, associated with the specimen preparation and the inherently low fracture surface energy, are still major obstacles to a reliable and accurate determination of K_{Ic} by means of self-consistent techniques. This situation favored the development of indentation-based experimental methods such as the indentation fracture (IF) ones [1–5]where a Vickers indenter is mostly used and fracture toughness is estimated from the geometrical characteristics of the indent (indentation size and indentation crack length). Nevertheless these methods need to be calibrated using values obtained on alternate standard methods and there still remain serious issues regarding the mechanical analysis [5,6].

The present study focuses on the SEPB test, examines the experimental conditions determining the stability of the ultimate fracture stage (from the pop-in precrack), and analyses the incidence of the preliminary indentation cracking characteristics. Environmental effects (humidity) are also

This chapter previously appeared as: T. To, F. Célarié, C. Roux-Langlois, A. Bazin, Y. Gueguen, H. Orain, M. Le Fur, V. Burgaud, T. Rouxel. Acta Materialia, 2018, vol. 146, p. 1-11.

discussed. The ultimate goal was to identify an experimental protocol based on "ideal" cracks, i.e. cracks with tip sharpness as close as possible to the one of propagating cracks during catastrophic failure under the assumption of pure elasticity, allowing for the determination of K_{Ic} in a self-consistent way. It was previously proposed by several investigators that such cracks are atomically sharp in brittle materials such as glass [7,8]. Chevron-Notched Beam (CNB) and Single-Edge Precracked Beam (SEPB) methods are well established self-consistent methods which proved to be suitable for the measurements of KIc of ceramics [9–11]. These methods will be compared to the indentation-based methods, which are far more common to estimate K_{Ic} of brittle materials. CNB method offers the advantage of stable crack propagation and of the ease for the measurement of the actual fracture surface energy. However, the estimation of the critical crack length corresponding to the maximum load, edge effects, and the difficult specimen preparation (especially the cutting of the Chevron-shape Notch), are major impediments. On the contrary, the SEPB method offers the advantage of a well-defined crack with a clear determination of the maximum load for the onset of crack extension, but requires a three-step protocol, sensitive optical means, and is mostly not suitable for stable crack extension. The SEPB test stability can be improved by using stiff loading device and mechanical testing machine. A specific testing machine, equipped with a ceramic loading set-up, a piezoelectric actuator and a very low compliance load cell was designed for this purpose. The mechanical stability of the SEPB test is discussed in the light of a quantitative modeling of the mechanical problem and numerical analysis.

The fracture toughness of four grades of commercially available glasses (optical quality), i.e. two borosilicate and two soda-lime-silicate glasses was estimated from the critical load for crack extension and from the overall energy spread to create the fracture surfaces as well. Results stemming from the onset for crack extension and from the crack propagation regime, in case of stable crack growth, were analyzed and compared. Both are expected to give slightly different K_{Ic} values due to different physics and chemistry behind both processes, such as environmental couplings, dynamic effects, a tortuous crack path, etc. However, in cases where the incidence of the environment remains limited, and where crack extension chiefly proceeds in the opening mode (mode I), a good correlation is expected and is indeed observed in many cases. Differences in both results are interesting though because they shed light on possible complicated features for the crack extension. The critical load corresponds to the initiation of crack propagation and is hence more subjected to history and to the precrack characteristics (tip sharpness, chemical alteration, residual stresses, etc.). In contrast, measuring the dissipated energy requires the occurrence of stable crack propagation but is likely to be more related to intrinsic material properties, as far as concomitant stress-corrosion permanent deformation phenomena remain limited.

III.3 Materials and experimental techniques

III.3.a. Glasses and experimental condition

Four commercial grades of glass were studied, namely two borosilicate glasses (Schott BK7 and Schott Borofloat® 33) and two soda-lime silica glasses (Pilkington Optiwhite™ and Saint-Gobain Comp. Planilux®). The chemical composition and some physical and mechanical characteristics (T_g, H, E, G, ν, K_{Ic}) of these glasses are reported in **Tables III.1** and III.**2** respectively. Glasses were chosen so as to i) cover some range in stiffness (E changes from 64 GPa to 82 GPa between the Borofloat and the BK7 grades respectively), ii) investigate the effect of humidity (soda-lime-silica glasses are more sensitive to water than borosilicate glasses [12]), iii) study the influence of changes in the indentation deformation mechanism on the fracture toughness values (borosilicate glasses are more prone to densification and cone/ring cracks under a Vickers indentation than soda-lime-silica glasses). All experiments were conducted in ambient atmosphere (~ 20 °C, 60 % humidity).

Table III.1: Approximate chemical compositions (in weight %). (from the technical sheets of the relevant companies or Ref. [13]).

Glasses	Na_2O	K_2O	CaO	MgO	BaO	B_2O_3	Al_2O_3	SiO_2
Borofloat® 33	4 (Na_2O + K_2O)		–	–	–	13	2	81
BK7	9.5	7.5	–	–	1.5	11.5	–	70
Optiwhite™	13	0.4	8.8	4.3	–	–	0.6	72.7
Planilux®	13.4	–	9.6	4	–	–	0.6	72

Table III.2: Glass transition temperature and mechanical properties. The data for Borofloat® 33, BK7, Optiwhite™, and Planilux® glasses, were extracted from the technical sheets of the relevant companies and Ref. [14]. H is averaged Meyer's hardness ($H = 2P/d^2$) over four measurements (load P of 9.81 N applied for 15 s).

Glasses	T_g (˚C)	H (GPa)	E (GPa)	G (GPa)	ν
Borofloat® 33	530	6.21	64	27	0.20
BK7	557	7.01	82	34	0.21
Optiwhite™	559	5.77	72	30	0.23
Planilux®	540	6.12	73	30	0.23

III.3.b. Vickers indentation fracture (VIF)

The Vickers indentation fracture toughness test, or VIF, is popular for its simplicity and ease in specimen preparation and measurement [5]. It is based on the measurement of the indentation

corner cracks and relies on an idealized crack pattern under the indent. Because of the complexity of the indentation cracking problem (crack arrest phenomenon, process zone, multiple cracks developing both during loading and unloading) [6], it is not a self-consistent method as it requires a calibration constant (pre-factor in the right-hand side term in Eqs. (1,2)).

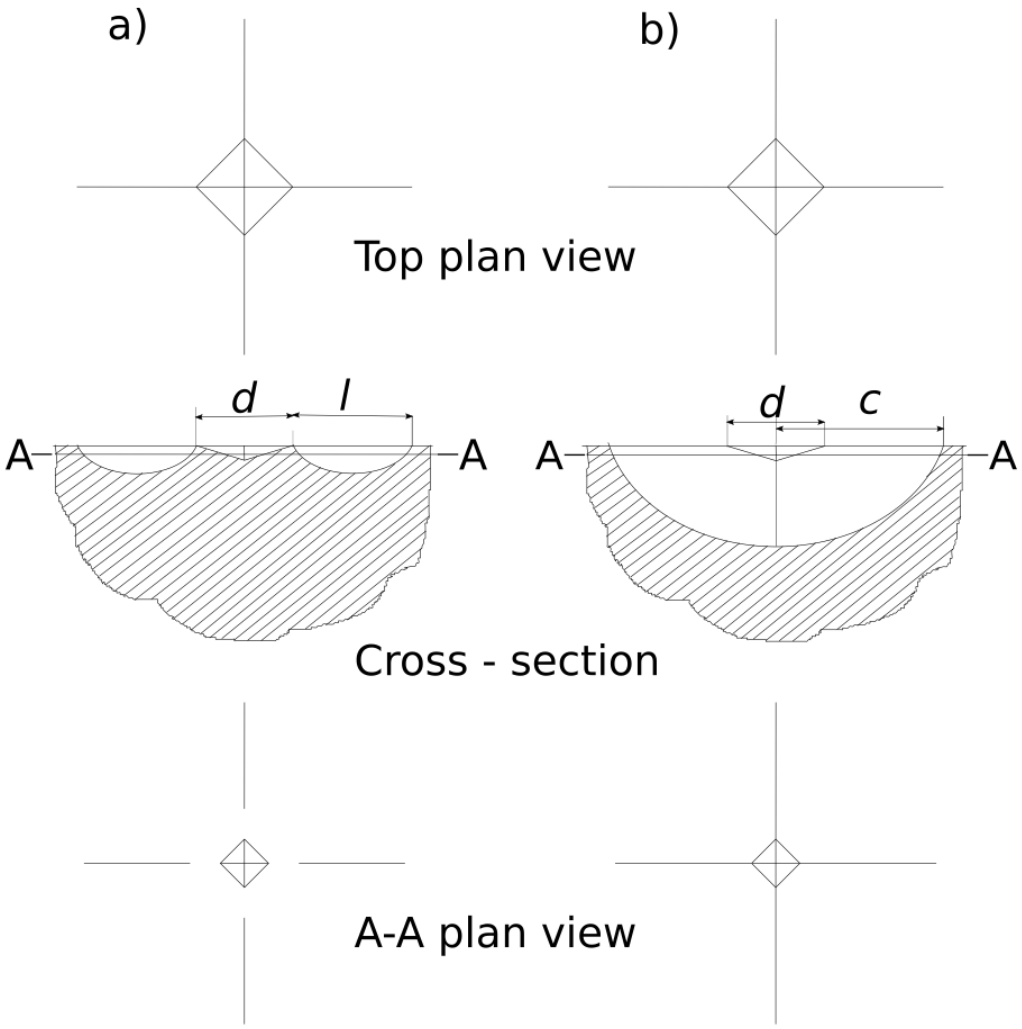

Fig. III.1: Schematic top plan view, cross-section, and AA plan view (after polishing) of a Vickers imprint site for a) a Palmqvist and b) a radial-median cracking pattern.

Indentation and crack observation

Specimens of the four grades of glass (2.5 to 4 mm thick) were polished to an optical finish down to a 1 µm grade diamond paste. Vickers indentations were then performed with a microhardness testing apparatus (Matsuzawa VMT-7S) with a load of 9.8 N for 15 s, which resulted in the formation of long cracks from the indentation corners without visible chips. Cracks were observed by optical microscopy (Olympus BX60 with a $\times 50$ objective). The indentation diagonal (d) and the crack length ($2c$) were measured two minutes after the indentation.

Crack pattern

Depending on the crack pattern (e.g. ring/cone, radial-median or Palmqvist), numerous models were developed to link the Vickers indentation load to the fracture toughness. Readers will find an exhaustive review of those in Refs. [4,5]. The first difficulty is to identify the crack geometry that cannot be elucidated from surface observation only. In an attempt to differentiate between the radial-median (also called half-penny) and the Palmqvist (surface-radial) microcracking patterns, the 9.8 N indented specimens were polished to about half of the indentation depth. The specimens were again observed by optical microscopy. A schematic of the expected surface patterns before and after polishing is shown in Fig. 1 for both the Palmqvist crack pattern (**Fig. III.1a**) and the radial-median crack pattern (**Fig. III.1b**). It is noteworthy however that even in the case where the radial cracks seem to be detached from the imprint after polishing, the presence of a process zone (hemispherical shape) in the surrounding, where densification occurred for instance, prevents from a definite conclusion regarding the microcracking pattern.

Fracture toughness calculation

The Vickers indentation fracture toughness was calculated using Eq. (III.1) for radial-median crack pattern [15] and Eq. (III.2) for Palmqvist crack pattern [16].

$$K_{VIF(Ans)} = (0.016 \pm 0.004)(E/H)^{1/2}.P/c^{3/2}, \quad \text{(III.1)}$$

$$K_{VIF(Nii)} = 0.018\,E^{2/5}H^{3/5}(d/2).l^{0.5}, \quad \text{(III.2)}$$

where E is the Young's modulus, H is the Meyer's hardness ($H = 2P/d^2$), P is the indentation load, d is the half indentation diagonal length, c is the half crack length, and l is equal to $c - (d/2)$ as shown in **Fig. III.1**. It is noteworthy that the prefactor in the right-hand side of Eqs. (III.1, III.2) was calibrated using chiefly ceramic materials and including a soda-lime-silica glass. Unlike most polycrystalline ceramics, glasses are known to allow for a significant densification upon indentation loading, because of i) pressure in the GPa range beneath the indenter and of ii) a relatively large amount of free volume [17]. The physics behind these equations (isochoric plasticity) is thus put into question in the case of glasses, and K_{Ic} values obtained by means of self-consistent techniques on various glasses might hardly compare with VIF ones, with perhaps the exception of soda-lime-silica glass.

III.3.c. Chevron-notched beam (CNB)

The Chevron-Notched Beam (CNB) method is known as a self-consistent standard method [11]. The method requires the machining of a V-shape notch (so-called chevron) in the middle of a beam. This shape is achieved by means of a two-step cutting procedure, involving two straight through

cuts. The chevron-notched beam is then loaded in bending mode (the tip of the remaining V-shape ligament being in the tensile side). Under the assumption that a planar crack with a straight front is propagating, the value of the maximal load (which corresponds to a critical crack extension) was tabulated as a function of K_{Ic} and the specimen geometry [18]. In order to ensure a stable crack extension, a chevron notch with a relatively acute angle (apex angle = 40°) was chosen and a full ceramic (SiC) three-point bending device was used for sake of stiffness.

Notch machining

Bulk samples of thickness varying from 2.5 to 4 mm (depending of the available glass sheets) were cut into rectangular beam specimens with the final height (W) varying from 2.85 to 4 mm, and broadness (B) varying from 2 to 3 mm and length of 30 ± 1 mm, and polished with a diamond paste down to 9 μm grades. The beam were mounted on and glued to a stainless steel support designed to have two symmetric inclination plans for machining the chevron notch as illustrated in **Fig. III.2**. Advantage in having these symmetric plans is that the same end of a specimen can be used as a reference to limit the offset between the first and the second cuts. Cutting was achieved by means of a 0.2 mm thick diamond wheel with a cutting speed of 23 $m.s^{-1}$, and a translation speed of 0.2 $mm.min^{-1}$. Typical final chevron geometry is shown in the result section.

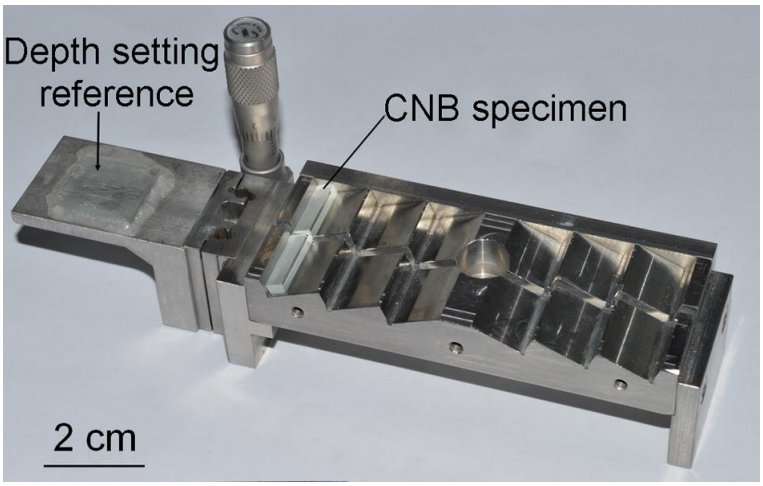

Fig. III.2: Grooved stainless steel support with a typical chevron notch specimen in position for the half chevron notch cutting (the final chevron apex angle is 40 °).

Three-point bending

In order to achieve a high resolution for the displacement together with a high precision for the specimen deflection measurement, combined with a small machine compliance ensuring the stable crack propagation, a mechanical testing equipment consisting of a piezoelectric displacement actuator (N-216 NEXLINE® Linear Actuator, Physik Instrumente company, Germany), a laser

interferometer displacement sensor (LK-G5000 series with LK-H008W head sensor, Keyence Corporation company of Japan), and a stiff load cell (MS02 load cell, 6.7 $MN.m^{-1}$ stiffness, 1 kN capacity, Scaime company, France) was designed (**Fig. III.3**). The displacement actuator is characterized by a 5 nm closed-loop resolution over a 20 mm displacement range, allowing for displacement rates between 0.01 $\mu m.s^{-1}$ and 400 $\mu m.s^{-1}$. The displacement sensor can detect displacements between − 500 µm and + 500 µm with an accuracy of 5 nm.

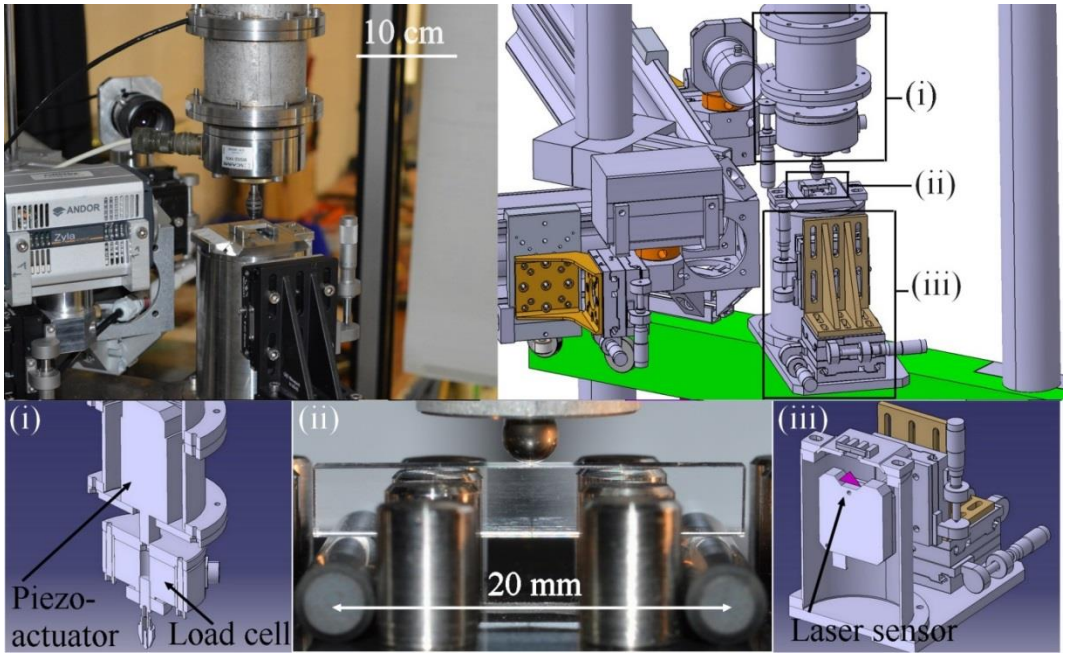

Fig. III.3: Mechanical testing equipment.

The parallelepiped glass bars with a chevron notch were fractured in three-point bending with a support span of 20 mm and a crosshead speed (actuator) of 0.01 $\mu m.s^{-1}$. The specimen deflection (u) was measured in situ by means of a laser interferometer displacement sensor focused on the tensile surface of the beam. The displacement was double-checked using the actuator position record and the whole loading set-up compliance (calibrated prior to the measurements).

Fracture toughness measurement

K_{Ic} was calculated either using the maximum load (P_{max}) or of the work of fracture (wof),

$$wof = \int_0^{u_f} P\mathrm{d}u \ , \tag{III.3}$$

where u_f is the final deflection corresponding to complete fracture, and wof is related to the fracture surface energy by,

$$wof = 2\gamma S \, , \tag{III.4}$$

where γ is the fracture surface energy, and S is an in-plane fracture surface (geometrical area). In the first method, the formula developed by Munz et al. [10] was used

$$K_{CNB}(P_{max}) = \frac{P_{max}}{B\sqrt{W}} Y_C^* \ , \tag{III.5}$$

where P_{max} is the maximum load (P-u curve), B and W are the specimen's broadness and height respectively, and Y_C^* is the critical dimensionless geometric coefficient calculated from both Slice and STCA (Straight Through Crack Assumption) approximation [18–21]. In the Slice model, the fracture chevron section is divided into many narrow slices and each slice is taken as a straight-through cracked section. In the STCA model, the fracture chevron section is taken as a straight-through cracked section with the same crack length and thickness as the chevron crack front. In the second method, the fracture toughness was calculated from the equation proposed by Irwin [22]:

$$K_{CNB}(\gamma) = \sqrt{2\gamma E'} \ , \tag{III.6}$$

where E' is taken equal to $E/(1 - \nu^2)$ (plane strain hypothesis in the bulk).

III.3.d. Single-edge-precracked beam

The Single-Edged Precracked Beam method, or SEPB method, is as a self-consistent standard method [11], which consists in creating a straight-through precrack in a beam from indents or saw notch via a technique called bridge-flexure (described below). The bridge-flexure technique generates a sharp planar precrack. The precracked beam is later fractured in the bending mode.

Precracking stage

Parallelepiped bars similar to those used for the CNB test were cut and polished down to 3 µm diamond grade, except the surface chosen to initiate the precrack that was polished down to 1 µm. The polishing of the specimen sides was aimed at eliminating surface residual stresses that might lead to uneven crack extension and affect the toughness measurement. Vickers indentations with their diagonal aligned with the specimen broadness proved to act as an efficient precursor for the precrack. The indentation load (usually between 1 to 10 N) was adapted for each glass grade to generate corner crack of about 50 µm in length (c in Eq. (III.1)) and a line of indentation with 300 µm between each imprint was performed. The resulting precrack, is within the cross-section (< 5° inclination) with a flat front (less than 10 % difference between the average precrack length and any measurement at 0.25, 0.50, and 0.75 of the specimen broadness). **Figure III.4** shows a typical indentation line on a specimen. The precrack is obtained by means of tungsten carbide bridge-

flexure (**Fig. III.5**) with the indented surface of the glass sample being over the groove and a loading rate of 0.05 mm.min^{-1}. During the bridge compression process, the propagation of the precrack length was observed from an optical camera. As explained in Nose and Fujii [9], the crack initiated and grew slowly in the indented area and then propagated suddenly. This stage is referred to as the pop-in precracking. The loading was stopped right after the pop-in precrack was visible (ultrasonic monitoring was used) to avoid further crack growth.

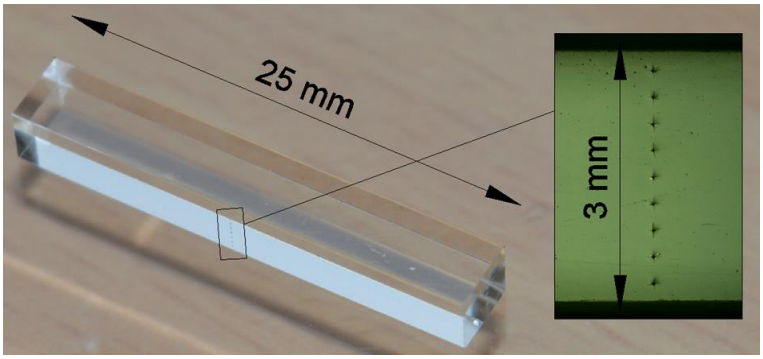

Fig. III.4: Typical indented SEPB specimen (Planilux) with zoom of the indentation line.

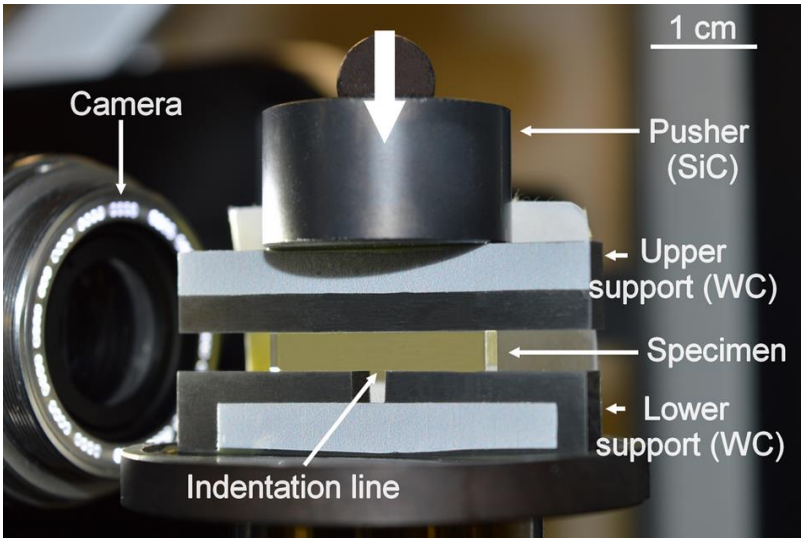

Fig. III.5: Compression fixture with indented specimen (Planilux).

The bridge-flexure geometry was optimized to have a pop-in precrack long enough to make the residual stresses stemming from the indentation site negligible (a_0/W = 0.35 according to the ASTM [11]), and short enough to avoid free surface perturbation (precrack length a_0/W < 60% according to ASTM recommendation [11]). Plane strain extended finite element simulation was performed for different geometries and crack lengths, and the stress intensity factor was computed. Tungsten

carbide (E = 490 GPa) is much stiffer than the glass sample (E ~ 70 GPa). For sake of simplicity in the calculation, the bridge-flexure is taken as perfectly rigid, so that prescribed normal displacements were thus enforced in the simulation. The simulation showed that once the sample and the bridge-flexure are long enough ($L > 3W$) fracture (stress intensity factor evolution) is governed by three geometrical parameters: the sample width W, the groove size b and the crack length a. The pop-in precrack length is an outcome that depends on b normalized by W. The pop-in precrack appears when the tension on the indents generated by the bridge compression fixture reaches a critical value T_c. It then stops at a position where K_I becomes lower than the toughness. The evolution of K_I with the crack propagation (a/W) is shown in **Fig. III.6** for different groove sizes, where K_I is normalized by T_c for each groove size; T_c is computed from the finite element simulation without crack. Since far enough from the indents, K_I and T_c are proportional to the load, this is equivalent to performing the simulation at the prescribed displacement generating the pop-in. This figure can then be used to determine the groove size needed to obtain the required precrack length. K_{Ic} and T_c being unknown, a preliminary test has to be performed for each considered material with an arbitrary groove size in order to compute K_{Ic}/T_c from the precrack length a_1 associated with this preliminary test. The groove size to obtain the required pop-in precrack length can then be identified for different b/W values. Although this process may require additional iterations due to the modelling approximation, it was successful in all tested cases. In case where a satisfactory precrack length cannot be achieved, whatever the b/W ratio, it is recommended to reduce the indentation load so as to increase the precrack length.

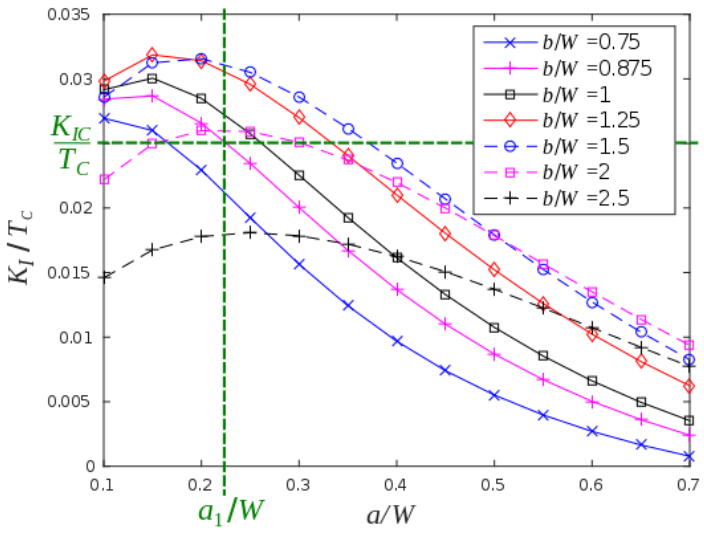

Fig. III.6: Stress intensity factor (normalized by the critical tension on the Vickers indents at the onset of the pop-in precrack formation) as a function of the crack length (normalized by the width W).

Fracture of the precracked specimen

In order to fracture the precracked specimens, a three-point bending loading rate of 0.1 µm.s^{-1} between two silicon carbide rollers at a distance of 20 mm is applied. The beam deflection is measured by means of a laser interferometer displacement sensor. Optical observations are also made by means of portable optical cameras.

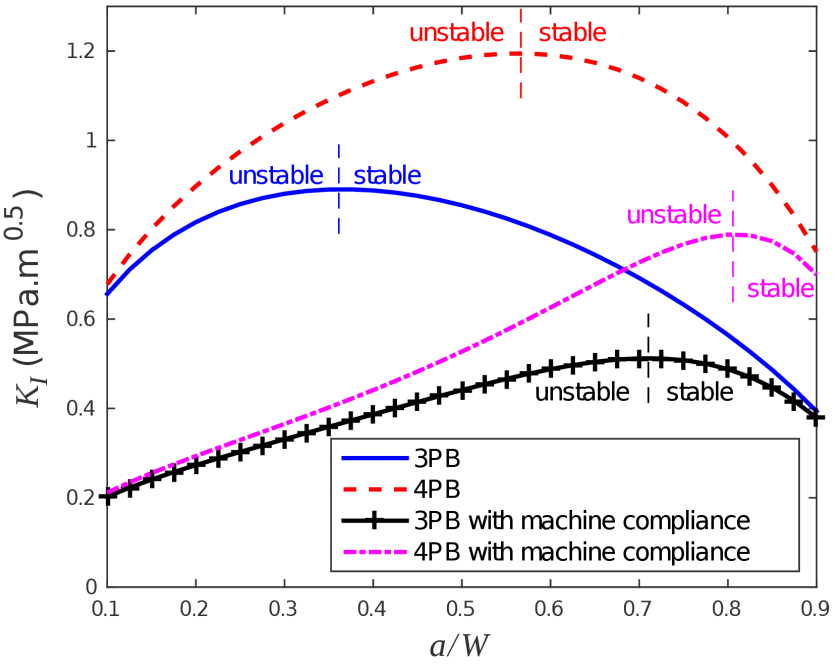

Fig. III.7: Stress intensity factor for a given prescribed displacement (u_d), for a 25×4(W)×3 mm^3 beam loaded in three or four point-bending (3PB and 4PB), with inner (4PB) and outer (3PB and 4PB) span lengths of 10 and 20 mm respectively.

Although it requires aligning accurately the precrack with the loading axis, three-point bending was preferred to four-point bending as it favors stable crack propagation, chiefly because of a smaller elastic energy storage upon reaching the critical load. Evidenced for a stable crack extension is illustrated in **Fig. III.7** where the evolution of the stress intensity factor is plotted as a function of the crack length for a given displacement. K_I was computed with a plane strain numerical simulation assuming punctual support and neglecting any friction. An increase of K_I (left-hand side of the curves) at constant displacement reflects an unstable crack extension. Accounting for the machine (including the loading device) compliance results in a lower value for K_I. Nevertheless the extent of the unstable range is always larger in four-point than in three-point bending. K_I is found to decrease as the crack grows from a/W = 0.35 in three-point bending and 0.56 in four point bending. This is the stable crack extension range. It is noteworthy that when the stiffness of the loading

device is accounted for, in agreement with Bar-On *et al.* [23], a very long precrack is needed for a stable crack growth.

Fracture toughness calculation

In analogy with the single edge notch beam (SENB) method, the SEPB one is based on the accurate measurement of the maximum load. To the best of the knowledge of the present authors, there was no attempt so far to estimate K_{Ic} from the *wof* associated with this test, very likely because tests were mostly unstable. In the present study, a stable extension of the SEPB precrack was achieved by properly tuning the precrack length, so that K_{Ic} could be calculated using both the maximum load (P_{max}) and the fracture surface energy (γ), by means of Eqs (III.3, III.5). P_{max} was calculated by finite element simulation under a plane strain assumption. The load is determined with a better than 0.12 N accuracy corresponding to a better than 0.02 MPa.m$^{0.5}$ accuracy for K_{Ic}.

III.4 Results

K_{Ic}, as obtained from the different methods on the four glass grades is summarized in **Table III.3** together with previously published data on these glasses. The present measurements of K_{Ic} (SEPB, unstable fracture) of the window glass (here the Planilux brand) are in good agreement with the values obtained with the SEPB method in air by Kato et al. [24] and Salem et al. [25]. However Quinn et al. [26] obtained significantly larger values, especially for the BK7, although the maximum testing velocities they used in air to prevent against stress-corrosion effects, are very close to the present velocities. The difference for BK7 is even larger in dry N2. Possible explanations for these differences include: i) the humidity levels in the ambience. In the present case, a humidity of ~ 60 % was recorded, which is about the upper bound for the humidty in [26], so that the maximum cross-head speed might still be insufficient to completely avoid environmental fatigue-like effects ; ii) in the case of the BK7 specimens, we noticed that the precrack length was systematically smaller than for the other glass grades, and lied at the lower limit per the ASTM standard [11]; and iii) In the present study, the precrack is initiated from a series of aligned Vickers micro-indents, whereas a scratch was used in [26]. Further investigations would be needed to provide a definite conclusion.

Table III.3: Fracture toughness (in MPa.m$^{0.5}$), as measured by means of different methods. (-): number of tests; ±: standard deviation. $K_{CNBslice}(P)$: CNB method using the maximum load with the Slice model approximation; $K_{CNBstca}(P)$: CNB method using the maximum load with STCA approximation; $K_{CNB}(\gamma)$: CNB method using γ (from *wof*); $K_{SEPBstable}(P)$: SEPB method using the maximum load for the stable crack propagation; $K_{SEPBunstable}(P)$: SEPB method using the maximum

load value for unstable crack propagation; $K_{SEPB}(\gamma)$: SEPB method using γ (from *wof*); [1)]One valid result among the three specimens with a final fracture angle < 5°; [2)]Average of three valid results among the six specimens. [3)]Soda-lime-silica type glass (float glass).

Glasses	**Borofloat® 33**	**BK7**	**Optiwhite™**	**Planilux®**
$K_{IF(Ans)}$ *(Eq. (1))*	0.99 ± 0.04 (5)	0.51 ± 0.01 (5)	0.66 ± 0.01 (5)	0.67 ± 0.02 (5)
$K_{IF(Nii)}$ *(Eq. (2))*	1.32 ± 0.03 (5)	1.01 ± 0.01 (5)	1.06 ± 0.00 (5)	1.09 ± 0.01 (5)
$K_{CNBslice}(P)$	0.77 ± 0.02 (2)	0.72 (3)[1)]	0.72 (3)[1)]	0.75 ± 0.04 (6)[2)]
$K_{CNBstca}(P)$	0.73 ± 0.01 (2)	0.67 (3)[1)]	0.67 (3)[1)]	0.71 ± 0.04 (6)[2)]
$K_{CNB}(\gamma)$	0.50 ± 0.05 (2)	0.55 ± 0.09 (3)	0.58 ± 0.04 (3)	0.66 ± 0.04 (6)
$K_{SEPBstable}(P)$	0.52 ± 0.01 (6)	0.47 ± 0.01 (2)	0.56 ± 0.04 (2)	0.56 ± 0.02 (12)
$K_{SEPBunstable}(P)$	0.65 ± 0.03 (6)	0.65 ± 0.01 (4)	0.67 ± 0.01 (4)	0.70 ± 0.01 (5)
$K_{SEPB}(\gamma)$	0.64 ± 0.01 (6)	0.65 ± 0.10 (2)	0.63 ± 0.00 (2)	0.66 ± 0.03 (12)
K_{Ic} (litterature, CNB)	1.03 ± 0.10 [27]	0.93 ± 0.04 [28]	0.73 ± 0.06 [29]	0.63 ± 0.10 [21]
K_{Ic} (litterature, SEPB)				
In air [24]	/	/	/	0.75 ± 0.05[3)]
In air [25,26]	0.73 ± 0.03 [26]	0.87 [26]	/	0.71 ± 0.01 [25][3)]
In dry N2 [26]	0.75 ± 0.03	0.92 ± 0.05	/	0.76 ± 0.03[3)]

III.4.a. VIF

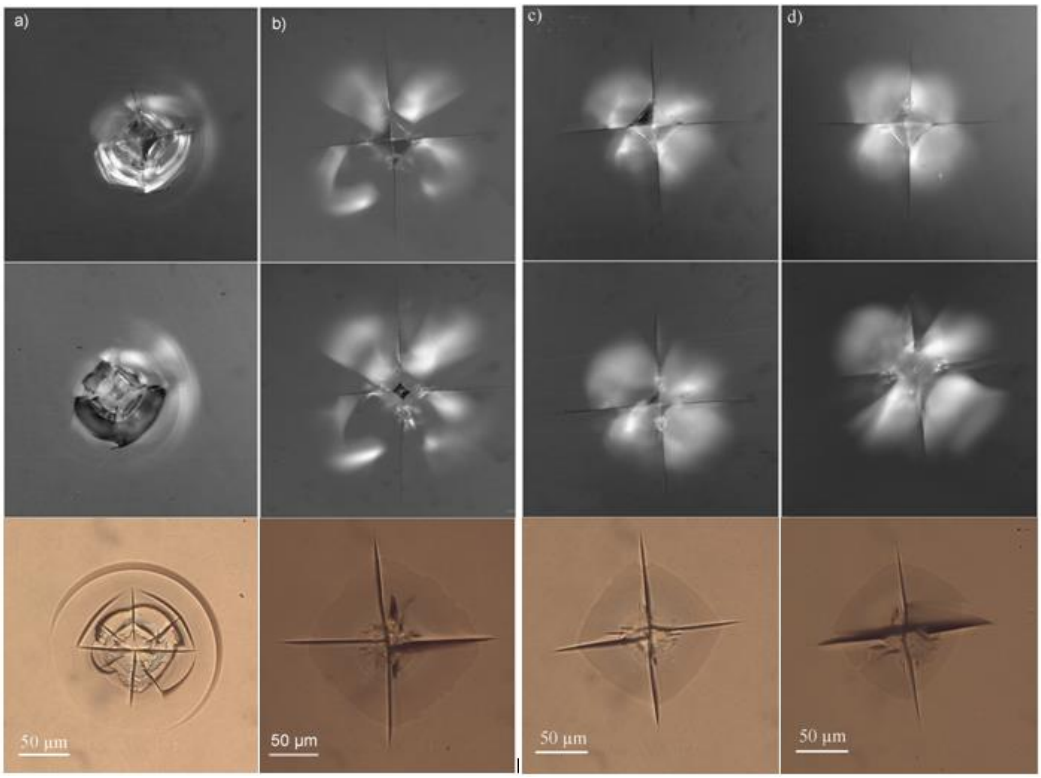

Fig. III.8: 9.8 N Vickers indentation of a) Borofloat 33, b) BK7, c) Optiwhite, d) Planilux. Top: views before polishing on the indented spcimens. Middle and bottom: views from front and back light, respectively, after polishing about half the indentation depth on the indented specimens.

Despite a careful observation and numerous studies existing on these well-known glasses, the cracking patterns remain debatable. Niihara et al. [16] and Lankford [30] suggested that when the $2c/d$ ratio is lower than 2.5 the surface cracks extending from the indentation corners remain near the surface and form the so-called Palmqvist pattern, as opposed to the half-penny pattern. Among the four grades of glass, only the Borofloat 33 exhibits $2c/d < 2.5$. However after polishing indentations made on all grades of glass with a 9.8 N (**Fig. III.8**), the (surface) radial cracks appear detached from the indentation imprint which would be the signature of Palmqvist patterns [31,32]. However, the gap between the radial cracks and the indent is rather blurry and the process zone where densification and extensive deformation show up at indentation site impedes a definite conclusion. Indeed, by changing the optical illumination conditions from front-light to back-light on the microscope, shadowy lines between the radial cracks are observed. Because of this uncertainty, both Eqs. (III.1, III.2) were used to calculate the indentation fracture toughness by the VIF method. The Niihara's equation (Eq. (III.2)) gives higher values of indentation fracture toughness whatever the glass (**table III.3**). Borofloat 33 which has the lowest $2c/d$ ratio has the greatest value of K_{Ic}. In contrast BK7, with the highest $2c/d$ ratio has the lowest toughness. Planilux and Optiwhite, which are all soda-lime silica glass, have indentation toughness comparable to other methods, which is not surprising owing to the fact that similar glasses were included in the calibration step for the development of VIF methods [15].

III.4.b. CNB

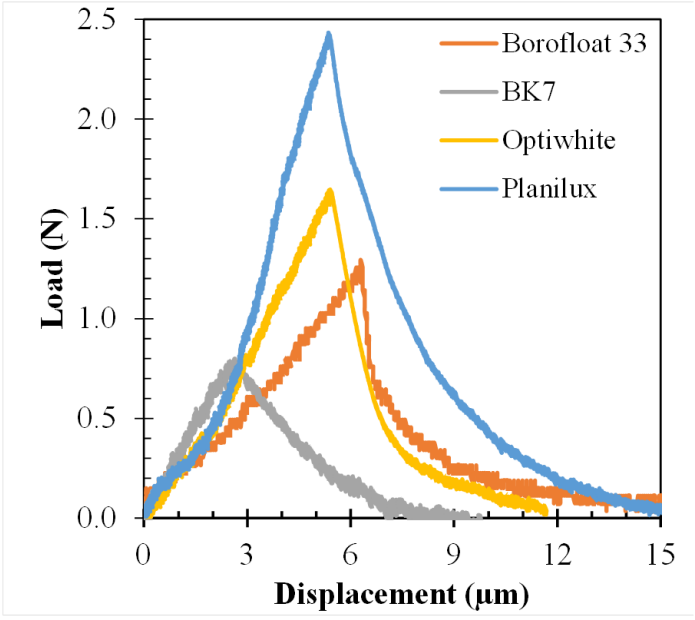

Fig. III.9: Typical stable load-displacement curves obtained with CNB specimens. Specimens having significantly different cross section areas were fractured in 3-point bending with a span length of 20 mm and a cross-head speed of 0.08 µm/s, except for Planilux that was fractured with a cross-head speed of 0.01µm/s.

Typical load-displacement curves of CNB specimens loaded in 3-point bending are shown in **Fig. III.9**. The post-mortem fracture surface showing the chevron-shaped ligament is illustrated in **Fig.**

III.10. In the chevron geometry, W, B, a_1, and a_0 are the specimen's height, broadness (associated with the V-shape ligament), and the geometrical characteristics of the notch (**Fig. III.10**). In the present study, W = 3 - 4 mm, B = 1.5 - 2 mm, a_1 = W and a_0 = 1.4 mm. The load versus displacement curve exhibits a relatively sharp maximum, which contrasts with the smooth shape quoted in ASTM [11] for specimens with slightly different geometrical characteristics, which were not applicable for the presently studied glass batches. Micro-cracks were observed at the tip and at the border of the chevron in most cases (**Fig. III.10**). These micro-cracks arose from the cutting of the chevron notch, as well as from the uneven crack propagation and the out-of-plane component of the crack propagation. The existence of a planar offset between the two parts of the notch can result in an overestimated K_{Ic} [33]. In the present study, the offset is smaller than 75 µm (30 % of the notch thickness), and is thus supposed to have little incidence on the toughness measurement [11]. K_{Ic} results as obtained using the Slice model (Slice), the Straight through Crack Assumption (STCA), and the *wof* are given in **Table III.3**. The STCA method gives a K_{Ic} value about 5 % smaller than the Slice one. Salem et al. [34] compared the toughness values calculated from Slice and STCA approximations with a 3D finite element analysis (FEA) and found a good agreement between FEA and STCA when a_1/W = 1 and with Slice when a_1/W < 1. In the present case a_1/W = 1, so that STCA will be considered further in the discussion. K_{Ic} as deduced from the *wof* is significantly smaller than Slice and STCA results, especially for Borofloat 33, BK7 and Optiwhite. This discrepancy will be discussed in the next section.

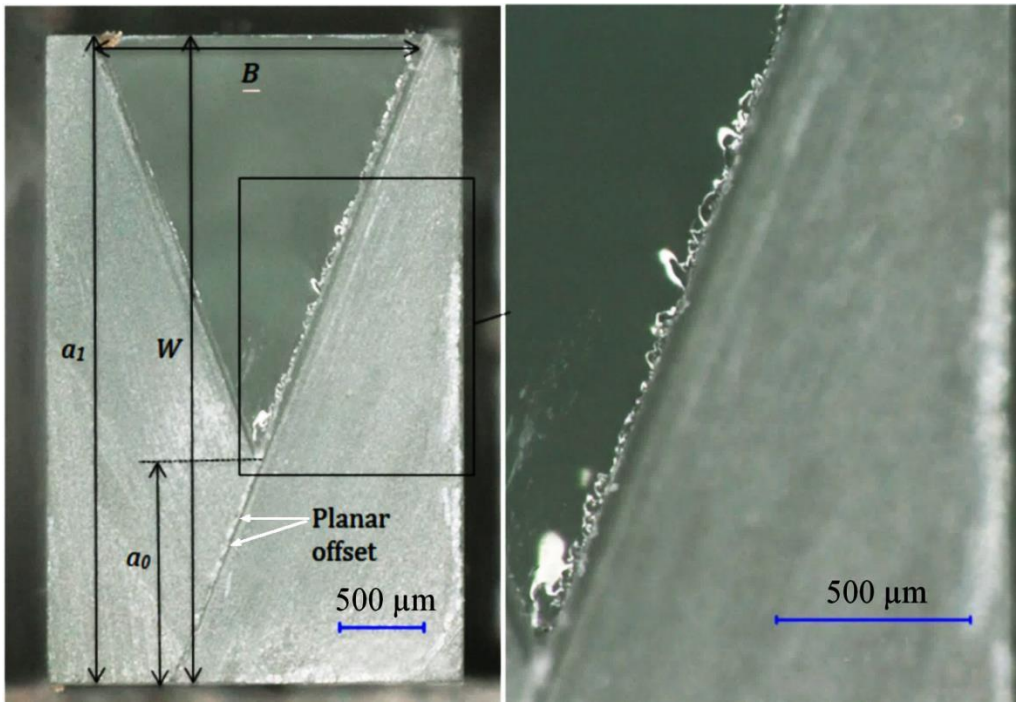

Fig. III.10: Left: typical in-plane fracture surface of a CNB specimen. Right: zoom-in along the edge of the ligament revealing secondary microcracks and chips.

III.4.c. SEPB

Two typical SEPB three-point bending fracture load-deflection (P-u) curves recorded with window glass specimens are shown in **Fig. III.11**, together with an optical fractography. The alignment of the Vickers imprints and the associated micro-cracks are visible at the bottom of the inset. The crack arrest line (black arrows) shows the precrack front. The precrack length and the remaining ligament of material are easily measurable. The two curves in **Fig. III.11** correspond to specimens with identical geometry and precrack length (a/W) but two different cross-head speeds: 2 µm.s^{-1} and 0.02 µm.s^{-1}. It is worth mentioning that obtaining twice the same precrack length is challenging, and was made possible by means a careful preliminary study (calibration) of the indentation cracking stage. The sudden decrease of the load at a displacement of ~ 2 µm on both curves is associated with the reopening of the precrack and will be showed in the synchronizing video in the next section. Indeed, the crack closes as the compression load is released just after the opening of the pre-crack with the bridge-flexure (pop-in). Hence, in the beginning of the subsequent bending experiment, the beam specimen exhibits stiffness similar to the one of a pristine, crack-free, specimen, consistently with the fact that no crack could be seen with the in-situ optical microscope. Then, as the displacement is increased beyond ~ 2 µm, a stable extension of the re-opened precrack is observed in the case of the smallest cross-head speed, while the unstable crack growth is produced at the largest cross-head speed. Stable and unstable tests result in different K_{Ic} values (**table III.3**). For the stable tests, K_{Ic} could also be estimated from the work of fracture ($K_{SEPB}(\gamma)$) for the four grades of glass. On the one hand $K_{SEPBstable}(P)$ is at least 16 % lower than $K_{SEPBunstable}(P)$. On the other hand, $K_{SEPB}(\gamma)$ is just slightly lower than unstable toughness. Note that the standard deviation for these measurements is rather low. The incidence of the loading rate on the test stability and on the final result for K_{Ic} will be discussed in the next section.

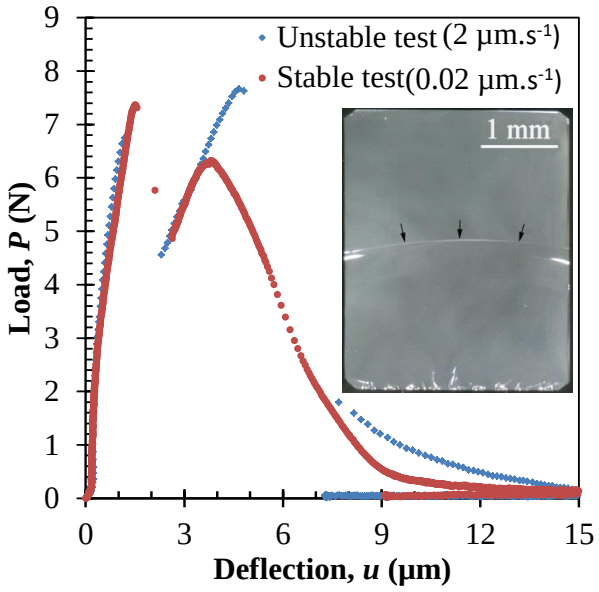

Fig. III.11: Load-deflection (P, u) curves of stable and unstable tests with identical precrack lengths (a ~ 0.5W). The stable and unstable tests were obtained in three-point bending using cross-head speeds of 0.02 and 2 µm.s^{-1}, respectively.

III.5 Discussion

III.5.a. VIF

Current VIF equations are based on strong assumptions regarding the constitutive law: no densification, perfect plastic flow, and no pressure-dependent material characteristics. These assumptions are obviously questionable in the case of glass. Nevertheless for Optiwhite™ and Planilux®, the $K_{IF(Ans)}$ values are comparable to K_{Ic} values measured by means of self-consistent method, e.g the SEPB one, likely because soda-lime-silica glass was included in the calibration protocol for the VIF method [15]. As soon as the glass properties depart from those of soda-lime-silica glass, VIF method mostly leads to biased results. For instance in the case of Borofloat, the indentation-derived K_{Ic} value is ~ 100 % larger. This is because densification and shear impede the formation of extensive radial/median cracking in such glass, as evidenced in **Fig. III.8a**, where the hertzian-type cone cracks intersecting the surface to form rings are visible and reflect the sensitivity of this glass to densification. A review of the effect of the glass composition on the indentation-induced densification and shear (pile-up of mater at the surface) was published elsewhere [35]. Having Poisson's ratio of ~ 0.2, both borosilicate glasses (Borofloat and BK7) might exhibit densification contribution accounting for up to 70 % of the volume of the Vickers imprint, while for Planilux the densification contribution is of ~ 60 % (~ 85 % for amorphous silica) [36].

III.5.b. CNB

In the present study, the notch angle (apex) is relatively small (~ 40°) so that owing to the thickness of the notch (0.25 mm) the crack path can shift from the cross section plane by an inclination angle up to 9.5°. For instance, an offset angle of 7.8° was measured post-mortem the Optiwhite specimen. This inclination induces a raise of the load necessary for the tearing process, and thus leads artificially to a larger toughness value. According to the ASTM standard for the SEPB method, the offset should be within less than 5°. Therefore specimens for which the inclination angle was larger than 5° were excluded from the analysis and were not reported in **table III.3**. Valid experiments show an excellent agreement between $K_{CNBstca}(P)$ and $K_{SEPBunstable}$(P). Post-fracture investigation is thus needed to validate the CNB test. K_{Ic} as calculated from the work of fracture $K_{CNB}(\gamma)$ appears underestimated, likely because of the presence of micro-cracks near the edges of the notch which would also be responsible for the increase of the roughness of the fracture surface near the notch in **Fig. III.10**.

III.5.c. SEPB

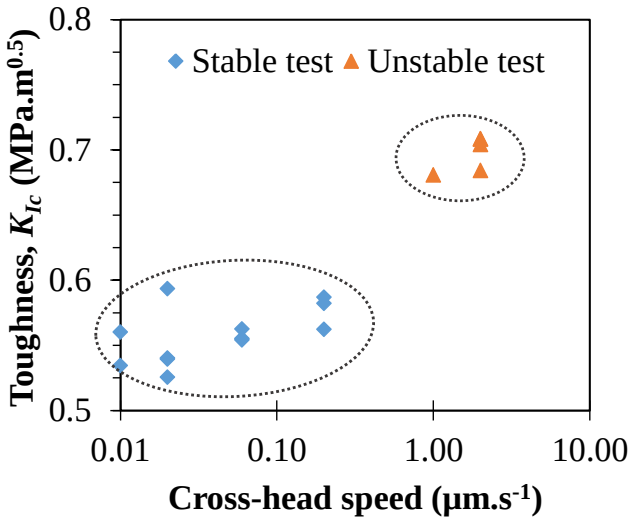

Fig. III.12: Toughness of Planilux from SEPB stable and unstable tests as a function of cross-head speed. In all the experiment, the precrack length to height (W) ratio is about 0.50.

The observed dependence of the experimental results on the loading rate shows that the precrack length (a/W = 0.53) is not a sufficient parameter to ensure stable crack propagation (**Fig. III.11**). The stable crack growth induced at small loading rates, when unstable crack propagation was indeed expected, brings to light the concomitant effect of the environment, and especially the atmospheric humidity. K_{Ic} is depicted as a function of the cross-head speed for Planilux specimens in **Fig. III.12**. For cross-head speeds below 0.2 µm.s^{-1}, fracture is stable and K_{Ic} is about 0.55 MPa.m$^{0.5}$. In contrast, for cross-head speeds larger than 1 µm.s^{-1}, fracture is unstable and K_{Ic} reaches 0.70 MPa.m$^{0.5}$, which is 20 % larger than the "stable fracture" value. Indeed, a monotonic increase of K_{Ic} was noticed as the cross-head speed was increased (**Fig. III.12**). Stress corrosion in this glass is due to H_2O molecules in the ambience reacting with and disrupting the Si-O bonds at the crack front. The kinetics of this chemical reaction is triggered by the large stresses occurring at the crack tip. The crack front velocity was monitored by means of a portable camera to get insight into the effect of stress corrosion influence for two Planilux specimens with the same precrack ratio of 0.50 corresponding to the stable and unstable tests in **Fig. III.11**.

a)

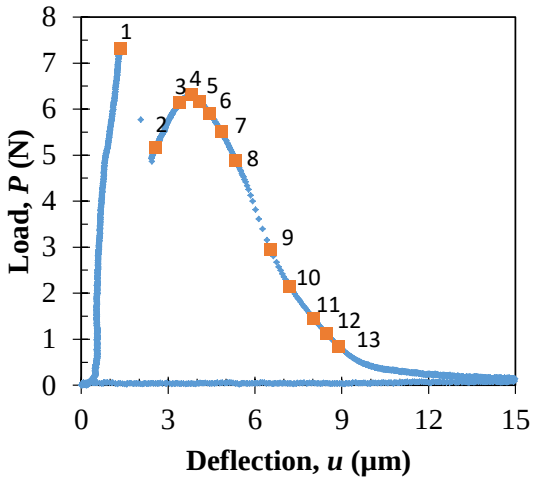

b)

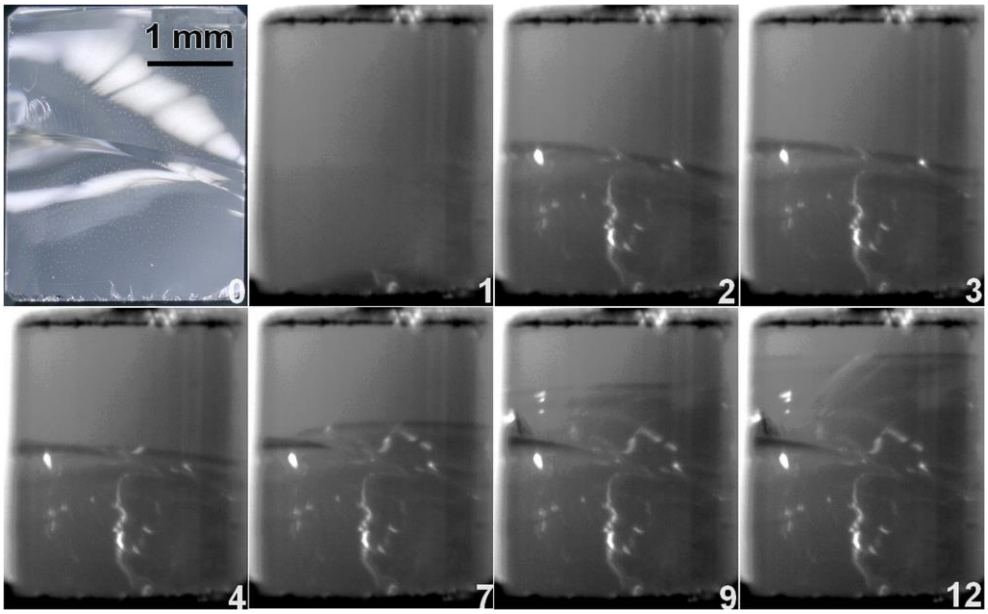

Fig. III.13. Live front tracking on a SEPB Planilux specimen tested in three-point bending with a cross-head speed of 0.2 µm/s. a) Load-Displacement curve. b) Pictures extracted from the video: Number 0 is the post-mortem optical crack, 1 is the onset of crack reopening, 2 shows the crack reopening, 3 shows crack front at the onset of extension, 4-13 shows the stable propagation of the crack.

This camera was synchronized with the load displacement record (**Fig. III.13**). A selection of thirteen points and corresponding pictures were used to illustrate the stable SEPB crack propagation (**Fig. III.13b**). Up to the first point the closure of the pre-crack is evidenced in **Fig. III.13b (1)** as well as by the fact that the bending bar shows up with a compliance identical to that of a crack free bar. This phenomenon has only been observed when the bridge-flexure loading was stopped immediately after the pop-in associated with the precrack formation. The peak load at the first point corresponds to the reopening of the precrack. Points 2 to 4 are associated with the loading of the precrack until K_I meets K_{Ic}. The corresponding pictures (**Fig. III.13b (2-4)**) shows that the crack front is stable at this stage. The subsequent points are associated with the stable crack extension process. The crack length was measured in-situ and is plotted as a function of the corresponding soaking time in **Fig. III.14**. The stress intensity factor was calculated for each of the measured crack length and the crack velocity was further calculated and compared with formerly published data on soda-lime-silica glass by Wiederhorn [37] (**Fig. III.16**). The change in the crack growth velocity with K_I for the presently studied glass at ~62 % humidity is in good agreement with the one observed in a rather similar glass by Wiederhorn [37] using a double cantilever beam specimen (DCB). The crack propagation is rather slow (< 0.3 $mm.s^{-1}$), especially in the beginning (points 3 to

5). Because of this humidity-assisted crack propagation process, K_{Ic} as calculated from load peak at points 3,4 ($K_{SEPBstable}(P)$ in table 3), which are located in the stress-corrosion regime (I) in **Fig. III.15**, is much lower than the expected K_{Ic} value. Nevertheless, it is clear in **Fig. III.15** that most points from the crack-extension curve in **Fig. III.13** are located in the plateau region (II) where K_I approaches K_{Ic}, so that K_{Ic} as obtained from the work of fracture ($K_{SEPB}(\gamma)$ in table 3) is in good agreement with the critical value corresponding to fast (unstable) fracture. In the case where unstable crack growth occurred, the average velocity of the crack propagation ($\Delta a/\Delta t$) was calculated from the crack length and corresponding time measured at the peak load and just after failure. This provides a lower bound for the unstable crack velocity. A velocity of 1.8×10^{-3} m.s^{-1} was estimated, which is greater than the velocity in region II with 100 % humid (~2.4×10^{-4} m.s^{-1}, **Fig. III.15**). Hence, $K_{SEPBunstable}(P)$ is assumed to be independent of stress corrosion. The standard deviation is smaller than 0.01 MPa$\sqrt{}$m for all glasses but Borofloat 33, where it values 0.03 MPa.m$^{0.5}$. Such a remarkable reliability stems from the control of the precrack geometrical characteristics (less than 10 % difference between the average precrack length and any measurement at 0.25, 0.50, and 0.75 of the specimen width), as well as from the refinement of the microindentation preliminary stage. The indentation load was always chosen small enough to limit the indentation crack to a length of less than ~ 50 µm, i.e. much smaller than the precrack one (~ 2 mm) and the alignement of small indents resulted in an angle between the pop-in precrack (hook angle) and the final fracture smaller than 5° (the standard allowance) (**Fig. III.16**).

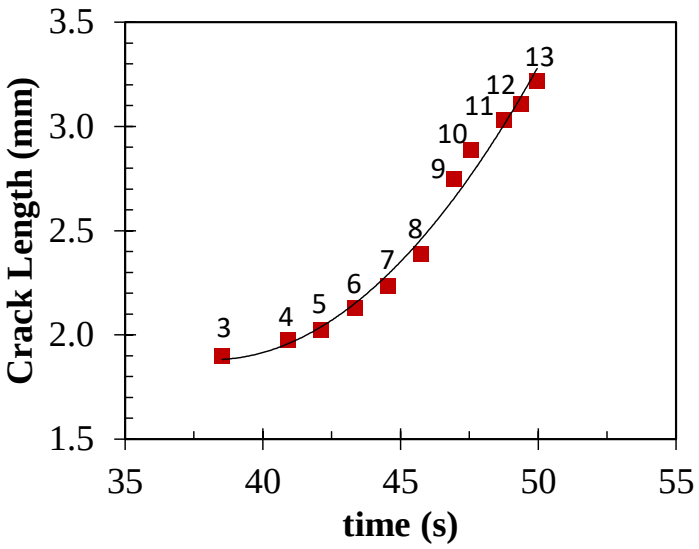

Fig. III.14. Crack length evolution. The solid square marks show the time at which the crack length is measured (same points as in **Fig. III.13**). The curve fitting corresponds to a second order polynomial regression.

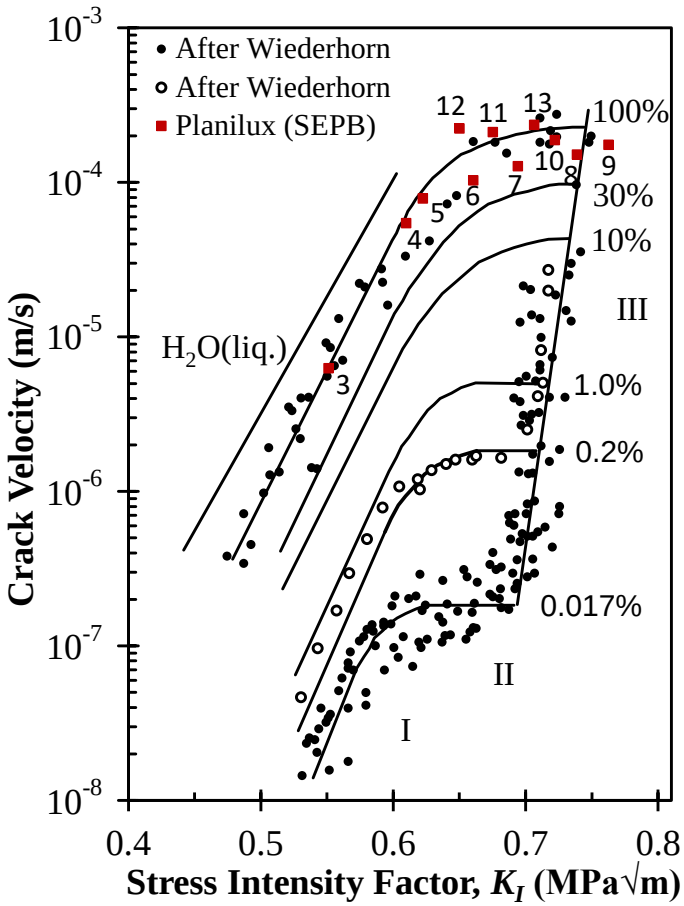

Fig. III.15. Crack growth data in soda-lime-silica glass (after Wiederhorn [37]) and in Planilux (this study – square red mark). Experiments on Planilux specimens were conducted under 62 % humidity.

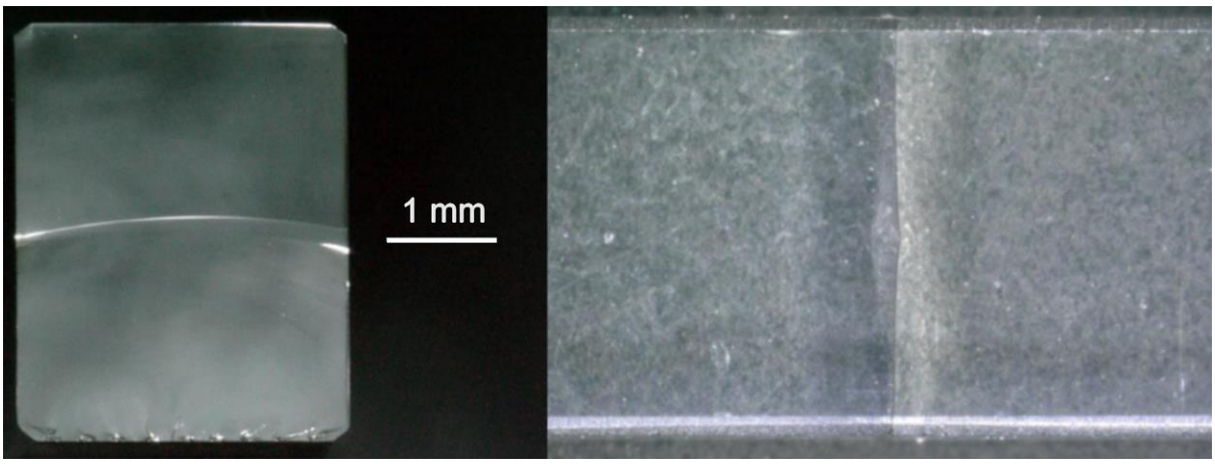

Fig. III.16. Window glass SEPB specimen; Left: fracture surface; Right: side view. The crack ran from the bottom to the top.

III.6 Conclusion

The crack-extension resistance of four commercially available oxide glasses was studied. We found that a stiff loading set-up, combined with a careful choice on the experimental and geometrical parameters, results in a stable fracture regime for SEPB specimens, especially when fracture is performed at low velocity in three-point bending. In such conditions, by means of an in-situ camera, a single SEPB experiment allows to obtain an entire fatigue resistance curve (V-K) for crack extension velocities (V) ranging between 10^{-6} and 10^{-3} m.s^{-1}. Regarding the K_{Ic} measurement, the following conclusions were drawn: 1) CNB is a self-consistent method that offers a remarkable opportunity for investigating the fracture surface energy, as stable crack extension can be relatively easily achieved. Nevertheless the work of fracture is fraught with uncertainty because of i) irregularities (secondary cracks) along the edges of the notch, and ii) offset inclination angle of the mean crack extension plane. Consequently, K_{Ic} as obtained from the peak load is more reliable and accurate than the alternate value deduced from the *wof*; 2) The SEPB technique is proved to be reliable, and K_{Ic} as derived from the *wof* is in good agreement with the intrinsic fracture toughness value. However, as long as the peak load is used to estimate K_{Ic}, unstable SEPB final fracture (high velocity) is recommended in order to limit stress corrosion effects. K_{Ic} values as calculated from the peak load associated with a stable crack extension regime is systematically ~ 20 % smaller than K_{Ic} as derived from the peak load during unstable SEPB experiments, or during stable CNB ones. Note that the two latter results are in excellent agreement.

III.7 Remarks

SEPB technique has been proved to be a self-consistent and reliable method to determine K_{Ic} of not only ceramics but also glasses with some modifications. The further research work is to apply this technique to laboratory glass with different compositions. The next question is whether there is a relation between the compositions and K_{Ic} of a glass. If we can find the major compositions that make the stronger and tougher glass, we can then synthesis a crack resistant glass. The study of the composition dependence of K_{Ic} will be presented in the next chapter.

III.8 References

[1] A.G. Evans, E.A. Charles, Fracture toughness determinations by indentation, J. Am. Ceram. Soc. 59 (1976) 371–372.

[2] B. Lawn, R. Wilshaw, Indentation fracture: principles and applications, J. Mater. Sci. 10 (1975) 1049–1081.

[3] M.T. Laugier, Toughness determination of some ceramic tool materials using the method of Hertzian indentation fracture, J. Mater. Sci. Lett. 4 (1985) 1542–1544.

[4] C.B. Ponton, R.D. Rawlings, Vickers indentation fracture toughness test Part 1 Review of literature and formulation of standardised indentation toughness equations, Mater. Sci. Technol. 5 (1989) 865–872.

[5] C.B. Ponton, R.D. Rawlings, Vickers indentation fracture toughness test Part 2 Application and critical evaluation of standardised indentation toughness equations, Mater. Sci. Technol. 5 (1989) 961–976.

[6] G.D. Quinn, R.C. Bradt, On the Vickers indentation fracture toughness test, J. Am. Ceram. Soc. 90 (2007) 673–680.

[7] H. Tanaka, Y. Bando, Y. Inomata, M. Mitomo, Atomically Sharp Crack in 15R Sialon, J. Am. Ceram. Soc. 71 (1988).

[8] B.R. Lawn, B.J. Hockey, S.M. Wiederhorn, Atomically sharp cracks in brittle solids: an electron microscopy study, J. Mater. Sci. 15 (1980) 1207–1223.

[9] T. Nose, T. Fujii, Evaluation of Fracture Toughness for Ceramic Materials by a Single Edge Precracked Beam Method, J. Am. Ceram. Soc. 71 (1988) 328–333.

[10] D. Munz, R.T. Bubsey, J.L. Shannon, Performance of chevron-notch short bar specimen in determining the fracture toughness of silicon nitride and aluminum oxide, J. Test. Eval. 8 (1980) 103–107.

[11] ASTM C1421-10, Standard Test Methods for Determination of Fracture Toughness of Advanced Ceramics at Ambient Temperature, ASTM International, West Conshohocken, PA, (2010).

[12] S.M. Wiederhorn, L.H. Bolz, Stress corrosion and static fatigue of glass, J. Am. Ceram. Soc. 53 (1970) 543–548.

[13] U. Fotheringham, Thermal Properties of Glass, in: H. Bach, N. Neuroth (Eds.), Prop. Opt. Glas., Springer Berlin Heidelberg, Berlin, Heidelberg, 1998: pp. 201–228.

[14] T. Rouxel, J.-C. Sangleboeuf, The brittle to ductile transition in a soda-lime-silica glass, J. Non. Cryst. Solids. 271 (2000) 224–235.

[15] G.R. Anstis, P. Chantikul, B.R. Lawn, D.B. Marshall, A critical evaluation of indentation techniques for measuring fracture toughness: I, direct crack measurements, J. Am. Ceram. Soc. 64 (1981) 533–538.

[16] K. Niihara, R. Morena, D.P.H. Hasselman, Evaluation ofK Ic of brittle solids by the indentation method with low crack-to-indent ratios, J. Mater. Sci. Lett. 1 (1982) 13–16.

[17] S. Yoshida, J.-C. Sangleboeuf, T. Rouxel, Quantitative evaluation of indentation-induced densification in glass, J. Mater. Res. 20 (2005) 3404–3412.

[18] D. Munz, R.T. Bubsey, J.E. Srawley, Compliance and stress intensity coefficients for short bar specimens with chevron notches, Int. J. Fract. 16 (1980) 359–374.

[19] J.I. Bluhm, Slice synthesis of a three dimensional “work of fracture” specimen, Eng. Fract. Mech. 7 (1975) 593–604.

[20] S.-X. Wu, Fracture toughness determination of bearing steel using chevron-notch three point bend specimen, Eng. Fract. Mech. 19 (1984) 221–232.

[21] T. Rouxel, Y. Laurent, Fracture characteristics of SiC particle reinforced oxynitride glass using chevron-notch three-point bend specimens, Int. J. Fract. 91 (1998) 83–101.

[22] G.R. Irwin, Analysis of stresses and strains near the end of a crack traversing a plate, Spie Milestone Ser. MS. 137 (1997) 16.

[23] I. Bar On, F.I. Baratta, K. Cho, Crack Stability and Its Effect on Fracture Toughness of Hot Pressed Silicon Nitride Beam Specimens, J. Am. Ceram. Soc. 79 (1996) 2300–2308.

[24] Y. Kato, H. Yamazaki, S. Yoshida, J. Matsuoka, Effect of densification on crack initiation under Vickers indentation test, J. Non. Cryst. Solids. 356 (2010) 1768–1773.

[25] J.A. Salem, L.J. Ghosn, Back-Face Strain for Monitoring Stable Crack Extension in Precracked Flexure Specimens, J. Am. Ceram. Soc. 93 (2010) 2804–2813.

[26] G.D. Quinn, J.J. Swab, Fracture toughness of glasses as measured by the SCF and SEPB methods, J. Eur. Ceram. Soc. (2017).

[27] A.A. Wereszczak, C.E. Anderson, Borofloat and Starphire float glasses: a comparison, Int. J. Appl. Glas. Sci. 5 (2014) 334–344.

[28] P. Vullo, M.J. Davis, Comparative study of micro-indentation and Chevron notch fracture toughness measurements of silicate and phosphate glasses, J. Non. Cryst. Solids. 349 (2004) 180–184.

[29] S. Dériano, A. Jarry, T. Rouxel, J.-C. Sangleboeuf, S. Hampshire, The indentation fracture toughness (K C) and its parameters: the case of silica-rich glasses, J. Non. Cryst. Solids. 344 (2004) 44–50.

[30] J. Lankford, Indentation microfracture in the Palmqvist crack regime: implications for fracture toughness evaluation by the indentation method, J. Mater. Sci. Lett. 1 (1982) 493–495.

[31] J.C. Glandus, T. Rouxel, Q. Tai, Study of the Y-TZP toughness by an indentation method, Ceram. Int. 17 (1991) 129–135.

[32] Z.Y. Yao, D. Möncke, E.I. Kamitsos, P. Houizot, F. Célarié, T. Rouxel, L. Wondraczek, Structure and mechanical properties of copper-lead and copper-zinc borate glasses, J. Non. Cryst. Solids. 435 (2016) 55–68.

[33] J.J. Swab, J. Tice, A.A. Wereszczak, R.H. Kraft, Fracture Toughness of Advanced Structural Ceramics: Applying ASTM C1421, J. Am. Ceram. Soc. 98 (2015) 607–615.

[34] J. Salem, L. Ghosn, M. Jenkins, G. Quinn, Stress Intensity Factor Coefficients for Chevron-

Notched Flexure Specimens and a Comparison Fracture Toughness Methods, 23rd Annu. Conf. Compos. Adv. Ceram. Mater. Struct. A Ceram. Eng. Sci. Proceedings, Vol. 20, Issue 3. (1999) 503–512.

[35] T. Rouxel, Driving force for indentation cracking in glass: composition, pressure and temperature dependence, Phil. Trans. R. Soc. A. 373 (2015) 20140140.

[36] H. Ji, V. Keryvin, T. Rouxel, T. Hammouda, Densification of window glass under very high pressure and its relevance to Vickers indentation, Scr. Mater. 55 (2006) 1159–1162.

[37] S.M. Wiederhorn, Influence of Water Vapor on Crack Propagation in Soda Lime Glass, J. Am. Ceram. Soc. 50 (1967) 407–414.

IV. Elasticity, Hardness, and Fracture Toughness of Sodium Aluminoborosilicate Glasses

IV.1. Abstract

Due to an increasing demand for oxide glasses with a better mechanical performance, there is a need to improve our understanding of the composition-structure-mechanical property relations in these brittle materials. At present, some properties such as Young's modulus can to a large extent be predicted based on the chemical composition, while others – in particular fracture-related properties – are typically optimized based on a trial-and-error approach. In this work, we study the mechanical properties of a series of twenty glasses in the quaternary Na_2O-Al_2O_3-B_2O_3-SiO_2 system with fixed soda content, thus accessing different structural domains. Ultrasonic echography is used to determine the elastic moduli and Poisson's ratio, while Vickers indentation is used to determine hardness. Furthermore, the single-edge precracked beam (SEPB) method is used to estimate the fracture toughness (K_{Ic}) for some compositions of interest. The compositional evolutions of Vickers hardness and Young's modulus are in good agreement with those predicted from models based on bond constraint density and strength. Although there is a larger deviation, the overall compositional trend in K_{Ic} can also be predicted by a model based on the strength of the bonds assumed to be involved in the fracture process.

Keywords: Elastic moduli, Vickers hardness, fracture toughness, crack path, glass properties

IV.2. Introduction

Oxide glasses find applications in a wide variety of industries, from window panes in cars, to protective screens in electronic devices, and optical fibers in high-speed internet cables. The continuing demand for such products and the desire to manufacture lighter and more durable glass materials promote the interest in designing stiffer, harder, and tougher glasses [1–3]. To some extent, this can be achieved through sophisticated compositional design, which has led to the discovery of oxide glasses with, e.g., high elastic moduli or crack resistance [4–6]. However, more attention should be devoted to this topic in order to improve our current understanding of the link between the chemical composition, the glassy network structure, and the mechanical properties in oxide glasses. Furthermore, it should be noted that many previous studies have focused on novel and "exotic" chemical compositions with, e.g., rare earth and transition metal elements [4–9]. Although such studies are indeed useful for providing insights into the fundamental physics,

This chapter previously appeared as: K. Januchta, T. To, M. S. Bødker, T. Rouxel, M. M. Smedskjaer. J. Am. Cer. Soc.,(2019).

chemistry, and solid mechanics of glasses, there is also a need to focus on industrially relevant compositions, typically involving cheap, non-hazardous, and abundant oxides.

The sodium aluminoborosilicate glass family is industrially relevant, as well as scientifically interesting due to the abundant structural features influencing the mechanical properties of the glasses. Although the impact of composition on the glass structure in this system can be accurately predicted [10], the speciation of the network-forming oxides is highly composition dependent [11–15]. Any changes to the structural characteristics give rise to large differences in mechanical properties as a function of chemical composition, as it has been shown for sodium borosilicates[16–19], sodium aluminosilicates [20–22], sodium aluminoborates [23], and sodium aluminoborosilicates [24,25]. Given these large variations within the quaternary Na_2O–Al_2O_3–B_2O_3–SiO_2 system, this is an interesting system for further study in order to improve our understanding of the composition-structure-mechanical property relations.

The twenty glasses studied herein contain between 0 and 75 mol% silica and boria, while the alumina content varies from 0 to 30 mol%. Compositions with higher Al_2O_3 contents are expected to crystallize upon quenching at rates achievable using traditional melt-quenching method [15,21]. The soda content is fixed at 25 mol% in order to reduce the number of analyzed glasses, while also eliminating the complexity of the comparison among the studied compositions. The system is designed to cover the two binary sodium borate and sodium silicate series, several aluminosilicates, borosilicates, and aluminoborates, as well as multiple quaternary glasses. The nominal compositions of all glasses are tabulated in Table 1. The glasses are characterized using a variety of techniques, including calorimetry and Archimedes principle to determine glass transition temperature (T_g) and density (ρ), respectively. Ultrasonic echography is used to determine the elastic properties such as Young's modulus (E), while micro-indentation is used to determine Vickers hardness (H_V). The single-edge precracked beam (SEPB) method [26] is finally used to measure fracture toughness (K_{Ic}) of selected compositions. The compositional trends in these mechanical properties are compared against predicted values based on existing physical models [27–32]. The agreement between the measured and predicted values in H_V, E, and K_{Ic} is discussed in terms of the cation-oxygen bond strengths, topology of the glassy networks, and expected propagation of the crack front during fracture.

IV.3. Structural review

In order to link the glass chemistry with different mechanical properties, the network former speciation needs to be known. This information is typically obtained experimentally, e.g., using

solid state nuclear magnetic resonance spectroscopy, but for the investigated sodium aluminoborosilicate system, the correlations between chemical composition and structural characteristics are well established. In the following, we summarize the equations used to predict the network structure, and the assumptions associated with them. The information extracted from the structural models is summarized in **Table IV.1**.

Table IV.1: Nominal compositions (all containing 25 mol% Na_2O), fraction of four-fold coordinated to total boron atoms (N_4), fraction of Si-tetrahedra with one NBO to total Si-tetrahedra (Q^3), density (ρ), atomic packing density (C_g), glass transition temperature (T_g), Young's modulus (E), shear modulus (G), Poisson's ratio (v), and Vickers hardness (H_V). All glasses contain 25 mol% Na_2O. The composition marked by * is taken from Ref. 22. The errors in ρ, C_g, T_g, E, G, v, and H_V do not exceed 0.01 g/cm^3, 0.002, 2 °C, 2 GPa, 1 GPa, 0.01, and 0.2 GPa, respectively.

$[Al_2O_3]$ (mol%)	$[B_2O_3]$ (mol%)	$[SiO_2]$ (mol%)	N_4 (-)	Q^3 (-)	ρ (g/cm^3)	C_g (-)	T_g (°C)	E (GPa)	G (GPa)	v (-)	H_V (GPa)
0	0	75	0.00	0.50	2.43	0.49	475	56	22	0.25	4.4
0	12.5	62.5	0.77	0.45	2.49	0.52	539	73	30	0.22	6.4
0	25	50	0.63	0.38	2.51	0.55	544	73	30	0.22	6.6
0	37.5	37.5	0.56	0.21	2.47	0.56	525	75	30	0.24	5.8
0	50	25	0.50	0.00	2.40	0.56	511	69	28	0.25	6.2
0	62.5	12.5	0.40	0.00	2.33	0.56	495	62	25	0.25	5.5
0	75	0	0.33	0.00	2.25	0.56	473	53	21	0.27	4.7
12.5	0	62.5	0.00	0.33	2.45	0.49	567	67	27	0.23	5.6
12.5	12.5	50	0.75	0.13	2.45	0.51	545	69	28	0.24	6.5
12.5	25	37.5	0.50	0.00	2.42	0.52	514	64	25	0.25	6.1
12.5	37.5	25	0.33	0.00	2.35	0.52	493	56	22	0.26	5.4
12.5	50	12.5	0.25	0.00	2.28	0.52	480	50	20	0.27	4.5
12.5	62.5	0	0.20	0.00	2.22	0.52	465	44	17	0.29	3.8
25*	0*	50*	0.00	0.00	2.50	0.49	792	72	30	0.21	6.6
25	12.5	37.5	0.00	0.00	2.42	0.49	611	62	25	0.25	6.0
25	25	25	0.00	0.00	2.36	0.49	511	51	21	0.26	4.9
25	37.5	12.5	0.00	0.00	2.29	0.50	468	46	18	0.28	4.0
25	50	0	0.00	0.00	2.25	0.50	459	44	17	0.29	3.5
30	45	0	0.00	0.00	2.36	0.50	528	55	22	0.27	4.9
30	32.5	12.5	0.00	0.00	2.28	0.50	469	47	18	0.29	3.7

Oxygen atoms in oxide glasses can act as bridging (BO) or non-bridging (NBO) units depending on whether they link two network-forming cations together or they depolymerize the network by linking a network-forming cation with a modifying cation. Schematic drawings of such structural units can be seen in **Fig. IV.1a**. The distribution of these oxygen species has an impact on the

flexibility of the network, which in turn affects the mechanical properties. For sodium aluminosilicate glasses, the fraction of Si-tetrahedra containing NBOs can be accounted for by considering the Na_2O and Al_2O_3 contents. As [Na_2O] is constant in the present series (25 mol%), only units with zero or one NBO per Si tetrahedron (Q^4 and Q^3, respectively) are expected. These can be calculated based on the assumption that each mol of added Al_2O_3 consumes one mol of Na_2O to charge stabilize AlO_4^-:[10,33,34]

$$Q^3 = \frac{2([Na_2O]-[Al_2O_3])}{[Na_2O]-[Al_2O_3]+[SiO_2]}, \quad (1)$$

$$Q^4 = 1 - Q^3. \quad (2)$$

Fig. IV.1: Schematic ball and stick representations of four different glassy networks: **(a)** binary sodium silicate, **(b)** binary sodium borate, **(c)** sodium aluminoborosilicate where [Al_2O_3]+[B_2O_3]=[Na_2O], and **(d)** sodium aluminoborosilicate where [Al_2O_3]>[Na_2O]. The O, B, Si, Al, and Na atoms are represented by red, violet, yellow, gray, and green, respectively.

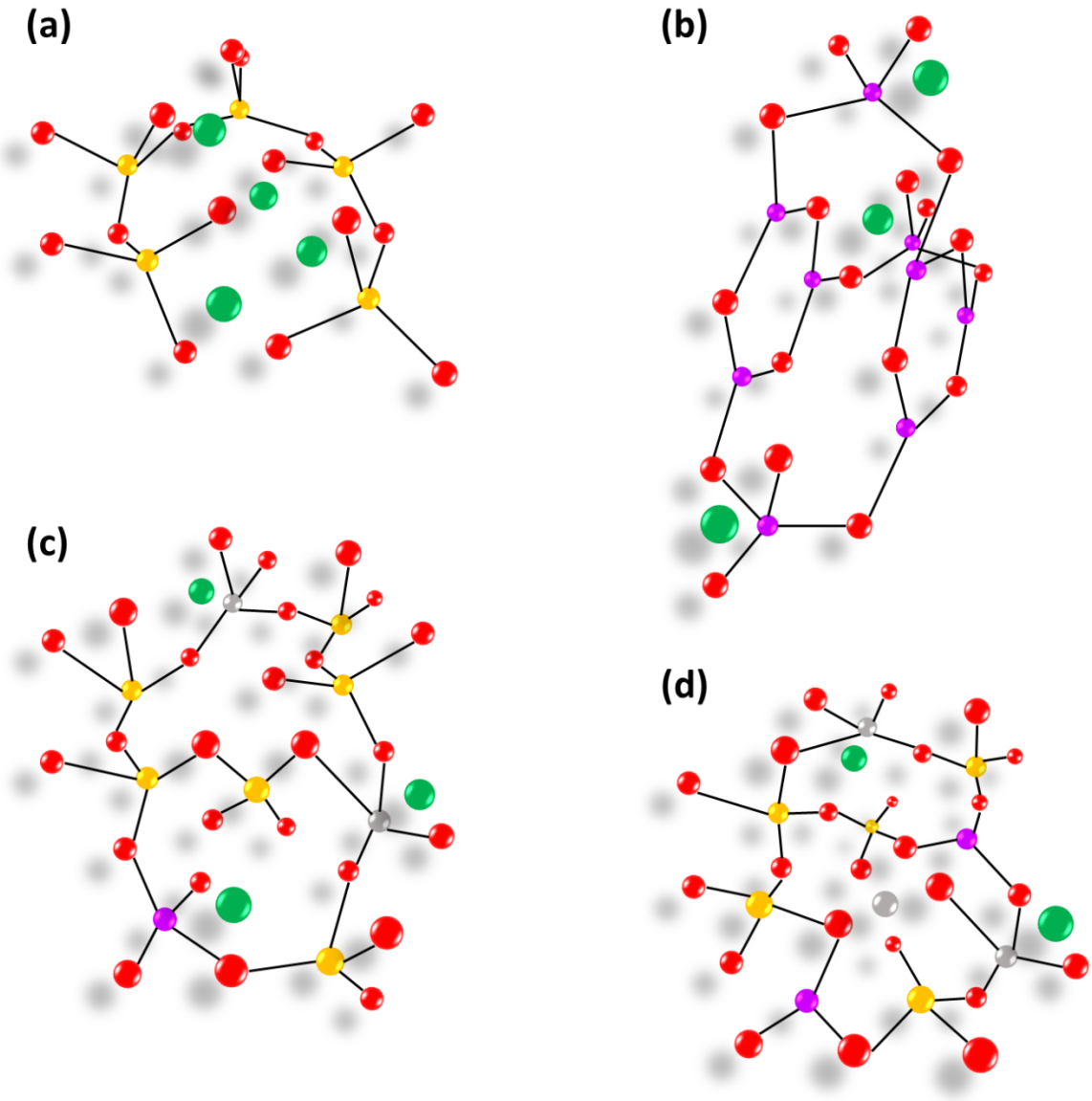

For sodium borosilicate glasses, the relative concentrations of SiO_2, B_2O_3, and Na_2O control the network former speciation. This is especially important for B atoms, since these can occur in three- or four-fold coordination with oxygen, which drastically changes the connectivity of the network. An example of a borate network with both planar trigonal and with tetrahedral units is schematically drawn in Figure 1b. The distribution of the B atoms also affects mechanical properties, with higher N_4 values (fraction of tetrahedral B atoms) resulting in a more rigid glassy network, which in turn manifests itself as a stiffer material. N_4 depends on the values of K and R, defined as $[SiO_2]/[B_2O_3]$ and $[Na_2O]/[B_2O_3]$ ratios, respectively. The following empirical formulas can be used to estimate N_4, within the compositional boundaries given below [10,35,36]:

$$R_{max} = 0.5 + 0.0625 \cdot K, \quad \text{(IV.3)}$$

$$R_{d1} = 0.5 + 0.25 \cdot K, \quad \text{(IV.4)}$$

$$R_{d2} = 1.5 + 0.75 \cdot K, \quad \text{(IV.5)}$$

$$R_{d3} = 2 + K \ . \quad \text{(IV.6)}$$

N_4 can then be calculated as follows [10]:

$$N_4 = \frac{8+K}{12}\left(1 - \frac{R}{2+K}\right) \ if \ R_{d1} < R < R_{d3}, \quad \text{(IV.7)}$$

$$N_4 = R_{max} \ if \ R_{max} < R < R_{d1}, \quad \text{(IV.8)}$$

$$N_4 = R \ if \ R < R_{max}. \quad \text{(IV.9)}$$

Similar expressions can be used to calculate the amount of trigonal B-units with zero, one or two NBOs [10]. However, within the studied system, there is only one composition with NBOs on B-triangles (fraction <1%). Hence, throughout this paper, all the NBOs are assumed to exist on Si-tetrahedra for the sake of simplicity. The fraction of Si-tetrahedra containing one NBO (Q^3) can be calculated as follows [10]:

$$Q^3 = \frac{3}{8} + \frac{13}{6}\left(\frac{(R-R_{d1})}{2+K}\right) \ if \ R_{d1} < R < R_{d3}, \quad \text{(IV.10)}$$

$$Q^3 = \frac{2(R-R_{max})}{K} \ if \ R_{max} < R < R_{d1}, \quad \text{(IV.11)}$$

$$Q^3 = 0 \ if \ R < R_{max}. \quad \text{(IV.12)}$$

When Al_2O_3 is introduced into the borosilicate network, Al-cations consume NBOs through association with Na-cations (see Figure 1c). This essentially reduces the effective value of R, since a given concentration of Na_2O is unable to charge-stabilize B-tetrahedra or induce NBOs on Si-tetrahedra. It is here assumed that each mol of added Al_2O_3 associates with one mol of Na_2O. To calculate N_4 and Q^3 in the glasses, R_{eff} replaces R in Eqs. (7)-(12), where R_{eff} is given as,

$$R_{eff} = \frac{[Na_2O]-[Al_2O_3]}{[B_2O_3]}. \quad \text{(IV.13)}$$

In peraluminous glasses, where [Al_2O_3] > [Na_2O], R_{eff} would become negative. In this case, all Na cations are assigned to charge-stabilize Al-tetrahedra, with the additional Al entering a modifying role in mostly five-fold coordination (see Figure 1d). The fraction of the latter (xAl^5) is small and herein estimated as,

$$xAl^5 = \frac{0.5([Al_2O_3]-[Na_2O])}{[Al_2O_3]}. \quad \text{(IV.14)}$$

The formation of Al^5 species results in an increased network stiffness induced by the increase in packing density [15,37]. However, any depolymerization associated with the creation of additional NBOs on the borosilicate network due to the modifying Al^5 units is neglected. This is because the high field strength of the Al cation prevents any significant weakening of the network stiffness compared to that observed for lower-field strength Na modifier cations.

Finally, the Na-cations can play two different roles in the glasses investigated herein. They can either depolymerize the network by forming NBOs on Si and B atoms, or they can charge stabilize Al and/or B tetrahedra without disrupting the network connectivity. The fraction of Na-cations that induce NBOs on Si tetrahedra ($x_{\text{Na-NBO}}$) can thus be calculated by subtracting the fractions that are used to charge stabilize the tetrahedral Al and B species, which are equal to the concentrations of Al_2O_3 and B_2O_3 in four-fold coordination,

$$x_{Na-NBO} = \frac{[Na_2O]-[Al_2O_3]-N_4\cdot[B_2O_3]}{[Na_2O]}. \quad \text{(IV.15)}$$

IV.4. Experimental

IV.4.a. Glass synthesis

Twenty different glass compositions (**Table IV.1**) were prepared by the traditional melt-quenching technique. SiO_2 (SigmaAldrich, > 99.5 %), Al_2O_3 (SigmaAldrich, > 99.5%), H_3BO_3 (Honeywell, > 99.5 %), and Na_2CO_3 (Honeywell, > 99.5 %) were used for the synthesis. For each glass composition, adequate amounts of the above mentioned chemicals were weighed to yield ~65 g batches, and mixed. The mixtures were then melted in an electric furnace (Entech) by stepwise addition to a Pt-Rh crucible. Afterwards, the liquids were homogenized for ~2 hours between 1100 and 1600 °C (depending on composition), quenched onto a brass plate, and transferred to an annealing furnace at their T_g values for ~3 hours.

We note that some degree of volatilization of Na_2O and B_2O_3 is expected during melt homogenization, resulting in a deviation between the actual and nominal compositions, in turn affecting the material properties. However, such evaporation losses are small compared to the differences between each of the investigated glass compositions (at least 12.5 mol% of a given

oxide), thus not interfering with our discussion of the compositional trends in properties. All the glasses were optically transparent and showed no evidence of phase separation or crystallization, with exception of the peraluminous aluminoborate composition that exhibited some crystallization. However, this was limited to a small area of the sample, which was cut and discarded. One of the glass compositions ($25Na_2O–25Al_2O_3–50\ SiO_2$) was taken from a previous study [22].

IV.4.b. Differential scanning calorimetry

Small disc-shaped specimens of each composition (~40 mg, Ø ~ 5 mm) were prepared for differential scanning calorimetry experiments (DSC 449C, Netzsch). The sample contained in a Pt-Rh crucible was heated at 10 °C/min in argon atmosphere at least 60 °C above its estimated T_g. T_g was determined from the DSC heat flow data by determining the intercept between the extrapolated sub-T_g signal and the tangent at the inflection point of the glass transition peak.

IV.4.c. Density determination

Density of each glass composition was determined by Archimedes' principle of buoyancy using ~20×20×5 mm^3 specimens, which were cut from the bulk samples. Each specimen was weighed in air and in ethanol ten times on an analytical balance. The average weights as well as the room and ethanol temperatures were used to calculate density. In addition, the atomic packing density (C_g) was calculated for all glasses using the molar fractions of oxides in the nominal compositions and their respective ionic radii taken from Ref.[38]. Since the ionic radii depend on the coordination numbers of the constituent atoms, assumptions with respect to those needed to be made. The coordination numbers of two for O, four for Si, and six for Na were assumed, resulting in ionic radii of 1.35, 0.26, and 1.02 Å, respectively. The ionic radii used for B (0.01 and 0.11 Å for three- and four-fold coordination, respectively) and Al (0.39, 0.45, and 0.54 Å for four-, five-, and six-fold coordination, respectively) varied according to their distributions (Table 1), which were taken from known structural data, or estimated based on existing structural models [10]. C_g was calculated as,

$$C_g = \frac{\rho \Sigma f_i [4/3\pi N (x r_R^3 + y r_O^3)]}{\Sigma f_i M_i}, \quad \text{(IV.16)}$$

where for the i^{th} oxide with chemical formula R_xO_y, f_i is the molar fraction of the oxide, r_R and r_O are the ionic radii of the cation and of the oxygen anion, respectively, M_i is the molar mass of the oxide, and N is Avogadro's number.

IV.4.d. Ultrasonic echography

The specimens (20×20×5 mm^3) were ground using SiC paper to obtain co-planar surfaces. The pulse-echo technique was then applied to determine the longitudinal and transverse sound wave velocities through the specimens (V_L and V_T, respectively) using an ultrasonic thickness gauge (38DL Plus, Olympus). 20 MHz delay line transducers were employed to induce the longitudinal

and transverse waves. V_L and V_T were calculated using the specimen thickness (measured using a digital micrometer) and the time between the initial wave impulse and echo. Using V_L, V_T, and ρ, the shear modulus (G), Young's modulus (E), bulk modulus (B), and Poisson's ratio (ν) were calculated as follows:

$$G = \rho V_T^2, \tag{IV.17}$$

$$\nu = \frac{V_L^2 - 2V_T^2}{2(V_L^2 - V_T^2)}, \tag{IV.18}$$

$$E = 2G(1 + \nu), \tag{IV.19}$$

$$B = \frac{E}{3(1-2\nu)}. \tag{IV.20}$$

IV.4.e. Vickers indentation

The specimens (20×20×5 mm^3) were polished in water using SiC paper with increasing decreasing abrasive particle size (up to 4000), followed by polishing in a water-free 1 µm diamond suspension. Twenty identical Vickers indentation cycles (CB500, Nanovea) were performed for each glass composition at ambient conditions (relative humidity = 35-50%). The applied indentation cycle consisted of loading (10 N/min), dwell (15 s) at 1 N target load (P), and unloading (10 N/min). Optical images of the indentation imprints were captured under 480x magnification using a lens attached to the indentation apparatus (Olympus). The indent diagonal lengths (d) were measured to determine Vickers hardness,

$$H_V = \frac{1.8544 \cdot P}{d^2}. \tag{IV.21}$$

Additional indentation cycles at higher loads were performed for six selected compositions (see Table S1 in Supporting Information) to probe the indentation cracking behavior. The target load was progressively increased, until images of indentation imprints with radial cracks emanating from the corners were captured. The distance from the center of the indent to the tip of the crack (c) was recorded in each case. The fracture toughness, as obtained by means of indentation (K_{Ic}^{IFT}) was then calculated [39],

$$K_{Ic}^{IFT} = (0.016 \pm 0.004) \cdot \left(\frac{E}{H}\right)^{1/2} \cdot P/c^{3/2}, \tag{IV.22}$$

where H is the Meyer's hardness ($H = 2P/d^2$, not to be confused with H_V).

IV.4.f. Single-edge precracked beam (SEPB) specimen

Parallelepipedic specimens (25×3×4 mm^3) of six selected compositions were prepared by grinding appropriately sized bars on SiC paper with varying grit size (up to 4000), and polished in water-free 1 µm diamond suspension to an optical finish. At least four specimens were prepared for each of the investigated compositions.

The prepared glass bars were then subjected to indentation (VMT-7S, Matsuzawa). A line of indents was placed through the middle of the specimen on one of the 25×3 mm^2 faces. The applied indentation load depended on the cracking behavior of the investigated glass. The desired load was chosen as low possible, but sufficiently large to induce radial cracking. The indents were separated from each other by a distance corresponding to ~3*c*.

The indented bars were finally subjected to bridge compression in order to induce a precrack using a grooved WC fixture. Each bar was placed on a lower WC support with the indent line situated on top of a groove. An upper WC support was then placed on top of the glass bar. The precrack was obtained by loading the fixture with a SiC pusher using a loading rate of 0.05 mm/min. An optical camera was used to monitor the "pop-in" and growth of the crack, which initiated from the indent line. The loading was stopped immediately after the precrack was visible. The load corresponding to the event of precrack pop-in was recorded in each case. More details on the procedure can be found in Ref. [26].

IV.4.g. Three-point bending

The precracked parallelepipedic specimens, now referred to as SEPB specimens, were subjected to failure mechanical testing by means of a three-point bending setup. The setup consisted of piezoelectric displacement actuator (N-216 NEXLINE® Linear Actuator, Physik Instrumente), laser interferometer displacement sensor (LK-G5000 equipped with a LK-H008W head sensor, Keyence Corporation), and load cell (MS02, Scaime) with 6.7 MN/m stiffness and 1 kN capacity. The SEPB specimens were placed on SiC rollers with 19 mm span and precrack front aligned with the ball pusher, and loaded at crosshead speed of 2 to 8 µm/s. The load-deflection curves were recorded.

Depending on the nature of fracture (stable or unstable), fracture toughness (K_{Ic}) was calculated using the work of fracture (*WOF*) or maximum load (P_{max}), respectively [26]. Examples of stable and unstable load-deflection curves are given in Figure S1 in Supporting Information. For stable fracture, *WOF* is calculated from the load-deflection curve as,

$$WOF = \int_0^{u_f} P\, du, \tag{IV.23}$$

where P is the load, u is the deflection, and u_f is the final deflection (i.e., where the specimen is fractured completely). Then, the fracture surface energy (γ) is calculated from *WOF* and the geometrical area of the fracture surface (S_{fra}) determined from a cross-section view of the broken specimen (Figure 2),

$$\gamma = \frac{WOF}{2S_{fra}}. \tag{IV.24}$$

K_{Ic} can then be calculated as,

$$K_{Ic}^{WOF} = \sqrt{\frac{2\gamma E}{1-\nu^2}}. \quad \text{(IV.25)}$$

Figure IV.2: Cross-section view of an SEPB specimen of the $25Na_2O–25Al_2O_3–25B_2O_3–25SiO_2$ glass composition. Cross-sections of the Vickers indents used to induce the precrack are visible at the top edge of the specimen. The precrack obtained during bridge compression proceeded through approximately ~1/3 of the specimen height. The fracture surface is determined by measuring the area of the cross-section from the precrack front to the bottom edge of the specimen.

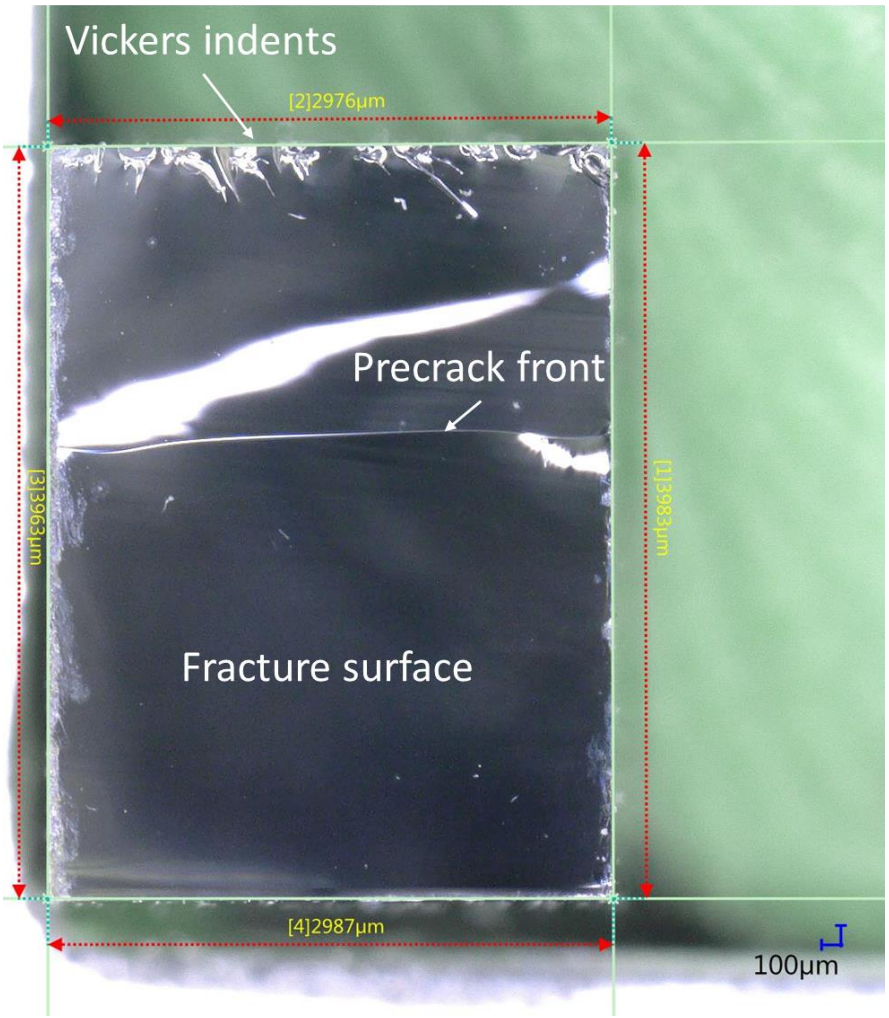

For unstable fracture, K_{Ic} is calculated from the values of P_{max} (i.e., load at fracture), specimen width (B) and height (W),

$$K_{Ic}^{Pmax} = \frac{P_{max}}{B\sqrt{W}} Y_C^*, \quad \text{(IV.26)}$$

where Y_C^* is a scaling factor calculated as,[40]

$$Y_C^* = \frac{3}{2}\frac{S}{W}\frac{\alpha^{1/2}}{(1-\alpha)^{3/2}} f(\alpha). \quad \text{(IV.27)}$$

Here S is the span between the two rollers supporting the SEPB specimen, α is the ratio between the crack length and specimen height W, and $f(\alpha)$ is given by,

$$f(\alpha) = A_0 + A_1\alpha + A_2\alpha^2 + A_3\alpha^3 + A_4\alpha^4 + A_5\alpha^5, \quad (28)$$

where the coefficients A_0 through A_5 are equal to 1.9109, −5.1552, 12.6880, −19.5736, 15.9377, −5.1454, respectively, in the case where S/W = 5.[40] The value of the scaling factor Y_C^* was also calculated from finite element analysis [26], and found to be in agreement with that calculated using Eq. (27) within ±1%.

The fracture angles (A_{fra}) were determined by *post mortem* examination of the specimen side views (see Figure S2 in Supporting Information). Specimens with variations of A_{fra} > 10° were discarded. More detail on the procedure can be found in Ref. [26].

IV.5. Experimental results

IV.5.a. Density and glass transition

Fig. IV.3a shows a contour plot of the density variation of the nineteen glasses synthesized for the purpose of this study, and one composition taken from a previous study [22]. The data is plotted in the pseudoternary diagram for constant Na_2O content of 25 mol%. The density values (and other property data) are also given in **Table IV.1**. Along the borosilicate edge in Figure 3a, there is a maximum in density around the borosilicate composition with equal Na_2O and B_2O_3 contents, in agreement with the fact that mixing of the two network formers SiO_2 and B_2O_3 results in a more efficient packing (Figure 3b). Upon addition of Al_2O_3 to the sodium silicate glass, the density increases slightly due to the larger weight of Al compared to Si. On the other hand, when Al_2O_3 is added to a borosilicate network, the density decreases, which indicates that a more open structure is achieved in aluminoborate and aluminoborosilicate networks compared to the Al-free ones. This is also evident from Figure 3b. However, for the sodium borate and borate-rich borosilicate glasses, the effect is reversed at higher Al_2O_3 content. This is due to the increasing fraction of higher coordinated and thus more efficiently packed Al-species [15,37]. As a result, the maximum and minimum in density within the investigated compositional range are situated around the borosilicate glass with [Na_2O] = [B_2O_3] and the metaluminous aluminoborate compositions, respectively. It should be further noted that the C_g values are calculated based on several assumptions with respect to the ionic radii, which depend on their chemical environment. Especially the variation in the radius of oxygen anions, which are the largest and most abundant in the investigated glasses, could have a significant impact on C_g [41].

Fig. IV.3: (a) Density (ρ) and **(b)** atomic packing density (C_g) dependence on composition of the sodium aluminoborosilicate glasses. The contour map represents a pseudoternary slice through the

quartenary phase diagram with [Na_2O] = 25 mol%. The isocontours are drawn as a guide for the eye, and are based on linear interpolation between the experimental data points marked by green diamonds.

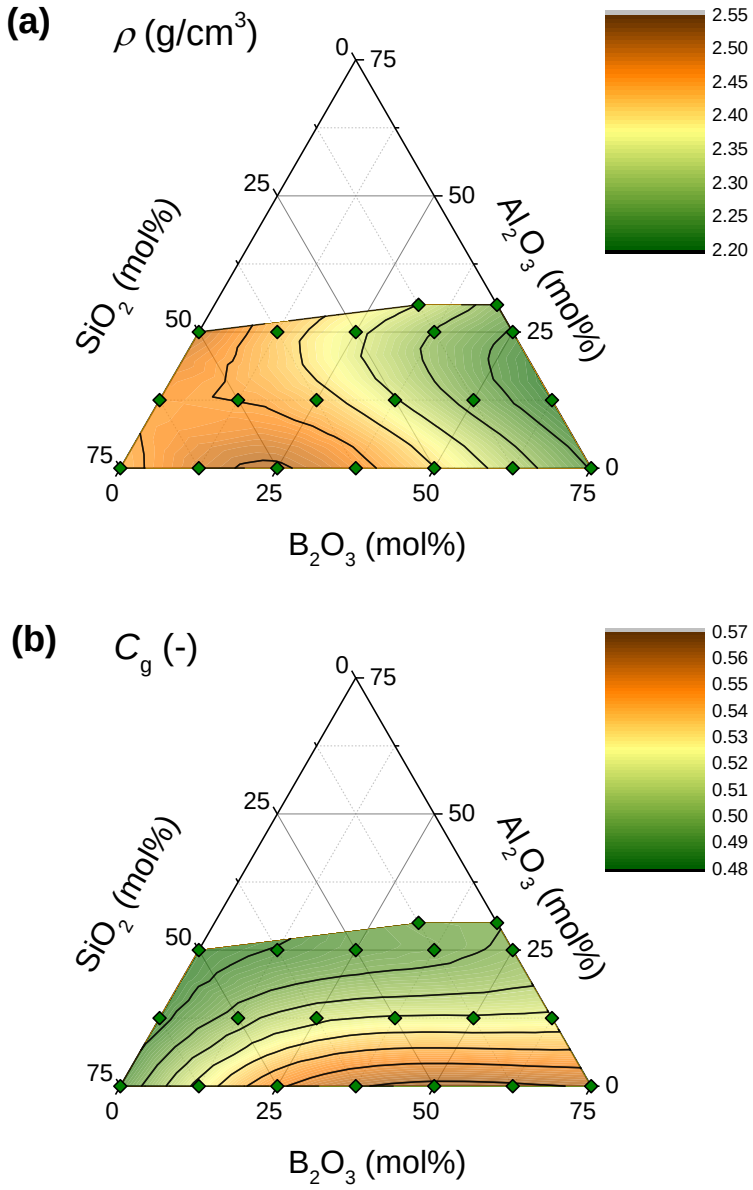

The compositional variation in T_g (Figure 4) differs from that in density. Starting from the binary sodium silicate composition, T_g increases upon incorporation of Al_2O_3 or B_2O_3 oxides (up to 25 mol%), which coincides with the increase in connectivity associated with the consumption of NBOs and formation of rigid Al- and B-tetrahedral units.[10,35,42] The binding energy of highly coordinated networks is larger than in depolymerized ones since the weak Na-O interactions do not participate in the network formation, which justifies the increase in T_g. Upon further addition of B_2O_3, T_g decreases again towards the value for the binary sodium borate glass with a relatively large fraction of flexible trigonal B-species. Addition of Al_2O_3 to the sodium borate or borate-rich borosilicate compositions yields an initial decrease in T_g, followed by an increase upon crossing the

metaluminous joint (i.e., [Al_2O_3] = [Na_2O]), where there is no longer a sufficient amount of Na-cations to charge-stabilize the Al-tetrahedra, causing Al to increase its coordination with oxygen. As such, the lowest recorded T_g value within the investigated system is found for the metaluminous sodium aluminoborate (459 °C), while the highest is found for the metaluminous sodium aluminosilicate (792 °C).

Fig. IV.4: Glass transition temperature (T_g) dependence on composition of the sodium aluminoborosilicate glasses. The contour map represents a pseudoternary slice through the quartenary phase diagram with [Na_2O] = 25 mol%. The isocontours are drawn as a guide for the eye, and are based on linear interpolation between the experimental data points marked by green diamonds.

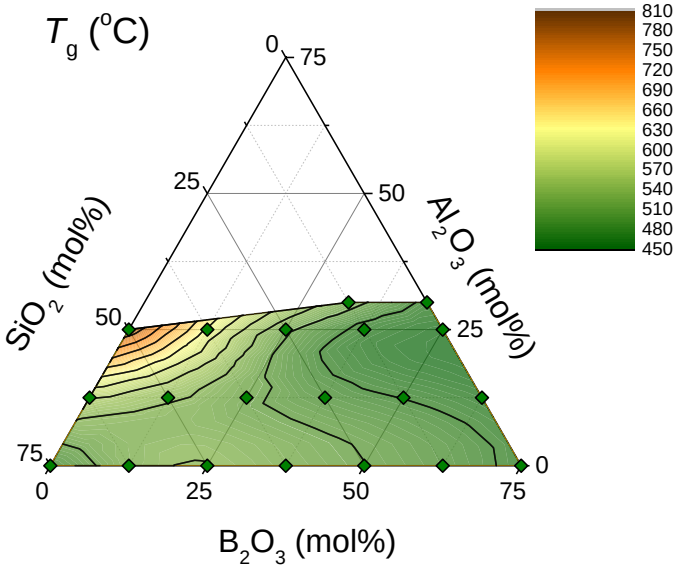

IV.5.b. Elastic moduli

The overall compositional dependences of elastic moduli (Figure 5) resemble that observed in density (Figure 3a). There are two local maxima in both *E* and *G* within the investigated range of chemical compositions. That is, around the $25Na_2O–25Al_2O_3–50SiO_2$ and $25Na_2O–25B_2O_3–50SiO_2$ compositions. The latter exhibits higher *E* and *G* values than the former, in agreement with its slightly higher density (Table 1), and with the fact that the strength of B–O bonds exceeds that of Al–O.[27,43] Two local minima in *E* and *G* can also be observed, situated around the $25Na_2O–75SiO_2$ and $25Na_2O–25Al_2O_3–50B_2O_3$ compositions. The network of the former glass is significantly depolymerized with many NBOs, while the latter consists mainly of trigonal B-units. Both of these structural features are expected to decrease the glass stiffness [28,44,45].

The compositional trend in v (Figure 5d) appears inverted compared to those found in E and G. This is in agreement with the expected composition dependence of network dimensionality, since high dimensionality generally leads to a low Poisson's ratio.[46] In other words, the stiff and highly cross-linked networks that exhibit high T_g, E, and G values have low v values (~0.21-0.22), while the more flexible networks exhibit higher v values (up to 0.30). In general, the B-rich glasses have higher v values compared to those rich in Si. It should be noted that incorporation of Al_2O_3 in the glasses yields a decrease in v for the binary sodium silicate glass, but an increase in v for the binary sodium borate and B-rich borosilicate glasses. The former effect can be explained from the changes in connectivity, since Al-for-Si substitution leads to consumption of NBOs and formation of rigid Al-tetrahedral species [22]. However, the connectivity along the aluminoborate edge in the present system is expected to be constant, as Al-for-B substitution results in an approximately one-to-one exchange of tetrahedral units [23]. The compositional variation in v of aluminoborate and B-rich aluminoborosilicate glasses can also be affected by the differences in C_g (**Fig. IV.3b**), since there is an overall positive correlation between C_g and v when considering different types of glasses [46].

Fig IV.5: (a) Young's modulus (E), **(b)** shear modulus (G), **(c)** bulk modulus (B), and **(d)** Poisson's ratio (v) dependence on composition of the sodium aluminoborosilicate glasses. The contour map represents a pseudoternary slice through the quartenary phase diagram with [Na_2O] = 25 mol%. The isocontours are drawn as a guide for the eye, and are based on linear interpolation between the experimental data points marked by green diamonds.

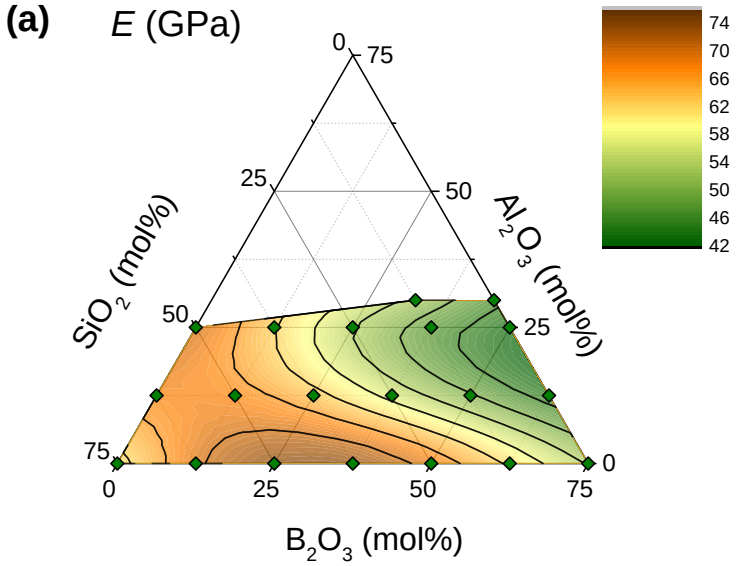

(b)

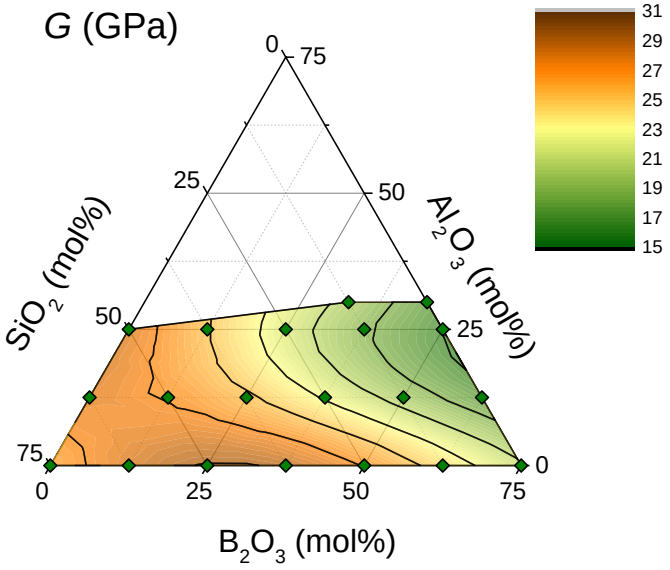
G (GPa)
31
29
27
25
23
21
19
17
15
0
75
25
50
SiO2 (mol%)
Al2O3 (mol%)
50
25
75
0
0
25
50
75
B2O3 (mol%)

(c)

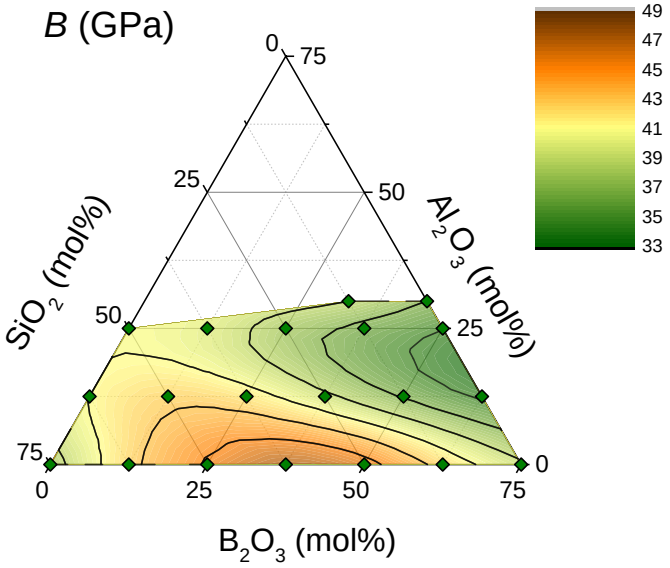
B (GPa)
49
47
45
43
41
39
37
35
33
0
75
25
50
SiO2 (mol%)
Al2O3 (mol%)
50
25
75
0
0
25
50
75
B2O3 (mol%)

(d)

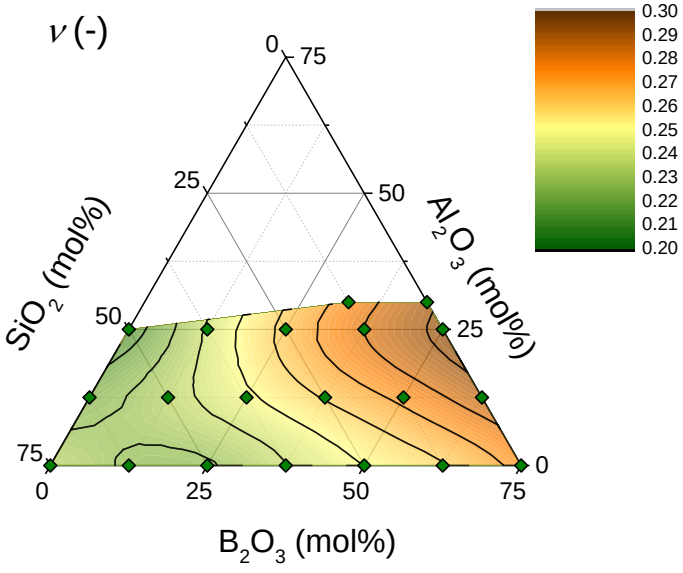
ν (-)
0.30
0.29
0.28
0.27
0.26
0.25
0.24
0.23
0.22
0.21
0.20
0
75
25
50
SiO2 (mol%)
Al2O3 (mol%)
50
25
75
0
0
25
50
75
B2O3 (mol%)

IV.5.c. Vickers hardness

Vickers hardness exhibits a significant compositional variation within the investigated system. The values measured at 1 N span from 3.5 GPa (metaluminous aluminoborate glass) to 6.6 GPa (metaluminous aluminosilicate glass), as illustrated in **Fig. IV.6**. Again, the impact of addition of Al_2O_3 and/or B_2O_3 on the role of the Na-cations needs to be considered. While these additions only induce NBOs in the binary sodium silicate glass, the formation of Al- and/or B-tetrahedral species requiring charge compensation results in a rearrangement of the Na-cations, resulting in a more constrained network. This manifests itself as a pronounced increase in H_V from 4.4 GPa (binary sodium silicate) to ~6.6 GPa (for the three compositions with $[Na_2O] = [B_2O_3] + [Al_2O_3]$). Upon further addition of B_2O_3, H_V gradually decreases due to the formation of flexible trigonal boron units. There is, however, one notable exception, as H_V increases upon addition of B_2O_3 to the $25Na_2O–37.5B_2O_3–37.5SiO_2$ composition (Figure 6), although this apparent increase in H_V is on the same order of the experimental error (~0.2 GPa).

Fig. IV.6: Vickers hardness (H_V) dependence on composition of the sodium aluminoborosilicate glasses. The contour map represents a pseudoternary slice through the quartenary phase diagram with $[Na_2O]$ = 25 mol%. H_V has been measured at a load of 1 N. The isocontours are drawn as a guide for the eye, and are based on linear interpolation between the experimental data points marked by green diamonds.

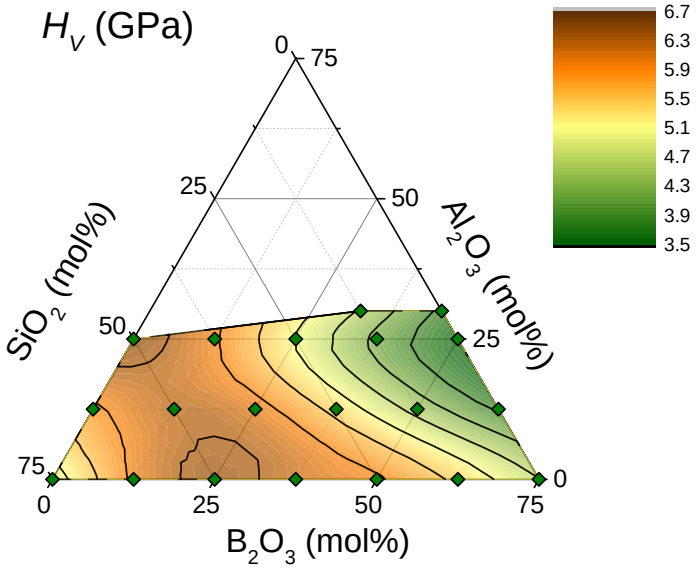

IV.5.d. Fracture toughness

Due to the time-consuming nature of the fracture toughness determination using the SEPB method, only six selected compositions were characterized. These compositions include a sodium

borosilicate, two sodium aluminoborates, and three sodium aluminoborosilicates to ensure a reasonable coverage of the phase diagram (see compositions and data in **Table IV.2**). Depending on the type of fracture (stable or unstable) for a given specimen, either K_{Ic}^{γ} or K_{Ic}^{Pmax} was used to compute the average K_{Ic}^{SEPB} value for each composition. Glass beams with uneven or twisted precracks were discarded from further analysis, following the guidelines described in detail elsewhere [26].

Table IV.2: Nominal compositions of the six glasses (all containing 25 mol% Na_2O) selected for fracture toughness measurements along with the predicted fracture surface energy (γ^{MODEL}) and fracture toughness (K_{Ic}^{MODEL}), as well as fracture toughness measured by means of indentation (K_{Ic}^{IFT}) and fracture toughness measured using the SEPB technique (K_{Ic}^{SEPB}). The errors in K_{Ic}^{IFT} and K_{Ic}^{SEPB} do not exceed 0.11 and 0.05 MPa√m, respectively. Note that different loads have been used to evaluate K_{Ic}^{IFT} (see Supporting Information).

$[Al_2O_3]$ (mol%)	$[B_2O_3]$ (mol%)	$[SiO_2]$ (mol%)	K_{Ic}^{IFT} (MPa·√m)	K_{Ic}^{SEPB} (MPa·√m)	γ^{MODEL} (J/m^2)	K_{Ic}^{MODEL} (MPa·√m)
0	50	25	0.53	0.66	4.72	0.83
12.5	12.5	50	0.80	0.79	3.71	0.73
12.5	62.5	0	0.56	0.67	4.49	0.65
25	12.5	37.5	0.52	0.58	3.51	0.68
25	25	25	0.70	0.58	3.74	0.65
30	45	0	0.64	0.67	3.98	0.64

The highest K_{Ic}^{SEPB} value (0.79 MPa√m) is observed for the $25Na_2O–12.5Al_2O_3–12.5B_2O_3–50SiO_2$ glass. The two aluminoborate compositions and the B-rich borosilicate composition display similar K_{Ic} values (0.66-0.67 MPa√m), suggesting that the borate-rich network governs the fracture characteristics in these glasses. Finally, the two metaluminous aluminoborosilicate glasses display the lowest K_{Ic} values (0.58 MPa√m). Overall, the results show that K_{Ic} features pronounced composition dependence, with similar K_{Ic} values for similar compositions. We also find that K_{Ic} does not scale very well with any of the other properties measured experimentally in this study.

In order to supplement the SEPB toughness measurements, toughness was assessed on the same glasses by means of an indentation cracking technique. These results are also given in **Table IV.2**. Due to the difference in indentation cracking threshold, crack length data are extracted from different loads to compute K_{Ic}^{IFT} for different compositions, which may lead to erroneous comparison across the compositional range. The different loads were selected for different composition to enable an accurate assessment of the indent characteristics, which would be

challenging for some of the composition at high loads (>10 N). This indentation analysis confirms that the $25Na_2O–12.5Al_2O_3–12.5B_2O_3–50SiO_2$ composition exhibits the highest toughness (0.80 MPa√m), although the large experimental error associated for this measurement should be considered (0.11 MPa√m). The remaining glasses display K_{Ic}^{IFT} values in the range from 0.52 to 0.70 MPa√m. It is noteworthy that dissimilar compositional trends in fracture toughness are observed for the SEPB and indentation techniques. For instance, the two metaluminous aluminoborosilicate glasses display equal K_{Ic}^{SEPB} values, while their K_{Ic}^{IFT} values differ by 0.18 MPa√m. This discrepancy supports the notion that determination of fracture toughness using indentation should be treated with caution. This is due to the complexity of the elastic stress field surrounding the indentation imprint, and the composition-dependent densification contribution to the indentation deformation mechanism in oxide glasses [47,48].

IV.6. Mechanical property prediction

IV.6.a. Atomic packing density

In previous studies concerning mechanical properties of oxide glasses, C_g was proven to strongly influence elastic moduli, deformation mechanism, as well as fracture toughness [7,46,49]. It is therefore relevant to evaluate how C_g affects the properties within the system investigated herein.

In Ref. [46] a clear sigmoidal trend was shown to exist between v and C_g when a broad range of different glass compositions is examined. In other words, more densely packed glasses are more keen on changing their shape upon loading trying to keep their volume constant, while loosely packed networks are maintaining their shape while changing their volume. For the glasses investigated in this study, there is no overall correlation between v and C_g (**Fig. IV.7a**). However, a more detailed inspection of the scatter plot shows that there is a systematic change of v with increasing C_g within each series of fixed Al_2O_3 content. In general, Al-rich glasses exhibit a large systematic increase in v, while glasses with low or zero Al_2O_3 content show a more complicated behavior with either a low initial increase or initial decrease in v, followed by a steep increase. This suggests that Al controls the correlation to some extent, but the three different trends in Figure 7a might indicate that this influence is only indirect. We suggest that v exhibits an increase upon increasing C_g in every case, but with a shift on the primary axis according to the fraction of tetrahedral boron content. In Figure 7b, it is evident that when data is indexed according to the product of molar B_2O_3 content and the corresponding N_4 values, three distinct trend lines emerge. Glasses with no tetrahedral boron have low C_g values, while glasses where approximately 25% of the available oxide consists of tetrahedral B_2O_3 exhibit ~0.05 higher C_g values. This is consistent

with the fact that increasing the coordination number of the network former results in a more efficient atomic packing [15,46]. We further note that the calculation of C_g is sensitive to the selected size of the ionic radii, especially the O anions [41]. Recalculation of C_g with a variable O ionic radius (here fixed at 1.35 Å) would change the ν vs. C_g correlation.

Fig. IV.7: Correlation between atomic packing density (C_g) and Poisson's ratio (ν) visualized in two ways. In **(a)**, the data points are indexed according to [Al_2O_3], while in **(b)** the data points are indexed according to the molar content of B_2O_3 in tetrahedral coordination (N_4 [B_2O_3]).

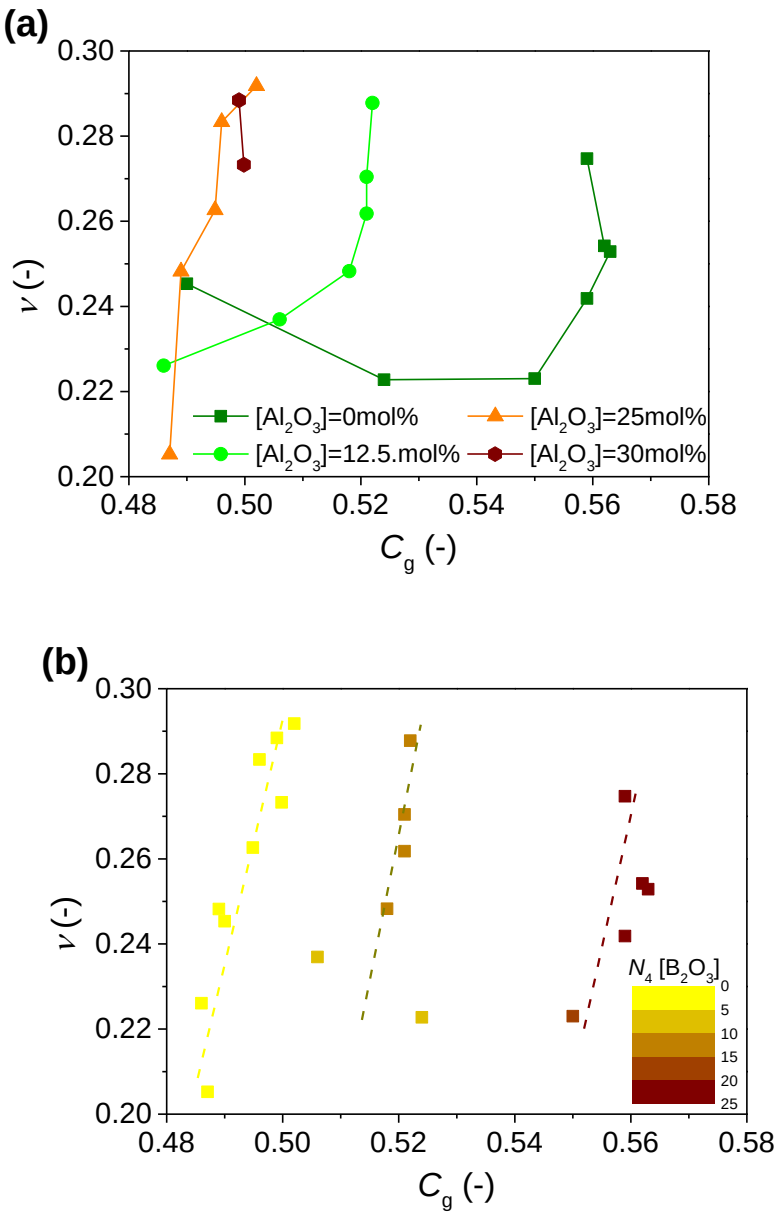

IV.6.b. Elastic moduli

Prediction of elastic moduli is important for the design of glasses for specific applications. For instance, glass fibers used for reinforcement of load-bearing structures need to be stiff, while glass used for protective screens need to be more flexible [50]. Elastic moduli depend on the bonding energy between the atoms constituting the material and the packing density of those atoms [46]. Bulk modulus, as a straightforward example, is thus related to the ratio of the interatomic bonding energy (U_0) and the molar volume (V_m). These can in turn be calculated based on the dissociation enthalpies of the constituent oxides (ΔH_{ai}), their molar fractions, molar masses and the glass density leading to Eq. (29):

$$B \propto \frac{U_0}{V_m} = \frac{\sum f_i \Delta H_{ai}}{(\sum f_i M_i)/\rho}. \quad \text{(IV.29)}$$

Using enthalpy values from Ref. [43] and the measured density values (**Table IV.1**) results in a poor correlation between B and U_0/V_m (Figure 8a). We note that similarly to the trend in Figure 7b, the data falls into three domains depending on the molar content of B_2O_3 in tetrahedral coordination, which is why the data points are indexed according to the product of N_4 and [B_2O_3] taken from **Table 1**. This suggests that Eq. (29) fails to predict the correlation between molar energy content and elastic moduli for the glasses investigated herein. Indeed, B_2O_3-rich glasses are sometimes deviating from the predicted trend [27,46,51]. This is probably due to the lack of consideration of network topology. As discussed in section 2, boron atoms can be coordinated to three or four oxygen atoms depending on the chemical composition. When large amounts of B_2O_3 in trigonal coordination are available in the glass, the dimensionality of the network decreases since two adjacent boron atoms are not necessarily linked by an oxygen atom (**Fig. IV.1b**). This must have an impact on the overall stiffness of the network. Eq. (IV.29) however, does not take this into account.

Fig. IV.8: Correlation between bulk modulus (B) and the molar energy content (U_0/V_m). In **(a)**, the dissociation enthalpy values from Ref. [43] were used, whereas in **(b)** the dissociation enthalpy for B_2O_3 in trigonal coordination was adjusted to optimize the fit. The data points are indexed according to the molar content of B_2O_3 in tetrahedral coordination (N_4 [B_2O_3]).

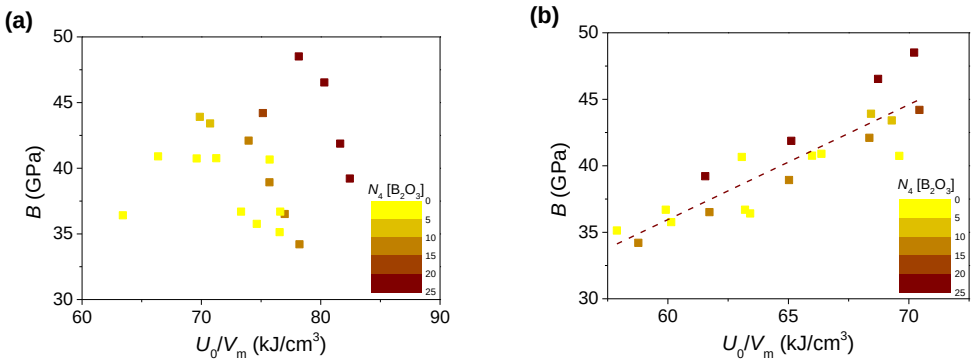

In order to optimize the fit, we suggest to use the B_2O_3 dissociation enthalpy taken from Ref. [43] for tetrahedral boron (2979 kJ/mol), and use a lower value for B_2O_3 in trigonal coordination. Using regression, we calculated this value to be 1719 kJ/mol (i.e., ~0.6 times that of tetrahedral boron). Applying this correction to Eq. (IV.29), the correlation between B and U_0/V_m improves significantly (Figure 8b). While this value is arbitrary and selected by minimizing the sums of errors, it is worth noticing that a boron atom in trigonal configuration has three atomic angular constraints, whereas a rigid tetrahedron exhibits five angular constraints per atom according to Philips-Thorpe methodology [52], which is in good agreement with the 3/5 ratio of the two dissociation enthalpy values.

Reducing the energy content in trigonal boron has been applied earlier by Makishima and Mackenzie [27], who suggested a semi-empirical methodology to predict elastic moduli of oxide glasses based on a similar approach. In their case, however, the ratio of the molar energy contents in trigonal and tetrahedral B_2O_3, respectively, is ~0.2 [27].

IV.6.c. Vickers hardness

Another mechanical property of industrial interest is hardness, as it relates to the resistance to scratching of exposed glass surfaces. Topological constraint theory [52,53] has been proposed and tested as an approach to predict H_V [29,30,54], with success for various oxide glasses [29,55–58], but also with some deviations for, e.g., aluminosilicates [59]. This approach reduces the complex atomic structure to a mechanical truss that is made rigid by bond stretching and bending constraints. The more constraints, the higher the resistance to deformation. In the original work of Smedskjaer et al. [29], H_V is calculated as,

$$H_V = \frac{dH_V}{dn_c}\left(n_c - n_{c,crit}\right), \quad \text{(IV.30)}$$

where dH_V/dn_c is a scaling factor, n_c is the average number of constraints per atom, and $n_{c,crit}$ is a critical number of constraints required to build a three-dimensional network (equal to 2.5, corresponding to 2-dimensional rigidity). Following the original work of Phillips and Thorpe [52,53], the number of constraints per atom is determined based on the coordination numbers (CN) of the atoms contributing rigid constraints, with nc = CN/2 for bond-stretching constraints and n_c = 2CN-3 for bond bending constraints.

Using this approach, a positive correlation between the experimentally determined and predicted H_V values is observed (Figure 9a). However, as in the case of E, the model tends to underestimate hardness for the Al-free glasses. Considering that the measured values of both E and H_V for the

borosilicate glasses are larger than those from the existing predictive models, it is possible that the actual fraction of tetrahedral B units is larger than that estimated from Eqs. (IV.7)-(IV.9). On the other hand, the model for hardness can be significantly improved by incorporating the adjustments suggested by Zheng et al. [30], as shown in Figure 9b. The adjustment is achieved by calculation of constraints per unit of volume rather than per atom, and by only counting the bond bending constraints (following the work of Bauchy[54]),

$$H_V = \frac{dH_V}{dn_{c\prime}}\left(n_{c\prime} - n_{c\prime,crit}\right), \quad \text{(IV.31)}$$

where $n_{c'}$ refers to the angular constraint density, while $dH_V/dn_{c'}$ and $n_{c',crit}$ correspond to a scaling factor and a critical constraint density. It has been suggested that hardness relates to the resistance to shear flow during indentation [60]. The propensity of a material to shear is governed by the three-body angular constraints, which is why the two-body radial constraints can be neglected [54]. Using Eq. (IV.31), the hardness of borosilicate and phosphosilicate series has previously been successfully predicted [30], as also found in the present case (**Fig. IV.9b**).

Another approach which could rationalize the deviation between experimental and predicted values of mechanical properties is the concept of granularity [61], which focuses on the heterogeneous structure of oxide glasses, resulting in fluctuations in rigidity on the nano-scale. In other words, some domains of the glass are more rigid than others, resembling granular media. The magnitude of a given local deformation may thus be dictated by the mechanical behavior of a certain domain of the glass rather than a mean average of the entire bulk [61,62]. Hence, medium-range order structures of the glasses investigated in this study may affect the properties as well, and could be investigated further in future work.

Finally, we note that H_V and E exhibit a strong positive correlation (inset of **Fig. IV.9b**). According to Baker [59], this criterion needs to be fulfilled in order to achieve accurate hardness predictions based on topological constraint theory. Furthermore, the correlation could suggest that within the aluminoborosilicate glass series investigated herein, the resistances to plastic and elastic deformations have common structural origin. In other words, the elastic moduli may be modelled by the application of topological constraint theory, while hardness can be modelled based on the dissociation energies of the constituent oxides. In both cases, the bond density is an important parameter, with more densely packed networks exhibiting higher resistance to deformation. This agrees with the positive correlation between E and C_g reported for a wide range of different materials including oxide, oxynitide, and metallic glasses [46]. Furthermore, it is known that both

hardness and elastic moduli increase linearly with increasing density upon isostatic pressure treatment [63].

Fig. IV.9: Correlation between values of Vickers hardness determined through indentation ($H_{V,exp}$) and the theoretically predicted ones ($H_{V,Smedskjaer}$ and $H_{V,Zheng}$). In **(a)**, the hardness is modelled by counting the number of constraints per atom following Eq. (IV.30) with dH_V/dn_c = 5.8 GPa. In **(b)**, the density of the angular constraints is used instead following Eq. (IV.31) with $dH_V/dn_{c'}$ = 0.21 GPa/nm and $n_{c',crit}$ = 18 nm^{-3}. The data points are indexed according to [Al_2O_3]. Inset in (b): Correlation between the experimentally determined values of Young's modulus (E_{exp}) and $H_{V,exp}$.

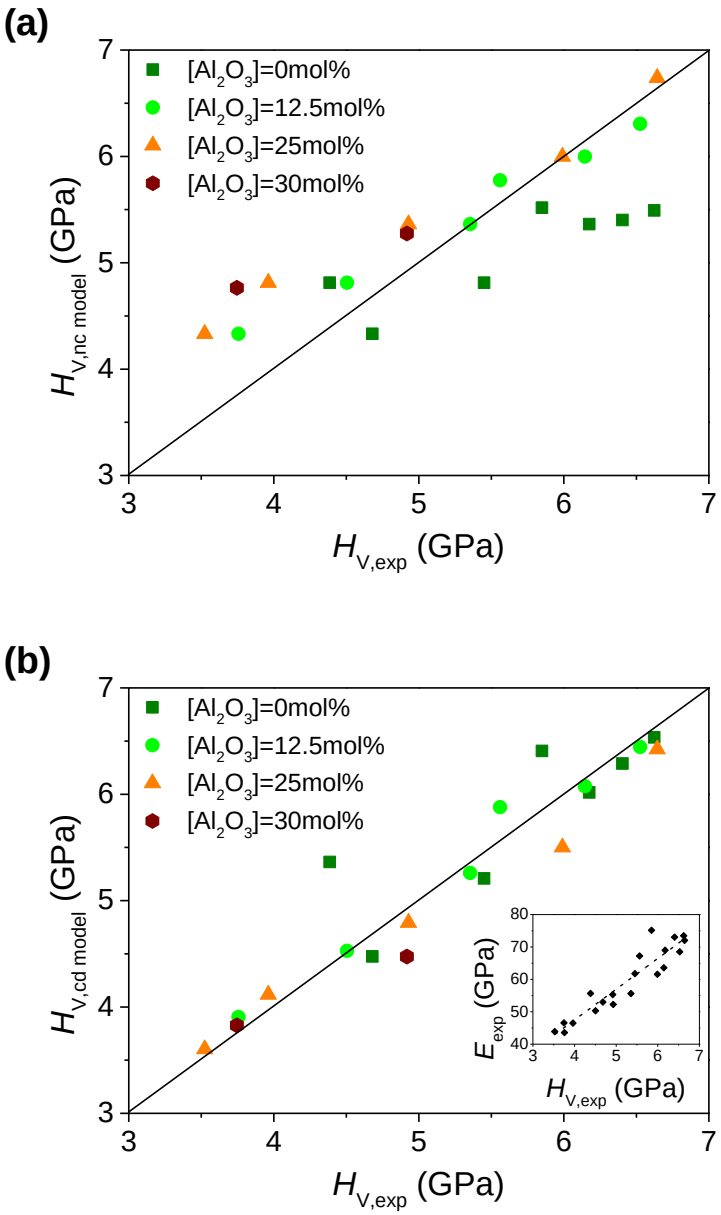

IV.6.d. Fracture toughness

Besides hardness and elastic moduli, fracture toughness is another important mechanical property. Nevertheless, there have only been few attempts to predict the compositional scaling of K_{Ic} in glasses based on chemical and structural information [31,49,64]. Most recently, Rouxel [31] used the strength of the bonds involved in the fracture process and the overall packing density to calculate the fracture surface energy (γ),

$$\gamma = \frac{1}{2}\left(\frac{\rho}{M_0}\right)^{2/3} \mathcal{N}^{-1/3} \sum x_i n_i U_{oi}, \tag{IV.32}$$

where M_0 is the molar mass of a representative unit (gram-atom of glass), $\mathcal{N}$ is the Avogadro number, x_i is the fraction of the i'th constituent, n_i is the number of bonds involved in the fracture process, and U_{oi} is the dissociation energy of a single cation-oxygen bond. Then, following fracture mechanics, K_{Ic} can be calculated as,

$$K_{Ic} = \sqrt{\frac{2\gamma E}{1-\nu^2}}. \tag{IV.33}$$

In this model, the glass structure needs to be considered to predict the probable path of the crack front. However, this is a complicated problem, since it is currently impossible to experimentally detect which bonds are being broken during fracture. Hence, for the present estimation, it is assumed that (i) no bonds are favored over others (i.e., the stoichiometric ratio of the bonds involved in the fracture matches that of the chemical composition), and (ii) the fracture proceeds through one cation-oxygen bond per structural unit (i.e., one Si-O bond needs to be broken to surpass a Si-tetrahedron). Inserting the bond strengths for the diatomic cation-oxygen molecules [65] into Eq. (IV.32) yields systematic compositional trends in γ. The energy spent on new surface formation (i.e., γ) increases with increasing B_2O_3 content and decreases with increasing Al_2O_3 content (**Fig. IV.10a**). The same trend is found using the bond strengths of Sun [43], if a correction factor of ~1.43 is applied (see Chapter S3 in Supporting Information) [31].

Fig. IV.10: (a) Fracture surface energy (γ) and **(b)** fracture toughness (K_{Ic}) predicted based on the model of Eqs. (IV.32)-(IV.33). The bond strength energies are taken from Ref. [65], and it is assumed that the crack front proceeds through one cation-oxygen bond per structural unit, and that the stoichiometric ratio of the bonds involved in the fracture process corresponds to that found in the bulk composition of the glasses. The isocontours are drawn as a guide for the eye, and are based on linear interpolation between the modelled data points marked by green diamonds.

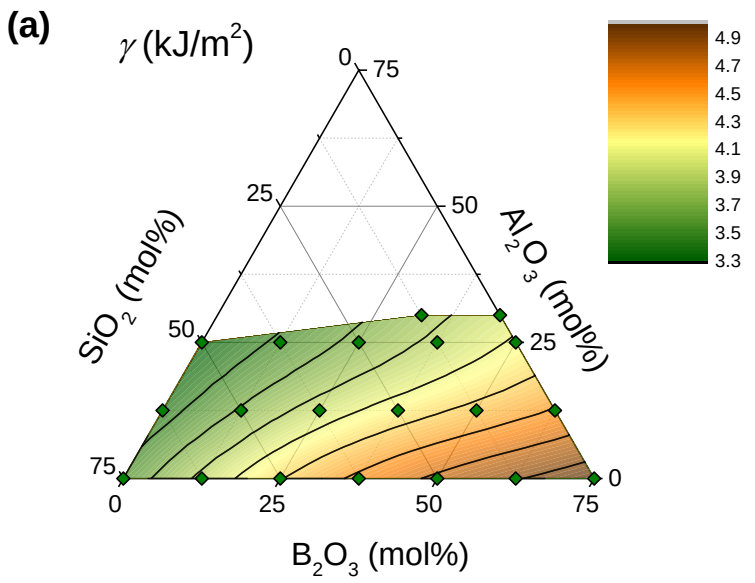

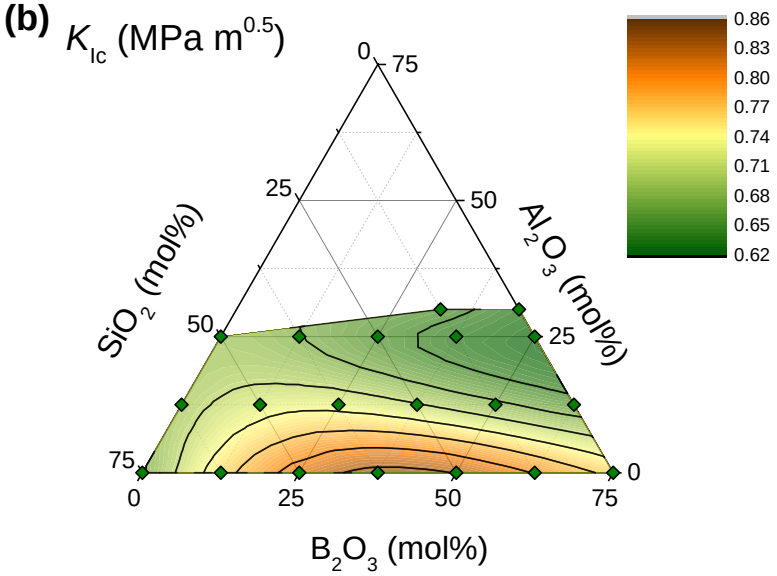

As K_{Ic} depends on the product of γ and E, the maximum predicted K_{Ic} value is situated around the borosilicate composition with equal amounts of SiO_2 and B_2O_3 (**Fig. IV.10b**). The lowest toughness is predicted to be found around the metaluminous aluminoborate composition, which is notable considering that this glass exhibits very high resistance to indentation cracking (i.e., high minimum indentation load needed to initiate radial cracks) [23]. However, there is not necessarily a positive correlation between these two quantities, mainly due to the large extent of energy dissipation aided by densification during an indentation process [5]. This is also reflected in the toughness values determined by means of indentation, which do not scale with the values determined using the SEPB technique (**Fig. IV.11**). The poor correlation between indentation and self-consistent methods to evaluate toughness has been intensively discussed [47–49]. Quantification of the indentation

deformation mechanisms could provide more insight into the correlation between crack resistance and fracture toughness, but this is beyond the scope of the present investigation.

Fig. IV-11: Correlation between fracture toughness determined using the SEPB technique (K_{Ic}^{SEPB}), indentation (K_{Ic}^{IFT}), and predicted according to the model of Eqs. (IV-32)-(IV-33) (K_{Ic}^{Rouxel}). Note that K_{Ic}^{IFT} is calculated using different indentation loads for different glasses due to the difference in their resistance to indentation cracking (see Supporting Information).

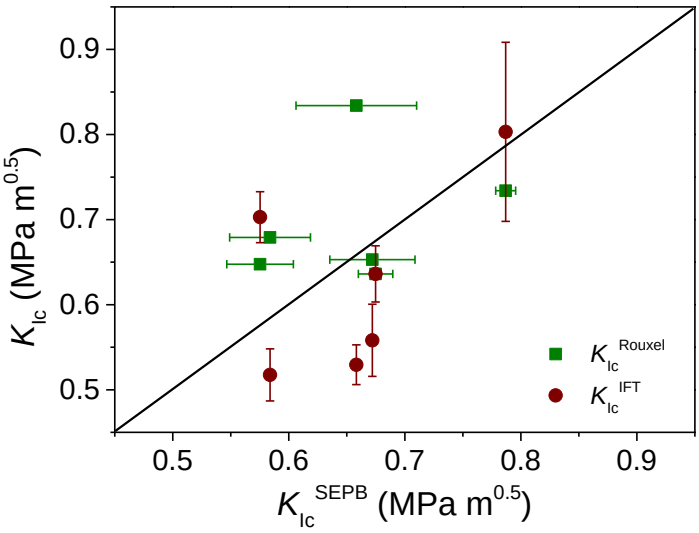

The model of Eqs. (IV-32)-(IV-33) yields realistic K_{Ic} values (i.e., within the range expected for most oxide glasses) [49], but relatively poor agreement between the absolute values of K_{Ic} from model and SEPB experiments (**Fig. IV.11**). Therefore, we reconsider the two model assumptions noted above. The first assumption is that the crack front proceeds through different cation-oxygen bonds with a probability corresponding to their abundance in the glassy network. However, as described in Ref. [31], an improved agreement between theoretical and experimental toughness values is obtained when the crack front is assumed to proceed through the weak modifier-oxygen bonds in highly modified sodium titanosilicate glasses. This adjustment is relatively simple to introduce into the model by setting up the following criterion for the sodium aluminoborosilicate glasses: the crack front proceeds through one Si-O bond when facing a Q^4 silicate unit with four bridging oxygens, while no Si-O bonds are broken when facing a Q^3 unit with three bridging oxygens and one NBO. In the latter case, only a Na-O bond is broken. This is schematically illustrated in **Fig. IV.12a**. Following this new assumption, the predicted value of K_{Ic} decreases by up to 0.15 MPa√m (in case of the binary sodium silicate glasses with largest Q^3 content). The K_{Ic} dependence on the oxygen speciation could also be investigated for the breakage of Al-O and B-O

tetrahedral bonds. However, it is assumed herein that all oxygen anions on tetrahedral Al and B units are bridging, yielding no dissimilar cation-oxygen bonds and thus no difference in K_{Ic} values.

Fig. IV-12: Ball and stick representations of two different glassy networks, which are shown to facilitate the discussion in the text about fracture toughness prediction (i.e., the structures are not obtained from any atomistic simulations). The O, B, Si, and Na atoms are represented by red, violet, yellow, and green, respectively. In **(a)**, the crack front could propagate through the weak Na-NBO bonds rather than the strong Si-NBO bonds in order to separate Si-atoms 1 and 2 from 4 and 5. This illustrates that high content of NBOs can decrease the fracture surface energy by lowering the average bond strength. In **(b)**, the crack could proceed through the network by separating B-atoms 2, 3, and 4 from 6, 7, and 8 without breaking any B-O bonds between two adjacent three-coordinated B-atoms. This illustrates that if the orientation of planar B-units is appropriate, the fracture can occur by breaking significantly fewer bonds than one bond per cation.

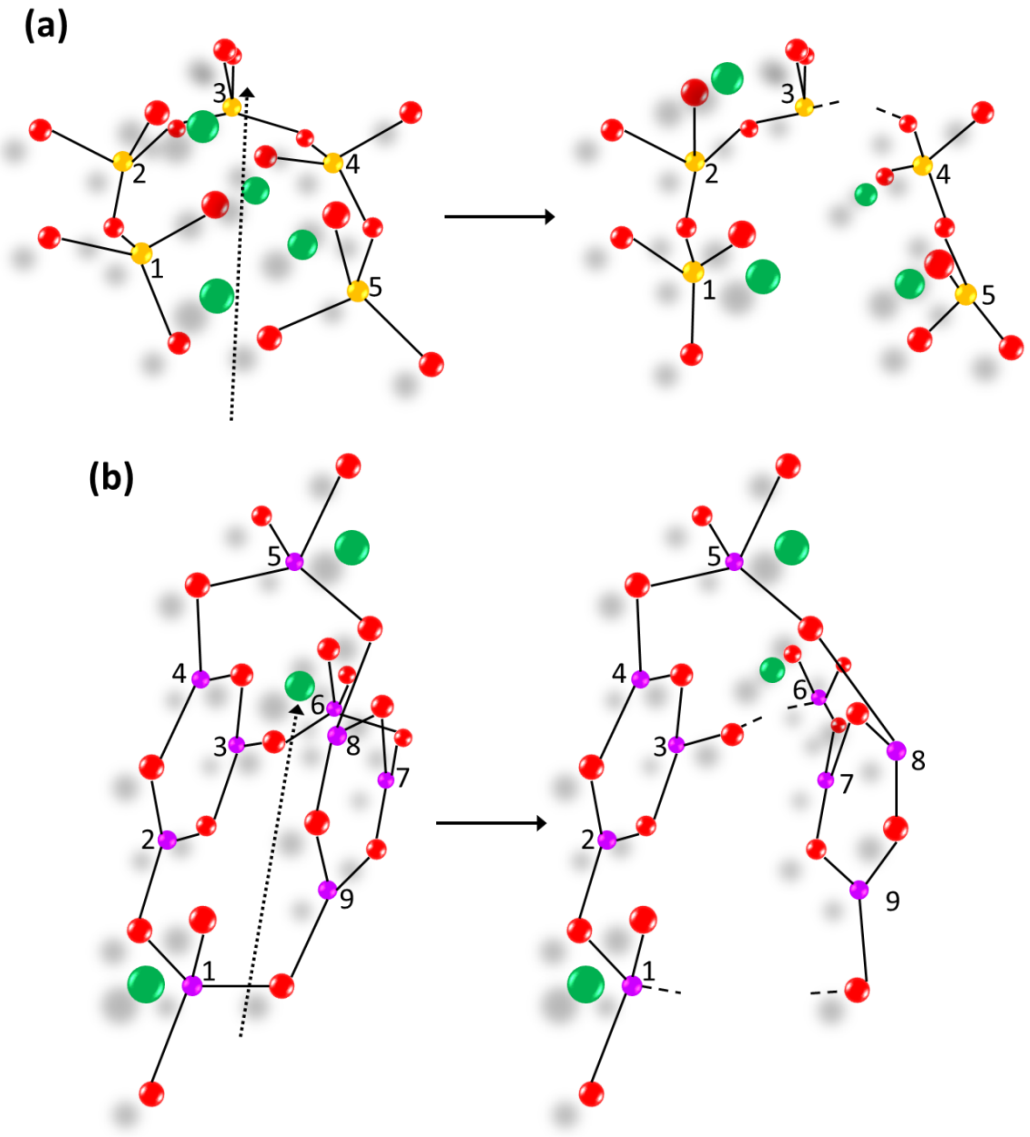

The second assumption relates to the number of cation-oxygen bonds to be broken per structural unit and it also impacts the predicted value of K_{Ic}. In the initial calculation used to construct the iso-contour map in **Fig. IV.10b**, it is assumed that exactly one cation-oxygen bond is broken to surpass a given structural unit regardless of the coordination number of the cation. In other words, the crack front needs to break the same number of B-O bonds for both trigonal and tetrahedral boron units. As discussed in previous section, the stiffness of the network depends largely on the coordination number of boron. It is assumed herein that the same holds for the fracture surface energy, especially when considering the geometrical arrangement of the structural units relative to each other. As schematically illustrated in **Fig. IV-12b**, the crack front always needs to break a B-O bond to surpass a rigid tetrahedron, while bond breakage might be avoided in the case of trigonal units. That is, borate rings can easily be "opened" by the application of tensile stress, since only van der Waals forces act between the planar rings. For example, if a particular borate ring is situated perpendicularly to the crack front, local fracture might be inevitable. We here incorporate the assumption that only a fraction *z* of B-O bonds in trigonal B units (ranging between zero and one) participate in the fracture process. Indeed, the predicted K_{Ic} value for the binary sodium borate glass (highest trigonal B content) can vary between 0.48 to 0.76 MPa$\sqrt{m}$ for *z* values of 0 and 1, respectively. We also note that K_{Ic} in these glasses strongly depends on C_g, which is in turn controlled by the coordination of boron.

The pronounced impact of the assumed crack path on the predicted K_{Ic} values suggests that the model contour maps of γ and K_{Ic} should be considered as estimates only (**Fig. 10a-b**). Alternatively, the model could be empirically optimized against the experimental values determined from the SEPB technique. However, in this study, the comparison of theoretical and experimental toughness values is limited by the fact that K_{Ic} has only been determined for six glass compositions. Hence, the validity of the model cannot be assessed across the entire compositional range studied herein.

IV.7. Conclusion

We have investigated twenty different sodium aluminoborosilicate glasses at fixed soda content, covering a large part of the glass-forming region. Ultrasonic echography, Vickers microindentation, and SEPB methods were used to evaluate the mechanical properties of the glasses. The sodium borosilicate glass with equal amounts of soda and boria exhibits the highest elastic moduli and hardness, which is ascribed to its high degree of cross-linking. The metaluminous aluminoborate glass displays the lowest elastic moduli and hardness, in agreement with its relatively flexible network compared to the remaining glasses investigated in this study. Both Young's modulus and

Vickers hardness could be predicted to a satisfactory degree using existing semi-empirical models when the glass network topology is taken into consideration. The SEPB measurements show that the metaluminous aluminoborosilicate glasses exhibit relatively low toughness values, which are smaller than the predicted ones, while the $25Na_2O–12.5Al_2O_3–12.5B_2O_3–50SiO_2$ composition shows the highest toughness of the glasses selected for toughness experiments. The experimental and theoretical fracture toughness values feature relatively poor agreement, when assuming that one cation-oxygen bond per structural unit is broken during fracture and that the crack proceeds through a random path with no preference for weak bonds. Adjusting the crack path to follow weaker bonds when favorable is found to have a pronounced impact on the toughness values, but more experimental data is needed to develop a predictive toughness model for aluminoborosilicate glasses.

IV.8. References

[1] L. Wondraczek, J.C. Mauro, J. Eckert, U. Kühn, J. Horbach, J. Deubener, T. Rouxel, Towards ultrastrong glasses, Adv. Mater. 23 (2011) 4578–4586.

[2] J.C. Mauro, A. Tandia, K.D. Vargheese, Y.Z. Mauro, M.M. Smedskjaer, Accelerating the Design of Functional Glasses through Modeling, Chem. Mater. 28 (2016).

[3] A.K. Varshneya, Stronger glass products: Lessons learned and yet to be learned, Int. J. Appl. Glas. Sci. 9 (2018) 140–155.

[4] G.A. Rosales-Sosa, A. Masuno, Y. Higo, H. Inoue, Crack-resistant Al_2O_3-SiO_2 glasses, Sci. Rep. 6 (2016) 23620.

[5] K. Januchta, R.E. Youngman, A. Goel, M. Bauchy, S.L. Logunov, S.J. Rzoska, M. Bockowski, L.R. Jensen, M.M. Smedskjaer, Discovery of Ultra-Crack-Resistant Oxide Glasses with Adaptive Networks, Chem. Mater. 29 (2017) 5865–5876.

[6] J. Sehgal, S. Ito, A New Low-Brittleness Glass in the Soda-Lime-Silica Glass Family, J. Am. Ceram. Soc. 81 (1998) 2485–2488.

[7] P. Sellappan, T. Rouxel, F. Celarie, E. Becker, P. Houizot, R. Conradt, Composition dependence of indentation deformation and indentation cracking in glass, Acta Mater. 61 (2013) 5949–5965.

[8] G. Scannell, L. Huang, T. Rouxel, Elastic properties and indentation cracking behavior of Na_2O-TiO_2-SiO_2 glasses, J. Non. Cryst. Solids. 429 (2015) 129–142.

[9] Z.Y. Yao, D. Möncke, E.I. Kamitsos, P. Houizot, F. Célarié, T. Rouxel, L. Wondraczek, Structure and mechanical properties of copper–lead and copper–zinc borate glasses, J. Non. Cryst. Solids. 435 (2016) 55–68. doi:10.1016/J.JNONCRYSOL.2015.12.005.

[10] C.L. Rountree, Recent progress to understand stress corrosion cracking in sodium borosilicate glasses: linking the chemical composition to structural, physical and fracture

properties, J. Phys. D. Appl. Phys. 50 (2017) 343002.

[11] G.N. Greaves, EXAFS and the structure of glass, J. Non. Cryst. Solids. 71 (1985) 203–217. 3.

[12] J. Zhong, P.J. Bray, Change in boron coordination in alkali borate glasses, and mixed alkali effects, as elucidated by NMR, J. Non. Cryst. Solids. 111 (1989) 67–76.

[13] F.A. Seifert, B.O. Mysen, D. Virgo, Three-dimensional network structure of quenched melts (glass) in the systems SiO_2-$NaAlO_2$, SiO_2-$CaAl_2O_4$ and SiO_2-$MgAl_2O_4$, Am. Mineral. 67 (1982) 696–717.

[14] R. Gresch, W. Müller-Warmuth, H. Dutz, ^{11}B and ^{27}Al NMR studies of glasses in the system Na_2O-B_2O_3-Al_2O_3 ("NABAL"), J. Non. Cryst. Solids. 21 (1976) 31–40.

[15] D.R. Neuville, L. Cormier, D. Massiot, Al coordination and speciation in calcium aluminosilicate glasses: Effects of composition determined by ^{27}Al MQ-MAS NMR and Raman spectroscopy, Chem. Geol. 229 (2006) 173–185.

[16] S. Yoshida, S. Isono, J. Matsuoka, N. Soga, Shrinkage Behavior of Knoop Indentations in Silica and Soda-Lime-Silica Glasses, J. Am. Ceram. Soc. 84 (2001) 2141–2143.

[17] Y. Kato, H. Yamazaki, Y. Kubo, S. Yoshida, J. Matsuoka, T. Akai, Effect of B_2O_3 content on crack initiation under Vickers indentation test, J. Ceram. Soc. Japan. 118 (2010) 792–798.

[18] R. Limbach, A. Winterstein-Beckmann, J. Dellith, D. Möncke, L. Wondraczek, Plasticity, crack initiation and defect resistance in alkali-borosilicate glasses: From normal to anomalous behavior, J. Non. Cryst. Solids. 417–418 (2015) 15–27.

[19] M. Barlet, J.M. Delaye, T. Charpentier, M. Gennisson, D. Bonamy, T. Rouxel, C.L. Rountree, Hardness and toughness of sodium borosilicate glasses via Vickers's indentations, J. Non. Cryst. Solids. 417–418 (2015) 1–15.

[20] S. Yoshida, A. Hidaka, J. Matsuoka, Crack initiation behavior of sodium aluminosilicate glasses, J. Non. Cryst. Solids. 344 (2004) 37–43.

[21] M. Tiegel, R. Hosseinabadi, S. Kuhn, A. Herrmann, C. R??ssel, Young's modulus, Vickers hardness and indentation fracture toughness of alumino silicate glasses, Ceram. Int. 41 (2015).

[22] T.K. Bechgaard, A. Goel, R.E. Youngman, J.C. Mauro, S.J. Rzoska, M. Bockowski, L.R. Jensen, M.M. Smedskjaer, Structure and mechanical properties of compressed sodium aluminosilicate glasses: Role of non-bridging oxygens, J. Non. Cryst. Solids. 441 (2016).

[23] K. Januchta, R.E. Youngman, A. Goel, M. Bauchy, S.J. Rzoska, M. Bockowski, M.M. Smedskjaer, Structural origin of high crack resistance in sodium aluminoborate glasses, J. Non. Cryst. Solids. 460 (2017) 54–65.

[24] Q. Zheng, M. Potuzak, J.C. Mauro, M.M. Smedskjaer, R.E. Youngman, Y. Yue,

Composition–structure–property relationships in boroaluminosilicate glasses, J. Non. Cryst. Solids. 358 (2012) 993–1002.

[25] H. Morozumi, S. Yoshida, J. Matsuoka, Composition dependence of crack formation probability in aluminoborosilicate glass, J. Non. Cryst. Solids. 444 (2016) 31–37.

[26] T. To, F. Célarié, C. Roux-Langlois, A. Bazin, Y. Gueguen, H. Orain, M. Le Fur, V. Burgaud, T. Rouxel, Fracture toughness, fracture energy and slow crack growth of glass as investigated by the Single-Edge Precracked Beam (SEPB) and Chevron-Notched Beam (CNB) methods, Acta Mater. 146 (2018) 1–11.

[27] A. Makishima, J.D. Mackenzie, Direct calculation of Young's modulus of glass, J. Non. Cryst. Solids. 12 (1973) 35–45.

[28] S. Inaba, S. Fujino, K. Morinaga, Young's Modulus and Compositional Parameters of Oxide Glasses, J. Am. Ceram. Soc. 82 (1999) 3501–3507. 2.x.

[29] M.M. Smedskjaer, J.C. Mauro, Y. Yue, Prediction of Glass Hardness Using Temperature-Dependent Constraint Theory, Phys. Rev. Lett. 105 (2010) 115503.

[30] Q. Zheng, Y. Yue, J.C. Mauro, Density of topological constraints as a metric for predicting glass hardness, Appl. Phys. Lett. 111 (2017) 011907-1–5.

[31] T. Rouxel, Fracture surface energy and toughness of inorganic glasses, Scr. Mater. 137 (2017) 109–113.

[32] M. Yamane, J.. Mackenzie, Vicker's Hardness of glass, J. Non. Cryst. Solids. 15 (1974) 153–164.

[33] H. Maekawa, T. Maekawa, K. Kawamura, T. Yokokawa, The structural groups of alkali silicate glasses determined from ^{29}Si MAS-NMR, J. Non. Cryst. Solids. 127 (1991) 53–64.

[34] H. Inoue, A. Masuno, Y. Watanabe, K. Suzuki, T. Iseda, Direct Calculation of the Physical Properties of Sodium Borosilicate Glass from its Chemical Composition Using the Concept of Structural Units, J. Am. Ceram. Soc. 95 (2012) 211–216.

[35] W.J. Dell, P.J. Bray, S.Z. Xiao, ^{11}B NMR studies and structural modeling of Na_2O-B_2O_3-SiO_2 glasses of high soda content, J. Non. Cryst. Solids. 58 (1983) 1–16..

[36] D. Feil, S. Feller, The density of sodium borosilicate glasses related to atomic arrangements, J. Non. Cryst. Solids. 119 (1990) 103–111.

[37] S. Takahashi, D.R. Neuville, H. Takebe, Thermal properties, density and structure of percalcic and peraluminus CaO–Al_2O_3–SiO_2 glasses, J. Non. Cryst. Solids. 411 (2015) 5–12.

[38] R.D. Shannon, Revised effective ionic radii and systematic studies of interatomic distances in halides and chalcogenides, Acta Crystallogr. Sect. A. 32 (1976) 751–767.

[39] G.R. Anstis, P. Chantikul, B.R. Lawn, D.B. Marshall, A critical evaluation of indentation techniques for measuring fracture toughness: I, direct crack measurements, J. Am. Ceram.

Soc. 64 (1981) 533–538.

[40] I. Bar-On, F.I. Baratta, K. Cho, Crack Stability and Its Effect on Fracture Toughness of Hot-Pressed Silicon Nitride Beam Specimens, J. Am. Ceram. Soc. 79 (1996) 2300–2308.

[41] A. Zeidler, P.S. Salmon, L.B. Skinner, Packing and the structural transformations in liquid and amorphous oxides from ambient to extreme conditions., Proc. Natl. Acad. Sci. U. S. A. 111 (2014) 10045–8.

[42] A.K. Varshneya, Fundamentals of inorganic glasses, Academic Press, 1994.

[43] K.-H. Sun, Fundamental Condition of Glass Formation, J. Am. Ceram. Soc. 30 (1947) 277–281.

[44] N. Soga, Elastic moduli and fracture toughness of glass, J. Non. Cryst. Solids. 73 (1985) 305–313.

[45] R.J. Eagan, J.C. Swearekgen, Effect of composition on the mechanical properties of aluminosilicate and borosilicate glasses, J. Am. Ceram. Soc. 61 (1978) 27–30.

[46] T. Rouxel, Elastic Properties and Short-to Medium-Range Order in Glasses, J. Am. Ceram. Soc. 90 (2007) 3019–3039.

[47] G.D. Quinn, R.C. Bradt, On the Vickers indentation fracture toughness test, J. Am. Ceram. Soc. 90 (2007) 673–680.

[48] M. Sakai, R.C. Bradt, Fracture toughness testing of brittle materials, Int. Mater. Rev. 38 (1993) 53–78.

[49] T. Rouxel, S. Yoshida, The fracture toughness of inorganic glasses, J. Am. Ceram. Soc. 100 (2017) 4374–4396.

[50] T.M. Gross, R. Youngman, Flexible glass: enabling thin, lightweight, and flexible electronics, 2017.

[51] M. Plucinski, J.W. Zwanziger, Topological constraints and the Makishima–Mackenzie model, J. Non. Cryst. Solids. 429 (2015) 20–23.

[52] J.C. Phillips, M.F. Thorpe, Constraint theory, vector percolation and glass formation, Solid State Commun. 53 (1985) 699–702.

[53] J.C. Phillips, Topology of covalent non-crystalline solids I: Short-range order in chalcogenide alloys, J. Non. Cryst. Solids. 34 (1979) 153–181.

[54] M. Bauchy, M.J.A. Qomi, C. Bichara, F.-J. Ulm, R.J.-M. Pellenq, Rigidity Transition in Materials: Hardness is Driven by Weak Atomic Constraints, Phys. Rev. Lett. 114 (2015) 125502.

[55] M.M. Smedskjaer, J.C. Mauro, R.E. Youngman, C.L. Hogue, M. Potuzak, Y. Yue, Topological Principles of Borosilicate Glass Chemistry, J. Phys. Chem. B. 115 (2011)

12930–12946..

[56] M.M. Smedskjaer, Topological Model for Boroaluminosilicate Glass Hardness, Front. Mater. 1 (2014) 23.

[57] C. Hermansen, X. Guo, R.E. Youngman, J.C. Mauro, M.M. Smedskjaer, Y. Yue, Structure-topology-property correlations of sodium phosphosilicate glasses, J. Chem. Phys. 143 (2015) 064510.

[58] C. Hermansen, R.E. Youngman, J. Wang, Y. Yue, Structural and topological aspects of borophosphate glasses and their relation to physical properties, J. Chem. Phys. 142 (2015)

[59] S. Baker, Topological Constraint Theory as a Predictor of Hardness in Glass, in: 2018 Glas. Opt. Mater. Div. Annu. Meet., 2018.

[60] J. Kjeldsen, M.M. Smedskjaer, J.C. Mauro, Y. Yue, On the origin of the mixed alkali effect on indentation in silicate glasses, J. Non. Cryst. Solids. 406 (2014).

[61] O. Benzine, S. Bruns, Z. Pan, K. Durst, L. Wondraczek, Local Deformation of Glasses is Mediated by Rigidity Fluctuation on Nanometer Scale, Adv. Sci. 5 (2018) 1800916.

[62] S. Sawamura, L. Wondraczek, Scratch hardness of glass, Phys. Rev. Mater. 2 (2018) 092601.

[63] S. Kapoor, L. Wondraczek, M.M. Smedskjaer, Pressure-Induced Densification of Oxide Glasses at the Glass Transition, Front. Mater. 4 (2017) 1.

[64] A. Abd El-Moneim, Quantitative analysis of elastic moduli and structure of B_2O_3–SiO_2 and Na_2O–B_2O_3–SiO_2 glasses, Phys. B Condens. Matter. 325 (2003) 319–332.

[65] Y.-R. Luo, J.-P. Cheng, Handbook of Chemistry and Physics, 86th ed., Talor & Francis, 1993.

V. Fracture toughness and crack behavior of dense SiOC glass ceramics*

V.1 Abstract

Four different SiOC glass ceramics were synthesized and investigated on their fracture behavior. Toughness of C1-SiOC (C_{free} < 1 vol.%) and C12-SiOC (C_{free} ~12 vol.%) has been studied to highlight the impact of varying amounts of segregated carbon. It has been shown that C12-SiOC (three phases – SiO_2-SiC-C) has greater toughness (about 1 $MPa \cdot m^{0.5}$) comparing to that (about 0.7 $MPa \cdot m^2$) of C1-SiOC (two phases – SiO_2-SiC). The impact of zirconium and hafnium modification has also been studied by adding about 5 vol.% of HfO_2/ZrO_2 into the materials, which results in four phases glass ceramics (SiO_2-HfO_2/ZrO_2-SiC-C). These four phases glass ceramics have the same toughness as the three phases materials. It is believed that the amounts of HfO_2/ZrO_2 are not enough to significantly increase the toughness. Moreover, predicted toughness by assuming the crack travels through the easiest crack path has been shown to have a good agreement with the experimented toughness.

Keywords: Fracture toughness; Glass ceramic; Silicon oxycarbide; Zirconium; Hafnium

V.2 Introduction

As a concept of mechanically improved vitreous silica glass, SiOC glasses were developed mainly starting from the late 1980s. It was expected that the partial substitution of bivalent oxygen atoms for tetravalent carbon atoms will lead to an increase of the network connectivity and hence improved mechanical properties [1]. This was demonstrated in the following years for example in the light of higher Young's modulus [1], viscosity [2] and hardness [3].

The main synthesis approach for SiOC materials relies on the thermal conversion of polyorganosiloxanes or precursors derived from sol-gel synthesis of organically modified alkoxysilanes under inert atmosphere [4,5]. Depending on the precursor used, different chemical composition can be achieved. This rather chemical approach additionally opens the possibility of a homogeneous modification with additional elements like alkali, earth alkali and transition metals at an atomic level, resulting in finely dispersed nanocomposites [6]. A significant amount of Si-O and Si-C bonds present in the polymeric precursors is preserved during the heat treatment to yield black SiOC glasses at 1000 °C. The partial substitution of oxygen for carbon was demonstrated by means of ^{29}Si MAS NMR measurements, where in SiOC glasses the chemical shifts related to so-called mixed-bonds $SiO_{4-x}C_x$ tetrahedra (with x = 0 to 4) are clearly visible [7]. In addition to this sp^3-

This chapter has been submitted to: T. To, , C. Stabler, E. Ionescu, R. Riedel, F. Célarié, T. Rouxel, Fracture toughness and crack behavior of dense SiOC glass ceramics, J. Eur. Cer. Soc., (2018).

hybridized network carbon, Raman spectroscopy [8,9] typically reveals the presence of a sp^2-hybridized segregated carbon phase. While SiOC glasses are fully X-ray amorphous, starting at a synthesis temperature of around 1250 °C broad reflections related to β-SiC nanoparticles are evolving in the diffractograms [10]. At the same time, the amount of SiO_4 and SiC_4 tetrahedra starts to increase at the expense of the SiO_3C, SiO_2C_2 and $SiOC_3$ mixed-bonds tetrahedra, as monitored by ^{29}Si MAS NMR [9,10]. This phase separation is a continuous process and is not finished at temperatures below 1400 °C [9]. Consequently, SiOC samples prepared at T > 1400 °C can be regarded as SiOC glass ceramics, where β-SiC nanoparticles and a segregated carbon phase are homogeneously dispersed in a vitreous silica matrix [11].

Whereas SiOC glass ceramics were already demonstrated to yield as well higher hardness and viscosity in comparison to vitreous silica [12–15], the fracture behavior of SiOC glass ceramics is not yet widely investigated in literature.

In the present study, we synthesized four different SiOC glass ceramics with varying chemical and phase composition. The aim was to highlight the impact of varying amounts of segregated carbon on the fracture behavior of SiOC glass ceramics. Moreover, the effect of the incorporation of ZrO2/HfO2 nanoparticles into SiOC was investigated.

V.3 Materials and Experimental Procedure

Table V.1: Chemical composition of the investigated glass ceramics and molar fractions of silicon oxide (SiO_2), silicon carbide (SiC), free carbon (C_{free}), and metal oxide (MO_2) phases (from [11] and [13]).

Sample	Chemical formula	SiO_2		SiC		C_{free}		MO_2	
		mol %	[vol%]	[mol %]	[vol%]	[mol %]	vol.%	[mol %]	[vol%]
C1-SiOC	$SiO_{1.41}C_{0.3}$	70.2 ± 0.5	83.0	29.3 ± 2.1	16.8	0.5 ± 2.7	0.2	/	/
C12-SiOC	$SiO_{1.6}C_{0.65}$	54.8 ± 0.3	75.7	14.1 ± 1.4	12.3	31.1 ± 1.7	11.9	/	/
SiHfOC	$SiO_{1.77}C_{0.42}Hf_{0.06}$	63.2 ± 0.4	80.5	13.4 ± 1.1	7.8	18.7 ± 1.4	7.2	4.6 ± 0.5	4.5
SiZrOC	$SiO_{1.82}C_{0.42}Zr_{0.1}$	60.8 ± 0.3	77.6	14.5 ± 0.7	8.5	16.9 ± 0.9	6.5	7.8 ± 0.4	7.4

Glass ceramics with four different compositions within the Si(-M)-O-C (M = Hf, Zr) chemical system, namely C1-SiOC, C12-SiOC, SiHfOC, and SiZrOC were synthesized from polymeric

precursors or using the sol-gel route. The preparation process of these glass ceramics was previously reported in detail [10,11,13,16,17]. Briefly, the C1-SiOC grade was derived from a sol-gel process involving the mixing of triethoxysilane and methyldiethoxysilane under vigorous stirring in a molar ratio of 2:1. The SiOC glass obtained from this process was later crushed to powder (< 40 µm), with subsequent densification using the field assisted sintering technique FAST at 1600 °C (50 MPa, argon atmosphere, dwell time of 15 minutes). The C12-SiOC grade was prepared from a commercially available polymethylsilsesquioxane Belsil PMS MK (Wacker GmbH, Burghausen, Germany). The polymer was cross-linked at 250 °C for two hours and then heated at 900 °C with dwell time of two hours. The obtained material was used to prepare a powder (< 40 µm) that was further hot-pressed (30 MPa, argon atmosphere, dwell time of 15 minutes). The SiHfOC and SiZrOC grades were prepared in a way similar to the one for C12-SiOC. The difference was that the PMS was modified with $Zr(O^nPr)_4$ or $Hf(O^nBu)_4$ (Sigma-Aldrich, München, Germany) prior ceramization and subsequent densification in the hot press. The chemical compositions of the synthesized glass ceramics with the molar fractions of SiO_2, SiC, C_{free}, and MO_2 (HfO_2 in SiHfOC and ZrO_2 in SiZrOC) phases are given in **Table V.1**.

The density of the samples (ρ) was measured by means of Archimedes' method in distilled water in room condition (20.5 °C) and averaged from three measurements of three different pieces (same batch) for each glass ceramic. The elastic moduli of the materials were estimated with different methods depending on the limitation due to the sample size and geometry. For C1-SiOC, Young's modulus (*E*) and shear modulus (*G*) were obtained from the measurements of the mechanical resonance frequencies of rectangular plates using an impulse excitation testing apparatus (RFDA HT 1050). Let *m*, *b*, *L*, *t*, f_f, T_1 and T_2 be the mass, width, length, thickness, fundamental resonant frequency in flexion, correction factor for fundamental bending mode and correction factor dependent on the width-to-thickness ratio (typically $T_2 \sim 0.01 - 0.02$) of the rectangular specimen, respectively, *E* and *G* are then obtained by means of **Eq. (V.1)** and **Eq. (V.2)**. For C12-SiOC and SiZrOC, *E* and *G* were measured by means of ultrasonic echography using 10 MHz piezoelectric transducers. In this measurement, velocities of longitudinal (V_L) and transverse (V_T) waves were calculated from the sample thickness (*L*) and transit time (τ). *E* and *G* were then obtained by means of Eq. (3) and **Eq. (V.4)**, respectively. For SiHfOC, the sample size was too small to allow for the measurement of the elastic moduli. Hence, for any future calculation concerning the SiHfOC grade, the elastic moduli of the SiZrOC grade will be taken as approximate values of the actual ones for the SiHfOC grade. Poisson's ratio (*v*) and bulk modulus (*K*) were further deduced from *E* and *G* by means of **Eq. (V.5)** and **Eq. (V.6)**.

$$E = 0.9465 \frac{m f_f^2}{b} \frac{L^3}{t^3} T_1 \quad \text{(V.1)}$$

$$G = \frac{4\, L\, m f_f^2}{b\, t} T_2 \quad \text{(V.2)}$$

$$E = \rho \frac{3V_L^2 - 4V_T^2}{(V_L/V_T)^2 - 1} \quad \text{(V.3)}$$

$$G = \rho V_T^2 \quad \text{(V.4)}$$

$$K = \frac{E}{3(1 - 2v)} \quad \text{(V.5)}$$

$$v = \frac{E}{2G} - 1 \quad \text{(V.6)}$$

Vickers indentation experiments were also conducted at ambient conditions (50 % RH, 20.5 °C) using a hardness tester (Matsuzawa, model VMT-7s, Japan) with a pyramid shaped diamond indenter (Vickers type). Five indents were made on the polished (2 µm diamond paste finish) sample surface with a load (*P*) of 9.81 N. Corner crack length (*c*) and diagonal length (*d*) were measured using an optical microscope (Keyence, model MVH 5000, Japan) with x2000 magnification. Meyer's hardness (*H*), which represents a mean normal stress (Eq. (V.7)) and fracture toughness (K_{Ic}^{VIF}) measured from Vickers Indentation Fracture (VIF) (Eq. (V.8)) [18] were derived from the indentation imprint and from the radial/median crack length respectively.

$$H = 2P/d^2 \quad \text{(V.7)}$$

$$K_{Ic}^{VIF} = 0.016\, (E/H)^{0.5} P/c^{1.5} \quad \text{(V.8)}$$

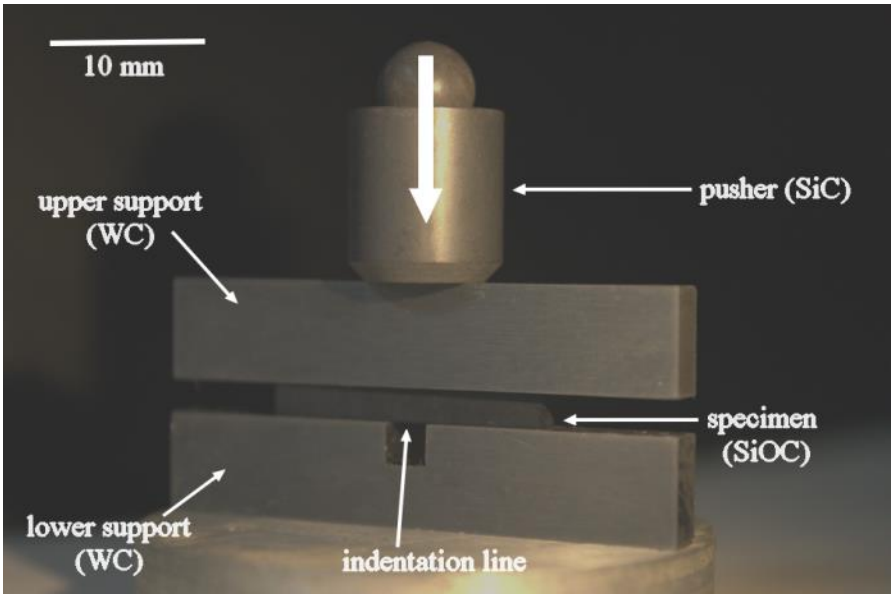

Fig. V.1: Compression fixture with indented specimen (C1-SiOC with the dimension of 2×2.6×25 mm^3)

After the indentation process, surface investigations were performed by means of optical microscopy (Keyence MVH5000). K_{Ic} was further determined by means of the single-edge precrack beam (SEPB), by far more reliable than the indentation cracking methods [8,9], following the experimental procedure give in [19,20], with some adjustment for the precracking detection to non-transparent materials (present situation). K_{Ic} was also predicted ab-initio from the chemical composition of the materials, following [21]. In the SEPB method, the C1-SiOC and SiHfOC rectangular specimens were obtained from the pellets having a thickness of 3 mm, and C12-SiOC and SiZrOC rectangular specimens from the pellets having a thickness of 4 mm. The 3 mm thickness pellets were cut into a beam of 3×4×25 mm^3, and the 4 mm thickness pellets into 4×5×25 mm^3 that were further grinded and polished down to 2×3×25 mm^3 (except for C1-SiOC, where 2×2.6×25 mm^3 beams were used) and 3×4×25 mm^3, respectively. The final stage is a mirror surface finish using a 0.25 µm diamond paste. An indentation line consisting of up to 30 Vickers indents was performed on one of the side face (Broadness B = 2 for C1-SiOC and SiHfOC, B = 3 for C12-SiOC and SiZrOC) of the polished beam with a force of 9.81 N for a dwell of 5 s (using 5 s instead of 15 s for sake of rapidity). The distance from one indent to the adjacent one was 100 µm, which resulted in 19 and 29 indents for beam with B = 2 mm and B = 3 mm respectively. The indented beam was then set in the compression fixture (**Fig. V.1**) to initiate the precrack. The indented surface was placed over the lower support and the indentation line was carefully positioned in the middle of the groove. On loading, the lower part of the beam is in tension whereas the upper part is in compression. This situation promotes the initiation of a precrack from the indentation line. The precrack propagates until its front reaches the compressive upper part of the beam. An acoustic emission sensor was placed beside the lower support to detect the precrack pop-in sound. Once the sound was detected, the loading was immediately interrupted. The length of the obtained precrack depends on the groove's size (b) and the tensile stress (T_C). To fulfill the ASTM standard requirements [22], the precrack length should be in between 0.35W and 0.60W (in the present case where the indentation load (9.81 N) is at least 5 times smaller than the values considered in the standard, it is anticipated that a larger range from 0.20W to 0.80W may be acceptable). This limitation is to ensure that the precrack is long enough to avoid some residual stress effects stemming from the Vickers indent and short enough so that there is no perturbation from the upper "free" surface. **Fig. V.2** shows the dependence of the stress intensity factor (K_I normalized by T_c) on the crack ratio (a/W) for different b, where T_c is computed by means of finite element calculation for a crack-free sample. Since K_I and T_c are unknown, a preliminary test needs to be performed before using the K_I/T_c- a/W curves.

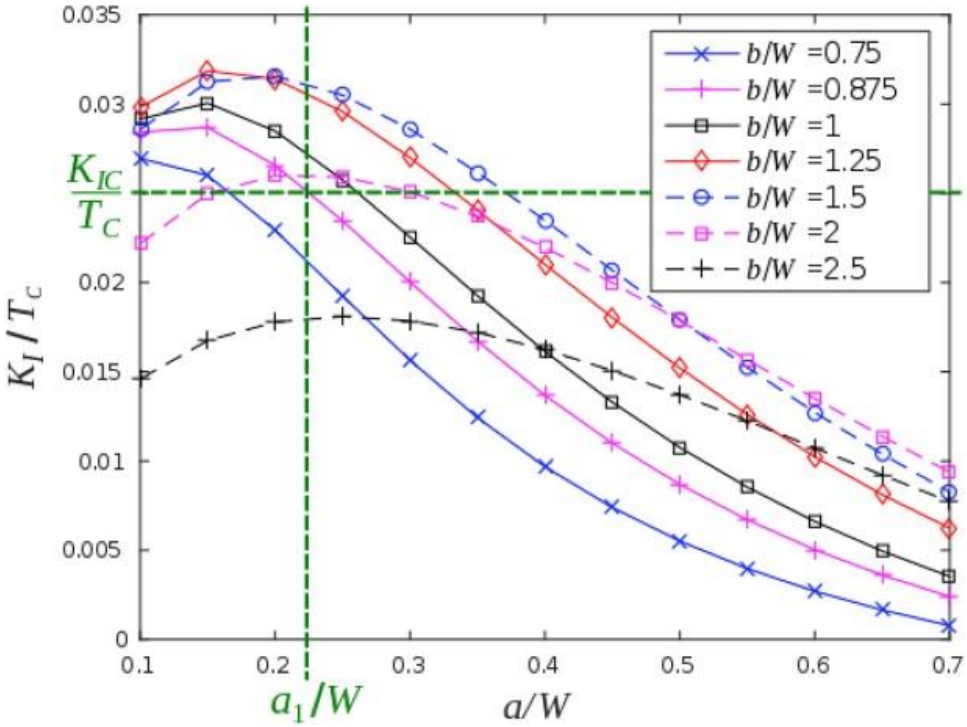

Fig. 2: Stress intensity factor as a function of the length of the precrack (from To et al., 2017 [20]).

The precrack beam was then fractured with three-point bending with the span length (S) of 20 mm and the cross-head speed of 0.05, 1 and 15 µm·s^{-1}. The 15 µm/s speed was used on all glass ceramics in this study to avoid the stress corrosion whereas the 0.05 and 1 µm·s^{-1} speeds were used on the small (2×2.6×25 mm^3 and 2×3×25 mm^3) and the large (3×4×25 mm^3) beams, respectively, to investigate stress corrosion effects. Three-point bending was chosen since it favors a stable crack propagation [20]. According to the precrack length, the cross-head speed and the sensitivity to humidity, test can be stable or unstable. In case of a stable test, toughness was calculated by means of the similarity principle,

$$K_{\mathrm{Ic}}^{\mathrm{SEPB}} = \sqrt{2\gamma E'} \tag{V.9}$$

The work of fracture (*wof*), where $\gamma = wof/2A$ is the fracture surface energy, is expressed as,

$$wof = \int_0^{\delta_f} P\mathrm{d}\delta \tag{V.10}$$

where δ_f is beam deflection at complete fracture. A is the area of one free surface, and factor 2 accounts for the resulting in two complementary free surfaces. E' is taken equal to $E/(1 - \nu^2)$ for the plan strain behavior. In the case of unstable test, the toughness was calculated from the maximum applied load (P_{max}) to fracture the beam in the three-point bending and thus as in Eq. (V.11) [23].

$$K_{Ic}^{SEPB} = \frac{P}{B\sqrt{W}} Y^{*} \text{ and } Y^{*} = \frac{3}{2}\frac{S}{W}\frac{\alpha^{1/2}}{(1-\alpha)^{3/2}} f(\alpha) \quad \text{(V.11)}$$

where $f(\alpha) = A_0 + A_1\alpha + A_2\alpha^2 + A_3\alpha^3 + A_4\alpha^4 + A_5\alpha^5$. The ($A_0$, A_1, A_2, A_3, A_4, A_5) coefficients are equal to (1.9109, −5.1552, 12.6880, −19.5736, 15.9377, −5.1454) respectively in the case where $S/W = 5$ and (1.9322, −5.1007, 12.3621, −19.0071, 15.4677, −4.9913) in the case where $S/W = 7$.

The theoretical value for toughness ($K_{Ic}^{the.}$) was calculated by means of Eq. (V.10), using experimental values for the elastic moduli and from an estimation of the theoretical fracture surface energy ($\gamma_{the.}$) based on the interatomic bond strength and the bond concentration along a fracture surface, assumed to follow the easiest path [21]. In the case of a multi-constituent material, the relevant bond strength (U_{0total}) is calculated by estimation the elementary bond density along with the fracture path. Let x_i be the i^{th} stoichiometric fraction of the main atom in a unit (taken as the central atom in tetrahedral units; for instance Si in SiO_2, C in SiC where CSi_4 units form, Hf in HfO_2 and Zr in ZrO_2), U_{0i} be the i^{th} bonding energy that bonds the main atoms to the other atom in the unit, and n_i be the number of the i^{th} bonds supposed to occur along with the fracture path. Then, U_{0total} is expressed as,

$$U_{0total} = \sum_i x_i n_i U_{oi} \quad (12)$$

The volume concentration (ρ_v) of the gram-atom of the glass ceramics is equal to $(\rho/M_0)\mathcal{N}$, where ρ is the glass ceramic density, M_0 is the molar mass, and $\mathcal{N}$ is the Avogadro number. The surface concentration (ρ_s) and theoretical fracture surface energy ($\gamma_{the.}$) are then expressed as,

$$\rho_s = \left(\frac{\rho}{M_0}\mathcal{N}\right)^{2/3} \quad \text{(V.13)}$$

$$\gamma_{the.} = \frac{1}{2}\rho_s U_{0total} \cdot \mathcal{N}^{-1}\ , \quad \text{(V.14)}$$

where the 1/2 pre-factor on the right-hand side member accounts for the fact that fracture produces two complementary surfaces. In the first approach, we assume that the presence of carbon and MO_x defines the structure of the materials. Containing less than 1 vol. % of carbon, sample C1-SiOC can be depicted as a two-phase composite where β-SiC nanoparticles are dispersed in the continuous silica matrix and between β-SiC and silica, there is an interface consisting of mixed-bonds $SiO_{4-x}C_x$ tetrahedral [3,13,15]. On the other hand, the C12-SiOC with 12 vol. % of carbon is depicted as a three-phase composite where sp^2-hybridized segregated carbon and β-SiC are embedded in the glassy SiO_2 matrix. Interfaces between carbon and silica are the mixed-bonds $SiO_{4-x}C_x$ [24]. The β-SiC nanoparticles exist in smaller amount in the glass matrix as 1) in C12-SiOC there are SiC 5 vol. % less than that in C1-SiOC and 2) the mixed-bonds $SiO_{4-x}C_x$ along sp^2-hybridized segregated

carbon consume a few of Si-C bonds. SiMOCs can be regarded as four-phase composite with smaller amount of β-SiC and sp²-hybridized carbon in comparison to C12-SiOC. Using this picture, a crack is supposed to proceed through different tetrahedral units namely SiO_4 and $SiO_{x-4}C_x$, polygonal unit namely HfO_8 or ZrO_8, and the segregated carbon layers (turbostratic carbon, sp^2-hybridized).

Indeed, U_{0i} (Eq. (V.12)) is never accurately known. Nevertheless, the approach was previously shown in [21] to provide sound values for $\gamma_{the.}$, and further for K_{Ic}, with an excellent agreement with experimental values obtained from self-consistent method such as the SEPB ones. In this study U_{0i} was taken as the fission enthalpy associated with the diatomic molecules, where the thermo-chemical characteristics were taken from ref. [25]. For example, U_{0total} of SiHfOC was calculated using Eq. (V.12) considering that one Si−O, one Si−C, one Hf−O and one C=C were broken per $Si-O_{4/2}$, $Si-O_x-C_{4-x}$, $Hf-O_{8/2}$ polygonal unit and C=C bond (**Fig. V.4**), respectively; it means that n_i = 1 for $Si-O_{4/2}$, $Si-O_x-C_{4-x}$[†] and $Hf-O_{8/2}$ and C=C. The stoichiometric fraction of the elementary relevant unit (centered on the so-called "main" atoms) is calculated from the molar fraction. This gives x_i = 0.254, 0.054, 0.075 and 0.020 for $Si-O_{4/2}$, $Si-C_{4/2}$, $Hf-O_{8/2}$ and C=C, respectively. With diatomic bond energy (the choice for the diatomic value was discussed in [21]) of 799.6, 447, 801 and 2×614 kJ·mol^{-1} for the Si−O, Si−C, Hf−O and C=C bonds, respectively, this gives a U_{0total} value of 333 kJ·mol^{-1}. To calculate $\gamma_{the.}$ using Eq. (V.14), it is necessary to calculate ρ_s using Eq. (V.13). With a density of 2.63 g·cm^{-3} and a gram-atom weight of 22.21 g·mol^{-1} for SiHfOC ($Si_{0.31}Hf_{0.02}O_{0.54}C_{0.13}$), a value of 1.72×10^{19} m^{-2} for ρ_s of the gram-atom unit. Values of 4.75 J·m^{-2} for $\gamma_{the.}$ and 0.92 MPa·m$^{-0.5}$ for $K_{the.}$ were then calculated by means of Eq. (V.14) and Eq. (V.9), respectively.

V.4 Results

The mechanical properties of the investigated glass ceramic materials are given in **Table V.2**. The density of C1-SiOC is larger than the one of C12-SiOC. This is likely because the C12-SiOC has more C_{free} than C1-SiOC (i.e. C1-SiOC has more SiC) and carbon density (ρ_C = 1.4-2 g·cm^{-3}) is lower than SiC density (ρ_{SiC} = 3.21 g·cm^{-3}). Similarly, the density of SiHfOC is larger in comparison to sample SiZrOC as the density of crystalline HfO_2 (ρ_{HfO2} = 9.68 g·cm^{-3}) is higher than that of crystalline ZrO_2 (ρ_{ZrO2} = 5.68 g·cm^{-3}). There are only small differences in the elastic moduli between the four glass ceramics. It is noteworthy that in the case of C1-SiOC, E as measured by resonance frequencies is a bit larger than as measured by ultrasonic echography, and both C1-SiOC

[†] x is in between 0 and 3. We assume that the crack will break Si−C bond (BDE = 447 kJ/mol) rather than Si−O bond (BDE = 799.6 kJ/mol).

and C12-SiOC have *v* as low as that of silica glass. This can be explained by the large fraction of amorphous silica in these two glass ceramics. Regarding hardness, C1-SiOC shows an increased value as compared to that of silica and this can be correlated to the reinforcing effect of the 16.8 vol% SiC hard nanoparticles present in the silica matrix. The decrease in SiC volume fraction (from 16.8 to 12.3 vol%) as well as the introduction of segregated carbon (11.9 vol%) induces a decrease of the hardness in C12-SiOC (as compared to C1-SiOC) and pushes it back to the level of silica. K_{Ic}^{VIF} is much greater than K_{Ic}^{SEPB}. It is very likely that densification, which occurs to a great extent in the present materials, impedes (prevents) the dissipation of the mechanical energy through crack formation. A large fraction of the mechanical energy is spread in the densification process that is not taken into account in Eq. 8. Vickers indentations, obtained with a 9.8 N load, are shown in Table 2. K_{Ic}^{SEPB} and $K_{Ic}^{the.}$ are in good agreement.

Table 2: Mechanical properties of the investigated glass ceramics. Average ± standard deviation. Values without standard deviation are either purely theoretical or estimated from a single measurement. Number of tests is in bracket. nm = not measured.

Properties	**C1-SiOC**	**C12-SiOC**	**SiHfOC**	**SiZrOC**
ρ [g.cm^{-3}]	2.38± 0.01 (3)	2.30 ± 0.01 (3)	2.63 ± 0.02 (3)	2.54 ± 0.02 (3)
E [GPa]	96.70	88.13 ± 0.68 (3)	nm	85.39 ± 0.98 (3)
G [GPa]	40.97	37.66 ± 0.33 (3)	nm	35.29 ± 0.48 (3)
K [GPa]	50.36	44.51 ± 0.24 (3)	nm	49.07 ± 0.34 (3)
v	0.18	0.17 ± 0.02 (3)	nm	0.21 ± 0.02 (3)
E' [GPa]	99.94	90.75 ± 0.68 (3)	nm	89.33 ± 0.98 (3)
H [GPa]	10.50 ± 0.37 (5)	6.29 ± 0.37 (5)	9.88 ± 1.50 (5)	9.63 ± 0.97 (5)
γ_{SEPB} [J·m^{-2}]	2.68	3.54 ± 0.35 (3)	6.95	5.43 ± 0.64 (2)
$\gamma_{the.}$ [J·m^{-2}]	3.71	5.71	4.75	4.66
K_{Ic}^{VIF} [MPa·m$^{-0.5}$]	2.08 ± 0.12 (5)	1.35 ± 0.04 (5)	1.55 ± 0.38 (5)	1.56 ± 0.18 (5)
K_{Ic}^{SEPB} [MPa·m$^{-0.5}$]	0.73	0.99 ± 0.02 (3)	0.99 ± 0.01 (3)	0.91 ± 0.04 (3)
$K_{Ic}^{the.}$ [MPa·m$^{-0.5}$]	0.86	1.02	0.92	0.91

V.5 Discussion

Glasses contain some free volume, to an extent that scales with the quenching rate from the melting temperature. The free volume provides some room for a densification process under hydrostatic pressure. For instance, a density change as large as 21 % is achieved in amorphous silica at pressure above 20 GPa [26]. Large hydrostatic pressure develops beneath the indenter upon sharp contact loading. As a matter of fact, the contribution of densification to the permanent deformation

(imprint) observed after complete unloading is as large as 80 to 90 % for a SiO_2 (~ 60 to 70 % for a soda-lime-silica glass) [27]. Densification in glass was found to correlate with Poisson's ratio [26–30]. Densification is favored in glasses exhibiting small ν values, such as amorphous silica (ν ~ 0.16) and silica-rich glass, as opposed to precious metal based metallic glasses for instance (ν ~ 0.4). Indeed, densification significantly reduces the residual stress that arises at the indentation site and contributes to the indentation cracking. The occurrence of densification is thus a major obstacle to the assessment of K_{Ic} by the indentation cracking methods, where the deformation is assumed to be isochoric [27,31]. In this study, C1-SiOC (silica-rich), with ν ~ 0.18, shows a similar surface cracking indentation pattern to that of silica glass, and its K_{Ic} calculated from Vickers indentation cracking methods is greatly overestimated. Similar discrepancies were reported recently by comparing K_{Ic} as obtained by means of differences methods (including indentation) for a borosilicate glass (Borofloat 33) with ν ~ 0.20 [20]. In the elastic-plastic stress analysis used by Lawn et al. [31], which is inspired by the Hill's inclusion approach, the relation between the plastic zone size (e) and the materials characteristics (E, H) is expressed as $e/d \propto (E/H)^{0.5}$, where d is the indentation diagonal. This relation derives from the assumption that the indentation volume (V_i^-) is totally distributed, uniformly, along the border of the plastic zone (volume V_p), inducing a strain scaling with V_i^-/V_p, and further a stress $E \cdot V_i^-/V_p$. A more suitable approach consists in accounting for densification (and pile-up) in the mechanical analysis, and following the method proposed by Yoffe (Love-Yoffe-Boussinesq) model.

At this stage one suitable tool allows characterizing the crack path at the atomic scale, and further investigates the physics and the chemistry of the cracking process, especially for complex chemical system. In this study we attempted to make a schematic drawing accounting for the available structural information and assuming that a crack tends to follow the easiest path (most favorable from an energy point of view). This model explains the good agreement between K_{Ic}^{SEPB} and $K_{Ic}^{the.}$. In MK-SiOC, there are 12 vol.% of segregated carbon and 12 vol.% of SiC. It is proposed that the interface SiC/SiO_2 is consisting of remaining mixed-bond $SiO_{4-x}C_x$ tetrahedra, whereas segregated carbon and silica matrix share a few mixed-bond $SiO_{4-x}C_x$ tetrahedra [3,15,32]. Hence, to finish a journey, the crack needs to travel through the silica domains, the interfaces and the segregated carbon phase as in **Fig. 4**, in which the blue dashed line is an example of the propagation path of the crack. The modification of SiOC with Hf/Zr as in SiHfOC/SiZrOC results in the decrease of the volume fraction of carbon from 12 vol.% to 6 vol.% and the existence of about 6 vol.% of HfO_2/ZrO_2. This modification enlarges the silica domains and introduces the HfO_2/ZrO_2 into these larger silica domains. In C1-SiOC, there is less than 1 vol.% of carbon, which results in

discontinuous segregated carbon phase. The energy to break through C1-SiOC is then in the same amount of that needed to break through silica glass whose fracture toughness is known to be about 0.73 MPa·$m^{0.5}$.

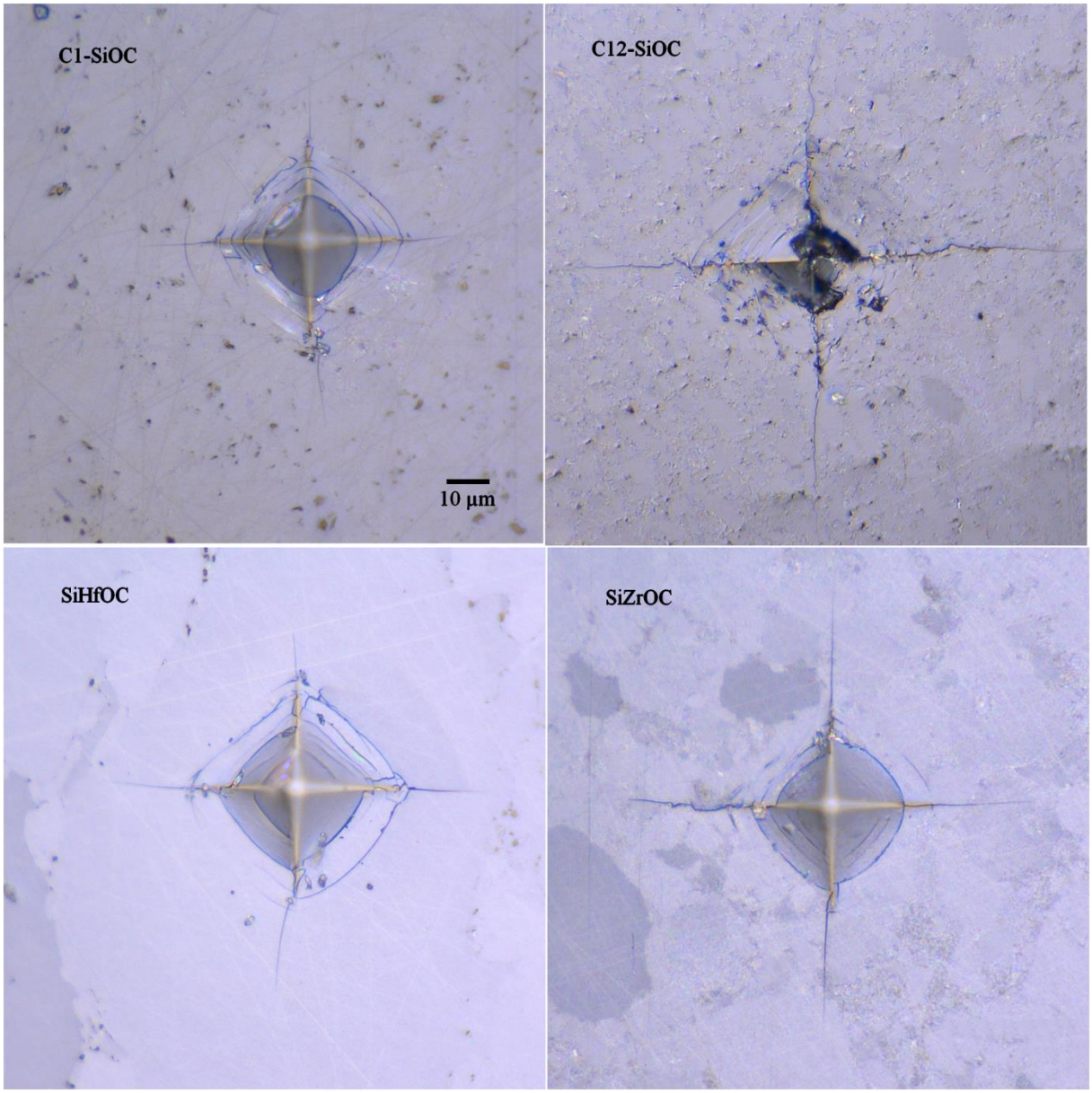

Fig. 3: Vickers indentation (9.8 N) of C1-SiOC, C12-SiOC, SiHfOC and SiZrOC.

V.6 Conclusion

In the present study, the impacts of varying amounts of segregated carbon and of zirconium and hafnium modification on the fracture behavior of SiOC glass ceramics were investigated by means of a self-consistent method (SEPB). The fracture toughness value obtained from the experiment was compared to that obtained from the theory by assuming that the crack goes through the weakest bonds in the glass ceramic system. The toughness from the two methods has a good agreement. By presenting 12 vol.% of segregated carbon into the glass ceramic (< 1 vol.% for C1-SiOC to 12

vol.% for C12-SiOC), the fracture toughness increases from about 0.7 MPa·m$^{0.5}$ to about 1 MPa·m$^{0.5}$. The incorporation of HfO_2/ZrO_2 (about 5 vol.%) into the SiOC glass ceramics shows the same increase in the toughness. The conclusion of the modification should be further investigated with greater amount of HfO_2/ZrO_2.

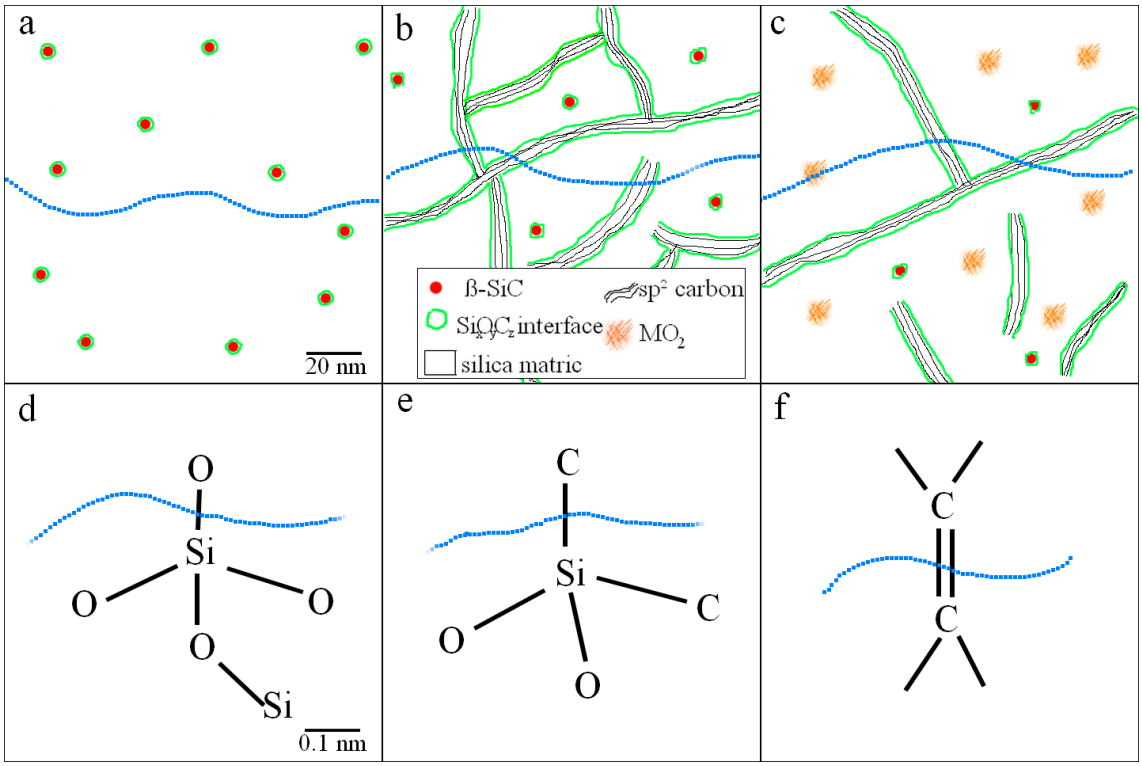

Fig. 4: Tentative schematic drawing of the atomic organization (structural model) together with the predicted crack path (blue dashed line) for a vertical tensile loading axis. a) C1-SiOC; b) C12-SiOC; c) SiMOC; d) the SiO_4; e) the SiO_2C_2 and f) the C=C. The carbon content in the C1-SiOC grade is < 1 vol% and is thus not depicted in the drawing. In the case of the C12-SiOC grade, the silica domains are enclosed by carbon network and Si-O-C bonds (between carbon and silica). In the case of SiMOC, there are HfO_2/ZrO_2 in the silica domains.

V.7 References

[1] G.D. Sorarù, E. Dallapiccola, G. D'Andrea, Mechanical Characterization of Sol--Gel-Derived Silicon Oxycarbide Glasses, J. Am. Ceram. Soc. 79 (1996) 2074–2080.

[2] T. Rouxel, G.-D. Soraru, J. Vicens, Creep Viscosity and Stress Relaxation of Gel-Derived Silicon Oxycarbide Glasses, J. Am. Ceram. Soc. 84 (2001) 1052–1058.

[3] H.-J. Kleebe, C. Turquat, G.D. Sorarù, Phase Separation in an SiCO Glass Studied by Transmission Electron Microscopy and Electron Energy-Loss Spectroscopy, J. Am. Ceram. Soc. 84 (2001) 1073–1080.

[4] P. Colombo, G. Mera, R. Riedel, G.D. Soraru, Polymer-derived ceramics: 40 years of research and innovation in advanced ceramics, J. Am. Ceram. Soc. 93 (2010) 1805–1837.

[5] C. Stabler, E. Ionescu, M. Graczyk-Zajac, I. Gonzalo-Juan, R. Riedel, Silicon oxycarbide glasses and glass-ceramics:"All-Rounder" materials for advanced structural and functional applications, J. Am. Ceram. Soc. 101 (2018) 4817–4856.

[6] E. Ionescu, C. Terzioglu, C. Linck, J. Kaspar, A. Navrotsky, R. Riedel, Thermodynamic Control of Phase Composition and Crystallization of Metal-Modified Silicon Oxycarbides, J. Am. Ceram. Soc. 96 (2013) 1899–1903.

[7] S.J. Widgeon, S. Sen, G. Mera, E. Ionescu, R. Riedel, A. Navrotsky, 29Si and 13C solid-state NMR spectroscopic study of nanometer-scale structure and mass fractal characteristics of amorphous polymer derived silicon oxycarbide ceramics, Chem. Mater. 22 (2010) 6221–6228.

[8] F. Rosenburg, E. Ionescu, N. Nicoloso, R. Riedel, High-Temperature Raman Spectroscopy of Nano-Crystalline Carbon in Silicon Oxycarbide, Materials (Basel). 11 (2018) 93.

[9] L. Bois, J. Maquet, F. Babonneau, D. Bahloul, Structural characterization of sol-gel derived oxycarbide glasses. 2. Study of the thermal stability of the silicon oxycarbide phase, Chem. Mater. 7 (1995) 975–981.

[10] G.D. Soraru, G. D'andrea, R. Campostrini, F. Babonneau, G. Mariotto, Structural Characterization and High-Temperature Behavior of Silicon Oxycarbide Glasses Prepared from Sol-Gel Precursors Containing Si-H Bonds, J. Am. Ceram. Soc. 78 (1995) 379–387.

[11] C. Stabler, A. Reitz, P. Stein, B. Albert, R. Riedel, E. Ionescu, Thermal Properties of SiOC Glasses and Glass Ceramics at Elevated Temperatures, Materials (Basel). 11 (2018).

[12] G.M. Renlund, S. Prochazka, R.H. Doremus, Silicon oxycarbide glasses: Part II. Structure and properties, J. Mater. Res. 6 (1991) 2723–2734.

[13] B. Papendorf, E. Ionescu, H.-J. Kleebe, C. Linck, O. Guillon, K. Nonnenmacher, R. Riedel, High-Temperature Creep Behavior of Dense SiOC-Based Ceramic Nanocomposites: Microstructural and Phase Composition Effects, J. Am. Ceram. Soc. 96 (2013) 272–280.

[14] E. Ionescu, C. Balan, H.-J. Kleebe, M.M. Müller, O. Guillon, D. Schliephake, M. Heilmaier, R. Riedel, High-Temperature Creep Behavior of SiOC Glass-Ceramics: Influence of Network Carbon Versus Segregated Carbon, J. Am. Ceram. Soc. 97 (2014) 3935–3942.

[15] C. Stabler, F. Roth, M. Narisawa, D. Schliephake, M. Heilmaier, S. Lauterbach, H.-J. Kleebe, R. Riedel, E. Ionescu, High-temperature creep behavior of a SiOC glass ceramic free of segregated carbon, J. Eur. Ceram. Soc. 36 (2016) 3747–3753.

[16] E. Ionescu, H.-J. Kleebe, R. Riedel, Silicon-containing polymer-derived ceramic nanocomposites (PDC-NCs): Preparative approaches and properties, Chem. Soc. Rev. 41 (2012) 5032–5052.

[17] E. Ionescu, C. Linck, C. Fasel, M. Müller, H.--J. Kleebe, R. Riedel, Polymer-Derived SiOC/ZrO2 Ceramic Nanocomposites with Excellent High-Temperature Stability, J. Am. Ceram. Soc. 93 (2010) 241–250.

[18] G.R. Anstis, P. Chantikul, B.R. Lawn, D.B. Marshall, A critical evaluation of indentation techniques for measuring fracture toughness: I, direct crack measurements, J. Am. Ceram. Soc. 64 (1981) 533–538.

[19] T. Nose, T. Fujii, Evaluation of Fracture Toughness for Ceramic Materials by a Single Edge

Precracked Beam Method, J. Am. Ceram. Soc. 71 (1988) 328–333.

[20] T. To, F. Célarié, C. Roux-Langlois, A. Bazin, Y. Gueguen, H. Orain, M. Le Fur, V. Burgaud, T. Rouxel, Fracture toughness, fracture energy and slow crack growth of glass as investigated by the Single-Edge Precracked Beam (SEPB) and Chevron-Notched Beam (CNB) methods, Acta Mater. 146 (2018) 1–11.

[21] T. Rouxel, Fracture surface energy and toughness of inorganic glasses, Scr. Mater. 137 (2017) 109–113.

[22] ASTM C1421-10, Standard Test Methods for Determination of Fracture Toughness of Advanced Ceramics at Ambient Temperature, ASTM International, West Conshohocken, PA, (2010).

[23] I. Bar On, F.I. Baratta, K. Cho, Crack Stability and Its Effect on Fracture Toughness of Hot Pressed Silicon Nitride Beam Specimens, J. Am. Ceram. Soc. 79 (1996) 2300–2308.

[24] M. Graczyk-Zajac, D. Vrankovic, P. Waleska, C. Hess, P.V. Sasikumar, S. Lauterbach, H.-J. Kleebe, G.D. Sorarù, The Li-storage capacity of SiOC glasses with and without mixed silicon oxycarbide bonds, J. Mater. Chem. A. 6 (2018) 93–103.

[25] D.R. Lide, Handbook of Chemistry and Physics, 86th edn. CRC, (2005).

[26] T. Rouxel, H. Ji, T. Hammouda, A. Moréac, Poisson's ratio and the densification of glass under high pressure, Phys. Rev. Lett. 100 (2008) 225501.

[27] T. Rouxel, Driving force for indentation cracking in glass: composition, pressure and temperature dependence, Phil. Trans. R. Soc. A. 373 (2015) 20140140.

[28] P. Sellappan, T. Rouxel, F. Celarie, E. Becker, P. Houizot, R. Conradt, Composition dependence of indentation deformation and indentation cracking in glass, Acta Mater. 61 (2013) 5949–5965.

[29] S. Yoshida, J.-C. Sanglebœuf, T. Rouxel, Indentation-induced densification of soda-lime silicate glass, Int. J. Mater. Res. 98 (2007) 360–364.

[30] S. Yoshida, J.-C. Sangleboeuf, T. Rouxel, Quantitative evaluation of indentation-induced densification in glass, J. Mater. Res. 20 (2005) 3404–3412.

[31] B.R. Lawn, A.G. Evans, D.B. Marshall, Elastic/plastic indentation damage in ceramics: the median/radial crack system, J. Am. Ceram. Soc. 63 (1980) 574–581.

[32] P. Kroll, Searching insight into the atomistic structure of SiCO ceramics, J. Mater. Chem. 20 (2010) 10528–10534.

VI. Temperature and environment dependence of K_{Ic} of glass

VI.1 Abstract

The fracture toughness (K_{Ic}) of glass with different compositions was measured by means of the single-edge precracked beam (SEPB) method. The temperature dependence of K_{Ic} was investigated by performing the up to 800 °C in air, with a loading rate of 10 MPa·√m·s^{-1}. The influence of the environment was studied at room temperature, performing both precracking and final fracture stages in a glass box (dry argon gas), and by comparison of the results attained in ambient atmosphere (relative humidity of about 60 %).

Keywords: Fracture toughness, single-edge precracked beam (SEPB), temperature dependence, environment dependence

VI.2 Introduction

The temperature and environment dependences of the fracture behaviour of glass is not well understood, and were investigated in a very limited number of publications, mostly focused on ceramics concerning the effect of temperature [1–8], and a-SiO_2 and window glass for the incidence of humidity [9–11]. Single-edge precrack beam (SEPB) is a reliable and self-consistent method to measure the fracture toughness of brittle materials [12–15]. However, to the best of our knowledge, the SEPB method was never performed at elevated temperature or in a glove box.

The present study focuses on 1) applying the SEPB method on glasses at different temperature up to 1.11T_g and compare to previously published reports and 2) performing the SEPB method (precracking and final fracture) in controlled atmosphere, especially in dry argon gas. SEPB tests were already performed with the final fracture step in dry N_2 atmosphere in previous works [14,16], but this is the first time that both precracking and bending steps were performed in a humidity-controlled atmosphere.

Regarding the temperature dependence, fracture toughness was measured from room temperature to 1.11T_g for two glasses in SiO_2-CaO-Na_2O and SiO_2-MgO-Na_2O chemical systems. As far as relatively small loading rates are applied (quasi-static regime), typically for $dK_I/dt \leq 10$ MPa·√m·s^{-1}, which corresponds to strain-rates, $\dot{\varepsilon}$, below 10^{-2}·s^{-1}, the brittle to ductile transition temperature is expected to be at around T_g. For environment dependence, the fracture toughness of four commercial glasses was studied in controlled atmosphere. Cross-head speeds as small as 0.01 µm/s and as large as 15 µm/s were applied during the SEPB bending experiment to investigate the

This chapter is a manuscript prepared for publication as T. To, F. Célarié, Y. Gueguen, N'G. Brou, V. Burgaud, M.l Le Fur, J. Chollet, H. Orain, T. Rouxel, (2019)

possible influence of the crack velocity. Finally, the results from the previously published "unstable" test (the unloading curve is continue from maximum load) in the ambient atmosphere and the test with only the final fracture stage in dry N_2 atmosphere from the literatures, and the present results in this study (both precracking and final fracture steps in dry argon atmosphere) were compared.

VI.3 Experimental Procedures

VI.3.a. K_{Ic} at elevated temperatures

Table VI.1: Compositions, mechanical properties and transition temperatures of studied glasses; [1)]Standard window glass, St-Gobain company; [2)]Silicon oxy-nitrite glass

Glass	**compositions**	***E* (GPa)**	***v***	***G* (GPa)**	**T_g (K)**
SiNaMgO	$SiO_2(80)Na_2O(14)MgO(6)$	66	0.17	28	773
Planilux[1)]	$SiO_2(71)Na_2O(13)MgO(6)CaO(10)$	72	0.23	29	813
N-Glass[2)]	$SiO_2(56)Al_2O_3(14)Y_2O_3(24)Si_3N_4(10)$	137	0.29	53	1207

K_{Ic} of three different glass compositions, with three different glass transition temperatures (T_g) as shown in **Table V.1,** were investigated by means of the SEPB method at elevated temperatures. The temperatures that were selected according to the T_g of the investigated glasses are room temperature (291 K = $0.35T_g$), $0.93T_g$, T_g, $1.03T_g$, $1.05T_g$, $1.07T_g$ and $1.11T_g$. In order to use the SEPB technique, parallelepiped bars were cut from glass batches using a diamond saw to get 3 × 4 × 20 mm^3 bars and polished down to 3 µm diamond paste. A series of 10 N Vickers indents, each 200 µm apart from the adjacent ones, were aligned at the center of the 3 × 20 mm^2 tensile face, along with broadness (B = 3 mm) as detailed in Ref. [15]. The bar specimens were then positioned in bridge-flexure anvil [17] to produce precracks as long as about half of the specimen width (W = 4 mm). The precracked specimens were finally fractured at elevated temperatures with a three-point bending device made of aluminum with a span length of 15 mm. A heating rate of 12 $K \cdot min^{-1}$ was used and a thermocouple was positioned close to the precracked specimens to measure the actual specimen temperature in-situ before fracture. After, the fracture specimens were cooled down to room temperature, the precrack length was measured (fractography), and K_{Ic} was calculated from the maximum load [15]. All experiments were conducted in ambient atmosphere (~ 60 %) with the cross-head speed of 15 $\mu m \cdot s^{-1}$ (loading rate of about 10 $MPa\sqrt{m} \cdot s^{-1}$), and the test temperature was known with an accuracy better than ± 1 K.

VI.3.b. K_{Ic} in argon gas atmosphere

Table VI.2: Compositions and mechanical properties of studied glasses

Glass	**Composition**	**E (GPa)**	**v**	**G (GPa)**
Planilux	SiO_2(71)Na_2O(13)MgO(6)CaO(10)	72 ± 2	0.23 ± 0.01	46 ± 2
Silice	SiO_2 (100)	70 ± 2	0.15 ± 0.01	30 ± 2
Borofloat 33	SiO_2(81)Na_2O(4)B_2O_3(13)Al_2O_3(2)	64 ± 2	0.20 ± 0.01	27 ± 2
BK7	SiO_2(70)Na_2O(9)B_2O_3(11)BaO(2)K_2O(8)	82 ± 2	0.21 ± 0.01	34 ± 2

Fig. VI.1: Argon gas box with gloves

In order to study the environmental effects, and more specifically the effect of humidity, three glass compositions were chosen and further characterized both in dry argon gas (T = 20 °C; RH ~ 0) and in ambient atmosphere (T = 20 °C; RH = 60 %). The experimental protocol for the SEPB technique in ambient condition was detailed in Ref. [15]. In the case of experiments conducted in dry argon gas, both precrack and final fracture steps were performed in a glove box filled with high purity dry argon. After indentation in the ambient conditions (to ease the precrack formation), the bar specimens were placed in the glove box (**Fig. VI.1**) and positioned in the anvil and loaded by means of a portable uniaxial testing machine (Deben, UK). During the precracking stage, a camera was used and focused on the middle of the specimen (where indentation was performed) to observe the pop-in of the precrack. The machine was manually stopped once the precrack appeared. The precracked specimens were then positioned in a three-point bending device with a span length of 15 mm, and the load was monitored by means of a 50N capacity load cell (K25, Scaime company, France) with an accuracy better than 0.02 N. The broken specimens were then taken out of the argon gas box to measure the precrack length and fracture toughness was calculated from the maximum load and the measured precrack length using Eq. (VI.5) in Ref. [15]. In the ambient

conditions (RH = 60 %), To *et al.* have shown that, with their stiff testing apparatus (6.7 $MN \cdot m^{-1}$), unstable test result is independent of slow crack growth as it is corresponding to high crack velocity. In order to produce the unstable test in the ambient conditions, a cross-head speed of 15 $\mu m \cdot s^{-1}$ was used. The cross-head speed for the experiments in the glove box was set at 0.05 µm/s, but for 1 extra experiment conducted on a Planilux with the cross-head speed of 5 µm/s (100 times faster than for other experiments) for comparison.

VI.4 Results

VI.4.a. Temperature dependence of K_{Ic}

Table VI.3: Fracture toughness and relative temperatures; K_{Ic} is in $MPa \cdot \sqrt{m}$.

T/T_g	0.35	0.93	1	1.03	1.05	1.07	1.11
K_{Ic}(Planilux)	0.73	0.66	0.64	0.63	0.63	/	/
K_{Ic}(SiNiMgO)	0.7	/	0.68	/	/	0.62	0.73

The dependence of K_{Ic} on temperature is illustrated in **Fig. VI.2** (data in **Table VI.2**). At high temperature, viscous flow induces same energy dissipation, hence reducing the energy available for the crack propagation. As a result, the experimental values for K_{Ic} are no longer intrinsic. Recall that K_{Ic} is related to Young's modulus and to the intrinsic fracture surface energy, γ_c, following:

$$K_{Ic}^{intrinsic} = \sqrt{2\gamma_c E'}, \quad (4.1)$$

where $E' = E$ in plane stress and $E' = E/(1-\nu^2)$ in plane strain, than, since both E' and γ are expected to decrease was the temperature is increased, K_{Ic} is also expected to decrease. This is actually the observed tendency from RT to ~$0.8T_g$. However, experimental investigation reported on glasses mostly show a rapid increase of K_{Ic} above T_g [10,11,18], but for fused silica glass [9,10]. This is because glasses do not behave in a purely elastic manner anymore! Actually, above $0.8T_g$, K_{Ic} becomes also loading-rate dependent. A transition temperature is observed above which some viscous relaxation and some crack tip blunting occur: this is the brittle-ductile transition (BDT) [11]. The loading rate dependence of the effective fracture toughness ($K_{Ic}(T)/K_{Ic}(T_{RT})$) is illustrated in **Fig. VI.2**. With a loading rate of 2 $MPa\sqrt{m}/s$, the BDT of SLS glass is at ~$0.89T_g$ and with a loading rate of 4 $MPa\sqrt{m}/s$, it is at ~$0.97T_g$ [11]. With the loading rates of 5 and 8 $MPa\sqrt{m}/s$, the BDT is at ~T_g [10,11]. With the loading rate of 10 $MPa\sqrt{m}/s$, the BDT of SLS (more particularly Planilux) could not be detected. However, the BDT of SiNaMgO is at ~$1.07T_g$ as shown in Table 2 and **Fig. VI.2**. From RT to ~$1.07T_g$, K_{Ic} of SiNaMgO slightly decreases, whereas from ~$1.07T_g$ to

~1.11T_g, K_{Ic} slightly increases, and at above 1.11T_g, there is no available data due to the limited number of specimens.

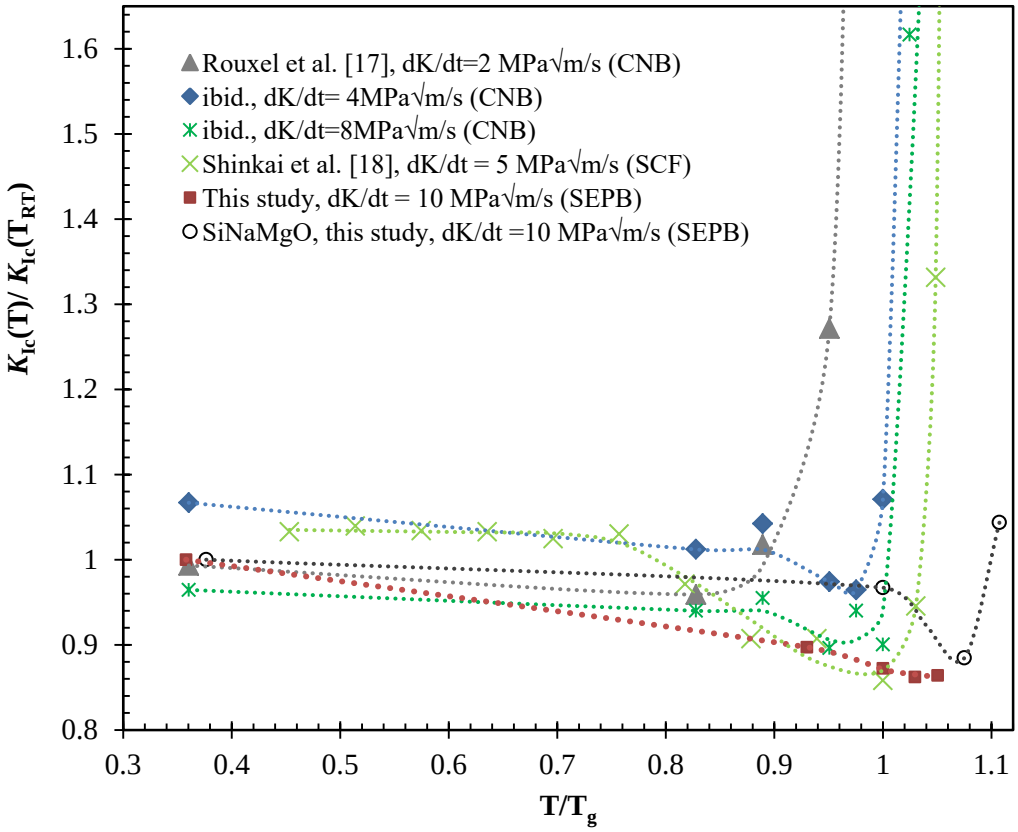

Fig. VI.2: Temperature dependence of the apparent fracture toughness of soda-lime-silica (all data except the orange circle) and SiNaMgO (the orange circle) glasses. Rouxel et al. [11] used chevron-notched beam (CNB) method and Shinkai et al. used surface crack in flexure (SCF) method [10].

VI.4.b. **Environment dependence of K_{Ic}**

Table VI.4: Cross-head speed dependence of K_{Ic} of Planilux in argon and ambient atmospheres

Argon atmosphere		**Ambient atmosphere**	
Cross-head speed (µm/s)	K_{Ic} (MPa.√m)	Cross-head speed (µm/s)	K_{Ic} (MPa.√m)
0.05	0.71 ± 0.03	< 0.3 (stable test)	0.55 ± 0.02 [15]
5	0.70 ± 0.02	> 1 (unstable test)	0.70 ± 0.01 [15]

The cross-head speed dependence of K_{Ic} of Planilux (a soda-lime-silicate glass (SLS)) is shown in Table 3. In ambient conditions, the results of the experimented K_{Ic} depend much on the cross-head speed. With the cross-head speed of lower than 0.3 µm/s, the test is stable and the K_{Ic} of glass is 0.55 MPa√m. On the other hand, with the cross-head speed of above 1 µm/s, the test is unstable and the K_{Ic} of glass is as high as 0.7 MPa√m. The unstable test was shown to have the crack velocity

fast enough to result in the K_{Ic} independent of stress corrosion (in the region 3 of the Wiederhorn v-K curve [19]) [15]. Besides, the dependence is not found in case of the experiment performed in the argon atmosphere. The K_{Ic} of the glass is 0.70 ± 0.02 MPa√m with the cross-head speed of 5 µm/s, and 0.71 ± 0.03 MPa√m with the cross-head speed of 100 times slower (0.05 µm/s). It can be concluded that there is no stress corrosion phenomenon in the dry argon atmosphere.

Table VI.5: Fracture toughness of glass by SEPB and theoretical prediction

Materials	**K_{Ic} (MPa. $\sqrt{m}$) by means of SEPB method and Theoretical values**			
	Dry Argon atmosphere	Ambient atmosphere (Instable experiment)	Dry N_2 atmosphere [14] (4-point bending)	Theoretical values (Eq.4.1)
Planilux	0.71 ± 0.03	0.70 ± 0.01 [15]	0.76 ± 0.03	0.72 ± 0.01
Silice	0.68 ± 0.04	0.69 ± 0.02	0.78 ± 0.06	0.72 ± 0.01
Borofloat 33	0.66 ± 0.02	0.65 ± 0.03 [15]	0.71 ± 0.03	0.73 ± 0.02
BK7	0.81 ± 0.03	0.82 ± 0.02	0.92 ± 0.05	0.85 ± 0.01

The comparison of fracture toughness measured by means of SEPB in different atmosphere together with the predicted values from theory (follow the concept in Ref. [12]) is shown in **Table VI.4**. The K_{Ic} values of all the four studied glasses measured in the argon atmosphere are in good agreement to those measured in the ambient atmosphere with unstable test and to those measured in N_2 atmosphere. Moreover these experimental values are in good agreement to the theoretical values predicted from the diatomic energy. It is noteworthy to say that the average values measured in N_2 atmosphere is slightly smaller than the other values in Table 4. This might result from the use of the 4-point bending device (in [14]) instead of the 3-point bending one (in this study).Recall that Quinn et al. [14] performed only the final fracture stage in dry N_2 while both precracking and final fracture stages were performed in dry argon, this means that the experiment with only final fracture stage in the controlled atmosphere is enough to get rid of the stress corrosion. Moreover, the experiment can be done in the ambient atmosphere once the crack velocity (by modifying the cross-head speed) is high enough to position the results in the region III of the Wiederhorn's v-K curve.

VI.5 Conclusion

The temperature dependence of K_{Ic} of two glasses, and the environment dependence of K_{Ic} of four commercial glasses were studied by means of the SEPB method. Regarding the effect of the temperature, we found that with a loading rate of 10 MPa√m·s^{-1}, the transition temperature of the

studied glasses is at about $1.07T_g$. However, more experiments are needed to support these preliminary investigations. Regarding the effect of the environment, the following conclusions were drawn: 1) As long as both the precracking stage and the final fracture in bending are conducted within a on hour period, it is found sufficient to only perform the bending fracture stage in the dry atmosphere to avoid stress corrosion; 2) it is sufficient to perform the SEPB experiment in the ambient atmosphere once the cross-head speed (or crack velocity) is fast enough (e.g. $> 2.4 \times 10^{-4}$ $m \cdot s^{-1}$ for SLS glass) to have the result values in region III of the Wiederhorn's v-K curve.

VI.6 References

[1] J.B. Quinn, I.K. Lloyd, Comparison of Methods to Determine the Fracture Toughness of Three Glass-Ceramics at Elevated Temperatures, J. Am. Ceram. Soc. 83 (2000) 3070–3076.

[2] A. Ghosh, M.G. Jenkins, K.W. White, A.S. Kobayashi, R.C. Brad, Elevated-temperature fracture resistance of a sintered α-silicon carbide, J. Am. Ceram. Soc. 72 (1989) 242–247.

[3] M. Mizuno, H. Okuda, VAMAS round robin on fracture toughness of silicon nitride, J. Am. Ceram. Soc. 78 (1995) 1793–1801.

[4] T. Fett, D. Munz, Determination of fracture toughness at high temperatures after subcritical crack extension, J. Am. Ceram. Soc. 75 (1992) 3133–3136.

[5] K.D. McHenry, R.E. Tressler, Fracture Toughness and High-Temperature Slow Crack Growth inSiC, J. Am. Ceram. Soc. 63 (1980) 152–156.

[6] A. Micski, B. Bergman, High temperature strength of silicon nitride HIP-ed with low amounts of yttria or yttria/alumina, J. Eur. Ceram. Soc. 6 (1990) 291–301.

[7] J.J. Brennan, K.M. Prewo, Silicon carbide fibre reinforced glass-ceramic matrix composites exhibiting high strength and toughness, J. Mater. Sci. 17 (1982) 2371–2383.

[8] J.L. Henshall, D.J. Rowcliffe, J.W. Edington, Fracture Toughness of Single-Crystal Silicon Carbide, J. Am. Ceram. Soc. 60 (1977) 373–375.

[9] S.M. Wiederhorn, H. Johnson, A.M. Diness, A.H. Heuer, Fracture of Glass in Vacuum, J. Am. Ceram. Soc. 57 (1974) 336–341.

[10] N. Shinkai, R.C. Bradt, G.E. Rindone, Fracture toughness of fused SiO2 and float glass at elevated temperatures, J. Am. Ceram. Soc. 64 (1981) 426–430.

[11] T. Rouxel, J.-C. Sangleboeuf, The brittle to ductile transition in a soda-lime-silica glass, J. Non. Cryst. Solids. 271 (2000) 224–235.

[12] T. Rouxel, Fracture surface energy and toughness of inorganic glasses, Scr. Mater. 137 (2017) 109–113.

[13] T. Rouxel, S. Yoshida, The fracture toughness of inorganic glasses, J. Am. Ceram. Soc. 100

(2017) 4374–4396.

[14] G.D. Quinn, J.J. Swab, Fracture toughness of glasses as measured by the SCF and SEPB methods, J. Eur. Ceram. Soc. 37 (2017) 4243–4257.

[15] T. To, F. Célarié, C. Roux-Langlois, A. Bazin, Y. Gueguen, H. Orain, M. Le Fur, V. Burgaud, T. Rouxel, Fracture toughness, fracture energy and slow crack growth of glass as investigated by the Single-Edge Precracked Beam (SEPB) and Chevron-Notched Beam (CNB) methods, Acta Mater. 146 (2018) 1–11.

[16] J.A. Salem, Transparent armor ceramics as spacecraft windows, J. Am. Ceram. Soc. 96 (2013) 281–289.

[17] T. Nose, T. Fujii, Evaluation of Fracture Toughness for Ceramic Materials by a Single Edge Precracked Beam Method, J. Am. Ceram. Soc. 71 (1988) 328–333.

[18] Q. Zheng, Y. Yue, J.C. Mauro, Density of topological constraints as a metric for predicting glass hardness, Appl. Phys. Lett. 111 (2017) 011907-1–5.

[19] S.M. Wiederhorn, Influence of Water Vapor on Crack Propagation in Soda Lime Glass, J. Am. Ceram. Soc. 50 (1967) 407–414.

VII. Concluding remarks

VII.1. Conclusions

Most effort in this thesis is devoted to the determination of fracture toughness and fracture surface energy of glasses. Self and non-self consistent methods to determine these parameters are presented in chapter 2 and 3 (paper I and II). Chapter 4 and 5 (paper III and IV) focuses on composition dependence of fracture toughness and chapter 6 (paper V) focuses on temperature and environment dependence.

VII.1.a. Surface flaw, strength and fracture toughness

The experimented strength of glass is not intrinsic, but dependent on the size of the surface flaw. A window float glass, with the as-fabricated surfaces, has the size of the critical flaw (tin side) of about 8 to 12 µm as estimated by biaxial flexure test on 35 mm diameter disks. Fused silica glass, with a surface polished down to 6 µm, has the same strength as that of the window as-fabricated float glass; when the sand blasting is applied on the surface of the described fused glass, the strength is 25 % lower. As strength is not intrinsic, it is needed to find the critical stress intensity factor (or fracture toughness K_{Ic}) of glass. To challenge the difficulty in determination of K_{Ic}, we found that SEPB and CNB methods are self-consistent. The stiff loading set-up, combined with a careful choice on the experimental and geometrical parameters, results in a stable fracture regime for SEPB specimens, especially when fracture is performed at low velocity in three-point bending. In such conditions, by means of an in-situ camera, a single SEPB experiment allows to obtain an entire fatigue resistance curve (V-K) for crack extension velocities (V) ranging between 10^{-6} and 10^{-3} m.s^{-1}. K_{Ic} as derived from the *wof* is in good agreement with the intrinsic fracture toughness value. However, as long as the peak load is used to estimate K_{Ic}, unstable SEPB final fracture (high velocity) is recommended in order to limit stress corrosion effects. K_{Ic} values as calculated from the peak load associated with a stable crack extension regime is systematically ~ 20 % smaller than K_{Ic} as derived from the peak load during unstable SEPB experiments, or during stable CNB ones.

VII.1.b. Composition dependence of fracture toughness

Fracture behavior of sodium aluminoborosilicate glasses

Twenty different sodium aluminoborosilicate glasses at fixed soda content, covering a large part of the glass-forming region, were studied. Ultrasonic echography, Vickers microindentation, and SEPB methods were used to evaluate the mechanical properties of the glasses. The sodium borosilicate glass with equal amounts of soda and boria exhibits the highest elastic moduli and hardness, which is ascribed to its high degree of cross-linking. The metaluminous aluminoborate glass displays the lowest elastic moduli and hardness, in agreement with its relatively flexible network compared to the remaining glasses investigated in this study. Both Young's modulus and Vickers hardness could be predicted to a satisfactory degree using existing semi-empirical models when the glass network topology is taken into consideration. The SEPB measurements show that the metaluminous aluminoborosilicate glasses exhibit relatively low toughness values, which are smaller than the predicted ones, while the $25Na_2O–12.5Al_2O_3–12.5B_2O_3–50SiO_2$ composition shows the highest toughness of the glasses selected for toughness experiments. The experimental and theoretical fracture toughness values feature relatively poor agreement, when assuming that one cation-oxygen bond per structural unit is broken during fracture and that the crack proceeds through a random path with no preference for weak bonds. Adjusting the crack path to follow weaker bonds when favorable is found to have a pronounced impact on the toughness values, but more experimental data is needed to develop a predictive toughness model for aluminoborosilicate glasses.

Fracture behavior of dense SiOC glass ceramics

The impacts of varying amounts of segregated carbon and of zirconium and hafnium modification on the fracture behavior of SiOC glass ceramics were investigated by means of a self-consistent method (SEPB). The fracture toughness value obtained from the experiment was compared to that obtained from the theory by assuming that the crack goes through the weakest bonds in the glass ceramic system. The toughness from the two methods has a good agreement. By presenting 12 vol.% of segregated carbon into the glass ceramic (< 1 vol.% for C1-SiOC to 12 vol.% for C12-SiOC), the fracture toughness increases from about 0.7 $MPa \cdot m^{0.5}$ to about 1 $MPa \cdot m^{0.5}$. The incorporation of HfO_2/ZrO_2 (about 5 vol.%) into the SiOC glass ceramics shows the same increase in the toughness. The conclusion of the modification should be further investigated with greater amount of HfO_2/ZrO_2.

VII.1.c. Temperature and environment dependence of K_{Ic}

The temperature dependence of K_{Ic} of two glasses and environment dependence of K_{Ic} of four commercial available glasses were both studied by means of SEPB. For the K_{Ic} in the elevated temperature, we found that with the loading rate of 10 MPa√m/s, the transition temperature of studied glasses is at about $1.07T_g$; however, more experiments should be perfumed in the future to verify this summary. For the environment dependence, the following conclusions were drawn: 1) it is sufficient to just perform the bending stage in the non-humidity influence atmosphere to avoid the stress corrosion; 2) it is sufficient to perform the SEPB experiment in the ambient atmosphere once the cross-head speed (or crack velocity) is fast enough to have the result values in region III of the Wiederhorn's v-K curve.

VII.2. Future research

The experiments performed in this thesis focus on the fracture toughness of glass in ambient, inert and elevated temperature environments. However, there is still room for more developments and enhancements.

Previous work from Wiederhorn et al. [1] focused on the crack velocity dependence of stress intensity factor (v-K) in elevated temperatures of some commercial glasses by using double-cantilever-cleavage technique, which by general requires large specimens (a normal specimen has the dimension of $75 \times 25 \times 2$ mm^3). By means of SEPB method, this kind of experiment can be applied on laboratory glass scales.

VII.3. References

[1] S.M. Wiederhorn, H. Johnson, A.M. Diness, A.H. Heuer, Fracture of Glass in Vacuum, J. Am. Ceram. Soc. 57 (1974) 336–341.

VIII. Summary in French

VIII.1. Introduction général

Le verre est un matériau fascinant en raison d'une combinaison unique de propriétés, telles que la possibilité d'être façonné à une température relativement basse (~1,1Tg) par formage viscoplastique, transparence, dureté, rigidité et durabilité. Au fil des années, le verre a été largement utilisé dans de nombreuses applications en tant que matériau de structure dans le secteur de l'automobile ou du bâtiment, ainsi que pour le confinement des déchets nucléaires, l'optique, les télécommunications, la médecine et les arts.

Face à cette forte demande, les scientifiques du verre ont recherché des verres plus solides et plus résistants pour améliorer la durée de vie des pièces en verre et réduire la consommation de matériaux de départ [1]. Afin de répondre à ces objectifs, plusieurs techniques ont été développées. La trempe thermique ou chimique induit des contraintes de compression à la surface du verre. Au moyen de particules ou de fibres de la seconde phase (voie composite) ou de la précipitation in situ d'une phase cristallisée (voie vitrocéramique), il a été tenté d'améliorer les performances mécaniques (dureté, dureté, résistance) avec un succès remarquable [2–6].

Néanmoins, la résistance intrinsèque (c'est-à-dire la résistance optimale atteinte en l'absence de tout défaut extrinsèque) du verre, mesurée par exemple sur des fibres cristallines, est bien supérieure à celle utilisée par les ingénieurs verriers et à celle résultant des expériences de rupture conduites sur des échantillons relativement grands [7–13]. La résistance théorique calculée du verre-à-vitre est d'environ 35 000 MPa [14], tandis que la résistance à la traction expérimentale d'un verre-à-vitre flotté est d'environ 125 MPa [9]. Des défauts sur la surface du verre (dus à la fabrication ou au transport) empêchent le verre d'atteindre sa résistance intrinsèque. La résistance à la traction d'une fibre de verre de silice, à surface immaculée, a été mesurée sous vide à 77 K et trouvée d'environ 14 000 MPa [15], tandis que celle d'une plaque de verre de silice polie normale est d'environ 100 MPa [10].

Comme pour tout matériau fragile, la résistance du verre dépend en grande partie des caractéristiques de la population de défauts (distribution, taille, etc.). En outre, les fissures sont généralement très vives (même considérées comme atomiquement nettes) et se fracturent avec les caractéristiques typiques associées à la fragilité (faible énergie de surface et ténacité). Par conséquent, il est primordial d'estimer la résistance intrinsèque du verre à la fracture et d'examiner plus avant ce qui peut être fait en jouant sur la composition et la microstructure.

VIII.1.a. Fondements de la mécanique de la rupture

Un article classique de Griffith en 1921 [16] expliquait le rôle des défauts dans la fracture des matériaux fragiles. L'analyse des contraintes réalisée par Inglis en 1913 en était un précurseur [17]. Inglis a analysé une plaque contenant un défaut elliptique de longueur 2*c* (le long de l'axe Y) et d'une largeur 2*b* (le long de l'axe X) sous une contrainte de traction appliquée uniforme σ (**Fig. VIII-1**). Le rayon de courbure minimal (ρ) est situé au sommet de l'axe principal de la faille elliptique et est exprimé par $\rho = b^2/c$. La contrainte au coin de la faille (σ_c) est exprimée comme suit :

$$\sigma_c = \sigma\left(1+2\frac{c}{b}\right) = \sigma\left(1+2\sqrt{\frac{c}{\rho}}\right) \qquad \text{(VIII.1)}$$

Dans le cas $b << c$ (pour un défaut étroit), $2\sqrt{(c/\rho)} >> 1$ et Eq. VIII.1 peut être réduit à $\sigma_c/\sigma = \sim 2c/b = 2\sqrt{(c/\rho)}$. Ce rapport est le facteur de concentration de contraintes au bord du trou elliptique (extrémité longue).

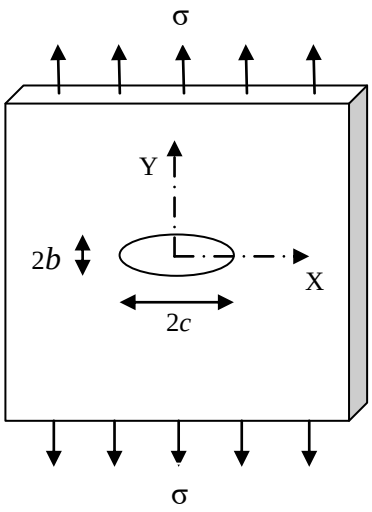

Fig. VIIVIII-1 : Plaque contenant un défaut elliptique sous contrainte de traction uniforme.

En se basant sur l'analyse Inglis, Griffith a examiné le cas d'un défaut elliptique «infiniment» étroit de longueur 2*c*, en supposant que $b \rightarrow 0$ sur **Fig. VIII-1**, soumis à une contrainte de traction constante. Dans son étude, Griffith a choisi le verre comme matériau modèle car il est supposé que le verre se comporte de manière élastique et linéaire et que le fond de la fissure dans le verre est extrêmement pointu [18,19]. Une relation entre la résistance à la rupture et l'énergie de surface de rupture a été formulée à partir des lois de la conservation de l'énergie. La contrainte critique à laquelle se produit la défaillance (σ_f) est exprimée comme suit :

$$\sigma_f = \sqrt{\frac{2E'\gamma}{\pi c}}, \qquad \text{(I.2)}$$

où *E'* est le module de Young *E* en contrainte plane, et $E/(1+v^2)$ en déformation plane, où *v* est le coefficient de Poisson, γ est l'énergie de surface de la fracture et *c* est la longueur critique de la fissure. Eq. VIII.2 indique la dépendance de la résistance à la taille de la fissure, tandis que *E'* et γ dépendent des compositions de verre. "*c*" dans Eq. VIII.2 est généralement beaucoup plus grand que l'espacement interatomique, de sorte que la force est beaucoup plus petite que la force intrinsèque idéale.

VIII.1.b. La point de la fissure et la fracture du verre

Quelle netteté la pointe de la fissure du verre et comment le verre casse sont toujours controversées. Irwin-Orowan [20] proposé une zone à petite échelle pour les éléments non linéaires, qui élimine la singularité du fond de fissure. Dans cette situation, la contrainte appliquée est transmise à la zone de traitement du fond de fissure par la région élastique linéaire. Deux hypothèses peuvent être envisagées. Dans le premier cas, la fracture se produit de manière fragile, c'est-à-dire $G_c \approx 2\gamma$, où G_c est la force critique d'extension de la fissure et γ est l'énergie de surface, et le fond de la fissure est atomiquement coupant. Dans le second cas, la fracture se produit de manière plastique ductile, c'est-à-dire $G_c >> 2\gamma$, et le fond de la fissure est émoussé.

Dans le cas des matériaux métalliques et polymères, G_c a plusieurs ordres de grandeur supérieurs à 2γ car la fracture se produit conformément au processus de séparation des fonds de fissures par des matières plastiques [18]. Cela signifie que la plus grande partie de l'énergie disséminée dans le processus de fracture n'est pas utilisée pour créer la nouvelle surface mais se dissipe à la place de la déformation irréversible de la région environnante. Dans le cas de matériaux fragiles, la valeur de Gc mesurée est généralement 2 ou 3 fois supérieure à la valeur prédite 2γ, et les mesures (ainsi que les prédictions) ne sont généralement pas très précises. Dans une étude classique sur la fracture du verre, Marsh [21] a suggéré que la fracture du verre était un plastique ductile et que le fond de la fissure était émoussé. Au contraire, Hillig [22] a conclu que la fissure est très pointue. Lawn et al. [18] ont observé la zone de traitement du fond de fissure dans quatre céramiques différentes au moyen de la microscopie électronique à transmission (MET) et ont conclu que le fond de fissure est extrêmement pointu pour des solides parfaitement cassants.

VIII.1.c. Corrosion sous contrainte

Lorsqu'un échantillon de verre est fracturé à une vitesse relativement faible (typiquement $\leq \sim 10^{-4}$ $m \cdot s^{-1}$) dans un environnement humide, on observe principalement une propagation lente de la fissure (corrosion sous contrainte), à $K_I << K_{Ic}$, ce qui s'explique par les molécules d'eau réagissant avec verre au fond de la fissure, selon un procédé chimique de corrosion sous contrainte.

Wiederhorn [23] a utilisé la méthode DCB (double cantilever beam) pour étudier ce comportement de type "fatigue". Il a constaté que le facteur d'intensité de contrainte, K_I, augmentait avec la vitesse de la fissure jusqu'à ce que certains seuils soient atteints, où la fissure est trop rapide pour que les molécules d'eau atteignent son front (**Fig. VIIVIII-**). De plus, pour atteindre les seuils, il faut produire une vitesse de fissure plus grande lorsque le taux d'humidité est élevé; par exemple, pour atteindre le seuil, il faut une vitesse de fissure de ~$2 \cdot 10^{-7}$ m·s^{-1} à une humidité relative de 0.017 % tandis que ~ $2 \cdot 10^{-4}$ m·s^{-1} est requise à un niveau relatif humidité de100 %. Plus tard, Michalske and Freiman [24] ont créé un modèle réussi (**Fig. VIIVIII-**) pour étudier l'effet de l'humidité.

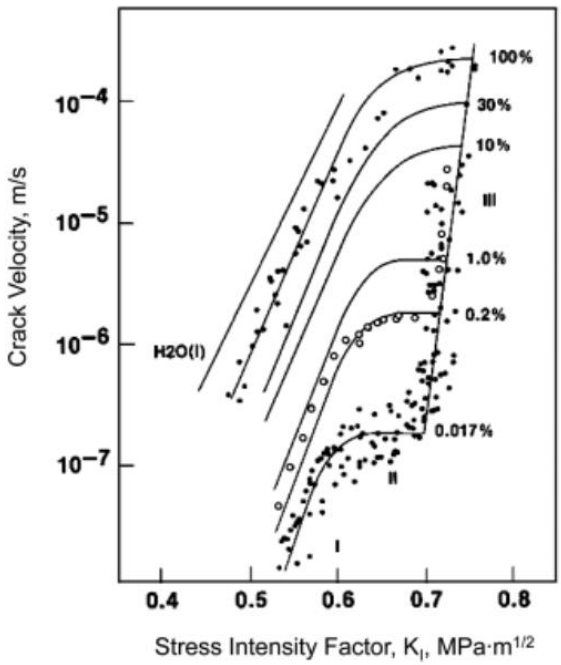

Fig. VIIVIII-2 : Données de croissance des fissures dans le verre sodocalcique-silice. Après Wiederhorn [23]. [100]

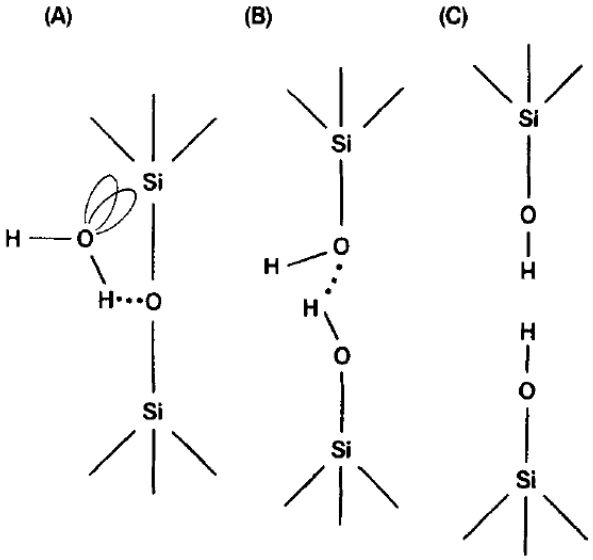

Fig. VIIVIII-3 : Représentation de la réaction proposée entre l'eau et une liaison contrainte S_i-O-S_i au fond de la fissure. Étape de réaction impliquent; (a) adsorption de l'eau sur la liaison S_i-O, (b) réaction concertée impliquant un transfert simultané de protons et d'électrons et (c) formulation d'hydroxyles de surface [24].

VIII.1.d. Ténacité à la rupture des matériaux fragiles

Dans les années 1950, Irwin et Orowan [25–27] ont étendu le concept de Griffith et popularisé les concepts de «facteur d'intensité de stress» et de «facteur d'intensité de stress critique». Le facteur

d'intensité de contrainte critique dans le mode d'ouverture de fissure (ou la résistance à la rupture, K_{Ic}) est principalement déterminé à l'aide de l'expression ci-dessous :

$$K_{Ic} \propto \sigma\sqrt{c} \ (\propto : \text{proportionnelle}), \qquad \text{(VIII-3)}$$

où σ est la contrainte de fracture réelle d'un échantillon avec un défaut préexistant de longueur c (taille critique de la fissure). La constante de proportionnalité dans Eq. VIII-3 (généralement ~1-2) dépend des caractéristiques de chargement, ainsi que de la géométrie des éprouvettes et des fissures.

Malgré l'importance primordiale de K_{Ic} pour les matériaux fragiles, la détermination de la caractéristique intrinsèque reste difficile. Il n'y a pas encore de méthode standard dans le cas du verre, mais pour la céramique. De nombreuses méthodes ont été développées et appliquées pour mesurer le K_{Ic} des verres. Dans les années 1970-1980, de nombreux chercheurs ont utilisé des méthodes de dalles plates, telles que Double Cantilever Beam (DCB) ou Double Torsion (DT) [28–30]. Juste un peu plus tard, au milieu des années 1970, une autre méthode, à savoir - Indentation Fracture (IF), principalement Vickers (Vickers Indentation Fracture, VIF), a été proposée et calibrée à l'aide de méthodes antérieures. VIF est rapidement devenu populaire en raison de sa facilité, de sa simplicité, de sa perte de temps et de son coût élevé [31–35]. Plus tard (principalement après 1980), les méthodes de poutre telles que le faisceau à encoche simple à bord (SENB), le faisceau à pré-fissure à bord unique (SEPB), le faisceau à entaille chevron (CNB), la fissure superficielle en flexion (SCF), etc. introduit et appliqué sur du verre [28,29,44–47,36–43]. Les configurations d'essais de ténacité à la rupture, ainsi que les avantages et inconvénients de ces méthodes, sont décrits dans [40] et [47].

VIII.1.e. Dépendance de la composition du K_{Ic}

Influence des compositions

Shinkai *et al.* [48] ont étudié E et K_{Ic} dans des verres ternaires PbO-ZnO-B_2O_3 avec B_2O_3 entre 30 et 70 mol% et PbO/ZnO égal à 1:0, 3:1, 1:1, 1:3 and 0:1. E et K_{Ic} ont été mesurés par les méthodes de la fréquence de résonance et de la fissuration superficielle en flexion (SCF), respectivement. Dans la technique SCF, l'indentation Vicker d'une charge de 5 N était indentée dans la surface de traction des éprouvettes testées, puis, afin d'éliminer la contrainte résiduelle, les éprouvettes indentées étaient recuites cinq minutes. Ils ont constaté que E

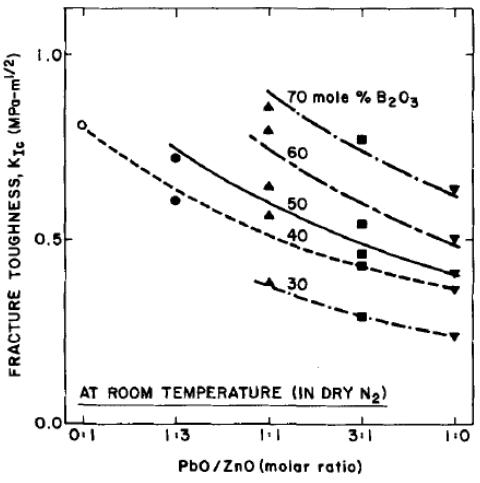

Fig. VIIVIII-4 : Effets du rapport PbO/ZnO et de la teneur en B_2O_3 sur K_{Ic} pour les verres PbO-ZnO-B_2O_3 [48].

et K_{Ic} augmentaient tous les deux avec l'augmentation de la teneur en B_2O_3 pour tous les rapports PbO/ZnO, et diminuaient avec l'augmentation du rapport PbO/ZnO pour tous les niveaux de B_2O_3 (**Fig. VIII-4**). Ils ont également conclu que le flux visqueux au fond de la fissure dans leurs verres étudiés était très limité.

Influence d'une séparation de phase et d'une structure de verre

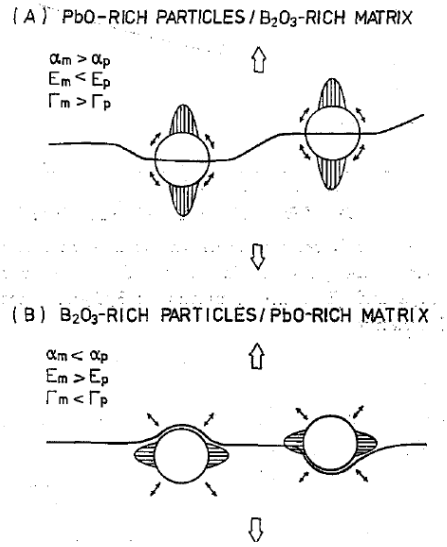

Fig. VIIVIII-5 : Schéma des trajectoires de fracture attendues pour les verres non miscibles au PbO-B_2O_3. Les flèches autour de chaque particule représentent les contraintes thermiques résiduelles dans la matrice. Les zones ombrées représentent les régions de la matrice concentrées en contraintes produites par le désaccord élastique. Les indices *m* et *p* se réfèrent à la matrice et à la particule, respectivement [49].

Miyata et Jinno [49] ont étudié les propriétés mécaniques des verres à séparation de phase PbO-B_2O_3: particules riches en B2O3 / matrice riche en PbO et particules riches en PbO / matrice riche en B_2O_3. L'effet de la quantité de chaque phase et de la microstructure sur les propriétés a été prouvé. Normalement, la dispersion de la seconde phase dans le verre entraîne une augmentation de l'énergie de surface de fracture ainsi que de la ténacité. En effet, la deuxième phase joue le rôle d'obstacle pour l'extension de la croissance des fissures. D'autre part, la dispersion de seconde phase peut avoir une fissure de microstructure qui conduit à une énergie de surface et à une ténacité inférieure. Pour les composites de verre à matrice riche en B_2O_3, la partie fracturée devrait traverser la particule (**Fig. VIII-5A**). Cependant, lors de la recherche de la partie facile à casser dans le matériau, la fissure subit une déviation locale par rapport à son plan de partie précédent. L'énergie de surface de fracture et la ténacité se sont révélées être dépendantes de la fraction volumique de la dispersion. En cas de composite avec matrice riche en PbO, la théorie de Lange-Evans [50,51] peut expliquer l'augmentation de (**Fig. VIII-5B**).

Lorsque des cristaux ou des nanostructures apparaissent dans la matrice de verre, la ténacité à la rupture est principalement modifiée. Schultz *et al.* [52] ont étudié le clivage monocristallin de matériaux fragiles. Ils ont montré que le K_{Ic} d'un agrégat poly-cristallin fragile était supérieur à celui d'un clivage monocristallin, car l'agrégat poly-cristallin n'avait pas la continuité de la fissure de clivage.

VIII.1.f. Approches de modélisation

Différentes approches ont été développées dans le monde pour prédire ou calculer la ténacité, afin de comprendre la dépendance vis-à-vis de la composition. Certaines utilisent des images simples du solide ou de l'organisation atomique, tandis que d'autres utilisent des outils numériques modernes tels que la théorie de la densité fonctionnelle (DFT), la simulation de dynamique moléculaire ab-initio (MD) et les approches de contraintes topologiques (CT) [1,53,62,54–61].

TC est une théorie dans laquelle une structure mécanique remplace et simplifie la structure atomique complexe. Dans cette théorie, les atomes sont connectés les uns aux autres par les interactions chimiques contraignant les longueurs et les angles des liaisons, et la connexion peut être présentée sous trois états: flexible, isostatique et rigide [63–65]. En connexion souple (nombre de degrés de liberté par atome $n_c = 3$), les degrés de liberté permettent une déformation locale; en connexion isostatique ($n_c < 3$), le système est rigide mais exempt de contrainte propre; et en rigide ($n_c > 3$), la connexion est bloquée et la contrainte propre est présente. Bauchy *et al.* [66] ont utilisé l'approche de TC en association avec MD pour étudier la ténacité des verres de silicate de sodium densifiés (NS) et des hydrates de silicate de calcium (CSH) densifiés. Ils ont constaté que les résistances à la rupture pour les deux verres et leurs comportements de résistance à la rupture étaient les plus optimaux dans le système isostatique. Ils ont conclu que cette théorie est prometteuse pour la conception de la composition de matériaux plus durs.

Rouxel [54] a prédit l'énergie de surface de rupture d'une variété de verres allant de la silice amorphe aux verres métalliques et a démontré un bon accord entre l'expérience SEPB et la modélisation lorsque l'énergie diatomique (enthalpie de fission) est prise en compte. Par ailleurs, lorsqu'il utilise l'enthalpie de dissociation du composé, il constate que la ténacité théorique est légèrement inférieure à celle de l'expérience ($K_{Ic,theo} \approx 0.7K_{Ic,exp}$). Il a prédit le chemin de fissure dans la matrice de verre et a établi la relation entre la ténacité et les compositions de verre. Il a également recueilli des données sur la résistance à la rupture des verres d'un groupe de chalcogénures à un groupe métallique et les a simplement résumées dans un graphique (**Fig. VIII-6**).

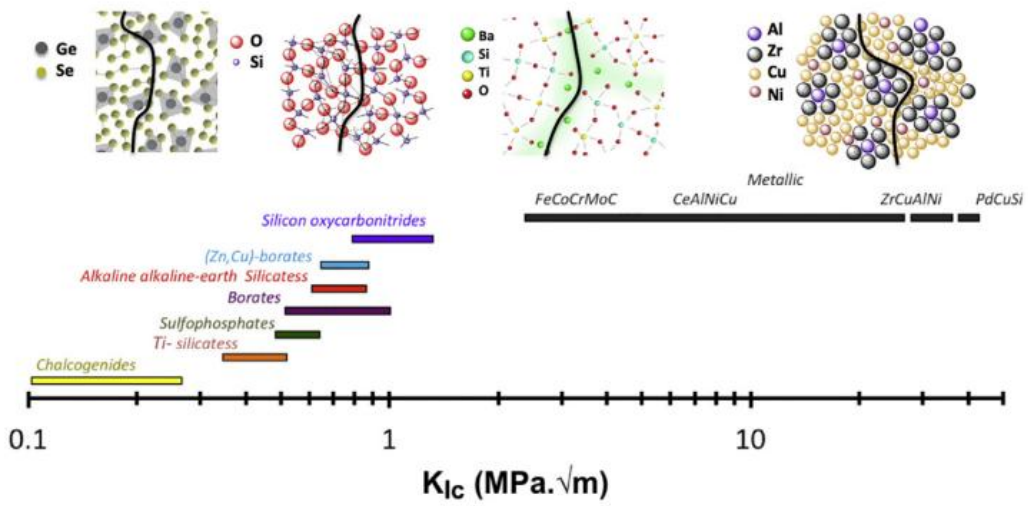

Fig. VIII-6 : La ténacité apparente des verres, obtenue par diverses méthodes expérimentales. Les dessins schématiques décrivent le chemin de fissure prévu, tendant à suivre les liaisons les plus faibles du réseau atomique (par exemple les liaisons Ba-O dans le verre $BaO(30)-TiO_2(30)-SiO_2(40)$) [54].

VIII.1.g. Dépendance à la température des propriétés du verre

Pour un matériau homogène adaptant un comportement élastique, le principe de similarité d'Irwin-Griffith donne : $K_{Ic} = \sqrt{(E\gamma/(1-\nu^2))}$. A l'échelle atomique, le module de Young (E) peut être mis en relation avec la force nécessaire pour modifier l'espacement interatomique [67]. Pour un déplacement atomique donné à partir de l'équilibre, la force est généralement plus petite lorsque la température augmente. Cela entraîne une diminution des modules d'élasticité à mesure que la température augmente. Une telle tendance a été observée sur un verre-à-vitre [45,68], avec une lente diminution de E de RT à T_g, et une chute rapide au-delà de T_g. Cependant, les expériences de Shinkai [45] et de Spinner [69] sur du verre de silice fondu de la température ambiante à environ T_g ont montré que la tendance opposée, c'est-à-dire que E du verre de silice fondu augmentait légèrement. Le coefficient de Poisson ν à température élevée, de la température ambiante à environ Tg, a légèrement augmenté dans les verres de maintien et de silice [45]. La mesure de la résistance à la rupture à haute température est à peine rapportée et la plupart d'entre elles concernent des céramiques et vitrocéramiques [70–77] et seulement quelques études sur des verres [29,45,68].

VIII.2. Travail de recherche

Dans cette thèse, le travail de recherche comprend deux parties principales. La première partie concerne la résistance du verre mesurée par l'expérience de flexion bi-axiale. Dans cette partie, la relation entre le défaut de surface, la résistance et la ténacité est traitée. Le détail de cette relation est présenté dans l'article I. La deuxième partie concerne la mesure de la résistance aux fractures du verre et des vitrocéramiques. La mesure, ainsi que l'analyse théorique, dans l'environnement de la

pièce, l'environnement argon et l'environnement à température élevée sont présentées dans cette seconde partie (les articles II, III et IV).

VIII.2.a. Défaut de surface et résistance des verres a-silica et SLS

Des forces allant de 50 à 180 MPa sont rapportées dans la littérature, en fonction des conditions d'état de surface [10,78–80]. Cependant, la taille des défauts de surface des verres flottants a-silica et SLS n'a pas été bien étudiée. Afin de résoudre ce problème, une expérience de flexion bi-axiale avec une configuration en anneau sur anneau est réalisée sur trois échantillons en série dans des conditions différentes. La série 1 se compose de 20 disques d'a-silice avec les deux surfaces polies jusqu'à une pâte de diamant de 6 µm afin d'obtenir une rugosité moyenne (R_a) d'environ 0,001 µm. La série 2 comprend les 20 autres disques d'a-silice avec une surface polie comme celle de la série 1 et une autre surface, qui est soumise à une contrainte de traction, traitée au jet de sable pour obtenir la surface Ra de 0,2 µm de cette dernière surface. La série 3 comprend 20 disques, soit 5 disques avec un état de surface traité, 5 disques avec un retrait de 10 N au milieu, 5 disques avec un retrait de 5 N, 1 disque avec un retrait de 1 N, 1 disque avec un retrait de 0,3 N, 1 avec un retrait de 0,2, 1 avec un retrait de 0,1 et l'autre 1 avec un retrait de 0,05 N.

La configuration anneau sur anneau est détaillée dans le document I ainsi que la description de l'alignement de la charge du piston sur la charge et les bagues de support afin que la précision du centrage soit inférieure à 2%. La résistance de l'échantillon a été calculée au moyen de réf. [81–84] représentant la position réelle de l'origine de la fissure.

Les tailles de défauts mesurées par les profils AFM sont plus petites que celles calculées à partir de la théorie de Griffith en mécanique de la rupture fragile. Ce désaccord suggère la présence de défauts relativement importants qui ne sont visibles ni à la surface à étudier ni par les microscopes optiques, ni par AFM. Sur la série 3, les longueurs de fissure d'angle mesurées à partir de l'indentation sont en bon accord avec les tailles calculées des défauts de surface pour la charge d'indentation supérieure à 1 N et moins conformes pour la charge d'indentation inférieure. Cela suggère que lorsque la charge est suffisamment élevée, le motif d'indentation est plus susceptible d'avoir la forme d'un demi-penny. La taille critique du défaut de surface de 8 µm est déterminée. Lorsque l'indentation produit une fissure d'angle supérieure à 8 µm, la résistance du verre dépend de l'indentation; toutefois, lorsque l'indentation produit une fissure de coin inférieure à 8 µm, la résistance du verre ne dépend pas de l'indentation.

L'énergie emmagasinée a été calculée à partir de la courbe charge-déviation, et le nombre de fragments a été compté en considérant les gros fragments situés sur le côté, c'est-à-dire y compris

les petits au milieu. Le nombre de fragments s'avère indépendant de l'état de la surface, mais de l'énergie emmagasinée avant la fracture. En outre, l'énergie de surface de fracture, calculée en comptabilisant l'énergie stockée divisée par la surface de fracture, est égale à 68 J/m² pour les deux séries et ne dépend pas du nombre de fragments. Cette valeur d'énergie de surface de fracture est environ 20 fois supérieure à celle de la littérature (~ 3,55 J/m²) [54]. Cette grande différence suggère que les surfaces de fracture peuvent en réalité être 20 fois plus grandes que les surfaces supposées car les surfaces de fracture angulaires, les surfaces de fracture de deuxième ligne et les surfaces des pièces totalement brisées n'ont pas été comptées dans les surfaces de fracture supposées.

VIII.2.b. Ténacité, énergie de rupture et corrosion sous contrainte du verre

La présente étude se concentre sur le test SEPB, examine les conditions expérimentales déterminant la stabilité du stade de fracture ultime (à partir de la pré-fissure à l'arrachement) et analyse l'incidence des caractéristiques de fissuration d'indentation préliminaire. Les effets environnementaux (humidité) sont également discutés. L'objectif ultime était d'identifier un protocole expérimental basé sur des fissures « idéales », c'est-à-dire avec une acuité de pointe aussi proche que possible de celle de propagation des fissures lors d'une défaillance catastrophique dans l'hypothèse de l'élasticité pure, permettant ainsi de déterminer le K_{Ic} dans une auto manière cohérente. Plusieurs chercheurs ont précédemment suggéré que de telles fissures sont nettes sur le plan atomique dans des matériaux fragiles tels que le verre [18,19]. Les méthodes de Chevron-Notched Beam (CNB) et de Single-Edge Precracked Beam (SEPB) sont des méthodes bien établies auto-cohérentes qui se sont avérées appropriées pour les mesures de K_{Ic} de la céramique [85–87]. Ces méthodes seront comparées aux méthodes basées sur l'indentation, qui sont beaucoup plus courantes pour estimer le K_{Ic} de matériaux fragiles. Les détails des trois méthodes sont présentés dans l'article II. Dans l'article, les discussions de chaque méthode sont dessinées comme suit:

Les équations VIF actuelles reposent sur de fortes hypothèses concernant la loi de comportement: absence de densification, écoulement plastique parfait et absence de caractéristiques du matériau dépendant de la pression. Ces hypothèses sont évidemment discutables dans le cas du verre. Néanmoins, pour Optiwhite ™ et Planilux®, les valeurs de $K_{IF(Ans)}$ sont comparables aux valeurs de K_{Ic} mesurées au moyen de la méthode auto-cohérente, par exemple celle du SEPB, probablement parce que du verre sodocalcique-silice a été inclus dans le protocole d'étalonnage du VIF méthode [88]. Dès que les propriétés du verre s'écartent de celles du verre sodocalcique-silice, la méthode VIF conduit principalement à des résultats biaisés. Par exemple, dans le cas de Borofloat, la valeur de K_{Ic} dérivée de l'indentation est environ 100% plus grande. En effet, la densification et le

cisaillement empêchent la formation de fissures radiales / médianes étendues dans ce verre, où les fissures de type cône de type hertzien coupant la surface pour former des anneaux sont visibles et reflètent la sensibilité de ce verre à la densification. Une revue de l'effet de la composition du verre sur la densification et le cisaillement induits par l'indentation (accumulation de matière à la surface) a été publiée ailleurs [89]. Avec un coefficient de Poisson d'environ 0,2, les deux verres borosilicatés (Borofloat et BK7) pourraient présenter une contribution à la densification représentant jusqu'à 70% du volume de l'empreinte Vickers, tandis que pour Planilux, la contribution à la densification est d'environ 60% (environ 85% pour les filtres amorphes). silice) [90].

Dans la présente étude, l'angle d'entaille (apex) est relativement petit (~ 40 °), de sorte qu'en raison de l'épaisseur de l'entaille (0,25 mm), le chemin de la fissure peut se décaler du plan de la section d'un angle d'inclinaison allant jusqu'à 9,5 °. Par exemple, un angle de décalage de 7,8 ° a été mesuré post-mortem avec le spécimen Optiwhite. Cette inclinaison induit une augmentation de la charge nécessaire au processus de déchirement et conduit donc artificiellement à une valeur de ténacité supérieure. Selon la norme ASTM pour la méthode SEPB, le décalage doit être inférieur à 5 °. Par conséquent, les échantillons pour lesquels l'angle d'inclinaison était supérieur à 5 ° ont été exclus de l'analyse et n'ont pas été signalés. Des expériences valides montrent un excellent accord entre $K_{CNBstca}(P)$ et $K_{SEPBunstable}(P)$. Un examen post-fracture est donc nécessaire pour valider le test CNB. K_{Ic} tel que calculé à partir du travail de fracture $K_{CNB}(\gamma)$ apparaît sous-estimé, probablement en raison de la présence de microfissures près des bords de l'entaille qui seraient également responsables de l'augmentation de la rugosité de la surface de fracture près de l'entaille.

Pour les vitesses transversales inférieures à 0,2 µm.s^{-1}, la rupture est stable et le K_{Ic} est d'environ 0,55 MPa.m^{0,5}. En revanche, pour les vitesses transversales supérieures à 1 µm.s-1, la fracture est instable et le K_{Ic} atteint 0,70 MPa.m$^{0.5}$, soit 20% de plus que la valeur de "fracture stable". En effet, une augmentation monotone de K_{Ic} a été constatée lorsque la vitesse transversale a été augmentée. La corrosion sous contrainte dans ce verre est due à la réaction des molécules de H_2O présentes dans l'atmosphère avec les liaisons Si-O au niveau de la fissure. La cinétique de cette réaction chimique est déclenchée par les fortes contraintes qui se produisent au fond de la fissure. La vitesse du front de fissure a été contrôlée au moyen d'une caméra portable afin de mieux comprendre l'effet de l'influence de la corrosion sous contrainte sur deux éprouvettes Planilux présentant le même rapport de pré-conditionnement à 0,50 correspondant aux essais de stabilité et d'instabilité. La variation de la vitesse de croissance de la fissure avec K_I pour le verre actuellement étudié à ~ 62% d'humidité est en bon accord avec celle observée dans un verre assez similaire de Wiederhorn

[23] en utilisant un échantillon à Double Cantilever Beam (DCB). Une vitesse de 1,8 × 10-3 m.s-1 a été estimée, ce qui est supérieur à la vitesse dans la région II avec 100% d'humidité (~ 2,4 × 10-4 m.s-1, Fig. 15). Par conséquent, on suppose que $K_{SEPBunstable}(P)$ est indépendant de la corrosion sous contrainte. L'écart type est inférieur à 0,01 MPa.m^{0,5} pour tous les verres, sauf le Borofloat 33, où il vaut 0,03 MPa.m^{0,5}. Une fiabilité aussi remarquable découle du contrôle des caractéristiques géométriques des pré-fissures (moins de 10% de différence entre la longueur moyenne des pré-fissures et toute mesure à 0,25, 0,50 et 0,75 de la largeur de l'éprouvette), ainsi que du raffinement de la micro-indentation préliminaire étape. La charge d'indentation a toujours été choisie suffisamment petite pour limiter la fissure d'indentation à une longueur inférieure à ~ 50 µm, c'est-à-dire beaucoup plus petite que celle de pré-fissure (~ 2 mm) et l'alignement de petites indentations a entraîné un angle entre l'enfoncement pré-fissure (angle de crochet) et la rupture finale inférieure à 5 ° (tolérance standard).

VIII.2.c. Approche théorique de la ténacité des vitrocéramiques denses SiOC

Il a déjà été démontré que les vitrocéramiques SiOC présentaient également une dureté et une viscosité supérieures à celles de la silice vitreuse [91–94]. Le comportement à la rupture des vitrocéramiques SiOC n'a pas encore été largement étudié dans la littérature. Dans la présente étude, nous avons synthétisé quatre différentes vitrocéramiques SiOC avec différentes compositions chimiques et de phases. L'objectif était de mettre en évidence l'impact de quantités variables de carbone séparé sur le comportement à la rupture des vitrocéramiques SiOC. De plus, l'effet de l'incorporation de nanoparticules de ZrO_2/HfO_2 dans SiOC a été étudié. Le procédé de préparation de ces vitrocéramiques (à savoir Cl-SiOC, C12-SiOC, SiHfOC et SiZrOC) est brièvement décrit dans l'article III.

La méthode SEPB, telle que décrite dans l'article II, est utilisée pour mesurer le K_{Ic} de ces quatre vitrocéramiques et les résultats sont comparés à la méthode VIF (également décrite dans l'article II) et à l'approche théorique [54]. K_{Ic}, au moyen de la méthode VIF, est beaucoup plus grande que K_{Ic} au moyen de la méthode SEPB. Il est très probable que la densification, qui se produit dans une large mesure dans les matériaux actuels, empêche la dissipation de l'énergie mécanique par la formation de fissures. Une grande partie de l'énergie mécanique est dispersée dans le processus de densification et n'est pas prise en compte dans l'énergie calculée. K_{Ic} par la méthode SEPB et une approche théorique sont en bon accord. Un dessin schématique prenant en compte les informations structurelles disponibles et supposant qu'une fissure a tendance à suivre la voie la plus facile (la plus

favorable du point de vue énergétique) est tentée. Ce modèle explique le bon accord entre K_{Ic}^{SEPB} et $K_{Ic}^{the.}$. Dans MK-SiOC, il y a 12% en volume de carbone séparé et 12% en volume de SiC. Il est proposé que l'interface SiC/SiO_2 soit constituée des tétraèdres $SiO_{4-x}C_x$ à liaisons mixtes restantes, alors que les matrices carbone et silice ségrégées partagent quelques tétraèdres $SiO_{4-x}C_x$ à liaisons mixtes [94–96]. Par conséquent, pour terminer un voyage, la fissure doit traverser les domaines de la silice, les interfaces et la phase carbone séparée. La modification de SiOC avec Hf/Zr comme dans SiHfOC/SiZrOC entraîne la diminution de la fraction volumique de carbone de 12% à 6% en volume et la présence d'environ 6% en volume de HfO_2/ZrO_2. Cette modification agrandit les domaines de la silice et introduit le HfO_2 / ZrO_2 dans ces domaines de la silice plus vastes. Dans C1-SiOC, il y a moins de 1% en volume de carbone, ce qui donne une phase de carbone séparée et discontinue. L'énergie nécessaire pour percer le C1-SiOC est alors égale à celle nécessaire pour percer le verre de silice dont la ténacité est connue comme étant d'environ 0,73 $MPa \cdot m^{0.5}$.

VIII.2.d. Dépendance de K_{Ic} à la température et à l'environnement

Les dépendances du comportement du verre avec fracture, liées à la température et à l'environnement, n'étant pas bien comprises, elles ont fait l'objet d'un nombre très limité de publications, axées principalement sur les céramiques concernant l'incidence d'humidité [70–77] [29,45,68]. SEPB (Single-Edge Precead Poutre) est une méthode fiable et cohérente pour mesurer la résistance à la rupture de matériaux fragiles [41,54,97,98]. Cependant, à notre connaissance, la méthode SEPB n'a jamais été réalisée à température élevée ni dans une boîte à gants.

La présente étude se concentre sur 1) l'application de la méthode SEPB sur des verres à différentes températures allant jusqu'à $1{,}11T_g$ et se compare aux rapports publiés précédemment et 2) la mise en œuvre de la méthode SEPB (pré-conditionnement et fracture finale) sous atmosphère contrôlée, en particulier sous argon sec. Des essais SEPB avaient déjà été effectués avec la dernière étape de fracture sous atmosphère sèche de N_2 lors de travaux antérieurs [41,99], mais c'est la première fois que des étapes de pré-fissuration et de flexion sont effectuées dans une atmosphère à humidité contrôlée.

En ce qui concerne la dépendance vis-à-vis de la température, la ténacité a été mesurée de la température ambiante à 1,11Tg pour deux verres de systèmes chimiques SiO_2-CaO-Na_2O et SiO_2-MgO-Na_2O. Dans la mesure où des taux de charge relativement faibles sont appliqués (régime quasi statique), typiquement pour $dK_I/dt \leq 10$ $MPa \cdot \sqrt{m} \cdot s^{-1}$, ce qui correspond à des taux de contrainte, $\dot{\varepsilon}$, inférieurs à $10^{-2} \cdot s^{-1}$, la température de transition fragile à ductile devrait se situer autour de T_g. Pour la dépendance vis-à-vis de l'environnement, la ténacité de quatre verres commerciaux a été étudiée

en atmosphère contrôlée. Des vitesses transversales aussi faibles que 0,01 µm/s et atteignant 15 µm/s ont été appliquées pendant l'expérience de flexion SEPB afin d'étudier l'influence possible de la vitesse de la fissure. Enfin, les résultats du test "instable" précédemment publié (la courbe de déchargement se poursuit à partir de la charge maximale) dans l'atmosphère ambiante et le test avec uniquement le stade de rupture final dans une atmosphère sèche d'azote N_2 à partir des littératures, et les résultats actuels de cette étude (les étapes de pré-fissuration et de fracture finale dans une atmosphère d'argon sec) ont été comparées.

VIII.3. Conclusions

La plupart des efforts dans cette thèse sont consacrés à la détermination de la ténacité et de l'énergie de surface de fracture des verres. Les méthodes auto et non cohérentes pour déterminer ces paramètres sont présentées aux chapitres 2 et 3 (articles I et II). Les chapitres 4 et 5 (articles III et IV) sont consacrés à la dépendance à la composition de la ténacité et le chapitre 6 (article V) à la dépendance à la température et à l'environnement.

VIII.3.a. Défaut de surface, résistance et ténacité

La résistance expérimentale du verre n'est pas intrinsèque, mais dépend de la taille du défaut superficiel. Un verre flotté de fenêtre, avec les surfaces telles que fabriquées, a la taille du défaut critique (côté étain) d'environ 8 à 12 µm, estimée par le test de flexion bi-axiale sur des disques de 35 mm de diamètre. Le verre de silice fondue, d'une surface polie jusqu'à 6 µm, a la même résistance que celui du verre flotté fabriqué à la fenêtre ; lorsque le sablage est appliqué sur la surface du verre fondu décrit, la résistance est inférieure de 25 %. La résistance n'étant pas intrinsèque, il est nécessaire de trouver le facteur d'intensité de contrainte critique (ou la résistance à la rupture K_{Ic}) du verre. Pour contester la difficulté de détermination de K_{Ic}, nous avons constaté que les méthodes SEPB et CNB sont cohérentes. La configuration de la charge rigide, combinée à un choix judicieux des paramètres expérimentaux et géométriques, confère aux spécimens SEPB un régime de fracture stable, en particulier lorsque la fracture est réalisée à basse vitesse en flexion à trois points. Dans de telles conditions, au moyen d'une caméra in situ, une seule expérience SEPB permet d'obtenir l'ensemble de la courbe de résistance à la fatigue (V-K) pour des vitesses d'extension de fissure (V) comprises entre 10^{-6} et 10^{-3} $m.s^{-1}$. Le K_{Ic} dérivé du *wof* est en bon accord avec la valeur intrinsèque de la résistance à la rupture. Cependant, tant que la charge de pointe est utilisée pour estimer K_{Ic}, une fracture finale instable du SEPB (vitesse élevée) est recommandée afin de limiter les effets de la corrosion sous contrainte. Les valeurs de K_{Ic} calculées à partir de la charge de pointe associée à un régime d'extension de fissure stable sont systématiquement inférieures

d'environ 20 % à celles de K_{Ic} telles qu'elles sont calculées à partir de la charge de pointe au cours d'expériences SEPB instables ou lors d'essais CNB stables.

VIII.3.b. Dépendance à la composition de la ténacité

Vingt verres différents d'aluminoborosilicate de sodium à teneur en soude fixe, couvrant une grande partie de la région de formation de verre, ont été étudiés. Des méthodes d'échographie ultrasonore, de microindentation de Vickers et de SEPB ont été utilisées pour évaluer les propriétés mécaniques des verres. Le verre borosilicaté de sodium avec des quantités égales de soude et de bore présente les modules d'élasticité et la dureté les plus élevés, ce qui est attribué à son degré élevé de réticulation. Le verre aluminoborat métallique présente les modules d'élasticité et la dureté les plus bas, ce qui est en accord avec son réseau relativement flexible par rapport aux autres verres étudiés dans cette étude. Le module de Young et la dureté de Vickers peuvent être prédits à un degré satisfaisant à l'aide des modèles semi-empiriques existants, lorsque la topologie du réseau de verre est prise en compte. Les mesures SEPB montrent que les verres aluminoborosilicates métallumineux présentent des valeurs de ténacité relativement basses, inférieures aux prévisions, alors que la composition $25Na_2O–12.5Al_2O_3–12.5B_2O_3–50SiO_2$ présente la plus grande ténacité des verres sélectionnés pour les expériences de ténacité. Les valeurs expérimentales et théoriques de ténacité de rupture présentent une concordance relativement faible en supposant qu'une liaison cation-oxygène par unité structurelle est rompue pendant la fracture et que la fissure suit un chemin aléatoire, sans préférence pour les liaisons faibles. Ajuster le chemin de la fissure pour suivre des liaisons plus faibles lorsque favorable a un impact prononcé sur les valeurs de ténacité, mais davantage de données expérimentales sont nécessaires pour développer un modèle prédictif de ténacité pour les verres en aluminoborosilicate.

Les impacts de différentes quantités de carbone séparé et de modifications de zirconium et d'hafnium sur le comportement à la rupture des vitrocéramiques SiOC ont été étudiés à l'aide d'une méthode auto-cohérente (SEPB). La valeur de ténacité à la rupture obtenue à partir de l'expérience a été comparée à celle obtenue à partir de la théorie en supposant que la fissure passe par les liaisons les plus faibles du système vitrocéramique. La ténacité des deux méthodes est un bon accord. En présentant 12% en volume de carbone séparé dans la vitrocéramique (<1% en volume pour C1-SiOC à 12% en volume pour C12-SiOC), la ténacité à la rupture augmente d'environ 0,7 $MPa.m^{0,5}$ à environ 1 $MPa.m^{0.5}$. L'incorporation de HfO_2/ZrO_2 (environ 5% en volume) dans la vitrocéramique SiOC montre la même augmentation de la ténacité. La conclusion de la modification doit être approfondie avec une plus grande quantité de HfO_2/ZrO_2.

VIII.3.c. Dépendance à l'environnement de la ténacité

La dépendance de K_{Ic} de deux verres en fonction de la température et la dépendance de K_{Ic} de quatre verres disponibles dans le commerce ont été étudiées au moyen de SEPB. Pour le K_{Ic} à la température élevée, nous avons constaté qu'avec un taux de charge de 10 MPa√m/s, la température de transition des verres étudiés est d'environ 1,07Tg ; cependant, il faudrait parfumer davantage d'expériences pour vérifier ce résumé. En ce qui concerne la dépendance vis-à-vis de l'environnement, les conclusions suivantes ont été tirées : 1) il suffit d'effectuer la phase de pliage dans l'atmosphère sans influence de l'humidité pour éviter la corrosion sous contrainte ; 2) il suffit de réaliser l'expérience SEPB dans l'atmosphère ambiante une fois que la vitesse transversale (ou vitesse de la fissure) est suffisamment rapide pour obtenir les valeurs de résultat dans la région III de la courbe v-K de Wiederhorn.

VIII.3.d. Perspectives

Les expériences menées dans cette thèse portent sur la ténacité du verre dans des environnements ambiants, inertes et à température élevée. Cependant, il reste encore de la place pour plus de développements et d'améliorations.

Les travaux antérieurs de Wiederhorn et al. [29] ont mis l'accent sur la dépendance du facteur d'intensité de contrainte (v-K) à la vitesse de la fissure à des températures élevées de certains verres du commerce, en utilisant la technique de clivage par double porte-à-faux, qui nécessite en général des échantillons de grande taille (un échantillon normal a la dimension $75 \times 25 \times 2$ mm^3). Grâce à la méthode SEPB, ce type d'expérience peut être appliqué aux balances de verre de laboratoire.

Références

[1] L. Wondraczek, J.C. Mauro, J. Eckert, U. Kühn, J. Horbach, J. Deubener, T. Rouxel, Towards ultrastrong glasses, Adv. Mater. 23 (2011) 4578–4586.

[2] R.D. Rawlings, Bioactive glasses and glass-ceramics, Clin. Mater. 14 (1993) 155–179.

[3] V.M. Sglavo, D.J. Green, Flaw-insensitive ion-exchanged glass: II, production and mechanical performance, J. Am. Ceram. Soc. 84 (2001) 1832–1838.

[4] M. Bornapour, M. Celikin, M. Cerruti, M. Pekguleryuz, Magnesium implant alloy with low levels of strontium and calcium: The third element effect and phase selection improve bio-corrosion resistance and mechanical performance, Mater. Sci. Eng. C. 35 (2014) 267–282.

[5] I.W. Donald, Methods for improving the mechanical properties of oxide glasses, J. Mater. Sci. 24 (1989) 4177–4208.

[6] B.M. Novak, Hybrid nanocomposite materials�between inorganic glasses and organic polymers, Adv. Mater. 5 (1993) 422–433.

[7] C.R. Kurkjian, P.K. Gupta, R.K. Brow, The strength of silicate glasses: what do we know, what do we need to know?, Int. J. Appl. Glas. Sci. 1 (2010) 27–37.

[8] I. Naray-Szabo, J. Ladik, Strength of silica glass, Nature. 188 (1960) 226–227.

[9] M.H. Krohn, J.R. Hellmann, D.L. Shelleman, C.G. Pantano, G.E. Sakoske, Biaxial flexure strength and dynamic fatigue of soda--lime--silica float glass, J. Am. Ceram. Soc. 85 (2002) 1777–1782.

[10] C.A. Klein, Characteristic strength, Weibull modulus, and failure probability of fused silica glass, Opt. Eng. 48 (2009) 113401.

[11] T.C. Baker, F.W. Preston, The effect of water on the strength of glass, J. Appl. Phys. 17 (1946) 179–188.

[12] F.O. Anderegg, Strength of Glass Fires, Ind. Eng. Chem. 31 (1939) 290–298.

[13] W.C. Levengood, Effect of origin flaw characteristics on glass strength, J. Appl. Phys. 29 (1958) 820–826.

[14] R. Horm, Résistance de verre de silice pour application aérospatiale par la méthode de la flextion be-axiale, anneau-sur-anneau, Master 2 Report, Univ. Rennes 1. (2018).

[15] B.A. Proctor, I. Whitney, J.W. Johnson, The strength of fused silica, Proc. R. Soc. Lond. A. 297 (1967) 534–557.

[16] A.A. Griffith, M. Eng, VI. The phenomena of rupture and flow in solids, Phil. Trans. R. Soc. Lond. A. 221 (1921) 163–198.

[17] C.E. Inglis, Stresses in a plate due to the presence of cracks and sharp corners, Trans Inst Nav. Arch. 55 (1913) 219–241.

[18] B.R. Lawn, B.J. Hockey, S.M. Wiederhorn, Atomically sharp cracks in brittle solids: an electron microscopy study, J. Mater. Sci. 15 (1980) 1207–1223.

[19] H. Tanaka, Y. Bando, Y. Inomata, M. Mitomo, Atomically Sharp Crack in 15R Sialon, J. Am. Ceram. Soc. 71 (1988).

[20] G.R. Irwin, Handbook of physics, in: Vol. 6, Springer, Berlin, 1958: pp. 551–590.

[21] Dm. Marsh, Plastic flow in glass, Proc. R. Soc. Lond. A. 279 (1964) 420–435.

[22] W.B. Hillig, Plastic Behavior and Fracture in Glass, Microplasticity, Eds., CJ McMahon. Interscience, New York. (1968) 383.

[23] S.M. Wiederhorn, Influence of Water Vapor on Crack Propagation in Soda Lime Glass, J. Am. Ceram. Soc. 50 (1967) 407–414.

[24] T.A. Michalske, S.W. Freiman, A molecular interpretation of stress corrosion in silica, Nature. 295 (1982) 511–512.

[25] G.R. Irwin, Analysis of stresses and strains near the end of a crack traversing a plate, J. Appl. Mech. 24 (1957) 361–364.

[26] G.R. Irwin, Fracture, in: S. Flügge (Ed.), Elast. Plast. / Elastizität Und Plast., Springer Berlin

Heidelberg, Berlin, Heidelberg, 1958: pp. 551–590.

[27] E. Orowan, Fracture and strength of solids, Reports Prog. Phys. 12 (1949) 185–232.

[28] S.M. Wiederhorn, A.G. Evans, D.E. Roberts, A fracture mechanics study of the Skylab windows, in: Fract. Mech. Ceram., Springer, 1974: pp. 829–841.

[29] S.M. Wiederhorn, H. Johnson, A.M. Diness, A.H. Heuer, Fracture of Glass in Vacuum, J. Am. Ceram. Soc. 57 (1974) 336–341.

[30] S.W. Freiman, T.L. Baker, J.B. Wachtman Jr, A computerized fracture mechanics data base for oxide glasses, Am. Ceram. Soc. Bull. 64 (1985) 1452–1455.

[31] A.G. Evans, E.A. Charles, Fracture toughness determinations by indentation, J. Am. Ceram. Soc. 59 (1976) 371–372.

[32] B. Lawn, R. Wilshaw, Indentation fracture: principles and applications, J. Mater. Sci. 10 (1975) 1049–1081.

[33] M.T. Laugier, Toughness determination of some ceramic tool materials using the method of Hertzian indentation fracture, J. Mater. Sci. Lett. 4 (1985) 1542–1544.

[34] C.B. Ponton, R.D. Rawlings, Vickers indentation fracture toughness test Part 1 Review of literature and formulation of standardised indentation toughness equations, Mater. Sci. Technol. 5 (1989) 865–872.

[35] C.B. Ponton, R.D. Rawlings, Vickers indentation fracture toughness test Part 2 Application and critical evaluation of standardised indentation toughness equations, Mater. Sci. Technol. 5 (1989) 961–976.

[36] S. Dériano, A. Jarry, T. Rouxel, J.-C. Sangleboeuf, S. Hampshire, The indentation fracture toughness (K C) and its parameters: the case of silica-rich glasses, J. Non. Cryst. Solids. 344 (2004) 44–50.

[37] T. Fett, K. Germerdonk, A. Grossmuller, K. Keller, D. Munz, Subcritical crack growth and threshold in borosilicate glass, J. Mater. Sci. 26 (1991) 253–257.

[38] M. Inagaki, K. Urashima, S. Toyomasu, Y. Goto, M. Sakai, Work of fracture and crack healing in glass, J. Am. Ceram. Soc. 68 (1985) 704–706.

[39] J.-K. Park, K. Yasuda, Y. Matsuo, Effect of crosshead speed on the fracture toughness of Soda-lime glass, Al2O3 and Si3N4 ceramics determined by the surface crack in flexure (SCF) method, J. Mater. Sci. 36 (2001) 2335–2342.

[40] G.D. Quinn, J.J. Swab, Adventures and Misadventures in Applying ASTM Standard Test Method C 1421 to Measurements of the Fracture Toughness, KIC, of Glasses, Mech. Prop. Perform. Eng. Ceram. Compos. XI. 606 (2017) 29–44.

[41] G.D. Quinn, J.J. Swab, Fracture toughness of glasses as measured by the SCF and SEPB methods, J. Eur. Ceram. Soc. 37 (2017) 4243–4257.

[42] K. Reddy, E.H. Fontana, J.D. Helfinstine, Fracture Toughness Measurement of Glass and Ceramic Materials Using Chevron Notched Specimens, J. Am. Ceram. Soc. 71 (1988).

[43] J. Salem, R. Tandon, Test method variability in slow crack growth properties of sealing

glasses, Int. J. Fatigue. 32 (2010) 557–564.

[44] J.A. Salem, L.J. Ghosn, Back Face Strain for Monitoring Stable Crack Extension in Precracked Flexure Specimens, J. Am. Ceram. Soc. 93 (2010) 2804–2813.

[45] N. Shinkai, R.C. Bradt, G.E. Rindone, Fracture toughness of fused SiO2 and float glass at elevated temperatures, J. Am. Ceram. Soc. 64 (1981) 426–430.

[46] A.A. Wereszczak, C.E. Anderson, Borofloat and Starphire float glasses: a comparison, Int. J. Appl. Glas. Sci. 5 (2014) 334–344.

[47] T. Rouxel, S. Yoshida, The fracture toughness of inorganic glasses, J. Am. Ceram. Soc. (n.d.).

[48] N. Shinkai, R.C. Bradt, G.E. Rindone, Elastic Modulus and Fracture Toughness of Ternary PbO-ZnO-B2O3 Glasses, J. Am. Ceram. Soc. 65 (1982) 123–126.

[49] N. Miyata, H. Jinno, Mechanical Properties of PbO-B_2 0_3 Immiscible Glasses, Bull. Inst. Chem. Res. Kyoto Univ. 59 (1981) 196–206.

[50] A.G. Evans, A method for evaluating the time-dependent failure characteristics of brittle materials-and its application to polycrystalline alumina, J. Mater. Sci. 7 (1972) 1137–1146.

[51] F.F. Lange, The interaction of a crack front with a second-phase dispersion, Philos. Mag. 22 (1970) 983–992.

[52] R.A. Schultz, M.C. Jensen, R.C. Bradt, Single crystal cleavage of brittle materials, Int. J. Fract. 65 (1994) 291–312.

[53] A.A. El-Moneim, Quantitative analysis of elastic moduli and structure of B2O3--SiO2 and Na2O--B2O3--SiO2 glasses, Phys. B Condens. Matter. 325 (2003) 319–332.

[54] T. Rouxel, Fracture surface energy and toughness of inorganic glasses, Scr. Mater. 137 (2017) 109–113.

[55] S. Chakravarty, D.G. Georgiev, P. Boolchand, M. Micoulaut, Ageing, fragility and the reversibility window in bulk alloy glasses, J. Phys. Condens. Matter. 17 (2004) L1.

[56] H. Zeng, Q. Jiang, Z. Liu, X. Li, J. Ren, G. Chen, F. Liu, S. Peng, Unique sodium phosphosilicate glasses designed through extended topological constraint theory, J. Phys. Chem. B. 118 (2014) 5177–5183.

[57] R.K. Kalia, A. Nakano, P. Vashishta, C.L. Rountree, L. Van Brutzel, S. Ogata, Multiresolution atomistic simulations of dynamic fracture in nanostructured ceramics and glasses, Int. J. Fract. 121 (2003) 71–79.

[58] S.W. King, G.A. Antonelli, Simple bond energy approach for non-destructive measurements of the fracture toughness of brittle materials, Thin Solid Films. 515 (2007) 7232–7241.

[59] J.J. Mecholsky Jr, Estimating theoretical strength of brittle materials using fractal geometry, Mater. Lett. 60 (2006) 2485–2488.

[60] R. Miller, E.B. Tadmor, R. Phillips, M. Ortiz, Quasicontinuum simulation of fracture at the atomic scale, Model. Simul. Mater. Sci. Eng. 6 (1998) 607–638.

[61] A. Tilocca, Structural models of bioactive glasses from molecular dynamics simulations, Proc. R. Soc. A Math. Phys. Eng. Sci. 465 (2009) 1003–1027.

[62] A. Bhatnagar, M.J. Hoffman, R.H. Dauskardt, Fracture and Subcritical Crack-Growth Behavior of Y-Si-Al-O-N Glasses and Si3N4 Ceramics, J. Am. Ceram. Soc. 83 (2000) 585–596.

[63] G.G. Naumis, Energy landscape and rigidity, Phys. Rev. E. 71 (2005) 26114-1–7.

[64] F. Wang, S. Mamedov, P. Boolchand, B. Goodman, M. Chandrasekhar, Pressure Raman effects and internal stress in network glasses, Phys. Rev. B. 71 (2005) 174201-1–8.

[65] M. V Chubynsky, M.-A. Briere, N. Mousseau, Self-organization with equilibration: A model for the intermediate phase in rigidity percolation, Phys. Rev. E. 74 (2006) 16116-1–9.

[66] M. Bauchy, B. Wang, M. Wang, Y. Yu, M.J.A. Qomi, M.M. Smedskjaer, C. Bichara, F.-J. Ulm, R. Pellenq, Fracture toughness anomalies: Viewpoint of topological constraint theory, Acta Mater. 121 (2016) 234–239.

[67] J.E. Shelby, Introduction to glass science and technology, Royal Society of Chemistry, 2007.

[68] T. Rouxel, J.-C. Sangleboeuf, The brittle to ductile transition in a soda-lime-silica glass, J. Non. Cryst. Solids. 271 (2000) 224–235.

[69] S.A.M. Spinner, Elastic moduli of glasses at elevated temperatures by a dynamic method, J. Am. Ceram. Soc. 39 (1956) 113–118.

[70] J.B. Quinn, I.K. Lloyd, Comparison of Methods to Determine the Fracture Toughness of Three Glass-Ceramics at Elevated Temperatures, J. Am. Ceram. Soc. 83 (2000) 3070–3076.

[71] A. Ghosh, M.G. Jenkins, K.W. White, A.S. Kobayashi, R.C. Brad, Elevated-temperature fracture resistance of a sintered α-silicon carbide, J. Am. Ceram. Soc. 72 (1989) 242–247.

[72] M. Mizuno, H. Okuda, VAMAS round robin on fracture toughness of silicon nitride, J. Am. Ceram. Soc. 78 (1995) 1793–1801.

[73] T. Fett, D. Munz, Determination of fracture toughness at high temperatures after subcritical crack extension, J. Am. Ceram. Soc. 75 (1992) 3133–3136.

[74] K.D. McHenry, R.E. Tressler, Fracture Toughness and High-Temperature Slow Crack Growth inSiC, J. Am. Ceram. Soc. 63 (1980) 152–156.

[75] A. Micski, B. Bergman, High temperature strength of silicon nitride HIP-ed with low amounts of yttria or yttria/alumina, J. Eur. Ceram. Soc. 6 (1990) 291–301.

[76] J.J. Brennan, K.M. Prewo, Silicon carbide fibre reinforced glass-ceramic matrix composites exhibiting high strength and toughness, J. Mater. Sci. 17 (1982) 2371–2383.

[77] J.L. Henshall, D.J. Rowcliffe, J.W. Edington, Fracture Toughness of Single-Crystal Silicon Carbide, J. Am. Ceram. Soc. 60 (1977) 373–375.

[78] D.C. Harris, Materials for infrared windows and domes: properties and performance, SPIE press, 1999.

[79] M. Zaccaria, M. Overend, Validation of a simple relationship between the fracture pattern

and the fracture stress of glass, in: Eng. Transparency. Int. Conf. Glas. Düsseldorf, Ger., 2012.

[80] P. Klocek, Handbook of infrared optical materials, CRC Press, 2017.

[81] S.. et al. Timoshenko, THEORY OF PLATES AND SHELLS, 1959.

[82] F.F. Vitman, V.P. Pukh, A method for determining the strength of sheet glass, Ind. Lab. 29 (1963) 925–930.

[83] R.J. ROARK, W.C. YOUNG, Formulas for stress and strain, (1975) 624 p. : ill. ; 24 cm.

[84] H. Fessler, D.C. Fricker, A Theoretical Analysis of the Ring-On-Ring Loading Disk Test, J. Am. Ceram. Soc. 67 (1984) 582–588. doi:10.1111/j.1151-2916.1984.tb19598.x.

[85] T. Nose, T. Fujii, Evaluation of Fracture Toughness for Ceramic Materials by a Single Edge Precracked Beam Method, J. Am. Ceram. Soc. 71 (1988) 328–333.

[86] D. Munz, R.T. Bubsey, J.L. Shannon, Performance of chevron-notch short bar specimen in determining the fracture toughness of silicon nitride and aluminum oxide, J. Test. Eval. 8 (1980) 103–107.

[87] ASTM C1421-10, Standard Test Methods for Determination of Fracture Toughness of Advanced Ceramics at Ambient Temperature, ASTM International, West Conshohocken, PA, (2010).

[88] G.R. Anstis, P. Chantikul, B.R. Lawn, D.B. Marshall, A critical evaluation of indentation techniques for measuring fracture toughness: I, direct crack measurements, J. Am. Ceram. Soc. 64 (1981) 533–538.

[89] T. Rouxel, Driving force for indentation cracking in glass: composition, pressure and temperature dependence, Phil. Trans. R. Soc. A. 373 (2015) 20140140.

[90] H. Ji, V. Keryvin, T. Rouxel, T. Hammouda, Densification of window glass under very high pressure and its relevance to Vickers indentation, Scr. Mater. 55 (2006) 1159–1162.

[91] G.M. Renlund, S. Prochazka, R.H. Doremus, Silicon oxycarbide glasses: Part II. Structure and properties, J. Mater. Res. 6 (1991) 2723–2734.

[92] B. Papendorf, E. Ionescu, H.-J. Kleebe, C. Linck, O. Guillon, K. Nonnenmacher, R. Riedel, High-Temperature Creep Behavior of Dense SiOC-Based Ceramic Nanocomposites: Microstructural and Phase Composition Effects, J. Am. Ceram. Soc. 96 (2013) 272–280.

[93] E. Ionescu, C. Balan, H.-J. Kleebe, M.M. Müller, O. Guillon, D. Schliephake, M. Heilmaier, R. Riedel, High-Temperature Creep Behavior of SiOC Glass-Ceramics: Influence of Network Carbon Versus Segregated Carbon, J. Am. Ceram. Soc. 97 (2014) 3935–3942.

[94] C. Stabler, F. Roth, M. Narisawa, D. Schliephake, M. Heilmaier, S. Lauterbach, H.-J. Kleebe, R. Riedel, E. Ionescu, High-temperature creep behavior of a SiOC glass ceramic free of segregated carbon, J. Eur. Ceram. Soc. 36 (2016) 3747–3753.

[95] H.-J. Kleebe, C. Turquat, G.D. Sorarù, Phase Separation in an SiCO Glass Studied by Transmission Electron Microscopy and Electron Energy-Loss Spectroscopy, J. Am. Ceram. Soc. 84 (2001) 1073–1080.

[96] P. Kroll, Searching insight into the atomistic structure of SiCO ceramics, J. Mater. Chem. 20 (2010) 10528–10534.

[97] T. Rouxel, S. Yoshida, The fracture toughness of inorganic glasses, J. Am. Ceram. Soc. 100 (2017) 4374–4396.

[98] T. To, F. Célarié, C. Roux-Langlois, A. Bazin, Y. Gueguen, H. Orain, M. Le Fur, V. Burgaud, T. Rouxel, Fracture toughness, fracture energy and slow crack growth of glass as investigated by the Single-Edge Precracked Beam (SEPB) and Chevron-Notched Beam (CNB) methods, Acta Mater. 146 (2018) 1–11.

[99] J.A. Salem, Transparent armor ceramics as spacecraft windows, J. Am. Ceram. Soc. 96 (2013) 281–289.

[100] S.W. Freiman, S.M. Wiederhorn, J.J. Mecholsky, Environmentally enhanced fracture of glass: A historical perspective, J. Am. Ceram. Soc. 92 (2009) 1371–1382.

ភាពសប្បាយ គឺភាពជោគជ័យ !

Feeling happy means success!

Se sentir heureux, c'est réussir !

UNIVERSITE MATIERE BRETAGNE MOLECULES LOIRE ET MATERIAUX

UNIVERSITÉ DE RENNES 1

Titre : Ténacité et énergie de surface de fracture de verres inorganiques et non métalliques

Mots clés : Ténacité, énergie de surface de fracture, SEPB, CNB, VIF, glass

Résumé :

La ténacité et l'énergie de surface de fracture de verres, de vitrocéramiques et de composites à matrice en verre ont été étudiées.

Tout d'abord, un test de flexion bi-axiale (configuration anneau/anneau) a été réalisé sur des verres de silice et des verre-à-vitres avec différentes conditions de surface afin d'identifier la relation entre le défaut de surface, la résistance et la ténacité du verre. Ensuite, trois méthodes d'expérimentation ont été mises en œuvre, principalement la méthode de poutre de flexion à pre-entaille droit (SEPB), la méthode de la poutre entaillée en chevron (CNB) et la méthode de la poutre avec indentations Vickers (VIF), afin de déterminer la ténacité de quatre verres produits industriellement et de déterminer les avantages et les inconvenients des différents méthodes selectionnées.

La méthode qui est apparue la plus fiable et autocohérente, la méthode SEPB (Single Edge Precrack Beam), a été appliquée à la détermination de la ténacité de nombreux verres et vitrocéramiques, afin d'étudier l'influence de la composition et de la microstructure sur les caractéristiques de fissuration (K_{IC} et énergie de fissuration, γ).

Enfin, l'influence de la température et de l'environnement sur la ténacité a été étudiée à l'aide de la méthode SEPB. Deux verres d'oxyde ont été testés à des températures élevées et avec une vitesse de charge de 10 MPa·√m/s, une température de transition de 1,11Tg a été trouvée. Quatre autres verres d'oxyde ont été testés en environnement inerte et les mêmes valeurs de ténacité ont été obtenues à partir de deux vitesses de charge (100 fois) différentes.

Title : Fracture toughness and fracture surface energy of inorganic and non-metallic glasses

Keywords : Fracture toughness, fracture surface energy, SEPB, CNB, VIF, glass

Abstract :

Fracture toughness and fracture surface energy of commercial and laboratory glasses, glass-ceramics and glass matrix composites have been studied.

First, bi-axial bending test (RoR configuration) was performed on fused silica and window float glasses with different surface conditions to identify the relationship between the surface flaw, the strength and fracture toughness. After, three experiment methods, mainly single-edge precracked beam (SEPB), chevron-notched beam (CNB) and Vickers indentation fracture (VIF) were performed to determine the fracture toughness of four commercial known glasses and to determine the advantages and inconveniences of the different selected methods.

The method that is appeared as the most reliable and self-consistent, the SEPB (Single Edge Precrack Beam) method, was applied to determine the toughness of the large amount of glasses and glass-ceramics, to study the influence of the composition and the microstructure on the characteristics of cracking (K_{IC} and fracture energy, γ).

Last but not least, the influence of the temperature and environment on the fracture toughness was studied by means of the SEPB method. Two oxide glasses were tested in elevated temperatures and with the loading rate of 10 MPa·√m/s, a transition temperature of $1.11T_g$ was found. Four other oxide glasses were tested in the inert environment and the same fracture toughness values were obtained from (100 times) two different cross-head speeds.